Phenomenology of the Higgs and Flavour Physics In the Standard Model and Beyond

D I S S E R T A T I O N

zur Erlangung des akademischen Grades

doctor rerum naturalium
(Dr. rer. nat.)
im Fach Physik

eingereicht an der
Mathematisch-Wissenschaftlichen Fakultät
Humboldt-Universität zu Berlin

von
M.Sc. Lina Alasfar
geboren am 27. 09. 1994 in Riad

Präsidentin der Humboldt-Universität zu Berlin:
Prof. Dr.-Ing. Dr. Sabine Kunst

Dekan der Mathematisch-Wissenschaftlichen Fakultät:
Prof. Dr. Elmar Kulke

Gutachter:
1. Prof. Dr. R. Gröber, Humboldt-Universität zu Berlin
2. Prof. Dr. Dr. M. Musterman, Potsdam-Institut fur Klimafolgenforschung
3. Prof. Dr. M. Mustermann2, Heidelberg

Tag der mündlichen Prüfung: 06. November 2013

Abstract

Since the discovery of the Higgs boson in 2012 at the Large Hadron Collider (LHC), most of its properties have been already measured with increasing accuracy. However, few of the Higgs's main properties are yet to be probed. The future runs of the LHC hold a lot of potential for further understanding of the Higgs boson's properties.

Many of Higgs production processes are plagued by large theoretical uncertainties. In order to reduce them, these processes need to be computed at higher precision. One of such processes is the production of the Higgs with he Z boson. This is a key process in measuring both the Higgs mass and its couplings with more precision. My collaborators and I have preformed such calculation using a novel method that can be used alongside other calculations via Padé approximants and then incorporated into Monte Carlo event simulations [1].

In an another project, we have studied the correlations between the Higgs self-interaction and other set of interactions involving four heavy quarks. Both interaction classes are equally weakly constrained from current LHC data. Using Markov-chain Monte Carlo (MCMC) Bayesian analysis, we have seen that there is a strong correlations amongst these observables. Revealing many challenges to probing Higgs self-coupling using current Higgs measurements [**?**].

The only direct way to study the Higgs self-coupling is to search for Higgs bosons produced in pairs. A process that is sought after in the High-Luminosity (HL)-LHC. We have used interpretable machine learning to improve upon the expected sensitivity of the HL-LHC and future colliders to this process. We were able to constrain both the Higgs's self interaction and its interaction with light quarks, and show that they are uncorrelated from this process [2**?**].

Since 2015, experimental data was hinting towards an anomaly involving the decay of composite particles known as B-mesons that could be a result of new physics beyond the Standard Model. We have used (MCMC) Bayesian analysis to show that the parameters characterising new physics in these decays are strongly related to other set of parameters in the Standard Model related to the interaction between the Z and Higgs bosons, and muons [3].

Keywords: Higgs Physics, Standard Model Effective Field Theory, Flavour observables, Statistical data analysis

Zusammenfassung

Schlagwörter: Higgs Physik, Standardmodell Effektive Feldtheorie, Flavour Anomalies, Statistische Datenanalyse

Contents

List of abbreviations

Colliders and working groups .

CERN Conseil européen pour la recherche nucléaire.

LHC Large Hadron Collider

HL-LHC High-Luminosity LHC

CMS Compact Muon Solenoid

ATLAS A Toroidal LHC ApparatuS

LEP Large Electron-Positron Collider

ALEPH Apparatus for LEp PHysics

SLC Stanford Linear Collider

FCC Future circular collider

HXSWG Higgs cross-section working group

PDG Particle data group

Higgs and Standard Model physics.

SM Standard Model

QCD Quantum chromodynamics

QED Quantum electrodynamics

EFT Effective field theory

SMEFT Standard Model effective field theory

HEFT Higgs effective field theory

EW Electroweak

VEV/ vev Vacuum expectation value

EWSB Electroweak symmetry breaking

EWPO Electroweak precision observables

EWChL Electroweak chiral Lagrangian

SSB Spontanious symmetry breaking

$SU(N)$ Special unitary (group) of dimension N

ggF Gluon fusion (processes)

$q\overline{q}$A Quark anti-quark anhitation (processes)

PDF Parton distribution functions

STXS Simplified template cross-sections

Higher order computations.

RGE Renormalisation group equation or evolution

LO, NLO ... Leading order, Next to leading order etc.

HPL Harmonic polylogarithms

GPL Generalised polylogarithms

Flavour.

CKM Cabibbo-Kobayashi-Maskawa-Matrix

$\mathcal{CP}$ Charge conjugation and parity

MFV Minimal flavour violation

AFV Aligned flavour violation

SFV Spontanious flavour violation

PDD Phenomenological data-driven

PMD Phenomenological model-driven

FCNC Flavour-changing neutral currents

LUV Lepton universality violation

Data analysis/statistics.

MC Monte Carlo (simulation)

ML Machine learning

BDT Boosted decision tree

XGBoost EXtreme gradient boosted decision tree

MCMC Markov chain Monte Carlo (Bayesian analysis)

PCo Principle component

FDR False discovery rate

ANOVA Analysis of variation

New Physics.

4F Four-fermion

NP New physics

BSM Beyond the Standard Model

VLQ Vector-like quarks

LQ Leptoquarks

2HDM Two-Higgs-doublet model

CHM Composite Higgs model

MSSM Minimal supersymmetric Standard Model

SILH Strongly interacting light Higgs

Part I

Higgs Physics

1 The Standard Model Higgs boson

> It's very nice to be right sometimes...
> it has certainly been a long wait.
>
> *Peter Higgs*

1.1 Spontaneous symmetry breaking

Before talking about symmetry breaking, we need to discuss the concept of symmetry in physics. Symmetry is a crucial part in studying physical systems. It manifests not only as a geometric feature of physical objects but also in the dynamics of physical systems. For example, one can find symmetries in the equation of motion, Lagrangians/Hamiltonians and actions. The magnetisation of materials is a good example of the role that symmetry plays in describing physical behaviour. For instance, paramagnetic materials have a positive magnetic susceptibility χ_B due to the random arrangement of their electrons' spins. The paramagnetic material spins arrangement will therefore possess rotational symmetry. The material has no *preferred direction* in space [4]. Au contraire ferromagnetic materials with the electrons' spins aligned in a certain direction, will not have such symmetry as there will be a preferred direction, see Figure 1.1.

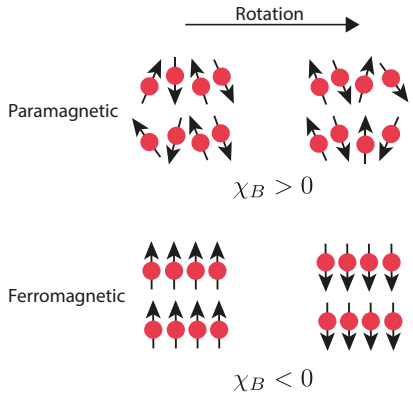

Figure 1.1. In paramagnetic materials, the spins are randomly distributed such that a rotation performed on the system will keep the spin distribution invariant. However, for ferromagnetic materials, where the spins are aligned in a single direction, the symmetry is broken, and the system has a preferred direction.

In particle physics and quantum field theory, symmetry plays an essential role in the

taxonomy and dynamics of elementary particles and their bound states, i.e. hadrons, cf. [5, 6]. There are two types of symmetries considered when studying elementary particles and their quantum fields: external and internal symmetries. The first is the symmetry of the spacetime background. Typically, this is a four-dimensional Poincaré symmetry. However, in some models, higher spacetime dimensions or non-flat geometries are considered. Though there is no current evidence of higher dimensions or indications of non-flat spacetime from colliders and cosmological observations [7]. The second class of symmetries is internal symmetries stemming from the quantum nature of these particles/fields. Because their state is described by a ray in complex Hilbert/Fock spaces, internal symmetries are simply symmetries of rotations in these spaces that keep the action variation unchanged. Internal symmetries are usually described in terms of simple or product of simple Lie groups, e.g. $SU(N)$ [1], and particles/fields will be arranged as multiplets in some representation of the groups. If the rotations of the states could be parametrised by constants, the symmetry is called global. Alternatively, if these transformations are themselves functions of the spacetime, the symmetry is then called local or **gauged**.

Gauge symmetries describe rotations in the state space that depend on spacetime, the generator of the gauge transformations could propagate between two spacetime points. This is the way particle interactions are described in quantum field theory. The generators of these gauge transformations are called gauge bosons, and they mediate the interactions between the particles and hence transform under the adjoint representation of the gauge group. Gauge symmetries are the basis of describing the fundamental interactions of nature, called gauge theories.

An example of a gauge theory that is realised in nature is the **Standard Model** (SM), which is a gauge theory based on the group $G_{\text{SM}} := SU(3)_C \otimes SU(2)_L \otimes U(1)_Y$. The first simple group is for the *strong* interaction described by quantum chromodynamics (QCD). The product of the two remaining groups $SU(2)_L \otimes U(1)_Y$ forms the Weinberg-Salam *electroweak* (EW) model [10–12], where $SU(2)_L$ describes the weak interaction which only couples to *left handed* fermions and $U(1)_Y$ is the weak hypercharge Y gauge group, defined by the formula

$$Y = 2(Q - T_3). \tag{1.1}$$

Where Q is the electric charge and T_3 is the third component of the weak isospin. A description of the matter content of the SM and their multiplicities with respect to G_{SM} is shown in Table 1.1

The SM has been very successful at describing particle interactions even when challenged by numerous precision tests at LEP and SLD [14–17], and later at DØ [18] and the LHC [19, 20] Nevertheless, it fails to describe the ground state if only the fermion and gauge sectors are considered. The reason for this shortcoming is that the $W^{\pm}$ and Z bosons are massive, this violates the EW gauge symmetry. This can be easily seen by

[1] Gauge theories based on finite groups have been proposed in the literature, but their phenomenological significance is yet to be further investigated [8, 9]

Particle/Field	G_{SM} multiplicity	mass [GeV]
	Quarks	
$Q = \binom{u_L}{d_L}, \binom{c_L}{s_L}, \binom{t_L}{b_L}$	$(\mathbf{3}, \mathbf{2})_{\frac{1}{6}}$	$m_u = 2.16 \cdot 10^{-3}$, $m_d = 2.67 \cdot 10^{-3}$
$U = u_R, c_R, t_R$	$(\mathbf{3}, \mathbf{1})_{\frac{2}{3}}$	$m_c = 0.93 \cdot 10^{-2}$, $m_s = 1.27$
$D = d_R, s_R, b_R$	$(\mathbf{3}, \mathbf{1})_{-\frac{1}{3}}$	$m_t = 172.4$, $m_b = 4.18$
	Leptons	
$L = \binom{\nu_{e,L}}{e_L}, \binom{\nu_{\mu,L}}{\mu_L}, \binom{\nu_{\tau,L}}{\tau_L}$	$(\mathbf{1}, \mathbf{2})_{-\frac{1}{2}}$	$m_e = 0.511 \cdot 10^{-3}$, $m_\mu = 1.05 \cdot 10^{-2}$
$E = e_R, \mu_R, \tau_R$	$(\mathbf{1}, \mathbf{1})_{-1}$	$m_\tau = 1.77$,m_ν =??
	Gauge bosons	
$g/G^A_\mu, \;\; A = 1 \ldots 8$	$(\mathbf{8}, \mathbf{1})_0$	0.0
γ/A_μ	$(\mathbf{1}, \mathbf{1})_0$	0.0
$W^\pm_\mu$	$(\mathbf{1}, \mathbf{3})_0$	80.379
Z_μ	$(\mathbf{1}, \mathbf{3})_0$	91.1876
	The Higgs boson	
h	$(\mathbf{1}, \mathbf{2})_{\frac{1}{2}}$	125.10

Table 1.1. The SM constituents, their multiplicities with respect to the SM gauge group $G_{\mathrm{SM}} := SU(3)_C \otimes SU(2)_L \otimes U(1)_Y$ and masses. The mass of the neutrinos ν is zero according to the SM prediction, but observations suggest that they are massive, and only the difference between the three masses is known [13]. The values of the masses are taken from the Particle Data Group (PDG) [7], and used throughout this thesis.

looking at the mass term of a spin 1 field B_μ^A

$$\mathcal{L} = m_B B^{A,\mu} B_\mu^A, \tag{1.2}$$

and performing an $SU(N)$ gauge transformation

$$B_\mu^A \to B_\mu^A + \partial_\mu \Lambda^A + g\,\varepsilon_{BC}^A B_\mu^B \Lambda^C. \tag{1.3}$$

We see that the mass term does not preserve gauge symmetry. Secondly, because the SM is a chiral theory, as only left-handed fermions are doublets under $SU(2)_L$. Thus, the Dirac mass term

$$\mathcal{L}_\mathrm{D} = m_D \overline{\psi}_L \psi_R + \mathrm{h.c.}, \tag{1.4}$$

cannot be a singlet under $SU(2)_L$, therefore violates the EW symmetry. Despite quark and lepton masses being forbidden by the EW symmetry, we have already measured their masses, and since they also carry charges this mass has to be a Dirac mass.

In order for the EW model to be consistent in the ground state like it is in the interaction states. A mechanism for spontaneous symmetry breaking (SSB) needed to be introduced.

1.1.1 Nambu-Goldstone theorem

Coming back to the example of the paramagnetic-ferromagnetic materials, when a ferromagnetic metal is heated above a certain temperature, known as the Curie Temperature T_C, it will undergo a phase transition and become paramagnetic. In the mean-field theory approximation the magnetic susceptibility is related to the temperature of the metal via the relation

$$\chi_B \sim (T - T_C)^{-\gamma}, \tag{1.5}$$

where γ is called a critical exponent. We see that if the metal temperature $T > T_C$ the metal is in an *disordered phase* and when $T < T_C$ it is in the *ordered phase*, i.e. χ_B is the order parameter of this system. At the Curie temperature, the system will be at the *critical point* and the susceptibility is divergent. The exponent γ cannot be used to describe the system at the critical point.

There is a "pictorial" description of the metal at the critical point which is helpful in understanding the Nambu-Goldstone theorem. Starting at $T > T_C$, the metal would be in a paramagnetic phase, where the spins are randomly arranged. As the temperature becomes lower and lower, thermal fluctuations start to lessen. In some regions of the metal, the spins will start to get aligned With continued cooling, nearing T_C, these turned spins will affect their neighbours by flipping their direction. At the critical point $T = T_C$, the system behaves in a peculiar manner, when one would see regions of spins in "up" and others in "down" directions. The system will resemble a fractal of these regions, becoming scale-invariant. Additionally, waves of oscillating local magnetisation will propagate. These waves, or spinless quasiparticles (called Magnons) are Goldstone bosons emerging from SSB Which will manifest at $T < T_C$ as the spins will be arranged

in a certain single direction and the metal becomes ferromagnetic.

The Nambu-Goldstone theorem

When a continuous symmetry has a conserved currents but broken in the ground state (vacuum) is called to be spontaneously broken. There is a scalar boson associated with each broken generator of this spontaneously broken symmetry. The modes of these bosons are fluctuations of the order parameter.

This theorem first emerged from condensed matter physics, particularly superconductors [21, 22]. However, it soon got applied to relativistic quantum field theories [23].

1.2 The Braut-Englert-Higgs mechanism

In order to solve the aforementioned shortcomings of the Weinberg-Salam model, Nambu-Goldstone theorem has been first proposed by P. W. Anderson [24]. However, the way that Anderson formulated his theory was unfamiliar to particle physicists and used a non-relativistic picture to illustrate how photons could gain mass in an electron plasma with a plasma frequency ω_p

$$m_\gamma^{\text{plasma}} = \frac{\hbar\omega_p}{c^2} \tag{1.6}$$

Later on, a theory that explains the mass generation of the EW gauge bosons has been published in an almost simultaneous manner by R. Braut and F. Englert [25], P. Higgs [26] and G. Guralnik, C. R. Hagen, and T. Kibble [27, 28][2]. The Higgs mechanism starts by considering the SSB of the electroweak sector of the SM via the pattern

$$SU(2)_L \otimes U(1)_Y \longrightarrow U(1)_Q \tag{1.7}$$

This is achieved by the vacuum expectation value (vev) of a complex scalar field $\phi \sim (\mathbf{1}, \mathbf{2}, +1/2)$, with the Lagrangian

$$\mathcal{L} = D_\mu\phi^* D^\mu\phi - V, \qquad V := \mu^2\phi^*\phi + \lambda(\phi^*\phi)^2, \tag{1.8}$$

with V denoting the Higgs potential, illustrated in Figure 1.2, which gives non-vanishing vacuum for $\mu^2 < 0$. The field ϕ is given explicitly by

$$\phi = \begin{pmatrix} \phi^1 + i\phi^2 \\ \frac{1}{\sqrt{2}}(h+v) - i\phi^3 \end{pmatrix} \tag{1.9}$$

The covariant derivative

$$D_\mu = \partial_\mu - ig_2\frac{\sigma_a}{2}W_\mu^a - ig_1\frac{1}{2}B_\mu, \tag{1.10}$$

[2] All of these authors have contributed to the theory of SM (SSB). By calling it the "Braut-Englert-Higgs" mechanism or the "Higgs" boson. I, by no means, have intended to ignore the role played by the rest, rather, I wanted to stick the most widely-used terminology in the field.

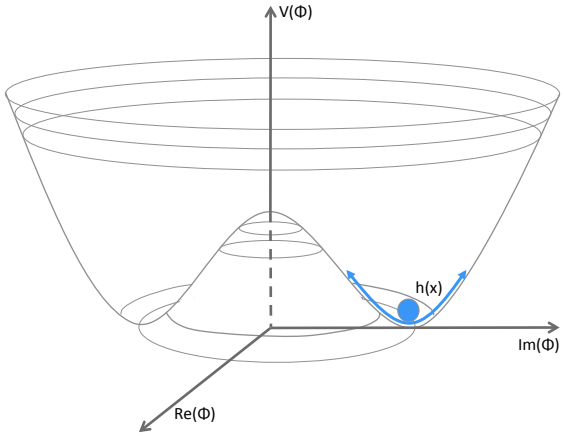

Figure 1.2. The characteristic shape of the Higgs potential showing a non-zero vacuum. While thee physical Higgs boson is an oscillation within the energy well illustrated in the diagram with blue arrows., this illustration is taken from [29].

dictates the coupling between the Higgs field and the EW gauge bosons and g_3, g_2 and g_1 are, respectively, the coupling constants of $SU(3)_C$, $SU(2)_L$ and $U(1)_Y$. The minimum of the scalar potential is obtained by

$$\frac{\partial V}{\partial \phi} \mid_{\phi \to v} = 0, \tag{1.11}$$

which for a tachyonic mass $\mu^2 < 0$ will have a real non-vanishing values v corresponding to the vev of this field $\langle \phi \rangle = \begin{pmatrix} 0 \\ \frac{v}{\sqrt{2}} \end{pmatrix}$.

According to Nambu-Goldstone theorem, the three broken generators of $SU(2)_L \otimes U(1)_Y$ will become massive, and they are the $W^{\pm}$ and Z bosons, while the photon will remain massless. We will have three massless Goldstone bosons $G^{\pm} = \frac{1}{2}(\phi^1 \pm i\phi^2)$ and $G^0 = \phi^3$ that are "eaten" by the aforementioned massive $W^{\pm}$ and Z bosons, where they become their longitudinal polarisations. In order to see this more concretely, we start by looking at the terms of the EW Lagrangian where the field ϕ couples to the gauge bosons, in the unbroken phase

$$D_\mu \phi^* D^\mu \phi = \frac{1}{2}|\partial_\mu \phi|^2 + \frac{1}{8} g_2^2 |\phi|^2 |W_\mu^1 + i W_\mu^2|^2 + \frac{1}{8}|\phi|^2 |g_2 W_\mu^3 - g_1 B_\mu|^2 \tag{1.12}$$

After SSB, we write the gauge bosons in the mass basis

$$\begin{aligned} W_\mu^\pm &= \frac{1}{\sqrt{2}}(W_\mu^1 \pm iW_\mu^2), \\ Z_\mu &= \frac{1}{\sqrt{g_1^2+g_2^2}}\left(g_2 W_\mu^3 - g_1 B_\mu\right), \\ A_\mu &= \frac{1}{\sqrt{g_1^2+g_2^2}}\left(g_2 W_\mu^3 + g_1 B_\mu\right). \end{aligned} \tag{1.13}$$

From this, the electric change is identified as the coupling constant to the photon A_μ

$$e = \frac{g_1}{\sqrt{g_1^2+g_2^2}}. \tag{1.14}$$

It is useful to define the Weinberg angle θ_W, an important EW parameter relating the electric charge to the weak coupling g_2

$$\sin\theta_W = \frac{e}{g_2} \approx 0.231214, \tag{1.15}$$

typically the sin and cos of the Weinberg angle are denoted by s_W and c_W, respectively. We use the unitary gauge, to absorb the Goldstone bosons into the $W^\pm$ and Z longitudinal polarisations. In this gauge the Higgs doublet can be written as

$$\phi \to \begin{pmatrix} 0 \\ \frac{1}{\sqrt{2}}(h+v). \end{pmatrix}, \qquad v = 246\,\text{GeV}. \tag{1.16}$$

With these substitutions, one can read off the masses of the gauge bosons from their bilinear terms in (1.12)

$$m_W = \frac{v g_2}{2} \qquad m_Z = \frac{v}{2}\sqrt{g_1^2+g_2^2} \qquad m_A = 0. \tag{1.17}$$

Since ϕ is a complex doublet. We have seen that it has four components, and three of them correspond to the Goldstone bosons, thus one remains physical field $h(x)$ which is what we now identify with the "Higgs boson" discovered in the Summer of 2012 [30, 31]. The couplings between the Higgs and the electroweak bosons is related to their mass via the vev

$$g_{hVV} = \frac{2m_V^2}{v}, \qquad g_{hhVV} = \frac{2m_V^2}{v^2}. \tag{1.18}$$

By substituting (1.16), into the Higgs potential (1.8) one can also write the mass of the physical Higgs boson in terms of the vev

$$m_h = \sqrt{2\lambda}v. \tag{1.19}$$

The Higgs boson mass is related to the μ parameter via the relation

$$m_h^2 = -2\mu^2, \tag{1.20}$$

One can see that the mass term after SSB changes its sign, characterising the order-parameter for this system, analogous to the magnetic susceptibility for the magnetisation of materials example. One could also identify the self-couplings of h, the trilinear and quartic couplings

$$g_{hhh} = 3\lambda v = 3\frac{m_h^2}{v}, \qquad g_{hhhh} = 3\lambda = 3\frac{m_h^2}{v^2}. \tag{1.21}$$

1.3 Yukawa interaction

It is possible to also use the Higgs vev to give fermions their masses by introducing Yukawa-interaction terms, first introduced by S. Weinberg [12]

$$\mathcal{L}_{\text{Yuk}} = -y_e\,\overline{L}\,\phi\,E - y_d\,\overline{Q}\,\phi\,D - y_u\,\overline{Q}\,\tilde{\phi}\,U \;\; + \text{h.c.}, \tag{1.22}$$

with $\tilde{\phi} = i\sigma_2\phi$ and y_e, y_d, y_u are 3×3 matrices. These matrices are free parameters in the SM. As the Higgs boson acquires a the vev, the fermions will acquire a mass $m_f = vy'_f$ and the Higgs boson coupling to the fermions is given by

$$g_{h\bar{f}f} = \frac{m_f}{v}, \tag{1.23}$$

and the Yukawa matrices will be fixed in the mass basis y'_f by measurements of the fermion masses.
Leptonic Yukawa matrix is diagonal, with a degeneracy between the flavour and masses basis, this manifests as lepton family number conservation (the lepton family operator commutes with the Hamiltonian.). However, for the quarks, the situation is more complicated. One can rotate these matrices to the mass basis via a bi-unitary transformation via the unitary matrices $\mathcal{V}_q, \mathcal{U}_q$ for $q = u, d$

$$y_q \longrightarrow y'_q = \mathcal{V}_q^\dagger\, y_q\, \mathcal{U}_q = \text{diag}\left(m_{q_1}, m_{q_2}, m_{q_3}\right). \tag{1.24}$$

However, the is no degeneracy here as the Hamiltonian does not commute with the quark flavour operator. This is because the transformation matrices for the up and down-type quarks are not the same. The charged EW quark currents contain flavour mixing described by the Kabibbo-Kobayashi-Maskawa (CKM) matrix [32, 33]. Figure 1.3 shows all the SM couplings' strengths, with the thickness of the chord is proportional to the strength of the coupling, on can see the Higgs couplings in orange. In this figure, we cannot easily see Higgs coupling to the fermions, except for its couplings to the third generation. Strictly speaking, if we further examined the Yukawa coupling using a logarithmic scale and focused on the quark sector as Figure 1.4 illustrates. We observe that these Yukawa couplings span about 6 orders of magnitudes with marked hierarchy

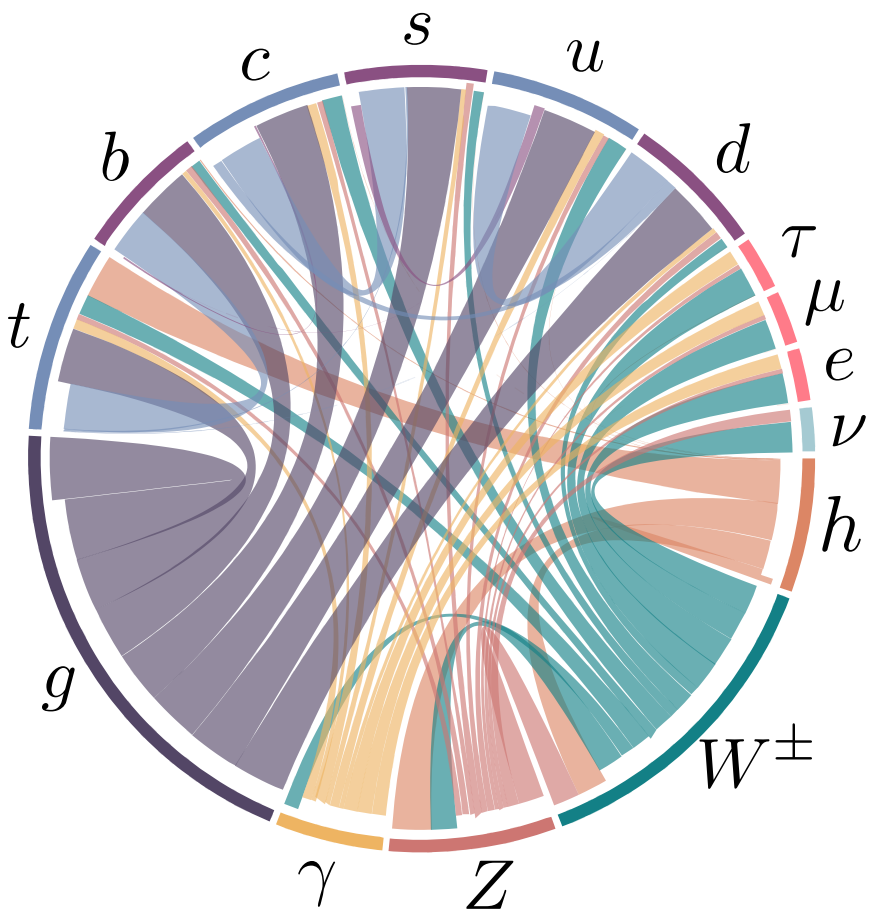

Figure 1.3. A chord diagram showing the SM couplings, with the coupling strength illustrated by the chord thickness. Higgs couplings are coloured in orange.

amongst generations. As these couplings are in fact free parameters in the SM, and only determined by the experimental measurements of the quark (or equally applies lepton) masses. This hierarchy of quark masses therefore cannot be explained by the SM Braut-Englert-Higgs mechanism, and sometimes known as the "old" flavour puzzle. In later chapters, we will examine the experimental effort to better measure these couplings and how Higgs pair production can be used to probe them in chapter 8. Even the potential of using techniques from *interpretable machine learning* to further improve Higgs pair sensitivity to probing light quarks Yukawa couplings **??**.

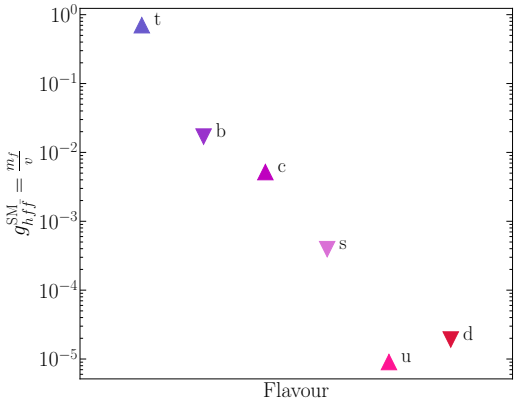

Figure 1.4. The SM Yukawa couplings are proportional to the quark masses, because of the the Higgs Yukawa couplings span about 6 orders of magnitude, as seen in the case of quarks here. This large hierarchy cannot be explained by the SM.

1.4 The Higgs and EW precision observables

Higgs physics is deeply intertwined with the EW sector as many of the Higgs parameters are linked to EW observables. For instance, the Higgs vev is determined from Fermi's constant $v = (\sqrt{2}G_F)^{-1/2}$, which is in tern fixed by the muon lifetime τ_μ measurements [34–37]. This can be seen when we examine the theoretical prediction for τ_μ

$$\tau_\mu^{-1} = \frac{G_F^2 m_\mu^5}{192\pi^3}\left(1 - \frac{8m_e^2}{m_\mu}\right)\left[1 - 1.810\frac{\alpha}{\pi} + (6.701 \pm 0.002)\left(\frac{\alpha}{\pi}\right)^2\right], \tag{1.25}$$

then comparing this formula with τ_μ experimental measurements. This confrontation leads to a very precise measurement on G_F [7]

$$G_F = 1.1663787(6) \cdot 10^{-5}\mathrm{GeV}^{-2}, \tag{1.26}$$

given the value of the fine structure constant $\alpha^{-1} = 137.03599976(50)$.

Another important EW precision observable (EWPO) is the ratio between the W and

Z masses

$$\rho = \frac{m_W^2}{c_W^2 m_Z^2}. \tag{1.27}$$

At leading order (LO), this parameter is equal to unity in the SM. The ρ parameter depends on the representation of the scalar sector of the EW model having ϕ_i scalars with T_i weak isospin and $T_{3,i}$ being its third component, and a vev v_i, via the relation [38, 39]

$$\rho = \frac{\sum_i [T_i(T_i+1) - T_{3,i}^2] v_i^2}{2\sum_i T_{3,i}^2 v_i^2}. \tag{1.28}$$

From (1.28) one can see that a real triplet scalar, for instance, would not fit the experimental EW measurement of ρ. Hence, a complex doublet is the simplest scalar possible for the EW symmetry breaking. However, radiative corrections to the EW gauge bosons mass from vacuum polarisation diagrams could potentially cause ρ to deviate significantly from unity. This is not the case, as the experimentally measured value of ρ [7]

$$\rho_{\text{exp}} = 1.00038 \pm 0.00020 \tag{1.29}$$

Additionally, it is possible to think of an extended Higgs sector, where there are multiple scalars with different $SU(2)_L$ multiplicities. Or, a composite Higgs sector, where the Higgs boson is a pseudo Nambu-Goldstone boson, cf. [40, 41]. How can such models be built assuring the ρ parameter is protected from change ? The answer to this question lies in a symmetry of the Higgs Lagrangian known as custodial symmetry.

1.4.1 Custodial symmetry

After SSB, a residual global symmetry known as the custodial symmetry protects the ρ parameter from obtaining large radiative corrections at higher orders in perturbation theory. This symmetry must be kept in extended or composite Higgs models. This symmetry can be seen by rewriting the Higgs potential as

$$V = \frac{\lambda}{4}\left(\phi_1^2 + \phi_2^2 + \phi_3^2 + \phi_4^2 - 2\mu^2\right)^2. \tag{1.30}$$

This potential is invariant under $SO(4) \simeq SU(2)_L \otimes SU(2)_R$ rotations. However, when the Higgs field acquires a non-vanishing vev, $\phi_4 \to h + v$, the potential becomes

$$V = \frac{\lambda}{4}\left(\phi_1^2 + \phi_2^2 + \phi_3^2 + h^2 + 2vh + v^2 - 2\mu^2\right)^2, \tag{1.31}$$

which is only invariant under $SO(3) \simeq SU(2)_V$ transformations, the diagonal part of the original group. This global SSB pattern comes alongside the EW-SSB of the gauge group $SU(2)_L \otimes U(1)_Y$ as global $SU(2)_L$ is itself the gauged $SU(2)_L$ group. Additionally the T_3 component of the $SU(2)_R$ global group is the gauged $U(1)_Y$ and the T^3 component of the custodial group $SU(2)_V$ is gauged as well and identified to be the electric charge

operator, i.e. the generator of $U(1)_Q$.

$$\underbrace{SU(2)_R}_{\supset U(1)_Y} \otimes \overbrace{SU(2)_L}^{\text{gauged}} \longrightarrow \underbrace{SU(2)_V}_{\supset U(1)_Q}. \tag{1.32}$$

This pattern indicates that the symmetry is already broken by the gauging of the diagonal part of $SU(2)_R$ (the hypercharge). The custodial symmetry is only *approximate* in the limit of $g_1 \to 0$, and $\rho = 1$ is a consequence of $g_1 \neq 0$. The symmetry breaking pattern $\mathbf{2} \otimes \mathbf{2} = \mathbf{3} \oplus \mathbf{1}$ also allows us to identify the Goldstone bosons as the custodial triplet and the physical Higgs h as the custodial singlet, explaining the electric charge pattern they have.
We could use the isomorphism between the special orthogonal and special unitary groups to parametrise the Higgs doublet as an $SU(2)_L \otimes SU(2)_R$ bidoublet

$$\mathcal{H} = (\tilde{\phi} \;\; \phi) = \frac{1}{\sqrt{2}} \begin{pmatrix} \phi_4 - i\phi_3 & \phi_1 + i\phi_2 \\ \phi_1 - i\phi_2 & \phi_4 + i\phi_3 \end{pmatrix}, \tag{1.33}$$

with the bi-unitary transformations

$$\mathcal{H} \longrightarrow \mathcal{U}_L \mathcal{H} \mathcal{U}_R^\dagger \tag{1.34}$$

which leaves any traces of the form $\mathrm{Tr}(\mathcal{H}^\dagger \mathcal{H})$, invariant. The Higgs potential could be rewritten in terms of the bidoublet

$$V = -\frac{\mu^2}{2} \mathrm{Tr}(\mathcal{H}^\dagger \mathcal{H} + \frac{\lambda}{4} \left(\mathrm{Tr}(\mathcal{H}^\dagger \mathcal{H} \right)^2 \tag{1.35}$$

The vev is hence written in this representation as

$$\langle \mathcal{H} \rangle = \frac{v}{\sqrt{2}} \mathbb{1}_{2\times 2}. \tag{1.36}$$

We can also look at the Yukawa sector, and observe that in the case where $y_u = y_d = y$, we can also write the left-handed and right-handed quarks as $SU(2)_L \otimes SU(2)_R$ bidoublets and $SU(2)_R$ doublets, respectively. Hence, the quark part of the Yukawa Lagrangian in (1.22) becomes

$$\mathcal{L}_{yuk} \supset \frac{y}{\sqrt{2}} (\overline{u}_L \;\; \overline{d}_L) \begin{pmatrix} \phi_4 - i\phi_3 & \phi_1 + i\phi_2 \\ \phi_1 - i\phi_2 & \phi_4 + i\phi_3 \end{pmatrix} \begin{pmatrix} u_R \\ d_R \end{pmatrix}, \tag{1.37}$$

which is invariant under custodial transformations, but when $y_u \neq y_d$, this Lagrangian term breaks custodial symmetry. Thus, the differences between the up-type and down-type quark masses $m_u - m_d$ are considered **spurions** of the custodial symmetry and one expects to see radiative corrections to ρ being proportional to these spurions.

In order to see this more concretely, we start by examining the radiative corrections

that could lead to a deviation of ρ from unity($\Delta\rho$). These corrections are known as the **oblique correction**, that come from electroweak vacuum polarisations $\Pi_{VV}(p^2)$, as shown in Figure 1.5, for more details on these corrections and their calculation see refs.. [42, 43]

The one-loop correction to the ρ parameter is given in terms of the Π_{VV} by

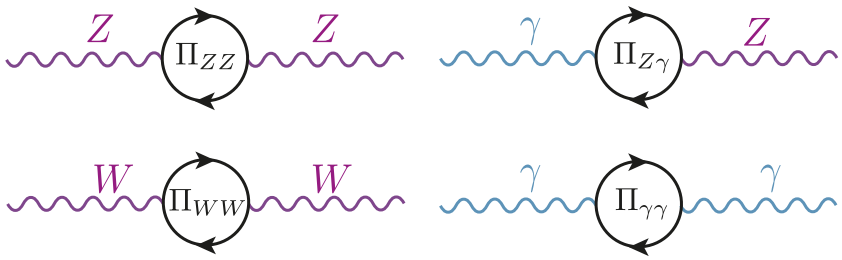

Figure 1.5. The oblique corrections, are radiative correction with electroweak gauge bosons propagators. Namely vacuum polarisations of the Z, $W^{\pm}$ and γ bosons.

$$\Delta\rho = \frac{\Pi_{WW}(0)}{m_W^2} - \frac{\Pi_{ZZ}(0)}{m_Z^2} \tag{1.38}$$

Where the dominant contributions are given by [44]

$$\Delta\rho = \frac{3G_F}{8\sqrt{2}\pi^2}\left((m_t^2 - m_b^2) - \frac{2m_t^2 m_b^2}{m_t^2 - m_b^2}\ln\frac{m_t^2}{m_b^2}\right) + \dots . \tag{1.39}$$

Since $m_b \ll m_t$, the correction is non-vanishing, and (1.39) shows clearly how the radiative corrections are proportional to the spurions of the custodial symmetry. However, this radiative correction is absorbed into the SM definition of ρ, i.e. the $\overline{\text{MS}}$ definition of the ρ-parameter $\rho^{\overline{\text{MS}}}$.

One can study new physics (NP) effects that violates custodial symmetry, by looking at deviations from $\rho = 1$coming from the NP degrees of freedom. Given the experimentally measured value of ρ (1.29) many NP models violating custodial symmetry can already be excluded. Nevertheless, ρ alone does not capture the full story of EWPO's. For instance, adding a new quark doublet would not necessarily violate the custodial symmetry though it still can be excluded by EWPO. It is hence useful to introduce new parameters known as **the oblique parameters** [43, 45–48] [3]

[3] The are also called the Peskin–Takeuchi parameters, however, W. Marciano and J. Rosner also D. Kennedy and P. Langacker published the same parametrisation proposals almost simultaneously. Therefore, I preferred not to use this eponym, instead calling them the oblique parameters, as they stem from the oblique corrections .

The oblique parameters

$$
\begin{aligned}
S &:= \frac{4c_W^2 s_W^2}{\alpha}\left[\frac{\Pi_{ZZ}^{\rm NP}(m_Z^2)-\Pi_{ZZ}^{\rm NP}(0)}{m_Z^2}-\frac{c_W^2-s_W^2}{c_W s_W}\frac{\Pi_{Z\gamma}^{\rm NP}(m_Z^2)}{m_Z^2}-\frac{\Pi_{\gamma\gamma}^{\rm NP}(m_Z^2)}{m_Z^2}\right],\\
T &:= \frac{\rho^{\overline{\rm MS}}-1}{\alpha}=\frac{1}{\alpha}\left[\frac{\Pi_{WW}^{\rm NP}(0)}{m_W^2}-\frac{\Pi_{ZZ}^{\rm NP}(0)}{m_Z^2}\right],\\
U &:= \frac{4s_W^2}{\alpha}\left[\frac{\Pi_{WW}^{\rm NP}(m_W^2)-\Pi_{WW}^{\rm NP}(0)}{m_W^2}-\frac{c_W}{s_W}\frac{\Pi_{Z\gamma}^{\rm NP}(m_Z^2)}{m_Z^2}-\frac{\Pi_{\gamma\gamma}^{\rm NP}(m_Z^2)}{m_Z^2}\right]-S.
\end{aligned}
\tag{1.40}
$$

The NP contributions to the EW vacuum polarisations $\Pi_{VV}^{\rm NP}(p^2)$) could either come from loop or tree-level effects. Typically both T and U are related to custodial symmetry violation. However, U has an extra suppression factor of $m_{\rm NP}^2/m_Z^2$ compared to T and S. The most recent fit result for these parameters is [7]

$$
\begin{aligned}
S &= -0.01 \pm 0.10,\\
T &= 0.03 \pm 0.13,\\
U &:= 0.02 \pm 0.11.
\end{aligned}
\tag{1.41}
$$

But since T and S tend to give stronger constraint on NP, due to the suppression factor of U. One can preform a two-parameter fit of S and T setting $U = 0$, thas shown in Figure 1.6, with the numerical values [7],

$$
\begin{aligned}
S &= 0.00 \pm 0.07,\\
T &= 0.05 \pm 0.06.
\end{aligned}
\tag{1.42}
$$

The oblique parameters are important in constraining effective operators in the Higgs sector , namely

$$
\begin{aligned}
\hat{O}_S &= \phi^\dagger \sigma_i \phi W^i_{\mu\nu} B^{\mu\nu},\\
\hat{O}_T &= |\phi^\dagger D_\mu \phi|^2.
\end{aligned}
\tag{1.43}
$$

For example, $\hat{O}_S$ appears in Technicolour models causing large deviations of S compared to its measured value [46, 49–51]. Moreover, The constraints on T parameter is important for top mass generation ans well as modifications to $Zb\bar{b}$ coupling in such models [52, 53]. We will revisit the $\hat{O}_T$ when we discuss the Higgs and effective field theories in chapter 3.

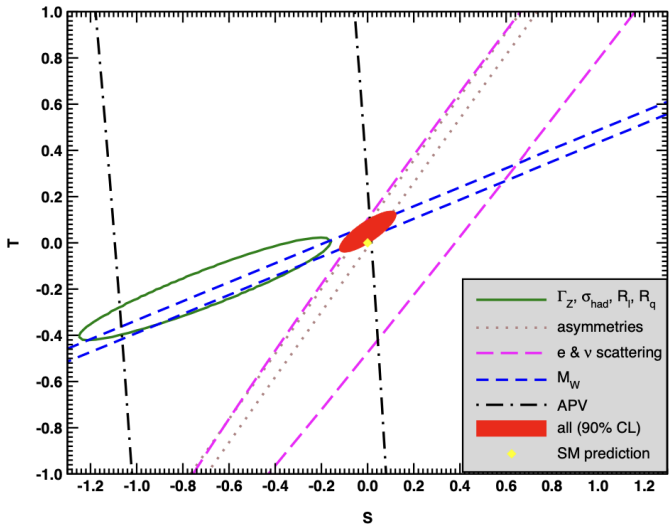

Figure 1.6. Fit results from various EWPO's for T and S setting $U =$. The contours show $1\,\sigma$ contours (39.35% for closed contours and 68% for the rest). This plot is obtained from the PDG [7].

1.5 Theoretical constraints on the Higgs

1.5.1 Electroweak precision data fits

Even prior to the discovery of the Higgs boson at LHC in 2012, many theoretical aspects of the Higgs sector provided marked bounds on the Higgs properties, particularly its mass. For instance, using the EWPO measurements at LEP provided an input for a fit based of radiative effects coming from the Higgs boson to such observables [14] as in diagram (a) of Figure 1.7, the bounds improved with the improvements of EWPO measurements, these bounds were known as the "blue band" plots seen with their progression in Figure 1.8.

1.5.2 Partial-wave unitarity

Another bound on Higgs mass emerged from studying the longitudinally polarised elastic scattering amplitudes of the EW vector bosons $V_L V_L \to V_L V_L$ at high energies $E \gg m_W$, where the Goldstone equivalence theorem holds [54], see diagrams (b) in Figure 1.7. This bound comes from applying the partial wave perturbative unitarity on the EW boson scattering amplitude. I will derive here this bound starting from the **Optical theorem**, which a direct result from the unitarity of the **S** matrix.

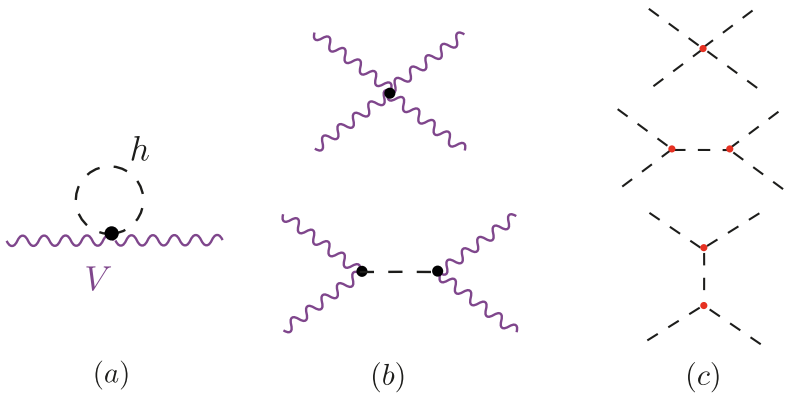

Figure 1.7. Diagrams contributing to theoretical bounds on the Higgs, (a) shows an example of radiative corrections to EWPO from the Higgs bosons. The diagrams in (b) show an elastic scattering of EW vector bosons leading to a bound on the Higgs mass from perturbative unitarity, similarly in (c) diagrams for $hh \to hh$ scattering leading to constraints on Higgs self-coupling.

The optical theorem

Let $\mathcal{M}_{aa}$ be a covariant matrix element for an elastic scattering process with for a particle a then the following relation applies

$$\sum_f \int d\Phi_n(p_a, p_i^f)|\mathcal{M}_{af}|^2 = 2\Im(\mathcal{M}_{aa}), \tag{1.44}$$

where the sum is over all intermediate n-particle states f with momenta p_i^f and $d\Phi_n(p_a, p_i^f)$ is the n-particle phase space.

If we only consider a $2 \to 2$ process with momentum states. $|\, p_1, p_2 \,\rangle \to |\, k_1, k_2 \,\rangle$, then

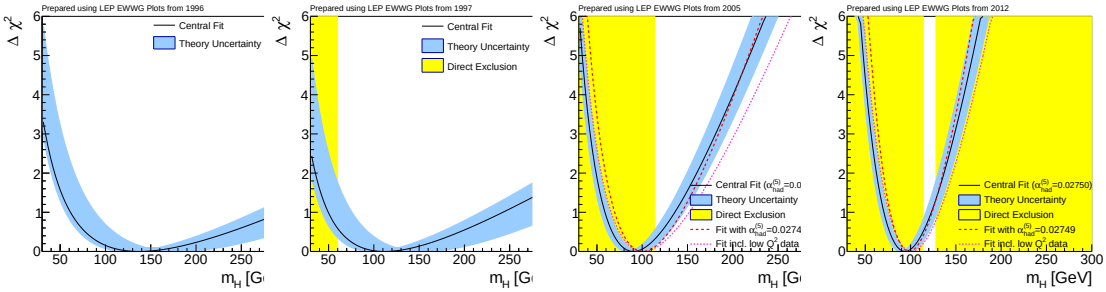

Figure 1.8. Progression of the "blue band" plots with LEP data from 1996 up to 2012 prior to the announcement of the Higgs boson discovery. There plots were taken from [29], based data from LEP [14].

the LHS of (1.44), after expanding the 2-particle phase space, simplifies to

$$\begin{aligned}&\int \frac{d^3k_1}{(2\pi)^3\,2E_1}\int \frac{d^3k_2}{(2\pi)^3\,2E_2}(2\pi)^4\delta^4(p_1+p_2-k_1-k_2)\,|\mathcal{M}(s,t)|^2,\\&=\frac{1}{16\pi}\int_{-1}^{1} d(\cos\theta)|\mathcal{M}(s,t)|^2,\end{aligned} \tag{1.45}$$

with the Mandelstam variables

$$\begin{aligned}s =& k_1+k_2,\\ t =& k_1-p_1,\\ u =& k_1-p_2,\\ s+t+&u=4m^{\cdot}\end{aligned} \tag{1.46}$$

By using the relation between the Mandelstam variable t, and the scattering angle for the elastic scattering

$$t=\frac{1}{2}(s-4m^2)(\cos\theta-1) \tag{1.47}$$

We could expand the matrix element $\mathcal{M}(s,t)$ in terms of *partial waves*, isolating s from scattering angle dependence

$$\mathcal{M}(s,t)=16\pi\sum_j(2j+1)a_jP_j(\cos\theta). \tag{1.48}$$

Where a_j are called the jth partial wave amplitude, and $P_j(\cos\theta)$ are the Legendre polynomials

$$P_j(z)=\frac{1}{j!}\frac{1}{2^j}\frac{d^j}{dz^j}(z^2-1)^j \tag{1.49}$$

Which satisfies the orthonormality condition

$$\int_{-1}^{1} dz\,P_j(z)P_k(z)=\frac{1}{2j+1}\delta_{jk} \tag{1.50a}$$

$$P_j(1)=1\ \ \forall j. \tag{1.50b}$$

We hence get for the LHS of (1.44) scattering

$$\begin{aligned}
&\int \frac{d^3k_1}{(2\pi)^3\,2E_1}\int \frac{d^3k_2}{(2\pi)^3\,2E_2}(2\pi)^4\delta^4(p_1+p_2-k_1-k_2)\,|\mathcal{M}(s,t)|^2,\\
&= \frac{1}{16\pi}\int_{-1}^{1} d(\cos\theta)\left[16\pi\sum_j (2j+1)a_j(s)P_j(\cos\theta)\right]\times\\
&\qquad\left[16\pi\sum_k (2k+1)a_k^*(s)P_k(\cos\theta)\right],\\
&\Rightarrow = 32\pi\sum_j (2j+1)|a_j(s)|^2. \qquad (1.51)
\end{aligned}$$

And the RHS of (1.44)

$$2\mathfrak{I}(\mathcal{M}_{aa}) = \underbrace{2\mathfrak{I}(\mathcal{M}(s,0))}_{t \text{ is integrated out.}} = 32\pi\sum_j (2j+1)\mathfrak{I}(a_j(s)). \qquad (1.52)$$

Otherwise large cancellations needed, $a_j(s)$'s are hierarchal. Thus, we could compare the partial wave amplitudes term-by-term

$$|a_j(s)|^2 \le \mathfrak{I}(a_j(s)) \quad \Rightarrow \mathfrak{R}(a_j(s))^2 + \mathfrak{I}(a_j(s))^2 \le \mathfrak{I}(a_j(s)) \qquad (1.53)$$

Rearranging terms, we get

$$\mathfrak{R}(a_j(s)) + \left(\mathfrak{I}(a_j(s)) - \frac{1}{2}\right)^2 \le \frac{1}{4} \qquad (1.54)$$

The partial wave amplitude must remain within the unitarity circle for the perturbation theory to be valid.

$$\mathfrak{R}(a_j(s)) \le \frac{1}{2} \qquad (1.55)$$

This is known as the perturbative partial wave unitarity bound.
When (1.55) is applied for $V_LV_L \to V_LV_L$, in the Goldstone boson equivalence theorem regime in particular for $V = W$ boson, we get for the S-wave ($j = 0$) partial amplitude

$$a_0 \sim \frac{m_h^2}{16\pi v^2}\left(2 + \mathcal{O}\left(m_h^2/s\right)\right). \qquad (1.56)$$

Looking at the asymptotic behaviour as $s \to \infty$, we obtain the bound

$$\frac{m_h^2}{8\pi v^2} < \frac{1}{2} \Leftrightarrow m_h \le 870\,\text{GeV}. \qquad (1.57)$$

Indeed this bound is obsolete now after th Higgs mass measurement, however it is very important to demonstrate the power of this technique in constraining Higgs parameters. As this method can be applied to any elastic scattering with the Higgs acts as a mediator

like $ZZ \to ZZ$, $WW \to ff$ and constrain the corresponding couplings $g_{ZZh}, g_{f\bar{f}h}$ and so on. An important bound can be derived by examining the Higgs elastic scattering $hh \to hh$ shown in (c) of Figure 1.7 in order to set bounds on Higgs self-interactions g_{hhh} and g_{hhhh}. This is what exactly has been done in ref. [55] where they have found that the S-wave partial amplitude for this process is given by

$$a_0 = -\frac{1}{2}\frac{\sqrt{s(s-4m_h^2)}}{16\pi s}\left[g_{hhh}^2\left(\frac{1}{s-m_h^2} - 2\frac{\log\frac{s-3m_h^2}{m_h^2}}{s-4m_h^2}\right) + g_{hhhh}\right], \tag{1.58}$$

which leads to unitarity bounds on the trilinear g_{hhh} and the quartic g_{hhhh} couplings

$$\left|g_{hhh}/g_{hhh}^{\mathrm{SM}}\right| \lesssim 6.5 \qquad \text{and} \qquad \left|g_{hhhh}/g_{hhhh}^{\mathrm{SM}}\right| \lesssim 65\,. \tag{1.59}$$

A more stringent constraint can be obtained by looking at the one-loop correction to the $hh \to hh$ scattering amplitude, within the full kinematic range. The unitarity bound here is obtained by looking at the one-loop amplitude at the threshold, and is given by

$$\left|g_{hhh}/g_{hhh}^{\mathrm{SM}}\right| \lesssim 6\,. \tag{1.60}$$

It should be noted that the unitarity bounds on the trilinear coupling depends on the ansatz use estimating the size the NP contributions to the scattering amplitudes. These bounds are, hitherto, the strongest on these two couplings even when compared to the ones coming from current experimental searches.

1.5.3 Other bounds

Further theoretical bounds can be obtained by studying quantum effects on the Higgs potential. For example, if we looked at the solution of the renormalisation group equation (RGE) for the Higgs self-coupling λ with the boundary condition $\lambda(v) = \lambda_0$ and ignoring other SM particle-contributions

$$\lambda(Q^2) = \frac{\lambda_0}{1 - \frac{3}{4\pi^2}\log\frac{Q^2}{v^2}} \tag{1.61}$$

We see that the running of λ will hit a pole, known as Landau pole when the denominator vanishes. This will happen at the scale

$$Q_{\mathrm{c}} = ve^{4\pi^2/3\lambda_0} = ve^{4\pi^2 v^2/3m_h^2} \tag{1.62}$$

This indicates that the theory will break down at scales larger or equal to Q_{c}. Since the "critical scale" is a function of the Higgs mass, this allows us to set an upper limit on the Higgs mass assuming the SM will be valid up to a certain scale Q_{c}. This bound is known as **quantum triviality** bound [56]. This is because the low energy behaviour of (1.61) leads to a vanishing interaction, and if we want the Higgs Lagrangian to be perturbative

for all scales, then λ has to be vanishing and the theory becomes non-interacting or *trivial*.

Another bound coming from the RGE of λ is the **stability bound** , which considers the stability of the Higgs potential given the running of λ by requiring that the Higgs potential is an operator bounded from below. This bound is obtained by approximating the solution of the RGE at small λ

$$\lambda(Q^2) \sim \lambda_0 + \frac{1}{16\pi^2}\left[-\frac{12m_t^4}{v^4} + \frac{3}{16}\left(2g_2^4 + (g_2^2 + g_1^2)^2\right)\right]\log\frac{Q^2}{v^2} \tag{1.63}$$

For the Higgs potential to be bounded from below $\lambda(Q^2)$ ought to be $\lambda(Q^2) > 0$. With th relation for λ_0 in terms of the mass, we get a bound on m_h

$$m_h^2 > \frac{v^2}{8\pi^2}\left[-\frac{12m_t^4}{v^4} + \frac{3}{16}\left(2g_2^4 + (g_2^2 + g_1^2)^2\right)\right]\log\frac{Q^2}{v^2} \tag{1.64}$$

Which leads to $m_h \approx 130$ GeV if we assume that the SM is valid up to the Grand Unified Theory (GUT) scale of $\sim 10^{16}$ GeV and $m_h \approx 180$ GeV for Q being at the Planck scale $\sim 10^{19}$ GeV.

More sophisticated calculations and discussion for the Higgs potential and vacuum stability has been a subject of great interest in pre and post-Higgs discovery eras cf. [56–59] and the most state-of-the-art calculation for the vacuum stability at two-loop level has been preformed in ref. [60] where they also included finite temperature effects to construct a phase diagram in the $m_t - m_h$ and $m_t - \lambda(M_{pl})$ planes as shown in Figure 1.9. Indicating that the measured Higgs mass in likely compatible with a metastable vacuum rather than absolute stability. This indicates that there is a finite probability for the Higgs vacuum (false vacuum) to decay into a lower energy state (true vacuum) via quantum tunnelling.

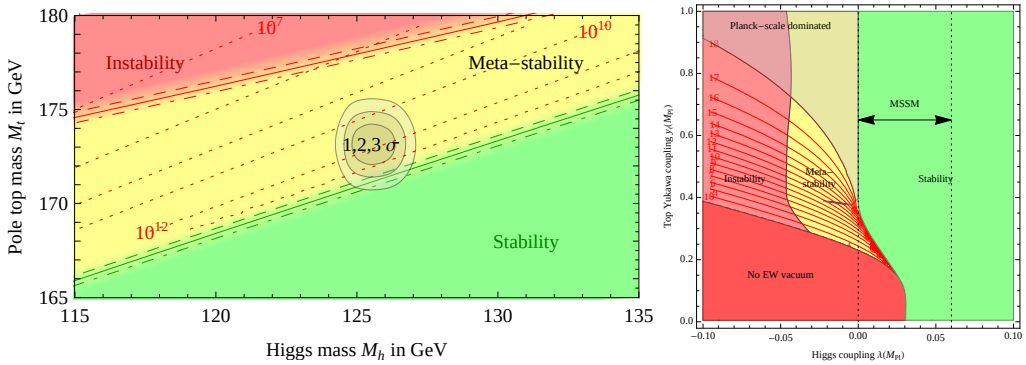

Figure 1.9. Phase diagrams of the Higgs vacuum in the $m_t - m_h$ (left) and $m_t - \lambda(M_{pl})$ (right) planes showing areas of instability, meta stability and absolute stability. In the $m_t - \lambda(M_{pl})$ diagram, the allowed range of the Higgs self-coupling λ in the Minimal Supersymmetric SM (MSSM), this plot is taken from [60].

2 Experimental measurements of the Higgs boson

The observation of the Higgs boson, along with the extensive measurement of its properties and couplings has been on the top of the LHC programme priorities [61]. In the time this thesis was written, the particle physics community will be celebrating a decade since the Higgs boson's discovery. Looking back 10 years ago, when I have witnessed the discovery of the Higgs boson via news press-conference in the summer of 2012, and decided to be a part of this enormous step that humanity has taken, I feel astonished by the progress made in understanding this newly discovered particle!
In this chapter, I will start by an overview of the extraordinary LHC and its experiments in section 2.1. Then, I will provide a state-of-the-art status review of the experimental measurements of the Higgs boson properties in section 2.2and its cross-sections and couplings in section 2.3, At the end I will discuss the challenges and outlook for the future runs of the LHC section 2.4. The rest of the thesis will be aiming to address a small part of these challenges.

2.1 Overview of the Large Hadron Collider

The Large Hadron Collider (LHC) is the largest particle accelerator in the CERN accelerators complex, with a circumference of about 26 km and over 9590 superconducting magnets cooled to 1.9 K. It was built as an upgrade to the Large electron positron collider (LEP) which ended its operation in the year 2000. The LHC contains four main experiments situated at the four beam collision points and detectors, these experiments are: ATLAS, CMS, LHCb and ALICE, there also smaller experiments such as LHCf, MilliQan,TOTEM and others. For more details about the LHC cf. [62, 63] or the LHC technical design report [64] for an in-depth review.
The LHC started operation in September 2008, with low energy proton beams, then gradually increased to an energy of 3.5 TeV per proton to reach a centre of mass energy $\sqrt{s}$ of 7 TeV, and data-taking period started from 2011 . By 2012, its energy has increased to $\sqrt{s} = 8$ TeV and operated at this energy for about year and half, then stopping in mid 2013 concluding what is known as **Run-I**. In 2015, **Run-II** started with almost double the energy $\sqrt{s} = 13$ TeV, and lasted for ca. 3 years. As this thesis being written, preparations are being made to get **Run-III** started and will last until 2024. During these runs, heavier nuclei such as ^{207}**Pb** and ^{131}**Xe** have been collided either with protons or with themselves [65].
From, 2025 and beyond, the **High-Luminosity** LHC (HL-LHC) era will commence,

see Figure 2.2. Where the LHC will be shutdown for extensive upgrades [66] to potentially increase its energy to $\sqrt{s} = 14$ TeV and higher collision rates hence the term *high luminosity*. Which leads us to an important notion in particle physics phenomenology *integrated luminosity*.

The performance of colliders depends on many factors, but for phenomenological studies, like this thesis, the most important of which are the centre-of-mass energy $\sqrt{s}$ and the integrated luminosity $\mathscr{L}$. This is mainly due to the fact that particle colliders experiments are basically "counting experiments", and all of the bounds on physical observables or model parameters are obtained from the number of signal versus background events, and the number of expected events N_{expec} for a given resonance R and a subsequent decay final state X at any collider experiments is given by

$$N_{expec} = \sigma(pp \to R)\,\mathrm{BR}(R \to X)\,\mathscr{L}\,\epsilon_{\mathrm{SEL}}. \tag{2.1}$$

Here ϵ_{SEL} is the selection efficiency, which depends on many factors like the detector geometry and particle identification performance etc. , as well as the signal one searches for, it can be improved by better detected or selection cuts. The production cross-section increases typically with quadratically with $\sqrt{s}$, hence comes the need for higher energies but this can only achieved by building new colliders from scratch. The integrated luminosity, on the other hand, can be increased by running the experiment for a longer time, without the need for a new collider, This is because the integrated luminosity is the time integral of the collider's luminosity $L(t)$ over its operation time T

$$\mathscr{L} = \int^{T} L(t). \tag{2.2}$$

Therefore, we see that the integrated luminosity for the LHC experiments will increase over time, when more collisions taking place, as seen in figure Figure 2.1 showing the integrated luminosity for ATLAS and CMS experiments. As the protons travel in the LHC in **bunches**,when these bunches cross, the protons inside of them collide at a certain frequency f. When two bunches with N_1 and N_2 protons per bunch, respectively collide, each bunch will have an effective cross-section $4\pi\sigma_i$ corresponding to their physical sizes $\sigma \sim 16\,\mu\mathrm{m}$, the luminosity is therefore given -approximately- by

$$L = \frac{f N_1 N_2}{4\pi\sigma_1\sigma_2}, \tag{2.3}$$

which is for the LHC averages to $\sim 10^{34}$ collisions $\mathrm{cm}^{-2}\,\mathrm{s}^{-1}$ [67, 68].
The total physics-viable *pp*-collisions integrated luminosity for Run-I was 4.57 fb^{-1} for 7 TeV and 20.3 fb^{-1} for 8 TeV (ATLAS [69]) and 5.55 fb^{-1} at 7 TeV and 21.8 fb^{-1} at 8 TeV (CMS [70]). As for Run-II the integrated luminosity is 139 fb^{-1} at 13 TeV (ATLAS [71]) and 137 fb^{-1} at 13 TeV (CMS [70]). The expected integrated luminosity by the end of Run-III is 300 fb^{-1} [72] and 3000 fb^{-1} by the end of the HL-LHC at energy of 14 TeV [66].

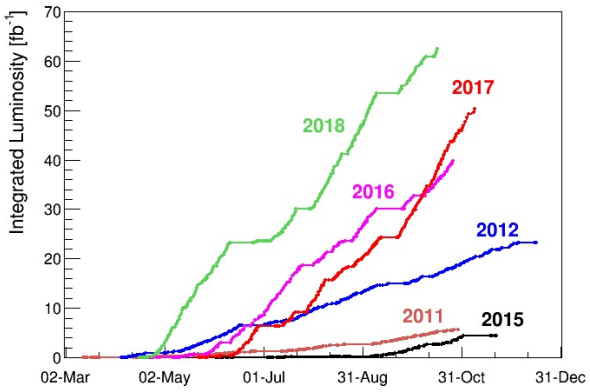

Figure 2.1. The integrated luminosity of the CMS and ATLAS experiments combined over the period from 2011-2018, source [67].

Figure 2.2. A timeline of the LHC operation showing Run-I, Run-II and future planned runs of the LHC, including the HL-LHC, source [65].

2.2 Higgs properties

2.2.1 Higgs boson mass measurements

In order to measure the mass of the Higgs boson with high precision, one need to consider final states that can be reconstructed with high momentum and mass resolutions, this is typically achieved when no hadronic constituents in the decays involved, such as

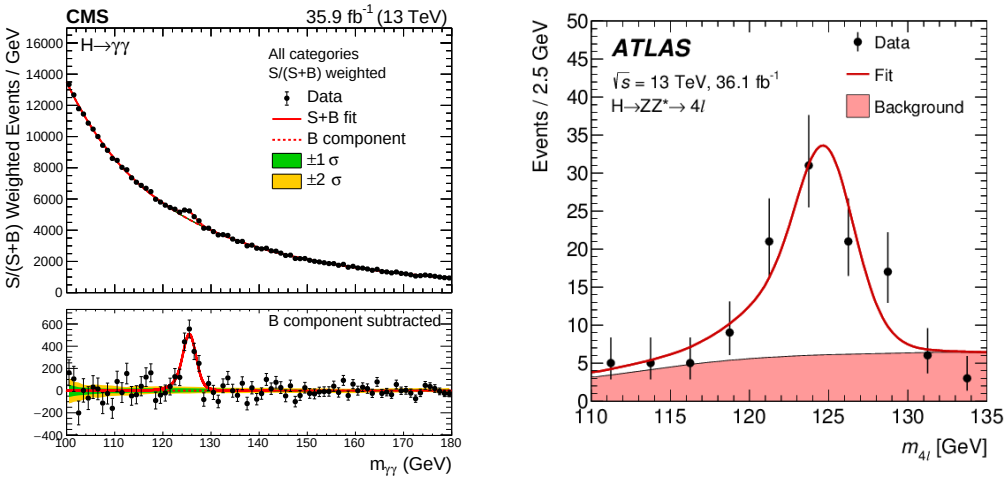

Figure 2.3. The invariant mass distributions of diphoton $m_{\gamma\gamma}$ (CMS [73]) and four lepton $m_{4\ell}$ (ATLAS [74]) final states showing a clear peak at the Higgs mass, with smooth background. These final states are ideal for Higgs mass measurements.

$h \to \gamma\gamma$ and $h \to ZZ^* \to 4\ell$. Reconstructing the invariant mass distributions $m_{\gamma\gamma}$ and $m_{4\ell}$ one observes that the Higgs peak is narrow over a relatively smooth background, see Figure 2.3, which is ideal for the measurement of the Higgs mass. It should be noted that the width of the resonance is due to the detector resolution and does not correspond to the actual Higgs width.

There have been consistent improvements of the Higgs mass measurements since its discovery. In Figure 2.4, I have preformed a meta-analysis on ATLAS and CMS measurements of the Higgs mass in Run-I and Run-II of the LHC for both diphoton and ZZ^* final states based on the data from the studies [73–76] using a random effects model [77]. The pooling of the studies yielded a mass measurement of $m_h = 125.21 \pm 0.10$, which translates to a 0.11% accuracy, the heterogeneity of the studies was found to be $I^2 = 49\%$ ($p = 0.05$) . Different measurements combination techniques were used in [73] and [7] yielded different central values but all of the results agree within the uncertainties.

2.2.2 Higgs full width

The SM values of the Higgs boson full width is $\Gamma_h = 4.1$ GeV and it can be accessed in the LHC by looking at the ratio of on-shell vs off-shell Higgs production and decay to the $ZZ^{(*)}$ state, and $ZZ^{(*)} \to 4\ell, 2\ell 2\nu$, namely

$$\frac{\sigma(gg \to h \to ZZ^*)}{\sigma(gg \to h^* \to ZZ)} = \kappa_g^2 \kappa_Z^2 \frac{4m_Z^2}{m_h \Gamma_h}, \tag{2.4}$$

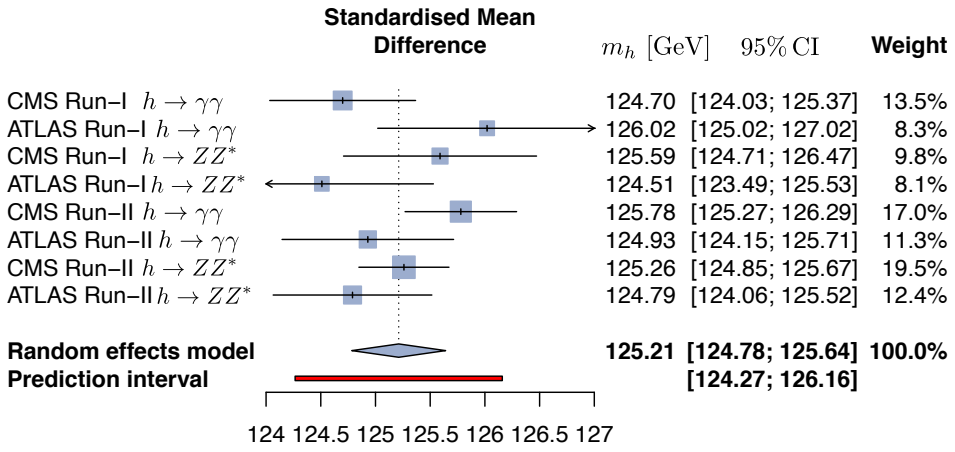

Figure 2.4. A meta analysis preformed to combine all the measurements of the Higgs mass from Run-I and Run-II, the combined result was obtained from pooling all of the studies using the random effects model method.

where the κ here denotes the ratio between the measured or modified coupling with the Higgs and the SM prediction, i.e.

$$\kappa_X := \frac{g_{XXh}}{g^{\text{SM}}_{XXh}}. \tag{2.5}$$

Which is commonly used in reporting experimental constrains/ of the Higgs couplings, the κ-formalism will be discussed more in chapter 3.
Unfortunately, it is not possible to directly measure the Higgs full width at the LHC, as this requires full reconstruction of the collision event and study the recoil mass which is only possible at lepton colliders [78, 79]. Alas, it is still possible to extract bounds on Γ_h using (2.4). ATLAS used this method to constrain the full width of the Higgs using Run-II data [80], while CMS has preformed the same analysis using Run-I and Run-II data combined [81], the results are 95% CL bounds of Γ_h

$$\Gamma_h < 14.4\,\text{GeV} \quad \text{(ATLAS)} \qquad 0.08\,\text{GeV} < \Gamma_h < 9.16\,\text{GeV} \quad \text{(CMS)}, \tag{2.6}$$

with the combined bound being $\sim 3\Gamma_h^{\mathrm{SM}}$.

2.2.3 Higgs spin and parity

According to the SM predictions, the Higgs boson in a scalar and $\mathcal{CP}$ even ($J^p = 0^+$). However, the discovery of a peak in the $m_{\gamma\gamma}$ distribution on its own would not automatically imply that the particle discovered is scalar, it could be a spin-2 boson, or a pseudoscalar ($J^p = 0^-$). In order to study the J^p properties of the Higgs, one needs to examine the differential distributions of angular variables such as rapidity y or transverse momentum p_T. Both ATLAS and CMS collaborations studied using Run-I data the angular distributions of the Higgs decays $h \to ZZ^*$, $h \to WW^*$ and $h \to \gamma$, to study an anomalous VVh coupling. Then test the alternative hypothesis for J^p against the SM [82, 83]. The analysis results show that the SM 0^+ hypothesis is favoured at $> 99.9\%$ CL.

2.3 Measurements of Higgs rates and couplings

2.3.1 Higgs cross-sections

The total inclusive Higgs cross-section has been measured using the the final states $h \to \gamma\gamma$ and $h \to ZZ^* \to 4\ell$. and their combinations. The measurements have been done at the three energies the LHC was operating at: 7 TeV, 8 TeV [84] and 13 TeV [85**?** , 86] . As shown in Figure 2.5, the measured inclusive cross-section is in agreement with the SM prediction across all of the LHC operation energies.

In addition to the inclusive cross-section measurements, differential cross-sections of the Higgs has been measured for p_T and y as we have seen in subsection 2.2.3 for Higgs's J^p determination. Additionally, the differential cross-sections for other variables have been measured, and they include $N_{jets}, p_T^{jet}, m_{jj}, \delta\phi_{jj}$ and others using the channels $h \to ZZ^*$, $h \to WW^*$ and $h \to \gamma$. The most recent results using the full Run-II data can be found in refs. [86–89].

A collection of measurements of Higgs production and decay rates has been carried out by both ATLAS and CMS. These measurements also carried out in, what is known as the "Standard Template Cross-Sections" (STXS) framework.The STXS's are fiducial cross-sections in exclusive phase-space regions or bins stratified by the Higgs boson production channels. They have the advantage of standardisation of cuts and final results such that measurements could be easily combined across analyses. More details about the STXS framework can be found in the reports of LHC Higgs cross-sections working group (HXSWG) cf. [90]. Table 2.1 presents a summary of the state-of-art measurements of the Higgs rates separated into production and decay channels using the total LHC Run-II data from ATLAS and CMS experiments. The HL-LHC projections from CMS experiment are given as a comparison. The results in this table are written in terms of the signal strength, which is directly extracted from measuring the number of events

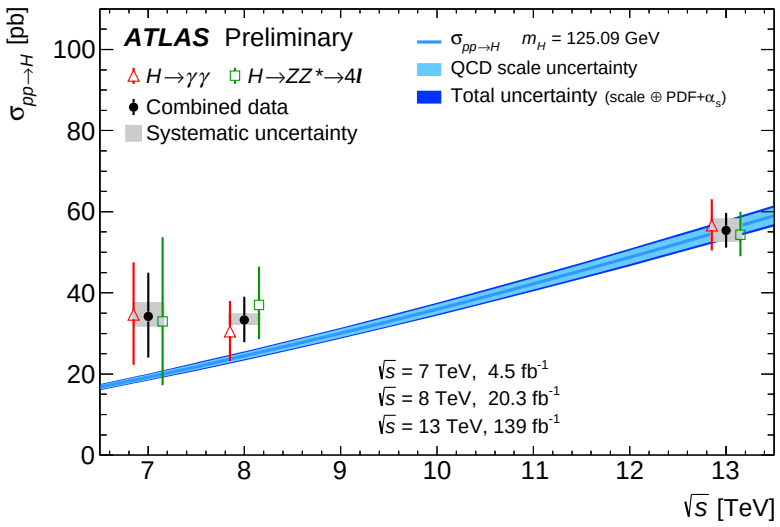

Figure 2.5. The total inclusive cross-section measurements by ATLAS collaboration [87] for 7, 8 and 13 TeV using $h \to \gamma\gamma$ and $h \to ZZ^* \to 4\ell$. channels and their combination (black points) compared to the SM prediction with the uncertainties shown as blue line with light and dark blue bands for QCD scale uncertainties and total uncertainties, respectively.

dividing them by the standard model,

$$\mu_{\text{Exp}} := \frac{\sigma \cdot \text{BR}}{\sigma^{\text{SM}} \cdot \text{BR}^{\text{SM}}}. \tag{2.7}$$

Production	Decay	$\mu_{\text{Exp}} \pm \delta\mu_{\text{Exp}}$ (symmetrised) **LHC Run-II** CMS $137\,\text{fb}^{-1}$ / ATLAS $139\,\text{fb}^{-1}$	$\mu_{\text{Exp}} \pm \delta\mu_{\text{Exp}}$ (symmetrised) **HL-LHC** CMS $3\,\text{ab}^{-1}$	Ref.
ggF	$h \to \gamma\gamma$	0.99 ± 0.12 1.030 ± 0.110	1.000 ± 0.042	[91–93]
	$h \to ZZ^*$	0.985 ± 0.115 0.945 ± 0.105	1.000 ± 0.040	[91, 93, 94]
	$h \to WW^*$	1.285 ± 0.195 1.085 ± 0.185	1.000 ± 0.037	
	$h \to \tau^+\tau^-$	0.385 ± 0.385 1.045 ± 0.575	1.000 ± 0.055	
	$h \to b\bar{b}$	2.54 ± 2.44 –	1.000 ± 0.247	[93, 94]
	$h \to \mu^+\mu^-$	0.315 ± 1.815 –	1.000 ± 0.138	[93, 94]
VBF	$h \to \gamma\gamma$	1.175 ± 0.335 1.325 ± 0.245	1.000 ± 0.128	[91–93]
	$h \to ZZ^*$	0.62 ± 0.41 1.295 ± 0.455	1.000 ± 0.134	[91, 93, 94]
	$h \to WW^*$	0.65 ± 0.63 0.61 ± 0.35	1.000 ± 0.073	
	$h \to \tau^+\tau^-$	1.055 ± 0.295 1.17 ± 0.55	1.000 ± 0.044	
	$h \to b\bar{b}$	– 3.055 ± 1.645	–	[91]
	$h \to \mu^+\mu^-$	3.325 ± 8.075 –	1.000 ± 0.540	[93]
$t\bar{t}h$	$h \to \gamma\gamma$	1.43 ± 0.30 0.915 ± 0.255	1.000 ± 0.094	[91–93]
	$h \to VV^*$	$0.64 \pm 0.64 (ZZ^*)$ 0.945 ± 0.465 (WW^*) 1.735 ± 0.545	1.000 ± 0.246 (ZZ^*) 1.000 ± 0.097 (WW^*) –	[91, 93, 94]
	$h \to \tau^+\tau^-$	0.845 ± 0.705 1.27 ± 1.0	1.000 ± 0.149	
	$h \to b\bar{b}$	1.145 ± 0.315 0.795 ± 0.595	1.000 ± 0.116	
Vh	$h \to \gamma\gamma$	0.725 ± 0.295 1.335 ± 0.315	1.000 ± 0.233 (Zh) 1.000 ± 0.139 ($W^\pm h$)	[91–93]
	$h \to ZZ^*$	1.21 ± 0.85 1.635 ± 1.025	1.000 ± 0.786 (Zh) 1.000 ± 0.478 ($W^\pm h$)	[91, 93, 94]
	$h \to WW^*$	1.850 ± 0.438 –	1.000 ± 0.184 (Zh) 1.000 ± 0.138 ($W^\pm h$)	[93, 95]
	$h \to b\bar{b}$	– 1.025 ± 0.175	1.000 ± 0.065 (Zh) 1.000 ± 0.094 ($W^\pm h$)	[91, 93]
Zh CMS	$h \to \tau^+\tau^-$ $h \to b\bar{b}$	1.645 ± 1.485 0.94 ± 0.32	–	[94]
$W^\pm h$ CMS	$h \to \tau^+\tau^-$ $h \to b\bar{b}$	3.08 ± 1.58 1.28 ± 0.41		

Table 2.1. The experimental single Higgs production and decay rates measurements from the complete data of LHC Run II and projections for the HL-LHC. The uncertainties were symmetrised here.

2.3.2 Constraints on Higgs couplings

The measurements of the Higgs rates and their combination have been used to set bounds on the Higgs couplings, the most recent bounds have been reported by ATLAS using the Higgs inclusive rates and STXS for the full Run-II data [96], and by CMS using Higgs rates shown in Table 2.1 [94]. In Figure 2.6, I present the aggregation the ATLAS and CMS bounds on the Higgs coupling modifiers in the κ formalism defined in eq. (2.5). The aggregation of these bounds was preformed taking into an account the between experiment effects, as described in [97] assuming there is no correlation between ATLAS and CMS measurements.

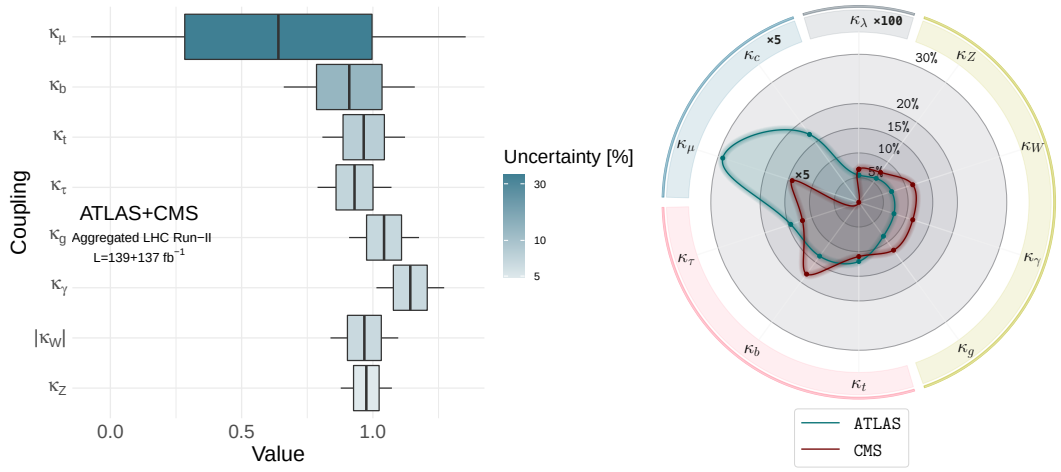

Figure 2.6. (left) Meta-analysis aggregation the most recent bounds from ATLAS [96] and CMS [94] on the Higgs couplings modifiers κ. (right) The individual 68% CI uncertainties on the coupling modifiers from ATLAS and CMS.

The measured bounds on the Higgs coupling to the gauge bosons, including the effective couplings to γ and g, as well as the couplings to the third-generation fermions are within few percent of the SM prediction. The bounds on the coupling to the W boson seems to favour a negative value in CMS fits, due to the channel used to constraint it $h \to WW$ which depends on κ_W^2, thus making the best fit value of ~ -1 within the SM prediction. An independent analysis on the relative signs of κ_W and κ_t was preformed using $th/t\bar{t}h$ processes in ref. [98], hence only the absolute value of κ_W is reported in my combination of the analysis results. Additionally, the observation of the decays $h \to b\bar{b}$ [99–101] and $h \to \tau\tau$ [102, 103] leading to direct measurements of the beauty and τ Yukawa couplings has made their bounds comparable to the gauge bosons and top couplings with the Higgs, having less than 10% uncertainty. Au contraire, bounds on the Yukawa couplings of second and first generation fermions remain very weak.

Recently, searches for the decay $h \to \mu\mu$ [104, 105] using the whole Run-II data conducted by both collaborations, showed an evidence (3σ) for observing this decay. Improving the constraints on κ_μ, though as seen in Figure 2.6, the uncertainty remains

high $\sim 36\%$. Searches for the Higgs decaying to charm pairs is significantly more challenging, thus only quoted an upper 95% CL bounds on $|\kappa_c|$ of 8.5 for ATLAS [106, 107] and 70 for CMS [108]. There is no planned direct searches for the first generation Yukawa couplings (*direct*) measurements planned for the LHC as it is not possible to directly access decays of the Higgs to up or down quarks. Other methods for probing these couplings will be extensively discussed in chapter 8.

By the end of the HL-LHC, it is projected that the couplings of the Higgs, including the couplings with gauge bosons, third generation fermions as well as the muon Yukawa will be measured at few percent level [109]. This is highlighted by Figure 2.7, showing the improvement in the κ measurement uncertainty expected by the HL-LHC compared to Run-II. Because

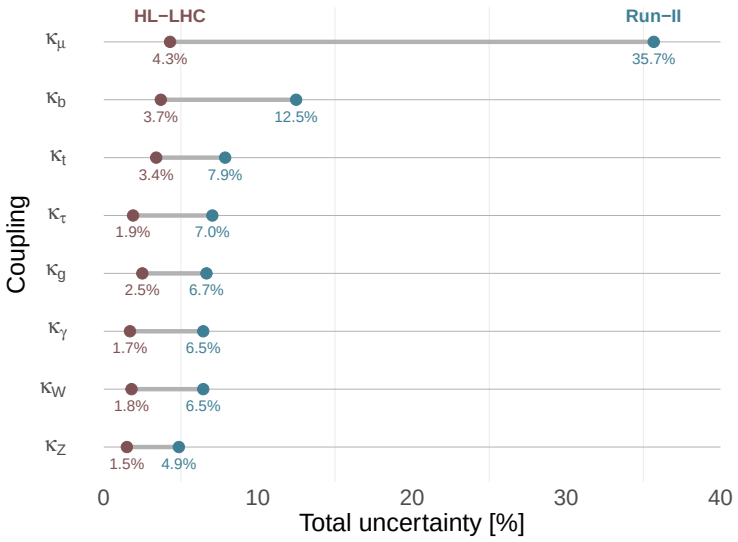

Figure 2.7. Dumbbell plot illustrating the improvement of the uncertainties on the Higgs coupling's measurement projected for the HL-LHC compared to the current combined CMS and ATLAS measurements from Run-II data.

2.4 Challenges and outlook

The future runs of the LHC hold a lot of potential for further understanding of the 10-year old Higgs boson. Although, for some processes and couplings there will still be a lot of challenges. For instance, the observation of $h \to c\bar{c}$ will require highly efficient charm-tagging, which is expected to improve at the HL-LHC by a factor of 2.5 [110]. The signal strength with rare decay $h \to Z\gamma$ currently is constrained to 3.6 times the SM values at 95% CL [111] and it is projected to be measured at the HL-LHC with $\sim 10\%$ uncertainty.

One of the couplings of the Higgs which we did not discuss above is the Higgs self-interaction (trilinear and quartic), as I have shown in subsection 1.5.2 that the perturbative unitarity bound derived in ref. [55] is the strongest on these couplings so far. In view of the fact that to experimentally measure Higgs self-couplings, it is imperative to observe multiple Higgs production. Namely, to access the trilinear self-coupling Higgs pair production must be observed. Similarly, triple Higgs production observation is needed for the quartic Higgs coupling measurement. Woefully, these processes are experimentally arduous to detect, due to their low inclusive cross-section ~ 30 fb for hh [112] and < 0.1 fb for hhh at LHC maximum expected operational energy of 14 TeV. The triple Higgs production will remain challenging even for future colliders, e.g for the FCC-hh at 100 TeV, this process has a cross-section of only ~ 5 fb [113]. To put these numbers in the context of single Higgs production, recall that the inclusive single-Higgs production cross-section of ~ 70 pb at the current LHC operation energy. The triple Higgs production thus, will not be accessible at the LHC and consequently the quartic self-coupling will not be measured. However, there is a promising outlook for the HL-LHC to measure the trilinear self-coupling.

In chapter 5 I will discuss the potential for using single-Higgs processes to indirectly probe the trilinear coupling, as proposed by several studies in refs. [114–121] and the challenges accompanying it. Later in chapter 7 the Higgs pair production at the LHC will be overviewed along the current and future searches for this process and the bounds from them on the trilinear Higgs self-coupling.

Light quark Yukawa couplings are another example of formidable couplings to probe at the LHC. chapter 8 will be dedicated to overviewing the potential for Higgs pair production in the measurement of these elusive couplings. The focal point of that chapter will be the use of multi-variate analysis in signal vs background separation.

3 Higgs and effective field theories

The study of the Higgs properties, couplings and rates aims to shed light on the structure of its potential, how and why it is responsible for the EW symmetry breaking. Explaining the vacuum expectation value and the mass of the Higgs has been the aim of many theoreticians and phenomenologists. This is because the SM provides no insights on the nature of the Higgs potential and its parameters, as in the SM these are input parameters that is needed to be provided from experimental observations. The Higgs potential shown in eq. (1.8) is the minimal one that could cause the EW symmetry breaking, but nature may not have taken this minimalist approach. In particular, that this potential suffers from severe fine-tuning as we have discussed in the hierarchy problem add a discussion about this.

In order to test whether the Higgs potential and the way it generates SSB is the minimalist SM way or there are other more complex structures involved one needs to measure Higgs rates and compare them with the SM, as overviewed in the previous chapter, using the κ formalism. Alas, this approach does not help in understanding what would the new physics (NP) structures be more likely to case a certain deviation, if any observed. Conversely, we would be interested in knowing what the allowed NP structures given the current (or future) measurements of the Higgs rates are. Of course, by looking at concrete models, one-by-one, confronting them with Higgs data one would get an insight on the aforementioned questions but withal very tedious as there are numerous ways NP might manifest itself.

In order to make our search for NP more accessible and model-agnostic, we could revert to **effective field theories** (EFT), one of the most perspicacious concepts of quantum field theory. In the EFT framework, the interactions mediated by the NP at small scale of an arbitrary complexity can be systematically simplified by approximating these interactions via integrating the UV degrees of freedom thus leaving only numerable operators added to the SM. The premise of EFT's can be simply illustrated in Figure 3.1, the LHC-for example- would not be able to resolve the UV degrees of freedom at their scale Λ, rather one can only observe the effective interactions they mediates. These new effective interactions are parametrised using a set of free parameters known as **Wilson coefficients**, that would be constrained from experiments. These " phenomenological Lagrangians" as called by Weinberg [122], are not necessarily renormalisable but would still allow for robust predictions that can be tested at colliders, including higher order effects . These predictions usually manifest as modifications to rates.

In this chapter I will be discussing the EFT's that modify Higgs rates, including single Higgs and Higgs pair production at leading order. In later chapters like **??** EFT operators from the top quark sector that modify Higgs rates at NLO will be shown. Lastly, in **??** more EFT operators that are responsible for lepton flavour universality

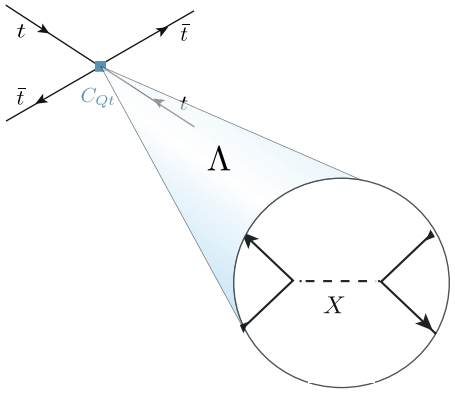

Figure 3.1. eft

violation also at NLO will be showcased. This chapter is organised as follows: In **??** the Higgs sector of Standard Model effective field theory (SMEFT) will be presented along with the parametrisation of single and di-Higgs rates in terms of the SMEFT Wilson coefficients. Au contraire to the SMEFT formalism, section 3.2 will present a non-linear EFT formalism known as the Chiral Lagrangian or (Higgs)EFT . Finally I will conclude this chapter with section 3.3.

3.1 Standard Model EFT

There is no unique way of defining an EFT for the Higgs boson $h(x)$. One could consider the field h as an EW singlet or as a par of the doublet ϕ like the SM. The first ansatz way is more compatible with a heaver Higgs and the effective coupling based on it could be derived from the EW chiral Lagrangian (EWChL) as we shall see in section 3.2. However, after the discovery of the Higgs, having a mass close to m_Z, the second option for an EFT seemed more fitting, though more restrictive. Assuming that the NP resonances would occur at masses $\Lambda \gg m_Z$, one could integrate them out yielding a set of effective operators of mass dimension > 4. Hence, one can think of the SM Lagrangian of mass dim 2 and 4 as a part of a more general EFT that contain the same fields and symmetries known as the Standard Model Effective field theory (SMEFT).

From simple dimensional analysis, we know that the Higher dimensional operators need to contain an inverse mass with some power $p = 4 - d$ in the couplings, we will have a clear power counting in the SMEFT Lagrangian, such that we could collect all operators of the same mass dimension d into a d-mass-dimensional Lagrangians taking the form

$$\mathcal{L}^{(d)} = \frac{1}{\Lambda^{d-4}} \sum_i C_i \mathcal{O}_i. \tag{3.1}$$

For any $d > 4$ the Lagrangian in eq. (3.1) is not be renormalisable in the strict sense, yet it is still predictive via fitting the Wilson coefficients C_i order-by-order. This power-

counting property allows for predictability even when we, in principle, have infinite number of free Wilson coefficients, as all of these operators are suppressed by the NP scale (irrelevant operators w.r.t. the renormalisation group) []. In order to illustrate this, we let $\Lambda = 1$, then the effects of dimension-six operators will be in percent level, while dimension-eight operators will have effects of order $\sim 10^{-4}$, allowing us to ignore the dimension-eight and higher operators. Regarding dimension-five, we have only one operators called the Weinberg operator [123]

$$\mathcal{O}_{\nu\nu} = (\tilde{\phi} L_p)^T \hat{C} (\tilde{\phi}^\dagger L_q), \tag{3.2}$$

were $\hat{C}$ is the charge conjugation operator. The Weinberg operator violates leptonic number and generates neutrino masses after EW symmetry breaking, similar effects are generated from dimension-seven operators [124]. These effects do not yield considerable collider phenomenology. Hence, I shall be discussing SMEFT with dimension-six operators only, for studies on Higher dimensional SMEFT operators cf. [124–127]. The SMEFT Lagrangian up to dimension-six operators is given by

$$\mathcal{L}^{d=6}_{\text{SMEFT}} = \mathcal{L}_{\text{SM}} + \frac{1}{\Lambda^2} \sum_i C_i \mathcal{O}_i. \tag{3.3}$$

The study of dimension-six effective operators in characterising NP effects at energies beyond colliders reach has been first proposed in [129, 130]. Nowadays, phenomenological studies of EFT's with dimension-six operators primarily focus on using a set of complete and non-redundant "basis". This is due to the fact that different effective operators will correspond to same observables e.g. same scattering amplitudes of SM particles. This is the case if the operators can be related by using equations of motion, Fierz transformations, integration by parts or field redefinitions. This leads to non-trivial and counter-intuitive relations between operators. Thus making the construction of basis for the dimension-six SMEFT Lagrangian of eq. (3.3) a cumbersome task. Such task has been accomplished recently by [128, 131] forming what is known as **Warsaw Basis**. Another set of basis is the strongly-interacting light Higgs basis (SILH), originally proposed by [132], before the Warsaw basis, and completed in [133, 134]. A more recent set of basis has been published in [135] using a subset of couplings characterising the interactions of mass eigenstates in the effective Lagrangian.
The complete $d = 6$ SMEFT is described by 2499 independent parameters [131]. However, if one suppresses the flavour indices, then the dimension-six operators themselves are much less, in the Warsaw basis for example, assuming Baryon number conservation and dropping the flavour indices one has only 59 operators, listed in Table 3.1. It should be noted that all of the basis of SMEFT will produce the same phenomenology, the choice of basis is sometimes helpful in simplifying the analysis. In this thesis, I will mainly focus on Warsaw basis.
The SMEFT operators can either modify SM parameters (couplings, masses) or introduce new vertices that do not exist in the SM, like four-fermion operators, or both like $\mathcal{O}_{\phi e}$. An example of operators modifying SM parameters is $\mathcal{O}_{\phi D}$, which leads to

X^3	
$\mathcal{O}_G$	$f^{ABC}G_\mu^{A\nu}G_\nu^{B\rho}G_\rho^{C\mu}$
$\mathcal{O}_{\widetilde{G}}$	$f^{ABC}\widetilde{G}_\mu^{A\nu}G_\nu^{B\rho}G_\rho^{C\mu}$
$\mathcal{O}_W$	$\epsilon^{IJK}W_\mu^{I\nu}W_\nu^{J\rho}W_\rho^{K\mu}$
$\mathcal{O}_{\widetilde{W}}$	$\epsilon^{IJK}\widetilde{W}_\mu^{I\nu}W_\nu^{J\rho}W_\rho^{K\mu}$

Pure Higgs	
$\mathcal{O}_{\phi\Box}$	$(\phi^\dagger\phi)\Box(\phi^\dagger\phi)$
$\mathcal{O}_{\phi D}$	$\left(\phi^\dagger D_\mu\phi\right)^*\left(\phi^\dagger D_\mu\phi\right)$
$\mathcal{O}_\phi$	$(\phi^\dagger\phi)^3$

$\psi^2\phi^3+\text{h.c.}$	
$\mathcal{O}_{e\phi}$	$(\phi^\dagger\phi)(\bar{l}_p e_r\phi)$
$\mathcal{O}_{u\phi}$	$(\phi^\dagger\phi)(\bar{q}_p u_r\widetilde{\phi})$
$\mathcal{O}_{d\phi}$	$(\phi^\dagger\phi)(\bar{q}_p d_r\phi)$

$X^2\phi^2$	
$\mathcal{O}_{\phi G}$	$\phi^\dagger\phi\, G^A_{\mu\nu}G^{A\mu\nu}$
$\mathcal{O}_{\phi\widetilde{G}}$	$\phi^\dagger\phi\,\widetilde{G}^A_{\mu\nu}G^{A\mu\nu}$
$\mathcal{O}_{\phi W}$	$\phi^\dagger\phi\, W^I_{\mu\nu}W^{I\mu\nu}$
$\mathcal{O}_{\phi\widetilde{W}}$	$\phi^\dagger\phi\,\widetilde{W}^I_{\mu\nu}W^{I\mu\nu}$
$\mathcal{O}_{\phi B}$	$\phi^\dagger\phi\, B_{\mu\nu}B^{\mu\nu}$
$\mathcal{O}_{\phi\widetilde{B}}$	$\phi^\dagger\phi\,\widetilde{B}_{\mu\nu}B^{\mu\nu}$
$\mathcal{O}_{\phi WB}$	$\phi^\dagger\tau^I\phi\, W^I_{\mu\nu}B^{\mu\nu}$
$\mathcal{O}_{\phi\widetilde{W}B}$	$\phi^\dagger\tau^I\phi\,\widetilde{W}^I_{\mu\nu}B^{\mu\nu}$

$\psi^2X\phi+\text{h.c.}$	
$\mathcal{O}_{eW}$	$(\bar{l}_p\sigma^{\mu\nu}e_r)\tau^I\phi W^I_{\mu\nu}$
$\mathcal{O}_{eB}$	$(\bar{l}_p\sigma^{\mu\nu}e_r)\phi B_{\mu\nu}$
$\mathcal{O}_{uG}$	$(\bar{q}_p\sigma^{\mu\nu}T^A u_r)\widetilde{\phi}\, G^A_{\mu\nu}$
$\mathcal{O}_{uW}$	$(\bar{q}_p\sigma^{\mu\nu}u_r)\tau^I\widetilde{\phi}\, W^I_{\mu\nu}$
$\mathcal{O}_{uB}$	$(\bar{q}_p\sigma^{\mu\nu}u_r)\widetilde{\phi}\, B_{\mu\nu}$
$\mathcal{O}_{dG}$	$(\bar{q}_p\sigma^{\mu\nu}T^A d_r)\phi\, G^A_{\mu\nu}$
$\mathcal{O}_{dW}$	$(\bar{q}_p\sigma^{\mu\nu}d_r)\tau^I\phi\, W^I_{\mu\nu}$
$\mathcal{O}_{dB}$	$(\bar{q}_p\sigma^{\mu\nu}d_r)\phi\, B_{\mu\nu}$

$\psi^2\phi^2D$	
$\mathcal{O}_{\phi l}^{(1)}$	$(\phi^\dagger i\overleftrightarrow{D}_\mu\phi)(\bar{l}_p\gamma^\mu l_r)$
$\mathcal{O}_{\phi l}^{(3)}$	$(\phi^\dagger i\overleftrightarrow{D}^I_\mu\phi)(\bar{l}_p\tau^I\gamma^\mu l_r)$
$\mathcal{O}_{\phi e}$	$(\phi^\dagger i\overleftrightarrow{D}_\mu\phi)(\bar{e}_p\gamma^\mu e_r)$
$\mathcal{O}_{\phi q}^{(1)}$	$(\phi^\dagger i\overleftrightarrow{D}_\mu\phi)(\bar{q}_p\gamma^\mu q_r)$
$\mathcal{O}_{\phi q}^{(3)}$	$(\phi^\dagger i\overleftrightarrow{D}^I_\mu\phi)(\bar{q}_p\tau^I\gamma^\mu q_r)$
$\mathcal{O}_{\phi u}$	$(\phi^\dagger i\overleftrightarrow{D}_\mu\phi)(\bar{u}_p\gamma^\mu u_r)$
$\mathcal{O}_{\phi d}$	$(\phi^\dagger i\overleftrightarrow{D}_\mu\phi)(\bar{d}_p\gamma^\mu d_r)$
$\mathcal{O}_{\phi ud}+\text{h.c.}$	$i(\widetilde{\phi}^\dagger D_\mu\phi)(\bar{u}_p\gamma^\mu d_r)$

$(\bar{L}L)(\bar{L}L)$	
$\mathcal{O}_{ll}$	$(\bar{l}_p\gamma_\mu l_r)(\bar{l}_s\gamma^\mu l_t)$
$\mathcal{O}_{qq}^{(1)}$	$(\bar{q}_p\gamma_\mu q_r)(\bar{q}_s\gamma^\mu q_t)$
$\mathcal{O}_{qq}^{(3)}$	$(\bar{q}_p\gamma_\mu\tau^I q_r)(\bar{q}_s\gamma^\mu\tau^I q_t)$
$\mathcal{O}_{lq}^{(1)}$	$(\bar{l}_p\gamma_\mu l_r)(\bar{q}_s\gamma^\mu q_t)$
$\mathcal{O}_{lq}^{(3)}$	$(\bar{l}_p\gamma_\mu\tau^I l_r)(\bar{q}_s\gamma^\mu\tau^I q_t)$

$(\bar{R}R)(\bar{R}R)$	
$\mathcal{O}_{ee}$	$(\bar{e}_p\gamma_\mu e_r)(\bar{e}_s\gamma^\mu e_t)$
$\mathcal{O}_{uu}$	$(\bar{u}_p\gamma_\mu u_r)(\bar{u}_s\gamma^\mu u_t)$
$\mathcal{O}_{dd}$	$(\bar{d}_p\gamma_\mu d_r)(\bar{d}_s\gamma^\mu d_t)$
$\mathcal{O}_{eu}$	$(\bar{e}_p\gamma_\mu e_r)(\bar{u}_s\gamma^\mu u_t)$
$\mathcal{O}_{ed}$	$(\bar{e}_p\gamma_\mu e_r)(\bar{d}_s\gamma^\mu d_t)$
$\mathcal{O}_{ud}^{(1)}$	$(\bar{u}_p\gamma_\mu u_r)(\bar{d}_s\gamma^\mu d_t)$
$\mathcal{O}_{ud}^{(8)}$	$(\bar{u}_p\gamma_\mu T^A u_r)(\bar{d}_s\gamma^\mu T^A d_t)$

$(\bar{L}L)(\bar{R}R)$	
$\mathcal{O}_{le}$	$(\bar{l}_p\gamma_\mu l_r)(\bar{e}_s\gamma^\mu e_t)$
$\mathcal{O}_{lu}$	$(\bar{l}_p\gamma_\mu l_r)(\bar{u}_s\gamma^\mu u_t)$
$\mathcal{O}_{ld}$	$(\bar{l}_p\gamma_\mu l_r)(\bar{d}_s\gamma^\mu d_t)$
$\mathcal{O}_{qe}$	$(\bar{q}_p\gamma_\mu q_r)(\bar{e}_s\gamma^\mu e_t)$
$\mathcal{O}_{qu}^{(1)}$	$(\bar{q}_p\gamma_\mu q_r)(\bar{u}_s\gamma^\mu u_t)$
$\mathcal{O}_{qu}^{(8)}$	$(\bar{q}_p\gamma_\mu T^A q_r)(\bar{u}_s\gamma^\mu T^A u_t)$
$\mathcal{O}_{qd}^{(1)}$	$(\bar{q}_p\gamma_\mu q_r)(\bar{d}_s\gamma^\mu d_t)$
$\mathcal{O}_{qd}^{(8)}$	$(\bar{q}_p\gamma_\mu T^A q_r)(\bar{d}_s\gamma^\mu T^A d_t)$

$(\bar{L}R)(\bar{L}R)+\text{h.c.}$	
$\mathcal{O}_{quqd}^{(1)}$	$(\bar{q}_p^j u_r)\epsilon_{jk}(\bar{q}_s^k d_t)$
$\mathcal{O}_{quqd}^{(8)}$	$(\bar{q}_p^j T^A u_r)\epsilon_{jk}(\bar{q}_s^k T^A d_t)$
$\mathcal{O}_{lequ}^{(1)}$	$(\bar{l}_p^j e_r)\epsilon_{jk}(\bar{q}_s^k u_t)$
$\mathcal{O}_{lequ}^{(3)}$	$(\bar{l}_p^j\sigma_{\mu\nu}e_r)\epsilon_{jk}(\bar{q}_s^k\sigma^{\mu\nu}u_t)$
$\mathcal{O}_{ledq}$	$(\bar{l}_p^j e_r)(\bar{d}_s q_{tj})$

Table 3.1. Complete list of the dimension-six SMEFT operators in the Warsaw basis [128]. The $\mathcal{CP}$ violating operators contains the dual fields $\widetilde{X}$. The flavour labels of the form p, r, s, t on the $\mathcal{O}$ operators are suppressed on the left hand side of the tables.

modification of the Z boson mass after EW symmetry breaking

$$\frac{C_{\phi D}}{\Lambda^2}|\phi^\dagger D_\mu \phi|^2 \to \frac{C_{\phi D} v^4}{16\Lambda^2}(g_2^2 + g_1^2) Z^\mu Z_\mu. \tag{3.4}$$

Additionally, from field redefinitions, we get indirect contributions to the W mass from $C_{\phi D}$, combining both effects as a deviation in the ρ parameter, we get

$$\delta\rho = \frac{v^2}{2\Lambda^2} C_{\phi D}. \tag{3.5}$$

Which allows us to constrain $C_{\phi D}$ from the T parameter

$$T = \frac{-2\pi v^2}{\Lambda^2} \frac{(g_1^2 + g_2^2)}{g_1^2 g_2^2} C_{\phi D} \tag{3.6}$$

Another operator that affects the oblique parameters directly is $\mathcal{O}_{\phi WB}$, as it modifies the S parameter in the following way

$$S = \frac{16\pi v^2}{g_1 g_2 \Lambda^2} C_{\phi WB} \tag{3.7}$$

Other SM coupling modifications by SMEFT operators related to EWPO's are investigated in [3], and chapter 9. Additionally, the contributions of the SMEFT Wilson coefficients to SM parameters are not only from tree-level effects like in eq. (3.4) but could also come at (N)NLO, either from finite or RGE contributions.
SMEFT is suitable as a low energy limit for supersymmetric models [136] or some classes of composite Higgs models [137, 138]

3.1.1 Single Higgs processes in SMEFT

Single Higgs production and decay processes are modified at LO by a relatively long list of operators summarised in eqs. (3.8), (3.9) and (3.10). Explicit formulae for the Higgs rates dependence on the Wilson coefficients of these operators can be found in [139]

SMEFT operators modifying Higgs rates at LO

Higgs operators

$$C_{\phi D},\ \mathcal{O}_{\phi\Box},\ \mathcal{O}_{\phi G},\ \mathcal{O}_{\phi W},\ \mathcal{O}_{\phi B},\ \mathcal{O}_{\phi WB},\ \mathcal{O}^{(1)}_{\phi l},$$
$$\mathcal{O}^{(3)}_{\phi l},\ \mathcal{O}_{\phi e},\ \mathcal{O}^{(1)}_{\phi q},\ \mathcal{O}^{(3)}_{\phi q},\ \mathcal{O}_{\phi u},\ \mathcal{O}_{\phi d},\ \mathcal{O}_{\tau\phi},\ \mathcal{O}_{t\phi},\ \mathcal{O}_{b\phi},\ \mathcal{O}_{tb\phi}. \tag{3.8}$$

Top-quark operators

$$\mathcal{O}_{tG},\ \mathcal{O}_{tW},\ \mathcal{O}_{tB}, \tag{3.9}$$

other

$$\mathcal{O}_{G},\ \mathcal{O}^{(1)}_{ll},\ \mathcal{O}^{(1),(3)}_{Qq},\ \mathcal{O}_{tu},\ \mathcal{O}^{(1),(8)}_{td},\ \mathcal{O}^{(1),(8)}_{Qu},\ \mathcal{O}^{(1),(8)}_{Qd}. \tag{3.10}$$

The third generation quarks are denoted by Q while the first and second generation quarks are assumed to have the same coupling and denoted by q, u, d.

Some of these operators are strongly constrained from EWPO data such as $\mathcal{O}_{\phi D}$ and $\mathcal{O}_{\phi WB}$. Others are weakly constrained from Higgs data alone like the four-fermion or top sector operators, and require additional experimental data to constrain them. Global fits on SMEFT Wilson coefficients can be found in [140]. Where they have used Higgs and EW data on a subset of the SMEFT Wilson coefficients of the operators listed above. The fit also includes RGE and NLO (even NNLO for m_W) effects. While in [141], a global fit for a larger set of operators, but only with LO effects, including EW, Higgs and top data for C_G the fits are found in [142]. More recent study [143] has utilised EWPO data to constrain the four-fermion operators appearing in Higgs rates at LO and others involving four heavy quarks, using their NLO effects to EW bosons pole masses. We shall see in chapter 5 that the four-fermions operators with all heavy quarks will contribute also to Higgs rates at NLO. A wider scope analysis including a wide range of Higgs, top, di-boson and EWPO data has been preformed in [144].
The dependence of single Higgs rates on the SMEFT Wilson coefficients gets more complicated once NLO and higher effects are taken into an account. As shown in the fit results reported from [140], the RGE of these Wilson coefficients introduces new operators that do not appear at LO, also loop corrections to masses of the EW and Higgs bosons as well as their process will depend on some SMEFT coefficients. A prominent example of an operator appearing only at NLO in single Higgs processes is $\mathcal{O}_{\phi}$, which modifies the Higgs self interactions, namely the trilinear coupling.
Typically, in order to probe the Higgs trilinear self-coupling directly, one ought to observe Higgs pair production, see Part III. However, due to the appearance of Higgs self-interaction and its modifiers- C_{ϕ} in SMEFT context- in (N)NLO EW [145, 146] and Higgs observables [114–121], one can extract bounds on the Higgs trilinear coupling from single Higgs and EWPO data. Figure 3.2 illustrates example Feynman diagrams of single Higgs processes of which the trilinear Higgs self-coupling enters via NLO corrections. Using the results from the aforementioned references, a global fit with all operators that enter at tree-level in addition to the loop effects from the Higgs self-coupling has been

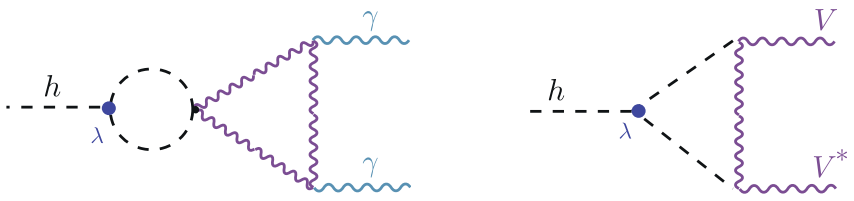

Figure 3.2. NLO EW corrections of single Higgs processes, were the Higgs trilinear self-coupling (the red circle) enters. Here the Higgs decay to two photons is shown as an example.

preformed in ref. [147] and later as we have seen in ref. [140]. Additionally, experimental searches for Higgs trilinear self-coupling have been presented by ATLAS [148] and CMS [94].

3.1.2 Higgs pair production and SMEFT

Higgs pair production in Hadron colliders is sensitive to six $\mathcal{CP}$ even SMEFT operators, under the assumption of Minimal Flavour violation (MFV) [1]. These operators are

$$\mathcal{O}_{\phi D},\ \mathcal{O}_{\phi\Box},\ \mathcal{O}_{\phi},\ \mathcal{O}_{t\phi},\ \mathcal{O}_{\phi G},\ \mathcal{O}_{tG}, \tag{3.11}$$

and their effects, with the corresponding colours are illustrated in Figure 3.3, except for $\mathcal{O}_{\phi D}$ and $\mathcal{O}_{\phi\Box}$, as they modify all SM Higgs vertices. However, MFV is not the only way to approach SMEFT, there exist more complex flavour structures that allow for significant enhancements of the first and second generation Yukawas with being excluded by flavour observables. Such formalisms will be discussed in chapter 8 and **??**, where I discuss the potential for Higgs pair production in probing operators modifying Light Yukawa couplings. Moreover, for Higgs pair production with $\mathcal{CP}$ operators, see ref. [149]. The main operator to constrain from Higgs pair as mentioned before is $\mathcal{O}_{\phi}$, for two reasons; a) the other operators are already strongly constraint from single Higgs and top processes b) the effect of $\mathcal{O}_{\phi}$ on Higgs pair production is significantly higher than in single Higgs or EW observables. This is illustrated in Figure 3.4, by comparing the relative change of the gluon fusion cross-sections at NLO QCD for single and di-Higgs production. This is not surprising, since C_{ϕ} appears at LO in Higgs pair production. Another advantage for Higgs pair production searches is the sensitivity of this process to non-linear couplings, for example diagrams (b) and (d) of Figure 3.3. Although in SMEFT these diagrams correspond to the same operators in (a) and (c), respectively, in an another EFT this is not necessary the case.

[1] MFV assumes that new physics operators will follow the same flavour hierarchies as the SM.

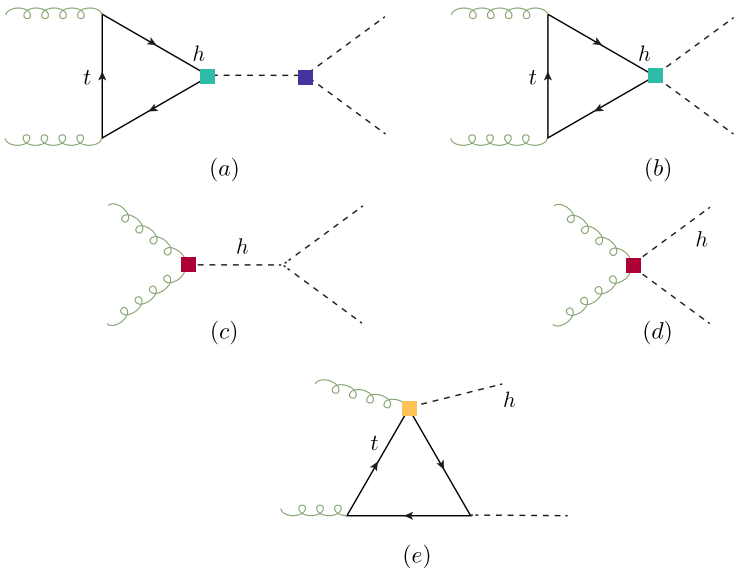

Figure 3.3. Example of diagrams illustrating how the dimension-six SMEFT operators enter in Higgs pair production at Hadron colliders.

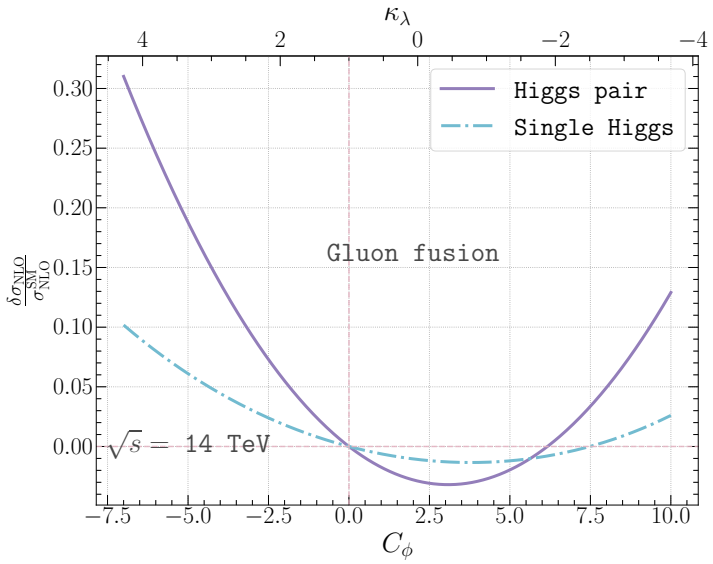

Figure 3.4. The relative change of the NLO QCD cross-section of gluon fusion production of single Higgs (dashed line) and Higgs pair (solid line) at a pp collider with $\sqrt{s} = 14$ TeV as a function of C_ϕ or the corresponding κ_λ.

3.2 The chiral Lagrangian

Given the strong bounds on the ρ parameter, it would plausible to assume that NP would maintain the custodial symmetry $SU(2)_V$, and treat the chiral symmetry breaking pattern $SU(2)_L \otimes SU(2)_R \to SU(2)_V$ in the same way the QCD chiral symmetry breaking is treated in terms of considering the pions as pNG bosons in order to describe their interaction. For pions this is known as **chiral perturbation theory** [150, 151]. The same mathematical description could be applied for the case of EW symmetry breaking by constructing the EW chiral Lagrangian (EWChL). In the EWChL y the Goldstone fields $\pi^a(x)$of the SM are part of $SU(2)$ unitary transformation

$$\mathcal{U}(x) = e^{i\pi^a(x)\sigma_a/v}, \tag{3.12}$$

which implies that the Goldstone fields transform non-linearly under $SU(2)_L \otimes SU(2)_R$. As for the Higgs field $h(x)$, it is added as an $SU(2)_L \otimes U(1)_Y$ singlet, and appears in the EWChL at any power in principle. As contrary to the power counting in the NP scale Λ like in SMEFT, in the EWChL, one counts the *chiral dimension* χ, defined for the fields as [152, 153]

$$[\phi]_\chi = 0,\ [X]_\chi = 0,\ [\partial_\mu]_\chi = 1,\ [\psi]_\chi = 2. \tag{3.13}$$

The zeroth order term of the EWChL will have $\chi = 2$, higher order terms could be considered as terms generated perturbatively from L loop interactions, with chiral dimensions $\chi = 2L + 2$, hence the first order EWChL or HEFT would have operators of $\chi = 4$.. Hence the expansion of the EWChL is in chiral order as well as in powers of $h(x)/v$. This power-counting results in some SMEFT dimension-six operators being considered of higher order in HEFT a prominent example of this is C_{tG} being of chiral dimension 5 in HEFT.
The relevant terms for single and di-Higgs production of the EWChL /HEFT is typically parametrised in the Unitary gauge by [147, 154]

$$\begin{aligned}
\mathcal{L}_{\text{HEFT}} = \frac{h}{v}\Bigg[& \left(\delta c_W m_W^2 W_\mu^+ W^{-\mu} + \delta c_Z \frac{m_Z^2}{2} Z_\mu Z^\mu\right) \\
& + c_{ww}\frac{g_2^2}{2} W^+_{\mu\nu} W^{-\mu\nu} + c_{w\Box} g_2^2 \left(W^-_\mu \partial_\nu W^{+\mu\nu} + \text{h.c.}\right) + c_{\gamma\gamma}\frac{\alpha}{8\pi} A_{\mu\nu} A^{\mu\nu} \\
& + c_{zz}\frac{g_2^2 + g_1^2}{4} Z_{\mu\nu} Z^{\mu\nu} + c_{z\gamma}\frac{e g_1}{16\pi^2} Z_{\mu\nu} A^{\mu\nu} + c_{z\Box} g_2^2 Z_\mu \partial_\nu Z^{\mu\nu} + c_{\gamma\Box} g_2 g_1 Z_\mu \partial_\nu A^{\mu\nu}\Bigg] \\
& + \frac{\alpha_s}{8\pi}\left(c_{gg}\frac{h}{v} + c_{gg}^{(2)}\frac{h^2}{2v^2}\right) \text{Tr}\left[G_{\mu\nu} G^{\mu\nu}\right] - \sum_f \left[m_f \left(c_f \frac{h}{v} + c_{ff}\frac{h^2}{2v^2}\right) \overline{f}_R f_L + \text{h.c.}\right] \\
& - c_{hhh}\frac{m_h^2}{2v} h^3 \ + \ldots,
\end{aligned} \tag{3.14}$$

I have omitted here the kinetic and mass terms of the Higgs, $\mathcal{CP}$ violating terms, as well as couplings not contributing to the LHC phenomenology and Higher chiral order operators. In addition to NP effects, this Lagrangian also includes the LO and NLO SM vertices, for example the parameter $\delta c_V = 1$ corresponds to the tree-level coupling between the Higgs field and the EW bosons $V = W, Z$. While the coupling $c_{gg} = 4/3$ corresponds to the SM effective coupling at NLO if the heavy top limit (HTL) $m_t \to \infty$. In contrast to eqs. (**??**) and (**??**) the couplings of one and two Higgs bosons to fermions or gluons become de-correlated. Giving this Lagrangian a richer phenomenology for Higgs pair production.
The HEFT coefficients modifying the Higgs pair production via gluon fusion are

$$c_{hhh},\ c_t\ (a),\ c_{tt}\ (b),\ c_{gg}\ (c),\ c_{gg}^{(2)}\ (d), \tag{3.15}$$

with the same colours highlighted in the operator insertions of Figure 3.3 and the letter next to the coefficient indicates the diagram its operator contributes to. Full parametrisation of the Higgs pair cross-section at NLO (inclusive and differential) and NNLO (inclusive) can be found in refs. [155–157] and implemented at NLO in `POWHEG-BOX` [158].
UV-complete models that yield in the EWChL are composite Higgs models [137, 138, 159], dilaton theories [160], techni-dilaton models [161], technicolour models [162] and other models with induced EW symmetry breaking [163, 164].

3.2.1 Translation between SMEFT and HEFT

In order to facilitate the translation between SMEFT and HEFT or to the κ-formalism, one needs to put the SMEFT Lagrangian into the canonical form, that is to convert the operators with covariant derivatives acting on the Higgs to canonically normalised Higgs kinetic term. This is done done by the field redefinition.

$$\phi = \begin{pmatrix} 0 \\ h(1 + c_{h,kin}) + v \end{pmatrix} \tag{3.16}$$

with

$$c_{h,kin} = \left(C_{\phi,\Box} - \frac{1}{4} C_{\phi D} \right) \frac{v^2}{\Lambda^2}\,. \tag{3.17}$$

This field redefinition will generate derivative interactions of the form $h(\partial_\mu h)^2$ and $h^2(\partial_\mu h)^2$. In order to remove these terms, and for sake of simplicity one needs to use a gauge-dependent field redefinition[2]

$$h \to h + c_{h,kin} \left(h + \frac{h^2}{v} + \frac{h^3}{3v^2} \right)\,. \tag{3.18}$$

This field redefinition hence leads to a dependence on $c_{h,kin}$ of all Higgs boson couplings. There are however some caveats to the translation between HEFT and SMEFT, for

[2] For gauge-independent formalism cf. [165].

example, HEFT is less restrictive than SMEFT and it covers loop effects. This makes some points of the HEFT parameter space unmappable to SMEFT. In addition, the power counting is different in both formalisms, as mentioned before there will be some operators present in SMEFT that are absent in HEFT and vice-versa. In Table 3.2, the translation between the HEFT and SMEFT Wilson coefficients of the operators relevant to Higgs pair production at LO is shown. More general translation between

HEFT	SMEFT (Warsaw)
c_{hhh}	$1 - 2\frac{v^4}{m_h^2}C_\phi + 3c_{h,kin}$
c_f	$1 + c_{h,kin} - C_{f\phi}\frac{v^3}{\sqrt{2}m_f}$
c_{ff}	$-C_{f\phi}\frac{3v^3}{2\sqrt{2}m_f} + c_{h,kin}$
c_{gg}	$8\pi/\alpha_s v^2 C_{\phi G}$
$c_{gg}^{(2)}$	$4\pi/\alpha_s v^2 C_{\phi G}$

Table 3.2. Translation between the Wilson coefficients of HEFT and SMEFT for the operators relevant to Higgs pair production

SMEFT in Warsaw and SILH basis and HEFT can be done automatically using `Rosetta` `package` [166]

3.2.2 EFT and κ-formalism

The κ formalism provides an experimentally accessible and well-defined in terms of QFT way to study the Higgs properties [167]. The κ parameters are part of more generalised formalism called the Higgs **Pseudo-observables** (PO's), which is discussed in chapter 4. If the new physics contributions do not generate new Lorentz structures there is a possible translation between the Wilson coefficients in the SMEFT Warsaw basis, and the κ formalism. In particular, taking the rescaling of the trilinear coupling, κ_λ, the translation is given by

$$\kappa_\lambda = 1 - \frac{v^4}{m_h^2}\frac{C_\phi}{\Lambda^2} + 3c_{h,kin}, \tag{3.19}$$

A similar relation exists for the rescaling of the quark Yukawa couplings κ_q

$$\kappa_q = 1 + c_{h,kin} - \frac{v^3}{\sqrt{2}m_q}\frac{C_{q\phi}}{\Lambda^2}. \tag{3.20}$$

One can see the similarities between κ-formalism and HEFT in these two examples, but this is not always the case. Other translations could be obtained by comparing how SMEFT operators modify the Higgs couplings with the SM, and matching it with the corresponding κ or other Higgs PO's.
However, one should be careful while interpreting results quoted in terms of Wilson

coefficients in the SMEFT framework extracted from di-Higgs, multi-Higgs or multi-vector bosons searches, as these results include couplings that are not present in the SM. For example, the $hhq\bar{q}$ coupling, though being linearly related to the quark Yukawa coupling $hq\bar{q}$, is not a rescaling of any SM Higgs coupling as has been discussed in **??**. With this in mind, one can strictly remain within a linear EFT and link the rescaling of the quark Yukawa, κ_q, to the $hhq\bar{q}$ coupling through

$$g_{hhq\bar{q}}^{\text{linear}-\text{EFT}} = -\frac{3}{2}\frac{1-\kappa_q}{v}\, g_{hq\bar{q}}^{\text{SM}}. \tag{3.21}$$

This relation will no longer hold once a non-linear EFT, like HEFT, is used. Hence, the κ-formalism, in a strict sense, is not applicable to multi-Higgs studies.

3.3 Conclusions

Effective field theories provide a systematic yet simplified approach for NP searches by simplifying its complex interaction structures. This can be though of as a dimensionality reduction approach by collapsing all the NP interaction into their effective ones as observed at colliders with energy reaches below the NP scale Λ. The linear approach to EFT is called the SMEFT, which preserves the SM fields and symmetries and the Higgs boson is a part of an $SU(2)_L$ doublet ϕ like the SM case. While non-linear approaches such as the chiral EW Lagrangian (or HEFT) treats that the Higgs boson as an added singlet. The latter approach is more general and introduces independent parameters involving multiple Higgs bosons. For example, the couplings $f\bar{f}h$ and $f\bar{f}hh$ will be both generated in SMEFT and HEFT, but in SMEFT they are related by the Wilson coefficient $C_{\phi f}$, while in HEFT they have independent Wilson coefficients c_f and c_{ff} respectively.
Most of the Wilson coefficients involving Higgs interactions are strongly bounds by EWPO's, Higgs and top data. In addition to theoretical bounds found in [168]. However, the Wilson coefficients modifying the Higgs self-couplings, though bounds from the first two aforementioned data and perturbative unitarity [55, 169] exist, these bounds remain weak. This can be improved by the searches for Higgs pair production at the HL-LHC, as this process is far more sensitive to these Wilson coefficients than EWPO and single-Higgs data, as they only appear at NLO in the theoretical predictions of the later two experimental observables. In **??**, I show the best bounds on the Wilson coefficients relearnt to Higgs production as well as heavy quark four-fermion operators, with a heatmap indicating the contribution of each operator in prominent Higgs, top and EW precision observables. Although this is a subset of the total SMEFT operators and observables used in the fits, one can see the interconnectivity of the measurements. The main objective of this thesis is to extend these connections by exploiting the potential of single-Higgs data and Higgs pair production to constrain the Higgs trilinear coupling modifiers (mainly in SMEFT) and the interplay between C_ϕ and heavy quark four-fermion operators in single Higgs data. Moreover, the SMEFT picture can be further extended by unravelling interplay between Light quark couplings modifiers in

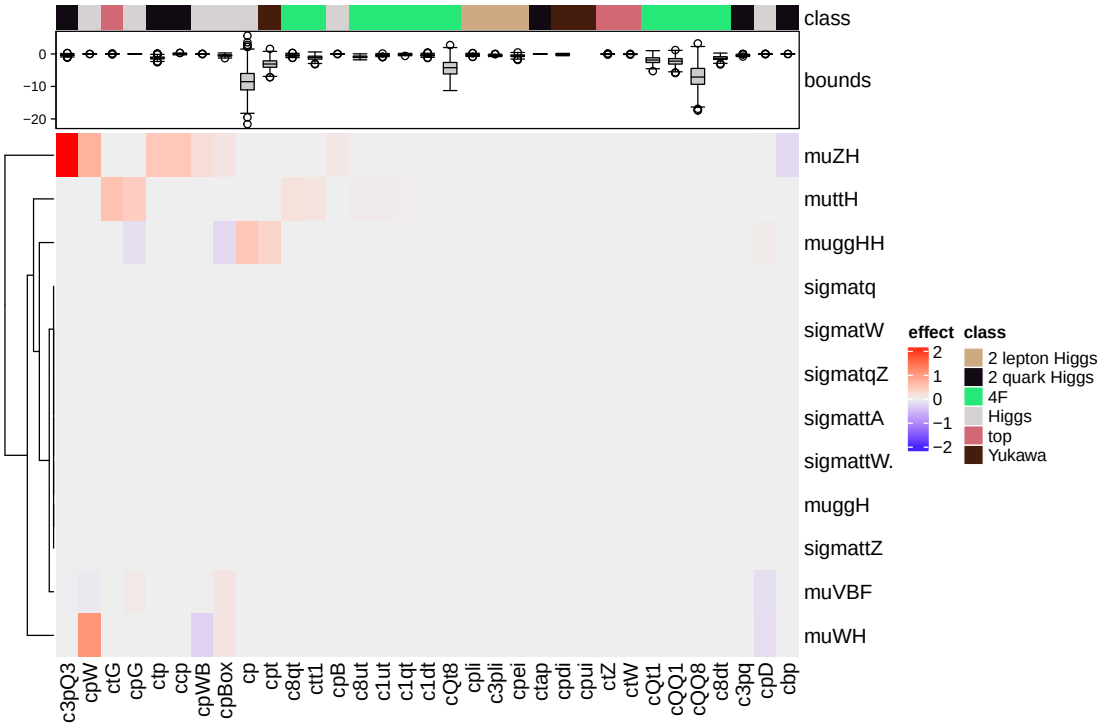
class
bounds
0
−10
−20
muZH
muttH
muggHH
sigmatq
sigmatW
sigmatqZ
sigmattA
sigmattW.
muggH
sigmattZ
muVBF
muWH
c3pQ3
cpW
ctG
cpG
ctp
ccp
cpWB
cpBox
cp
cpt
c8qt
ctt1
cpB
c8ut
c1ut
c1qt
c1dt
cQt8
cpli
c3pli
cpei
ctap
cpdi
cpui
ctZ
ctW
cQt1
cQQ1
cQQ8
c8dt
c3pq
cpD
cbp
effect
2
1
0
−1
−2
class
2 lepton Higgs
2 quark Higgs
4F
Higgs
top
Yukawa

Figure 3.5

Higgs pair production. Lastly, I will show another connection between Higgs operators in SMEFT and flavour anomalies. Emphasising the complex interconnectivity between experimental observables and SMEFT operators.

Part II

Single Higgs Processes at the LHC

4 Overview of Higgs production at colliders

The production of the Higgs boson at the LHC occurs via four distinct processes: gluon fusion (ggF), vector boson fusion (VBF), associated production with electroweak boson (Vh) and the production with top (and anti-top) pair ($th/t\bar{t}h$). It should be noted that sometimes the ggF category will include the quark anti-quark annihilation, but this is negligible in the SM, but becomes important for significant modifications of light Yukawa couplings. These process are illustrated in Figure 4.1, and their details were summarised in Table 4.1. All of these four channels have been observed at the LHC with $> 5\sigma$ precision.
Since the experimental measurements of this Higgs were discussed previously in section 2.3, the aim of this chapter is to provide an overview of the current theoretical status of these channels in section 4.1. I will then conclude this overview in section 4.2.

Process	Cross-section 13 TeV (pb)	Theo. accuracy	Exp. uncertainty (%)	Contribution (%)
ggF	48.51	N3LO QCD & NLO EW	6.5	88
tth & th	0.58	NLO QCD & NLO EW	20.0	1
VBF	3.78	NNLO QCD* & NLO EW	10.0	7
Vh	2.25	NNLO QCD & NLO EW	15.0	4

Table 4.1. Summery of the Higgs production processes at the LHC.

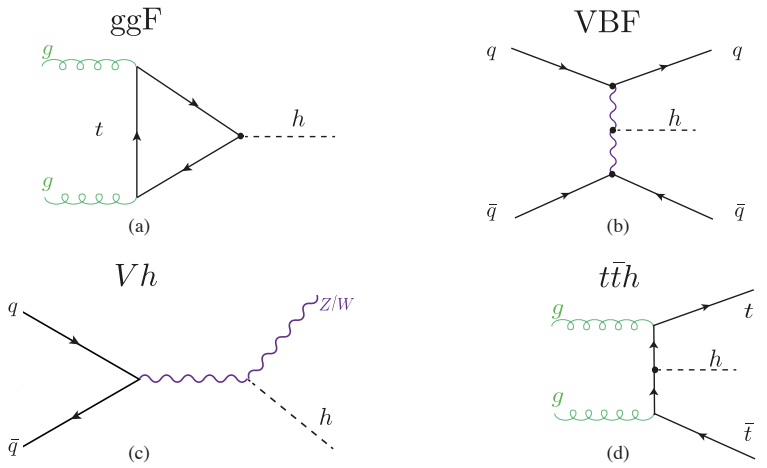

Figure 4.1. Feynman diagram examples of the leading processes for Higgs production at the LHC.

4.1 Current status of the Higgs production channels

4.1.1 Gluon fusion

The ggF channel has the highest cross-section amongst the Higgs production channels, and consequently has the lowest experimental uncertainties. In order to increase the precision of the channel, Higher order corrections need to be included. The current state-of-the-art theoretical computation for the Higgs inclusive cross-section is N^{3}LO in QCD and NLO in EW [170]. A full differential cross-section for the final state $gg \to h \to \gamma\gamma$ has been computed recently to N^{3}LO in QCD for the kinematic variables y_h, y_{γ_1}, y_{γ_2}, $\Delta y_{1,2}$ using the projection-to-born method [171]. The same final state fiducial differential cross-section in p_T with experimental cuts has been computed up to third re-summed and fixed order, i.e. N^{3}LL′ N^{3}LO dependence [172], the theoretical computation of this fiducial cross-section with difference orders compared to the experimental measurement by ATLAS [88] is shown in Figure 4.2. We can see that the resummed result has significantly smaller theoretical uncertainties. The current total theoretical uncertainty with this order calculation is 5.4%, with only 2.7% of it coming from the perturbation order cut-off of the calculation, while the rest comes from the branching fraction, PDF+α_s, EW corrections and mass uncertainties. When compared to Table 2.1, the projected experimental uncertainty of this final states at the HL-LHC is 4.2%, we see that the uncertainties will becomes comparable, and if the PDF uncertainties are reduced the uncertainties will remain experimentally-dominated for this channel. The predictions can be further improved by the computation of mixed QCD-EW effects.

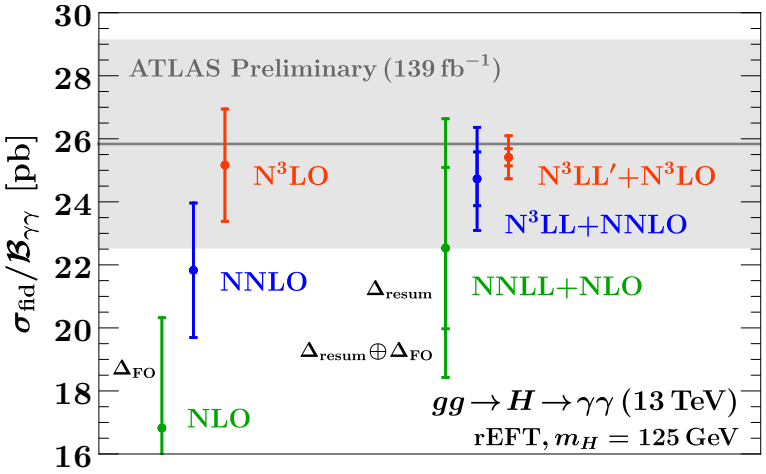

Figure 4.2. The total fiducial cross-section for the final state $gg \to h \to \gamma\gamma$ at both fixed and resumed third order compared to the experimental ATLAS measurement [88] this figure is taken from [172]

Alas, these computations invokes three-loop integrals with both gluons and EW bosons, computed in [173] or two-loop ones with two particle final states appearing in the real

corrections with the process $gg \to hg$ computed in [174] using differential equations. The computation was completed by inclusion of light quark initial states for the real corrections in [175] with exact quark mass dependence, reducing the EW uncertainty from 2% to $\sim 0.6\%$.
The computation of the three-loop form-factors with full top-mass dependence has been achieved in [176, 177] correction the cross-section by -0.26%. However, there remains an intricate interplay between the mass effects of gg, qg and qq initial states for the real matrix elements that cannot be fully controlled due to the light quark mass effects.
NLO corrections to the $h + j$ and $h + 2j$ processes were computed by [178] in the FT approximation, which used exact born and real correction amplitudes, and approximates the two-loop virtuals by

$$|\mathcal{A}^{2-\text{loop}}(m_t, \mu_R^2)|^2 \approx |\mathcal{A}^{1-\text{loop}}(m_t \to \infty, \mu_R^2)|^2 \frac{|\mathcal{A}^{1-\text{loop}}(m_t)|^2}{A^{(0)}(m_t) \to \infty|^2}. \tag{4.1}$$

Although this approximation works very well even for $p_T \gg m_t$, the full top mass effects computations have been carried out in [179–181] using the high energy expiation technique.

4.1.2 Vector boson fusion

The VBF channel has a very distinctive signature, making it very suitable channel for Higgs signal extraction. The suppressed colour exchange between the quarks result in a little jet activity in the central rapidity region, and the quarks will be scattered resulting in two forward jets. The decay products of the Higgs are found in the region between these two forward jets. These features allows for excellent measurement of Higgs couplings and more difficult decays, and $\mathcal{CP}$ properties determination. Some of these features are also shared with the Vh production channel via Higgs-strahlung. Both of these channels contain the VVh vertex which could be written generally as [154]

$$T^{\mu\nu}(p_1, p_2) = a_1 g^{\mu\nu} + a_2 \left(g^{\mu\nu} - 2\frac{p_2^\mu p^\nu}{p_1 \cdot p_2} \right) + a_3 \frac{p_1^\alpha p_2^\beta}{p_1 \cdot p_2} \epsilon^{\mu\nu\alpha\beta}. \tag{4.2}$$

In the SM only $a_1 \neq 0$, and the other coefficients represent the anomalous coupling, for example if $a_3 \neq 0$ then the Higgs is $\mathcal{CP}$ odd. The study of the azimuthal angle distribution $d\sigma_{VBF}/d\Delta\phi_{jj}$ allows for the determination of these coefficients, with very little dependence on the Higher order corrections on VBF [182].
The NLO QCD inclusive cross-section is known since the 90's [183], and later these corrections were made for the differential distributions cf. [184, 185]. Unlike the ggF channel, that has an NLO K-factor of 1.6 at 13 TeV [186] , the VBF NLO corrections are small $\sim 10\%$. The two-loop NNLO QCD cross-section has been computed, the most recent is via the structure function approach [187] and later in STXS level 1.2 bins with EW corrections [188] implemented in an MC generator `HAWK`. Despite these corrections being small, they are non-negligible and their inclusion is important for uncertainties

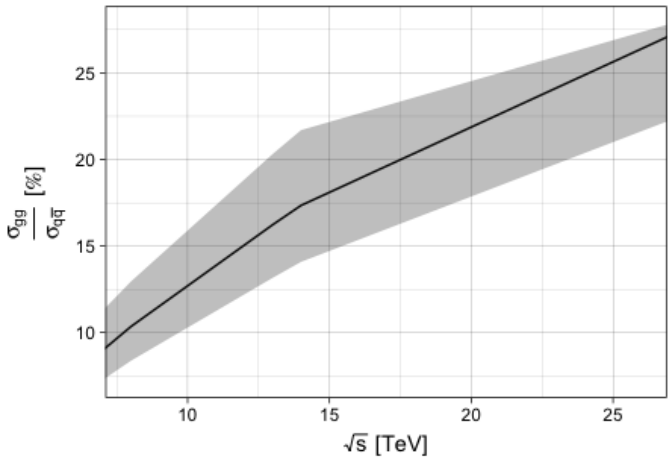

Figure 4.3. The ratio of the LO gluon fusion production cross-section $gg \to Zh$ (σ_{gg}) with respect to the NLO Drell-Yan process $q\bar{q} \to Zh$ cross-section ($\sigma_{q\bar{q}}$) at a pp collider with centre-of-mass energy $\sqrt{s}$. The error band captures the total theoretical uncertainties on both cross-sections dominated by σ_{gg} .

reduction.

4.1.3 Associated production with EW bosons

The channels $pp \to Wh/Zh$ are quark-initiated tree-level processes at LO interpreted as **Drell-Yan process** [189, 190]. These process has been computed up to NNLO in QCD ($\sim \alpha_s^2$), and NLO EW ($\sim \alpha^2$) [191].

Despite arising for the first time at NNLO in perturbation theory to the partonic cross-section, the gluon fusion channel $gg \to Zh$ has a non-negligible contribution to the hadronic cross-section $pp \to Zh$, which could reach $> 16\%$ of the total cross-section contribution at 14 TeV [192], see Figure 4.3. The contribution becomes more significant when looking at large invariant mass bins in the differential cross-section. This is due to the significant abundance of gluons at the LHC for large energy faction Q as well as the extra enhancement coming from the top quark initiated contribution near the $t\bar{t}$ threshold [193]. The gluon fusion channel has a higher scale uncertainties than the quark induced one, as one can see from the uncertainty band of Figure 4.3 predominantly coming from the gluon fusion part σ_{gg}. With that in mind, and the absence of gluon fusion channel for Wh channel, the Zh channel has higher theoretical uncertainties. This further motivates NLO calculation of the $gg \to Zh$ channel to higher orders in perturbation theory, in order to reduce these uncertainties. Facilitating the precision measurement of the Zh channel at the future LHC runs, which in term provides better constraints on several observables, such as sign and magnitude of the top Yukawa coupling, dipole operators [194].

The leading order (LO) contribution to the $gg \to Zh$ amplitude, given by one-loop

diagrams, was computed exactly in refs.[195, 196]. However, for the NLO, the virtual corrections contain multi-scale two-loop integrals some of which are still not known analytically (for the box diagram). The first computation of the NLO terms has been done by [197] using an asymptotic expansion in the limit $m_t \to \infty$ and $m_b = 0$, and pointed to a K-factor of about ~ 2. Later, the computation has been improved via soft gluon resummation, and including NLL terms found in ref.[198], the NLL terms has been matched to the fixed NLO computation of [197]. Top quark mass effects to the $gg \to Zh$ process were first implemented using a combination of large-m_t expansion (LME) and Padé approximants [199]. A data-driven approach to extract the gluon fusion dominated non-Drell-Yan part of Zh production using the known relation between Wh and Zh associated production when only the Drell-Yan component of the two processes is considered has been investigated in ref.[200]. The differential distributions of $gg \to Zh$ at NLO was studied in ref.[201] via LO matrix element matching.

More recent studies of the NLO virtual corrections to this process were based on the high-energy (HE) expansion improved by Padé approximants with the LME, which extended the validity range of the HE expansion [202]. However, this expansion is only valid for in the invariant mass region $\sqrt{\hat{s}} \gtrsim 750\,\text{GeV}$ and $\sqrt{\hat{s}} \lesssim 350\,\text{GeV}$, which only covers $\sim 32\%$ of the hadronic cross section. Additionally, numerical computation of the two-loop virtual corrections, though implemented exactly in [203], are rather slow for practical use in MC simulations. This highlights the importance of an analytical method that can cover the remaining region of the cross-section and can be merged with the HE expansion via Padé approximants. Fortunately, the two-loop corrections to the triangle diagrams can be computed exactly. And the loop integrals appearing in the box correction having no analytic expression can be expanded in small Z (or Higgs) transverse momentum, p_T. This method was first used for Higgs pair production in [204], to compute the NLO virtual corrections to the box diagrams in the forward kinematics. In chapter 6, I will discuss the calculation preformed by my collaborators and myself and published in [1], which includes the full top mass dependence of the virtual two-loop correction to $gg \to Zh$ in an analytic form using the same p_T expansion technique.

4.1.4 Associated production with top quarks

The largest part of the $t\bar{t}h/th$ uncertainty budget comes from the theoretical modelling of this process's backgrounds, mainly $t\bar{t}b\bar{b}$, $t\bar{t}W$ as backgrounds for $t\bar{t}(h \to b\bar{b})$ and $t\bar{t}(h \to$ multileptons), respectively. There have been several theoretical developments regarding these backgrounds. Starting with $t\bar{t}W$, the differential cross-section at NNL+ NLO QCD calculation of this channel has been done in [205, 206] including EW corrections. The fully decayed final state at NLO QCD [207–209] and at NLO-EW [210] have been computed. Additionally, these calculations were implemented in `POWHEG-BOX` [211]. The comparison between the NLO-QCD with parton showering vs on-shell can be found in [212]. As for $t\bar{t}b\bar{b}$, the progress in obtaining higher order corrections is faced with challenges posed by the complexity of this channel. However, progress has been made, for instance the off-shell effects in the fully decayed $pp \to 2\ell 2\nu 4b$ with NLO corrections was studied in [213, 214]. Further discussion of the theoretical developments of these

channels is beyond the scope of this thesis.
Regarding the higher order corrections to the $t\bar{t}h/th$ channel itself, the NLO QCD+EW effects on the off-shell multileptons final state were studied in [215], while the NLO corrections including SMEFT operators were calculated in[216]. The NLO QCD+EW with parton showering is available in all event generators, and the SMEFT operators at NLO are available in `MadGraph5_aMC@NLO` . As of the time of writing this thesis, there is no NNLO calculation of $t\bar{t}h/th$ available.

4.2 Concluding remarks

The precise determination of the Higgs boson properties is one of the main focus of the Large Hadron Collider (LHC) physics programme. In order to achieve precision-level Higgs measurements both experimental and theoretical uncertainties need to be improved. Though the first can be improved with Higher luminosities and energies, better detectors and improved analysis techniques. Theoretical uncertainties require higher-order calculations, inclusion of mixed EW and QCD terms , inclusion of mass effects and suitable parton distribution functions with Higher order in QCD. As we have seen, a lot of effort is being put into improving the theoretical predictions of Higgs production channels. Moreover, many computer tools have been made available to compute these cross-sections, for example `iHixs2` [217] or to generate full events, like `POWHEG` [218–224] and `MadGraph5_aMC@NLO` [225], and many others can be found with greater detail in the Higgs cross-sections working group [226].
Sometimes, to improve the measurement of the process, it is not sufficient to only improve the theoretical prediction of the channel itself, but also its backgrounds, which is particularly important for $t\bar{t}h$. Hence, higher order calculations of processes like $t\bar{t}W$ with parton-shower effects as well as improved analysis to distinguish $t\bar{t}(h \to b\bar{b})$ have a significant impact on $t\bar{t}h$ measurements. Event generator tools with SMEFT implementation in Higgs processes with patron showing interface capabilities have been implemented in a `MadGraph5_aMC@NLO` model `SMEFTatNLO` [227] which enabled loop computations with SMEFT operators and consequently fits of the SMEFT Wilson coefficients with Higgs data at NLO as we have seen in chapter 3.
There is plenty of room for future improvements in the reduction of theory uncertainty budget, and providing better theoretical prediction of the Higgs processes in the SM and beyond. From inclusion of patron shower matching , merging and validation to inclusion of two-loop calculations of gluon fusion Zh and EW NLO effects of $t\bar{t}h$, all in preparation to the HL-LHC Higgs precision era !

5 Four top operator in Higgs production and decay

In chapter 3, the SM effective field theory has been portrayed as a pragmatic yet robust parametrisation of potential NP degrees of freedom for LHC searches, with the ansatz that these degrees of freedom have masses that are higher than the LHC reach. From the discussion and overview of Higgs-related SMEFT operator in that chapter, the operator $\mathcal{O}_\phi$ stood out as one of the weakly constrained amongst them. This is due to the current low experimental sensitivity on the Higgs self-coupling as shown in **??**.

The physics of the top quark is deeply intertwined with Higgs physics, and when one starts looking at the operators entering at NLO of Higgs processes, and by restricting oneself to pure Higgs or EW operators, one would miss the full picture in a global fit. Namely, the top quark operators. Though many of these operators are strongly constraint from top observables, a subset of them remain as weakly constraint as the trilinear Higgs self-coupling. These operators are four-fermion operators involving the third generation quarks. They would be constrained directly from the production of four tops observation. However, this process has small cross-section at the LHC of $\sim$ 12 fb [228], which is more or less comparable to the Higgs pair production signal strength. In addition, we have seen in the previous chapter that the theoretical predictions of $t\bar{t}b\bar{b}$ remain limited. Experimental searches for the production of four top quarks has been first made by CMS [229] combining different LHC runs, followed by ATLAS [230], the latter reporting a 4.3σ observation of this processes with cross-section of 24^{+7}_{-6} fb. When the whole third generation quarks is included, one sees the same story with $t\bar{t}b\bar{b}$ contact interaction which require the observation of $t\bar{t}b\bar{b}$ production for a direct constraint, see [231, 232] for experimental searches and [233, 234] for SMEFT fits. It should be noted that for the production of four tops, or two tops two beauty quarks in SMEFT, the contact terms do not interfere with the SM process, and only appear proportional to $\mathcal{O}(1/\Lambda^4)$. This makes the SMEFT global analysis of these operators depend highly on the EFT truncation scheme used, i.e. whether to keep quadratic terms or not.

These four-fermion operators enter in single Higgs processes at NLO, in a similar manner as the Higgs self-coupling. In this chapter, the exact NLO corrections to the Higgs rates, i.e. production and decay, due to these four-fermion operators have been competed, and it was found to be significantly larger or at the same scale as the corrections from C_ϕ. Since the four-fermions operators are weakly constrained they should be included in fits involving Higgs data. We shall demonstrate that, there is a significant correlation amongst the Higgs self-coupling and the four-fermion operators.

As the direct bounds for $t\bar{t}t\bar{t}$ and $t\bar{t}b\bar{b}$ contact interactions are weak, single Higgs data provides competitive bounds of there operators alongside other alternative constraints

like top quark pair production [227] and electroweak precision data [235] .

The chapter is based on a the paper [236] and structured as follows: in **??** the full NLO calculation of Higgs rates due to the four-fermion operators is illustrated. Afterwards, in section 5.2, a fit from Higgs data combining the Higgs trilinear coupling and the four-fermion operators is presented, for both Run-II and HL-LHC, with more elaborate results for the latter is found in **??**. The results are further discussed in section 5.3.

5.1 Contribution of four-fermion operators to Higgs rates at NLO

We will consider the following dimension-six SMEFT operators in the NLO calculations

Four-Heavy-quarks SMEFT operators modifying Higgs rates at NLO

Operators with homogenous chiral structure, i.e. (RR)(RR) or (LL)(LL)

$$\mathcal{O}_{tt},\ \mathcal{O}_{bb},\ \mathcal{O}_{tb}^{(1)},\ \mathcal{O}_{tb}^{(8)},\ \mathcal{O}_{QQ}^{(1)},\ \mathcal{O}_{QQ}^{(3)}. \tag{5.1}$$

Operators with heterogeneous chiral structure, i.e. (LR)(LR) or (LL)(RR)

$$\mathcal{O}_{Qt}^{(1)},\ \mathcal{O}_{Qt}^{(8)},\ \mathcal{O}_{Qb}^{(1)},\ \mathcal{O}_{Qb}^{(8)},\ \mathcal{O}_{QtQb}^{(1)},\ \mathcal{O}_{QtQb}^{(8)} \tag{5.2}$$

The explicit definition of these operators can be found in Table 3.1. However, the notation is slightly modified from the standard Warsaw basis one. The flavour indices were suppressed since only the the third generation is considered throughout this chapter. Adopting the same notation from previous chapters, Q denotes the (heavy) left-handed $SU(2)_L$ doublet quarks while t and b refer to the right-handed singlets. In studies involving SMEFT fits, such as [141] the $SU(3)_C$ singlet and octet left-handed operators $\mathcal{O}_{QQ}^{(1),SU(3)}$, $\mathcal{O}_{QQ}^{(8)}$ are used instead of the singlet and triplet of $SU(2)_L$ appearing in the stabdard Warsaw basis. These two conventions' Wilson coefficients are related via the relations

$$\begin{aligned} C_{QQ}^{(1),SU(3)} &= 2C_{QQ}^{(1)} - \frac{2}{3}C_{QQ}^{(3)}, \\ C_{QQ}^{(8)} &= 8C_{QQ}^{(3)}. \end{aligned} \tag{5.3}$$

Additionally, all of these Wilson coefficients are assumed to be real.

From here on, only operators that induce sizeable NLO correction to Higgs processes are taken into account. These operators turns out to be the ones that introduce loop corrections to the top or beauty Yukawa, top or beauty masses and finite corrections from top loops. Such corrections will be proportional to the top mass. On the contrary, corrections from beauty loops are highly suppressed by m_b. Also, operators that have chiral structure that does not enable them to enter in the Yukawa renormalisation group

equation (RGE)'s will not be constrained from Higgs data as they would only contribute through small finite terms, as we shall see later. Hence, only four top and the $\mathcal{O}_{QtQb}^{(1),(8)}$ operators will be considered, as they will possess corrections with top quark loops.

This section will demonstrate the calculation of NLO Higgs production and decay rates from the four-heavy-quarks operators discussed above. For the production of Higgs via gluon fusion or Higgs decay to gluon, photons and beauty quarks, the results were computed fully analytically and presented in this section. However, for the associated production of the Higgs with top pair $t\bar{t}h$, the corrections were computed numerically, due to the length of the the analytic expressions if the result.

5.1.1 Analytic calculations

The NLO corrections to gluon fusion, $h \to gg$, $h \to \gamma\gamma$ and $h \to b\bar{b}$ all come from the sub-diagrams listed in Table 5.1, with top loops entering in the mass renormalisation or to/beauty Yukawa vertex correction. Where $N_c = 3$ the number of colours, and $c_F = (N_c^2 - 1)/(2N_c) = 4/3$ the $SU(3)$ quadratic Casimir in the fundamental representation. The effect of beauty loops coming from for $C_{QtQb}^{(1/8)}$, can be easily read from this table by

Diagram	colour factor		mass/coupling
	singlet	octet	
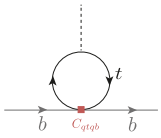	$2N_c + 1$	c_F	$y_t\, m_b\, m_t^2$
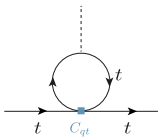	1	c_F	$y_t\, m_t^3$
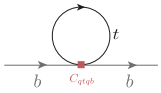	$2N_c + 1$	c_F	m_t^3
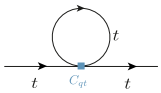	1	c_F	m_t^3

Table 5.1. The sub diagrams contributing to the NLO corrections of gluon fusion Higgs production higgsdecasy to gluon, photon and beauty quarks.

exchanging $t \leftrightarrow b$, which is significantly smaller than the corrections coming from top loops.

We see that these corrections correspond to the Wilson coefficients appearing in the RGE's include them in the appendix, and operators with (LL)(LL) or (RR(RR)) chiral structures do not contribute to these processes.
By considering the two-loop corrections to the gluon fusion illustrated in Figure 5.1 we find that such correction contain the sub-diagrams shown in Table 5.1, except for diagram (e), which is found to be vanishing for on-shell gluons. Additionally, these diagrams indicated that the two-loop corrections will be reduced to a product of two one-loop functions after the integral reduction.
Following the Feynman rules derived in ref. [237] for the four-fermion operators of interest here, the *ggtoh* two-loop amplitude was calculated, then Dirac algebra and further algebraic manipulations were preformed in Mathematica using `PackageX` [238]. Reduction of the resulting two-loop to Master integrals has been preformed using `KIRA` [239], all of the resulting master integrals were indeed products on one-loop functions as expected. The computation has been cross-checked independently by my collaborators, using a different pipeline : `FeynArts` [240], for amplitude generation then `FeynRules` [241] and `Fire` [242] for algebraic manipulation and loop-integral reduction.

The sub-diagrams appearing in the two-loop calculation, correspond to mass and vertex renormalisation, hence they contain poles that require counter-terms. A mixture of on-shell (OS) and $\overline{\text{MS}}$ – schemes has been used for the mass and $hq\bar{q}$ coupling renormalisation, respectively. The renormalisation of SM quantities in the OS and NP ones in the $\overline{\text{MS}}$ scheme was proposed by [243], which provides consistency since the NP is assumed to be of a Higher scale than the SM.

The top/beauty mass renormalisation can be expressed as

$$m_{t/b}^{\text{OS}} = m_{t/b}^{(0)} - \delta m_{t/b}, \tag{5.4}$$

with the corresponding counter-terms

$$\begin{aligned}\delta m_t =& \frac{1}{16\pi^2}\frac{C_{Qt}^{(1)} + c_F C_{Qt}^{(8)}}{\Lambda^2} m_t^3 \left[\frac{2}{\bar{\epsilon}} + 2\log\left(\frac{\mu_R^2}{m_t^2}\right) + 1\right] \\ &+ \frac{1}{16\pi^2}\frac{(2N_c+1)C_{QtQb}^{(1)} + c_F C_{QtQb}^{(8)}}{\Lambda^2}\left[\frac{1}{\bar{\epsilon}} + \log\left(\frac{\mu_R^2}{m_b^2}\right) + 1\right] m_b^3\,,\end{aligned} \tag{5.5}$$

$$\delta m_b = \frac{1}{16\pi^2}\frac{(2N_c+1)C_{QtQb}^{(1)} + c_F C_{QtQb}^{(8)}}{\Lambda^2}\left[\frac{1}{\bar{\epsilon}} + \log\left(\frac{\mu_R^2}{m_t^2}\right) + 1\right] m_t^3\,, \tag{5.6}$$

with $\bar{\epsilon}^{-1} = \epsilon^{-1} - \gamma_E + \log(4\pi)$, in dimensional regularization with $d = 4 - 2\epsilon$. It is possible

to convert from OS to the $\overline{\text{MS}}$ – scheme for mass counter-terms via the following relations

$$\delta m_t^{\overline{\text{MS}}} = \frac{1}{8\pi^2}\frac{C_{Qt}^{(1)} + c_F C_{Qt}^{(8)}}{\Lambda^2} m_t^3 \frac{1}{\bar{\epsilon}} + \frac{1}{16\pi^2}\frac{(2N_c+1)C_{QtQb}^{(1)} + c_F C_{QtQb}^{(8)}}{\Lambda^2}\frac{1}{\bar{\epsilon}} m_b^3 \,, \tag{5.7}$$

$$\delta m_b^{\overline{\text{MS}}} = \frac{1}{16\pi^2}\frac{(2N_c+1)C_{QtQb}^{(1)} + c_F C_{QtQb}^{(8)}}{\Lambda^2}\frac{1}{\bar{\epsilon}} m_t^3 \,. \tag{5.8}$$

The effect of changing to the mass renormalisation scheme is small for the top mass but rather significant, up to 100% for the beauty mass.
The top/beauty Higgs coupling in SMEFT, is written as

$$g_{ht\bar{t}/hb\bar{b}} = \frac{m_{t/b}}{v} - \frac{v^2}{\Lambda^2}\frac{C_{t\phi/b\phi}}{\sqrt{2}} \,. \tag{5.9}$$

Hence, a modification of the Higgs couplings to bottom and top quarks is generated by operator mixing, even if $C_{t\phi/b\phi}$ are zero at Λ. From this, the $\overline{\text{MS}}$ counter-term should take the form

$$\delta g_{ht\bar{t}/hb\bar{b}} = \frac{m_{t/b}}{v}\delta m_{t/b} - \frac{v^2 \delta C_{t\phi/b\phi}}{\sqrt{2}}, \tag{5.10}$$

where $\delta C_{t\phi/b\phi}$ is directly read from the anomalous dimension, see App for the explicit expression of the RGE's.

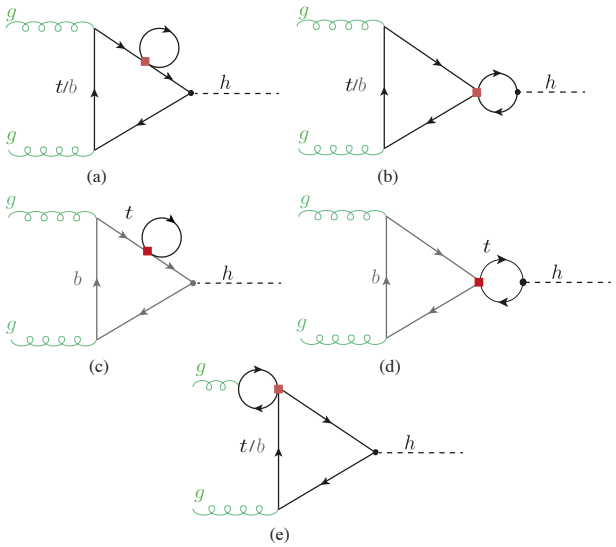

Figure 5.1. Example Feynman diagrams for four-fermion-operator contributions to the Higgs production via gluon fusion. The red box indicates the four-fermion operator.

Correction to gluon fusion and $h \to gg$

The modification of the Higgs production via gluon fusion can be written as

$$\frac{\sigma_{ggF}}{\sigma_{ggF}^{\mathrm{SM}}} = 1 + \frac{\sum_{i=t,b} 2\mathrm{Re}\left(F_{\mathrm{LO}}^{i} F_{\mathrm{NLO}}^{*}\right)}{\left|F_{\mathrm{LO}}^{t} + F_{\mathrm{LO}}^{b}\right|^{2}} \tag{5.11}$$

with

$$F_{\mathrm{LO}}^{i} = -\frac{8m_i^2}{m_h^2}\left[1 - \frac{1}{4}\log^2(x_i)\left(1 - \frac{4m_i^2}{m_h^2}\right)\right] \tag{5.12}$$

and

$$\begin{aligned} F_{\mathrm{NLO}} =& \frac{1}{4\pi^2\Lambda^2}(C_{Qt}^{(1)} + c_F C_{Qt}^{(8)}) F_{\mathrm{LO}}^{t}\left[2m_t^2 + \frac{1}{4}(m_h^2 - 4m_t^2)\left(3 + 2\sqrt{1 - \frac{4m_t^2}{m_h^2}}\log(x_t)\right)\right. \\ &\left. + \frac{1}{2}(m_h^2 - 4m_t^2)\log\left(\frac{\mu_R^2}{m_t^2}\right)\right] \\ &+ \frac{1}{32\pi^2\Lambda^2}((2N_c+1)C_{QtQb}^{(1)} + c_F C_{QtQb}^{(8)})\left[F_{\mathrm{LO}}^{b}\frac{m_t}{m_b}\left(4m_t^2 - 2m_h^2\right.\right. \\ &\left.\left. -(m_h^2 - 4m_t^2)\sqrt{1 - \frac{4m_t^2}{m_h^2}}\log(x_t) - (m_h^2 - 4m_t^2)\log\left(\frac{\mu_R^2}{m_t^2}\right)\right) + (t \leftrightarrow b)\right]. \end{aligned} \tag{5.13}$$

Only top quark loops contribute to the parts proportional to $C_{Qt}^{(1),(8)}$. The variable x_i for a loop particle with mass m_i is given by

$$x_i = \frac{-1 + \sqrt{1 - \frac{4m_i^2}{m_h^2}}}{1 + \sqrt{1 - \frac{4m_i^2}{m_h^2}}}\,. \tag{5.14}$$

Using the same amplitudes, the $h \to gg$ partial width modification can be written as

$$\frac{\Gamma_{h\to gg}}{\Gamma_{h\to gg}^{\mathrm{SM}}} = 1 + \frac{\sum_{i=t,b} 2\mathrm{Re}\left(F_{\mathrm{LO}}^{i} F_{\mathrm{NLO}}^{*}\right)}{|F_{\mathrm{LO}}^{t} + F_{\mathrm{LO}}^{b}|^{2}} \tag{5.15}$$

Correction to Higgs decays to photons

Analogously, since the decay $h \to \gamma\gamma$ contains the same topologies as gluon fusion, we could use the result from the above calculation to calculate the correction to the partial width for this decay

$$\frac{\Gamma_{h\to\gamma\gamma}}{\Gamma_{h\to\gamma\gamma}^{\mathrm{SM}}} = 1 + \frac{2\mathrm{Re}\left(F_{\mathrm{LO},\gamma} F_{\mathrm{NLO},\gamma}^{*}\right)}{|F_{\mathrm{LO},\gamma}|^{2}}. \tag{5.16}$$

However, one should pay attention to the change in the prefactors, and the extra

EW contributions for $h \to \gamma\gamma$

$$F_{\mathrm{LO},\gamma} = N_C\, Q_t^2 F_{\mathrm{LO}}^t + N_C\, Q_b^2 F_{\mathrm{LO}}^b + F_{\mathrm{LO}}^W + F_{LO}^G, \tag{5.17}$$

and $F_{\mathrm{NLO},\gamma}$ is obtained from F_{NLO} by replacing the LO form factor that appears inside of it by $F_{\mathrm{LO}}^i \to N_c\, Q_i^2 F_{\mathrm{LO}}^i$, with the charges $Q_t = 2/3$ and $Q_b = -1/3$. The W boson contribution

$$F_{\mathrm{LO}}^W = 2\left(1 + 6\frac{m_W^2}{m_h^2}\right) - 6\frac{m_W^2}{m_h^2}\left(1 - 2\frac{m_W^2}{m_h^2}\right)\log^2(x_W), \tag{5.18}$$

with m_W the W mass, and the Goldstone contribution

$$F_{\mathrm{LO}}^G = 4\frac{m_W^2}{m_h^2}\left(1 + \frac{m_W^2}{m_h^2}\,\log^2(x_W)\right). \tag{5.19}$$

Four-fermion operators also affect the $h \to Z\gamma$ partial width. However, as in the diphoton case, the effect is expected to be small due to the dominance of the W boson loop. Because of this, and given the smallness of the $h \to Z\gamma$ branching ratio and the relatively low precision expected in this channel at the LHC, the effects of four-fermion interactions in this decay are neglected.

Correction to Higgs decays to $b\bar{b}$

The dominant four-fermion contributions to decay channel $h \to b\bar{b}$ come from the operators with Wilson coefficients $C_{QtQb}^{(1),(8)}$. The corresponding diagram at NLO is shown in fig 5.2. Adopting the same renormalisation procedure as outlined in the previous subsection, we obtain the following expression for the correction to the $h \to b\bar{b}$ decay rate in the presence of $\mathcal{O}_{QtQb}^{(1),(8)}$,

$$\begin{aligned}\frac{\Gamma_{h\to b\bar{b}}}{\Gamma_{h\to b\bar{b}}^{\mathrm{SM}}} =& 1 + \frac{1}{16\pi^2}\frac{m_t}{m_b}(m_h^2 - 4m_t^2)\frac{(2N_c+1)C_{QtQb}^{(1)} + c_F C_{QtQb}^{(8)}}{\Lambda^2} \\ &\times\left[2 + \sqrt{1 - \frac{4m_t^2}{m_h^2}}\log(x_t) - \log\left(\frac{m_t^2}{\mu_R^2}\right)\right],\end{aligned} \tag{5.20}$$

which carries an enhancement factor of m_t/m_b and is hence expected to be rather large.

The results of the NLO effects from the four-fermion operators reported above, do not take into an account the running of the Wilson coefficients. This would be based on the assumption that these coefficients are defined at the process scale. Nevertheless, when we want to compare different process or assume that the four-fermion operators are defined at the UV scale, i.e. Λ, for example after matching with some UV model. One has take into an account the running of these Wilson coefficients from Λ down to the process scale Those running effects can be included via the renormalisation group

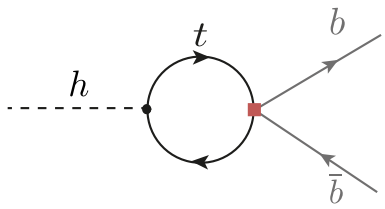

Figure 5.2. Feynman diagram contributing to the NLO $h \to b\bar{b}$ process.

equation (RGE) for the operators with Wilson coefficient $C_{t\phi}$ and $C_{b\phi}$ [244, 245], that lead approximatively to

$$C_{t\phi}(\mu_R) - C_{t\phi}(\Lambda) = \frac{1}{16\pi^2 v^2}\left[-2y_t(m_h^2 - 4m_t^2)(C_{Qt}^{(1)} + c_F C_{Qt}^{(8)})\log\left(\frac{\mu_R^2}{\Lambda^2}\right)\right. \\ \left. + \frac{y_b}{2}(m_h^2 - 4m_b^2)\left((2N_c+1)C_{QtQb}^{(1)} + c_F C_{QtQb}^{(8)}\right)\log\left(\frac{\mu_R^2}{\Lambda^2}\right)\right] \tag{5.21}$$

and

$$C_{b\phi}(\mu_R) - C_{b\phi}(\Lambda) = \frac{y_t}{32\pi^2 v^2}\left[(m_h^2 - 4m_t^2)\left((2N_c+1)C_{QtQb}^{(1)} + c_F C_{QtQb}^{(8)}\right)\log\left(\frac{\mu_R^2}{\Lambda^2}\right)\right], \tag{5.22}$$

where $y_{t/b} = \sqrt{2}m_{t/b}/v$. Note that the combinations of Wilson coefficients appearing in (5.21)(5.22) are the same as in F_{NLO} in (5.13). Effectively, we can then obtain the result under the assumption that the four-fermion operators are the only non-zero ones at the high scale by replacing in (5.13) $\mu_R \to \Lambda$, noting that we have renormalised the top and beauty quark masses in the OS scheme. Including the leading logarithmic running of $C_{b\phi}$ of (5.22) from the high scale Λ to the electroweak scale is achieved by setting in (5.20) $\mu_R \to \Lambda$. The expression in (5.20) agrees with results obtained from the full calculation of the NLO effects in the dimension-six SMEFT, first computed in [246].

5.1.2 SMEFT-NLO calculation of $t\bar{t}h$

Unlike the previous processes, the associated production of the Higgs with top quark pair involves new topologies not limited to Yukawa vertex or mass renormalisation. At the LHC, there are two sub-processes responsible for the $t\bar{t}h$ production: gluon-initiated process illustrated in Figure 5.3 and quark-initiated one, see in Figure 5.4. We see the new *finite* topologies induced by the four-fermion operator corrections in (d) triangle and (e) box topologies in Figure 5.3 and (b) triangle topology in Figure 5.4. Additionally, the $t\bar{t}g$ vertex correction in the quark-initiated process (diagram (c)) of Figure 5.4 is non-vanishing as the gluon is off-shell. This vertex correction has a UV pole that requires a

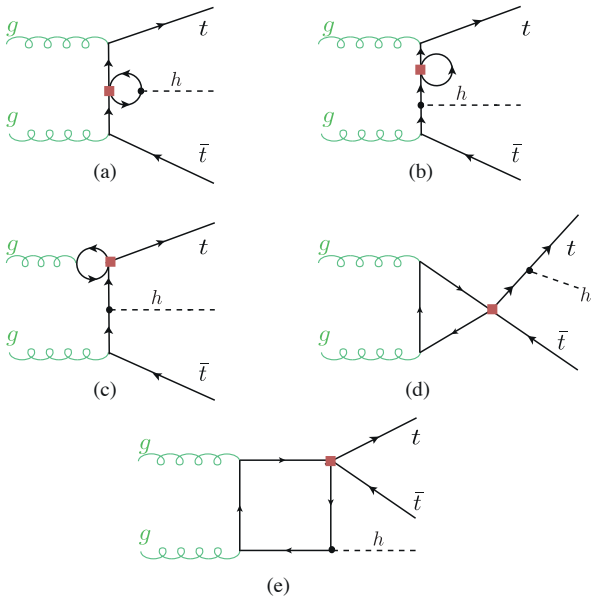

Figure 5.3. Feynman diagrams including the four-fermion loop contributions to the $gg \to t\bar{t}h$ subprocess.

counter-term for its cancellation

$$= \frac{ig_s}{12\pi^2\Lambda^2} T^A_{ij} p_g^2 \gamma^\mu \left(C_{tt} P_R + \left(C^{(1)}_{QQ} + C^{(3)}_{QQ} \right) P_L + \frac{C^{(8)}_{Qt}}{4} \right) \left(\frac{1}{\bar{\epsilon}} - 1 \right). \quad (5.23)$$

Another difference between $t\bar{t}h$ and the rest of the processes considered, is that this process has multiple colour projectors, as the quark anti quark triplets or the gluon pairs do not have to recombine to only a singlet state rather to both a singlet and an octet, according to the expansion of product $\mathbf{3} \otimes \overline{\mathbf{3}} \to \mathbf{1} + \mathbf{8}$. This breaks the degeneracy between the singlet and octet Wilson coefficients. Lastly, due to the new topologies and $t\bar{t}g$ vertex correction, operators with single chirality will contribute to NLO corrections, namely Ctt and $C^{(1,3)}_{QQ}$.

All of the four-fermion operators are implemented in the loop-capable UFO model `SMEFTatNLO` [227] and their contribution to NLO corrections of $t\bar{t}h$ can hence be computed via `Madgraph_aMCNLO` [225] (version 3.1.0) with some tweaking to remove the NLO QCD corrections. This is done via a use-defined loop filter function in Madgraph. The results were reproduced by an analytic computation based on the reduction of one-loop amplitudes via the method developed by G. Ossola, C.G. Papadopoulos and R. Pittau (OPP reduction) [247]. The OPP reduction was done using the `CutTools` programme [248]. This programme take the full one-loop amplitude and then reduces it to terms with 1,2,3 and 4-point loop functions in four dimensions, keeping spurious terms from the ϵ part of the amplitude. To correct for such terms, one needs to compute the

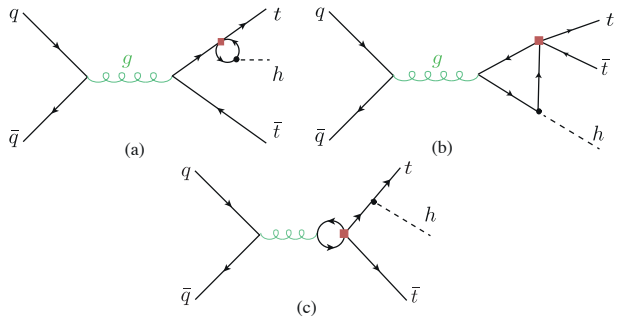

Figure 5.4. Feynman diagrams including the four-fermion loop contributions to the $q\bar{q} \to t\bar{t}h$ subprocess.

divergent UV counter-term as well as a finite rational terms, denoted R_2 as in Ref. [249].[1] The amplitudes were generated in the same way as for gluon fusion. The UV and R_2 counter-terms, that need to be supplemented to `CutTools`, were computed manually following the method detailed in [249]. For both codes, the NNPDF23 parton distribution functions set at NLO [250] was used.

The singlet and octet operators $\mathcal{O}^{(1),(8)}_{QtQb}$ contribute to $t\bar{t}h$ only via beauty loops and in principle, could be directly dismissed like the other beauty quark operators mentioned above. However, it is instructive to investigate their effect albeit it is expected to be small. Since the `SMEFTatNLO` model does not have these operators, it was needed to implement them manually in that model. This is simply done by include the vertices generated by these operators as well as their UV and R_2 counter-terms, only relevant for $t\bar{t}th$ calculation. The calculation of the NLO correction by these operators was done both in Madgraph using a modified UFO model and with the code based on `CutTools`. The effects where comparable to the leading log effects computed using `SMEFTsim` package [251] of $\sim 10^{-6}$. Hence confirming the expectation that beauty quark loops have a negligible effect.

In order to take the effect of Wilson coefficients' running, the relevant contribution for the gluon-initiated process as the same as the stated for the gluon fusion in (5.21). While for the quark-initiated process, one needs to consider the operator mixing in the running, particularly between operators that contain second and third generation quarks mixed together. These corrections can be obtained from the RGEs in refs. [131, 244, 245].

5.1.3 Results

The NLO correction from the four-fermion operators of the third generation quarks on the Higgs rates i.e., partial width Γ or cross-section σ., is extracted from the above

[1] Another rational term R_1 appears due to the mismatch between the four and d dimensional amplitudes, but this is computed automatically in `CutTools`.

computation using the formula

$$\delta R(C_i) = R/R^{\rm SM} - 1, \tag{5.24}$$

here effect from the operator with Wilson coefficient C_i on the Higgs rate R is denoted by $\delta R(C_i)$. Only contributions linear in the Wilson coefficients are considered. In order to isolate the finite terms from the ones coming from the RGE leading log approximation, the correction is further expanded to finite $\delta R^{fin}_{C_i}$ and leading log terms $\delta R^{log}_{C_i}$ as follows

$$\delta R(C_i) = \frac{C_i}{\Lambda^2}\left(\delta R^{fin}_{C_i} + \delta R^{log}_{C_i}\log\left(\frac{\mu_R^2}{\Lambda^2}\right)\right). \tag{5.25}$$

Using this formula, one can obtain the correction at any NP scale Λ, though in the remainder of this chapter this scale is set to 1 TeV. In Table 5.2, the finite and logarithmic corrections for the operators considered in this study is reported. Using this table in filling the formula (5.25) will give the correction to Higgs rates. However, since some of the rates are Higgs partial widths, the Higgs total width Γ_h will be affected and therefore all of Higgs rates are changed. An important observation from Table 5.2 is that the finite terms, are either larger or at the same order than the leading log ones, except for $h \to b\bar{b}$ corrections from $C^{(1),(8)}_{QtQb}$. This highlights the importance of thee full NLO calculation for these corrections in constraining these four-fermion operators, in particular $\mathcal{O}^{(1),(8)}_{Qt}$.

As mentioned earlier, there is a degeneracy amongst the singlet and octet operators, seen clearly in the analytic result for gluon fusion and Higgs decays considered. This degeneracy is though broken for $\mathcal{O}^{(1),(8)}_{Qt}$ due to $t\bar{t}h$. Since, the effect of $\mathcal{O}^{(1),(8)}_{QtQb}$ is negligible for this process, thee true degree of freedom for these operators' Wilson coefficients is the linear combination

$$C^{+}_{QtQb} = (2N_c + 1)C^{(1)}_{QtQb} + c_F C^{(8)}_{QtQb}. \tag{5.26}$$

5.2 Fit to Higgs observables

Using the results from the previous NLO calculations, and combining them with the calculations of NLO Higgs rates from the trilinear Higgs self-coupling λ_3,preformed in refs. [115–118, 120] we could expand on the previous fits for λ_3 from Higgs data, to include four-fermion SMEFT Wilson coefficients as well. In order to examine the true sensitivity of single Higgs observables to λ_3. Although combined fits from Higgs data including λ_3 and SMEFT operators modifying Higgs rates at LO has been preformed [147]. Such fits would not be sufficient in determine the actual sensitivity for λ_3, in particular when the SMEFT operators are weakly constraint and possess significant modifications to Higgs rates as we have seen in Table 5.2. This chapter does not include a global SMEFT fit, but merely motivates it by illustrating how thee sensitivity for probing the Higgs-self coupling from single Higgs data gets diluted when the four-fermion operators are included, and how these two are correlated.

Operator	Process	μ_R	$\delta R_{C_i}^{fin}$ [TeV^2]	$\delta R_{C_i}^{log}$ [TeV^2]
$\mathcal{O}_{Qt}^{(1)}$	ggF	$\frac{m_h}{2}$	$9.91 \cdot 10^{-3}$	$2.76 \cdot 10^{-3}$
	$h \to gg$	m_h	$6.08 \cdot 10^{-3}$	$2.76 \cdot 10^{-3}$
	$h \to \gamma\gamma$		$-1.76 \cdot 10^{-3}$	$-0.80 \cdot 10^{-3}$
	$t\bar{t}h$ 13 TeV	$m_t + \frac{m_h}{2}$	$-4.20 \cdot 10^{-1}$	$-2.78 \cdot 10^{-3}$
	$t\bar{t}h$ 14 TeV		$-4.30 \cdot 10^{-1}$	$-2.78 \cdot 10^{-3}$
$\mathcal{O}_{Qt}^{(8)}$	ggF	$\frac{m_h}{2}$	$1.32 \cdot 10^{-2}$	$3.68 \cdot 10^{-3}$
	$h \to gg$	m_h	$8.11 \cdot 10^{-3}$	$3.68 \cdot 10^{-3}$
	$h \to \gamma\gamma$		$-2.09 \cdot 10^{-3}$	$-1.07 \cdot 10^{-3}$
	$t\bar{t}h$ 13 TeV	$m_t + \frac{m_h}{2}$	$6.81 \cdot 10^{-2}$	$-2.40 \cdot 10^{-3}$
	$t\bar{t}h$ 14 TeV		$7.29 \cdot 10^{-2}$	$-2.48 \cdot 10^{-3}$
$\mathcal{O}_{QtQb}^{(1)}$	ggF	$\frac{m_h}{2}$	$2.84 \cdot 10^{-2}$	$9.21 \cdot 10^{-3}$
	$h \to gg$		$1.57 \cdot 10^{-2}$	$9.21 \cdot 10^{-3}$
	$h \to \gamma\gamma$	m_h	$-1.30 \cdot 10^{-3}$	$-0.78 \cdot 10^{-3}$
	$h \to b\bar{b}$		$9.25 \cdot 10^{-2}$	$1.68 \cdot 10^{-1}$
$\mathcal{O}_{QtQb}^{(8)}$	ggF	$\frac{m_h}{2}$	$5.41 \cdot 10^{-3}$	$1.76 \cdot 10^{-3}$
	$h \to gg$		$2.98 \cdot 10^{-3}$	$1.76 \cdot 10^{-3}$
	$h \to \gamma\gamma$	m_h	$-0.25 \cdot 10^{-3}$	$-0.15 \cdot 10^{-3}$
	$h \to b\bar{b}$		$1.76 \cdot 10^{-2}$	$3.20 \cdot 10^{-2}$
$\mathcal{O}_{QQ}^{(1)}$	$t\bar{t}h$ 13 TeV	$m_t + \frac{m_h}{2}$	$1.75 \cdot 10^{-3}$	$1.84 \cdot 10^{-3}$
	$t\bar{t}h$ 14 TeV		$1.65 \cdot 10^{-3}$	$1.76 \cdot 10^{-3}$
$\mathcal{O}_{QQ}^{(3)}$	$t\bar{t}h$ 13 TeV	$m_t + \frac{m_h}{2}$	$1.32 \cdot 10^{-2}$	$5.48 \cdot 10^{-3}$
	$t\bar{t}h$ 14 TeV		$1.24 \cdot 10^{-2}$	$5.30 \cdot 10^{-3}$
$\mathcal{O}_{tt}$	$t\bar{t}h$ 13 TeV	$m_t + \frac{m_h}{2}$	$4.60 \cdot 10^{-3}$	$1.82 \cdot 10^{-3}$
	$t\bar{t}h$ 14 TeV		$4.57 \cdot 10^{-3}$	$1.74 \cdot 10^{-3}$

Table 5.2. The NLO effects of the four.heavy-quarks operators on the Higgs rates. The effects are separated into finite $\delta R_{C_i}^{fin}$ and leading log parts, in correspondence with (**??**). Effects of $\mathcal{O}(10^{-5} - 10^{-6})$ TeV^{-2} have been omitted from this table. This table has been published in [236]

In the previous references, the modification to Higgs self coupling was reported in terms of the κ-formalism, for the consistency of this analysis, the NLO corrections from the trilinear self-coupling will be converted from this formalism to the SMEFT notation, in terms of the Wilson coefficient C_ϕ. For more details on the conversion between SMEFT and κ-formalism see subsection 3.2.2. In order to keep track of power counting (in terms of Λ) in SMEFT, we expand the results of [116] after converting it to SMEFT , to get

$$\delta R_{\lambda_3} \equiv \frac{R_{\rm NLO}(\lambda_3) - R_{\rm NLO}(\lambda_3^{\rm SM})}{R_{\rm LO}} = -2\frac{C_\phi v^4}{\Lambda^2 m_h^2} C_1 + \left(-4\frac{C_\phi v^4}{\Lambda^2 m_h^2} + 4\frac{C_\phi^2 v^8}{m_h^4 \Lambda^4}\right) C_2. \tag{5.27}$$

In (5.27), the coefficient C_1 corresponds to the contribution of the trilinear coupling to the single Higgs processes at one loop, adopting the same notation as [116]. The values of C_1 for the different processes of interest for this paper are given in **??**. The coefficient

C_2 describes universal corrections and is given by

$$C_2 = \frac{\delta Z_h}{1 - \left(1 - \frac{2C_\phi v^4}{\Lambda^2 m_h^2}\right)^2 \delta Z_h}\,, \tag{5.28}$$

where the constant δZ_h is the SM contribution from the Higgs loops to the wave function renormalisation of the Higgs boson,

$$\delta Z_h = -\frac{9}{16}\frac{G_F m_h^2}{\sqrt{2}\pi^2}\left(\frac{2\pi}{3\sqrt{3}} - 1\right). \tag{5.29}$$

The coefficient C_2 thus introduces additional $\mathcal{O}(1/\Lambda^4)$ (and higher order) terms in δR_{λ_3}. In ref. [116] considering the κ formalism the full expression of (5.28) is kept, while we define two different descriptions: one in which we expand δR_{λ_3} up to linear order and an alternative scheme in which we keep also terms up to $\mathcal{O}(1/\Lambda^4)$ in the EFT expansion. Keeping the full expression in (5.28) and including terms up to $\mathcal{O}(1/\Lambda^4)$ in C_2 lead to nearly the same results as the simple $\mathcal{O}(1/\Lambda^4)$ fit.

Process	C_1	$\delta R^{fin}_{C_\phi}$
ggF/ $gg \to h$	$6.60 \cdot 10^{-3}$	$-3.10 \cdot 10^{-3}$
$t\bar{t}h$ 13 TeV	$3.51 \cdot 10^{-2}$	$-1.64 \cdot 10^{-2}$
$t\bar{t}h$ 14 TeV	$3.47 \cdot 10^{-2}$	$-1.62 \cdot 10^{-2}$
$h \to \gamma\gamma$	$4.90 \cdot 10^{-3}$	$-2.30 \cdot 10^{-3}$
$h \to b\bar{b}$	0.00	0.00
$h \to W^+W^-$	$7.30 \cdot 10^{-3}$	$-3.40 \cdot 10^{-3}$
$h \to ZZ$	$8.30 \cdot 10^{-3}$	$-3.90 \cdot 10^{-3}$
$pp \to Zh$ 13 TeV	$1.19 \cdot 10^{-2}$	$-5.60 \cdot 10^{-3}$
$pp \to Zh$ 14 TeV	$1.18 \cdot 10^{-2}$	$-5.50 \cdot 10^{-3}$
$pp \to W^{\pm}h$	$1.03 \cdot 10^{-2}$	$-4.80 \cdot 10^{-3}$
VBF	$6.50 \cdot 10^{-3}$	$-3.00 \cdot 10^{-3}$
$h \to 4\ell$	$8.20 \cdot 10^{-3}$	$-3.80 \cdot 10^{-3}$

Table 5.3. The NLO dependence of single Higgs rate on C_ϕ, these results were computed in [120]. The C_1 coefficients are to be used in eq. (5.27), while for a direct comparison with the effect of the four-fermion operators, we quote the translated effect $\delta R^{fin}_{C_\phi}$, which can be used directly in eq. (5.25). If the value of $\sqrt{s}$ is not indicated the effect is the same for both 13 and 14 TeV. This table has been published in [236]

A Bayesian fit was preformed using Markov-chain Monte Carlo (MCMC) method. Using a flat prior s $\pi(C_i) = const.$ and a log likelihood of a Gaussian distribution

$$\log(L) = -\frac{1}{2}\left[(\vec{\mu}_{\text{Exp}} - \vec{\mu})^T \cdot \mathbf{V}^{-1} \cdot (\vec{\mu}_{\text{Exp}} - \vec{\mu})\right]. \tag{5.30}$$

Constructed as follows:

Experimental input $\vec{\mu}_{\text{Exp}}$ The signal strength from experimental measurements of single Higgs rates defined as

$$\mu_{\text{Exp}} \equiv \sigma_{\text{Obs}}/\sigma_{\text{SM}}. \tag{5.31}$$

These measurements as taken from LHC Run II for centre-of-mass energy of $\sqrt{s} = 13$ TeV and integrated luminosity of $139\,\text{fb}^{-1}$ for ATLAS and $137\,\text{fb}^{-1}$ for CMS. In addition to HL-LHC projections by CMS for $\sqrt{s} = 14$ TeV and integrated luminosity of $3000\,\text{fb}^{-1}$. Both of these input types have been already discussed in chapter 2 and summarised in Table 2.1.

Theoretical prediction $\vec{\mu}$ The corresponding theoretical predictions for each of the experimental measurement /projection have been built using the modification to the cross-sections and branching ratios coming from the SMEFT four-fermion operators and C_ϕ. To keep with the power-counting, the signal strength is also expanded in powers of Λ, keeping only Λ^{-2} terms.

$$\mu(C_\phi, C_i) = \frac{\sigma_{\text{Prod}}(C_\phi, C_i) \times \text{BR}(C_\phi, C_i)}{\sigma_{\text{Prod,SM}} \times \text{BR}_{\text{SM}}} \approx 1 + \delta\sigma(C_\phi, C_i) + \delta\Gamma(C_\phi, C_i) - \delta\Gamma_h(C_\phi, C_i). \tag{5.32}$$

Uncertainties and correlations V The correlation matrix $\mathbf{V}$ is build from thee experimental uncertainties found in Table 2.1. For Run-II data, only ATLAS collaboration reported the correlation amongst different channels, and only correlations $> 10\%$ are considered. While for the HL-LHC, the whole correlation matrix found on the webpage [252]. The HL-LHC projections for the S2 scenario explained in [192] were used. These assume the improvement on the systematics that is expected to be attained by the end of the HL-LHC physics programme, and that theory uncertainties are improved by a factor of two with respect to current values. Theoretical uncertainties were not considered in this fit

The python package `pymc3` [253] was used to construct the posterior distribution. We use the `Arviz` Bayesian analysis package [254] to extract the credible intervals (CIs) from the highest density posterior intervals (HDPI) of the posterior distributions, where the intervals covering 95% (68%) of the posterior distribution are considered the 95% (68%) CIs. In the Gaussian limit, these 95% (68%) CIs should be interpreted as equivalent to the 95% (68%) Frequentist Confidence Level (CL) two-sided bounds. `HEPfit` [255] code was used to validate the fits. Given that current bounds on these operators are rather weak, one may wonder about the uncertainty in our fits associated to the truncation of the EFT. Note that, since the four-quark operators only enter into the virtual corrections at NLO, Higgs production and decay contain only linear terms in $1/\Lambda^2$ in the corresponding Wilson coefficients, i.e. the quadratic terms coming from squaring the amplitudes are technically of next-to-NLO. Hence, the quadratic effects in the signal strengths come from not linearising the corrections to the product $\sigma_{\text{Prod}} \times \text{BR}$. These

effects have been investigated, and found to have a negligible effect on the fit. The operators of single chirality $\mathcal{O}_{tt}$ and $\mathcal{O}_{QQ}^{(1)/(3)}$ were not included in the fit, as their effect on Higgs rates is limited to small δR for $t\bar{t}h$. Thus, they cannot be contained simultaneously with C_ϕ using single Higgs data.

5.2.1 Fit results

In Figure 5.5 and Figure 5.6 the 68% and 95% highest posterior density contours of the two-parameter posterior distributions and their marginalisation for the two-parameter fits involving C_ϕ and one of the four-heavy quark Wilson coefficients, evaluated at the scale $\Lambda = 1$ TeV for Run-II LHC measurements . Both linearised and quadratically truncated δR_{λ_3} fits are shown, and we observe that the 95% CI bounds (shown on top of the panels) and correlations depends on the truncation.

We observe that the four-fermion operators are strongly correlated with Higgs self-coupling modifier $\mathcal{O}_\phi$, in the linear fit. With Pearson's correlation of $\gtrsim 0.7$ with p-value $< 10^{-4}$. In the case of quadratic δR_{λ_3} fit, we observe diminished Pearson correlation, but in this scenario Pearson's correlation test is not particularly applicable, as we have non-linear relation between the variables.

The two-parameter fit results for thee four-fermion Wilson coefficients are mesmerised in the forest plots in Figure 5.7 marginalising the posteriors distributions over C_ϕ. The finite effects were isolated by preforming fits with δR^{fin} only. The finite effects are small for $O_{QtQb}^{(1)/(8)}$ but dominant for the four-top operators $O_{Qt}^{(1)/(8)}$mainly coming from $t\bar{t}h$. The effect of EFT truncations of δR_{λ_3} can also be observed as shifts in the mean value for the Wilson coefficients, but the 95% CI's themselves are not significantly affected. In these plots, the fits results from this study are also confronted with the limits obtained from fits to top data [141, 144, 233, 234, 256, 257] and EWPO fits from [143]. Showing that when the Wilson coefficient running is taken into an account, the 95% CI bounds obtained from Higgs data are consistently stronger than the ones from top data.

In Figure 5.8 the fit results for C_ϕ after marginalising over the four-fermion Wilson coefficients in both EFT truncations schemes of δR_{λ_3}. In addition to a single parameter fit for C_ϕ. Additionally the current 95 % CL bound on C_ϕ extracted from Higgs pair production search using th final state $b\bar{b}\gamma\gamma$ preformed by ATLAS using Run-II data [258], translated from κ formalism.
The mean values and the 95%CI's change depending on the four-fermion Wilson coefficient that was paired with C_ϕ in the two.-parameter fit. As expected, the single parameter fits for C_ϕ yield stronger bound on C_ϕ than the two-parameter fits, thus the inclusion of the four-fermion operators in single Higgs data dilutes C_ϕ bounds . Additionally, the truncation order of δR_{λ_3} appears to have a significant effect on the length of the CI's, with quadratic fits giving more stringent constraint on C_ϕ. Instead, for Higgs pair production is makes only a negligible effect if linear or up to quadratic terms in the EFT expansion are kept for the $C_\phi > 0$ bound, while the bound weakens at linear order in $1/\Lambda^2$ for $C_\phi < 0$ [259]. For instance, the quadratic single parameter fit for C_ϕ is comparable to the direct bound from Higgs pair production. However, this changes

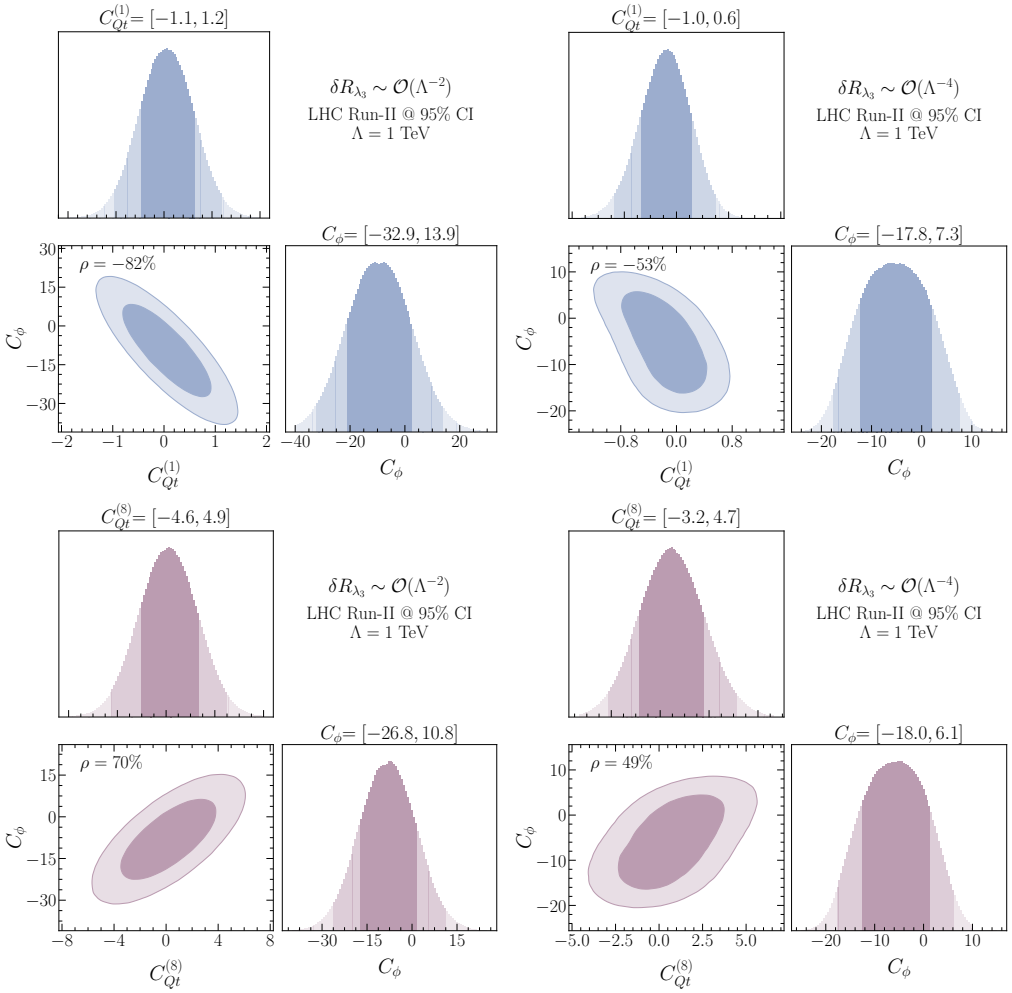

Figure 5.5. The posterior distributions of the Run-II data fits for C_ϕ with $C_{Qt}^{(1)}$ (up) and C_ϕ with $C_{Qt}^{(8)}$ (down). With 68% and 95% highest density posterior contours indicated. The limits shown on top of the plots indicate the 95% CI's. Plots on the left are made for the fully linearised n δR_{λ_3}, while the ones on the right include the quadratic effects. This figure has been published in [236].

dramatically, when one includes the four-fermion operators in a combined fit, and the single Higgs data constraints on C_ϕ become less significant compared to the direct hh bounds.
It should be noted that the strongest bound on the Higgs self-coupling currently comes from the perturbative unitarity bound of ref. [55], as discussed in chapter.

One of the important aspects of multivariate studies is the correlation among variables. Apart from the two-parameter fits discussed above, here we also consider a four-parameter fit to C_ϕ plus the three directions in the four heavy-quark operator parameter

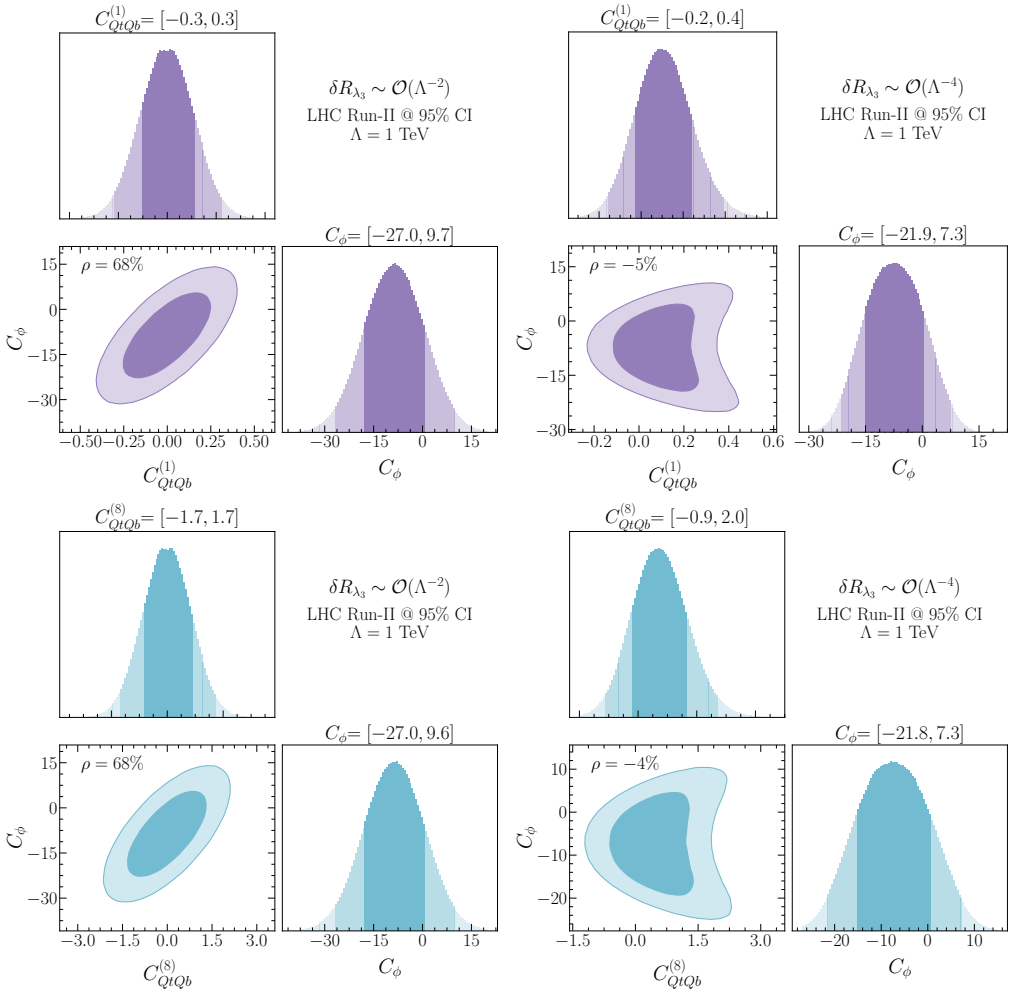

Figure 5.6. The posterior distributions of the Run-II data fits for C_ϕ with $C^{(1)}_{QtQb}$ (up) and C_ϕ with $C^{(8)}_{QtQb}$ (down). With the same annotations as in Figure 5.5. This figure has been published in [236].

space that the Higgs rates are mostly sensitive too, i.e. neglecting $C^{(1),(3)}_{QQ}$ and C_{tt}, and trading $C^{(1)}_{QtQb}$ and $C^{(8)}_{QtQb}$ by C^{+}_{QtQb}. When considering two- or four-parameter fits of C_ϕ and the four-heavy-quark Wilson coefficients, we observe a non-trivial correlation patterns amongst these coefficients. Figure 5.9 illustrates these correlation patterns clearly for the four-parameter fit. We observe that the Wilson coefficients $C^{(1),(8)}_{Qt}$ are strongly correlated because, in analogy to $C^{(1),(8)}_{QtQb}$, they only appear in certain linear combination whenever correcting the Yukawa coupling. However, unlike $C^{(1),(8)}_{QtQb}$ they are not completely degenerate because the main part of the NLO correction to $t\bar{t}h$ does not

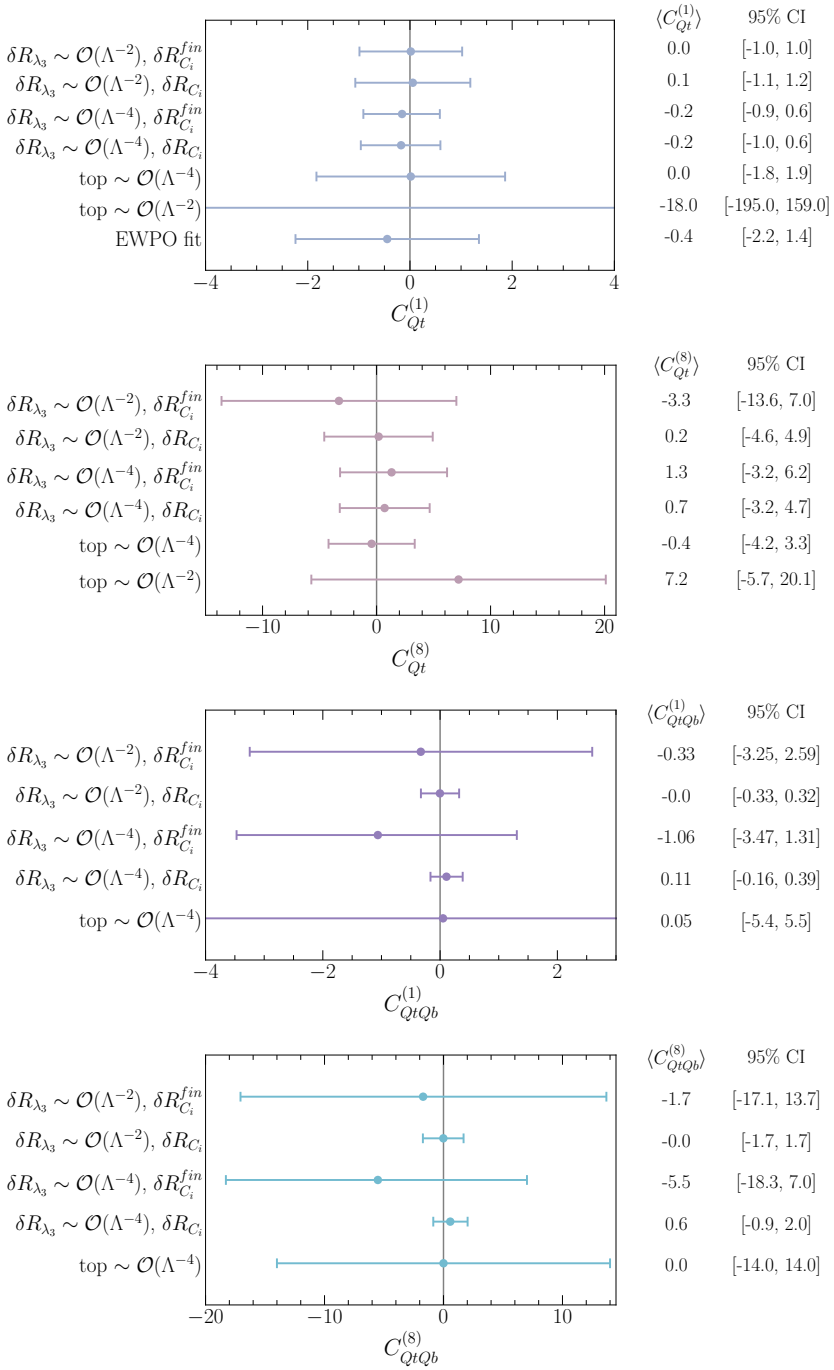

Figure 5.7. Forest plots illustrating the means and 95% CI's constraints on the four-heavy-quark Wilson coefficients C_i from Run-II data. These bounds are obtained from two-parameter fits including the aforementioned coefficients along with C_ϕ, then marginalising over the latter. The different fits with only the finite part of the NLO correction included VS the full results, as well as the EFT truncation scheme for the trilinear coupling, linear vs quadratic. Fits from top data [141] for $C^{(1),(8)}_{Qt}$ and [234] for $C^{(1),(8)}_{QtQb}$ as well as EWPO fits from [143] were included for comparison.This figure has been published in [236].

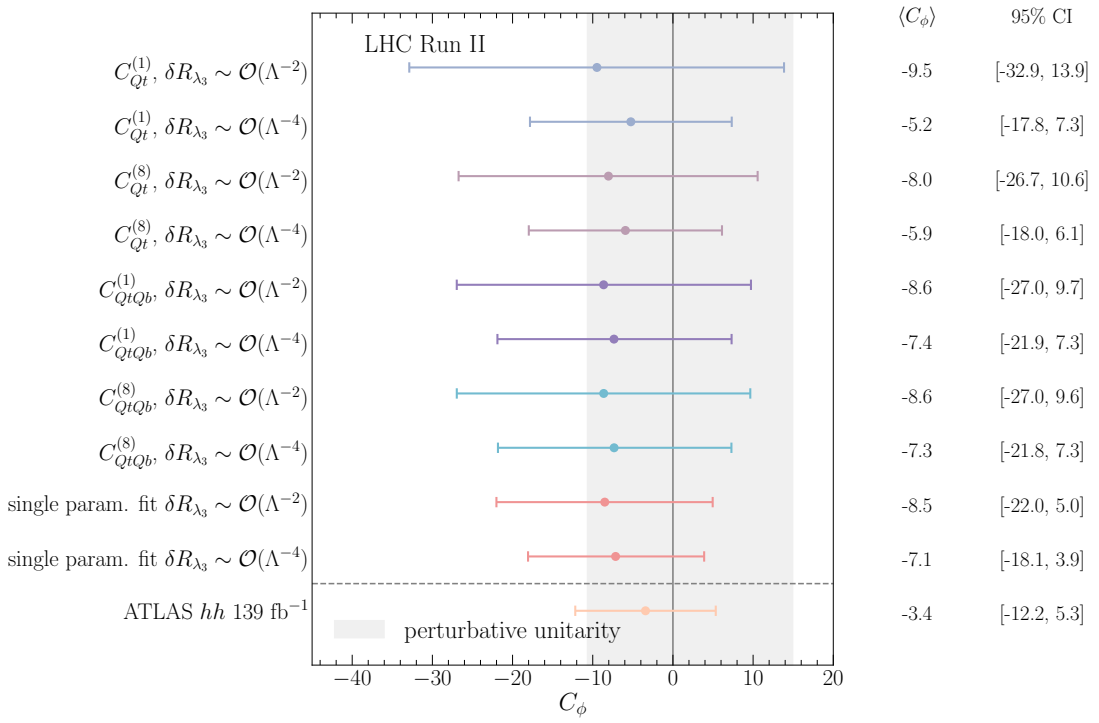

Figure 5.8. A forest plot illustrating the means and 95% CI's bounds for C_ϕ from the two-parameter fit with the four-fermion operators marginalised. The fits results for C_ϕ from full run-II Higgs data keeping terms up to $\mathcal{O}(1/\Lambda^2)$ or $\mathcal{O}(1/\Lambda^4)$ in δR_{λ_3} are shown. For comparison, also the 95% CI and means for the single parameter fit for C_ϕ with the same single Higgs data is shown as well as the bounds on C_ϕ from the 139 fb^{-1} search for Higgs pair production [258]. The horizontal grey band illustrates the perturbative unitarity bound [55]. This figure has been published in [236].

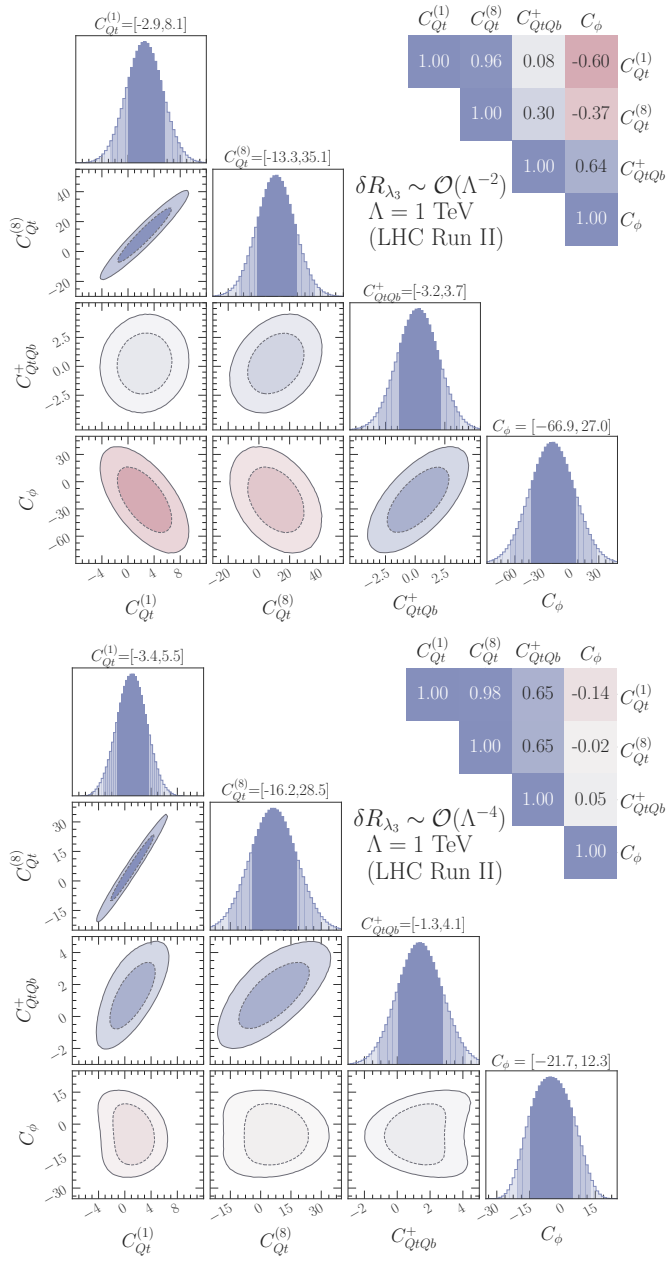

Figure 5.9. The marginalised 68% and 95% Highest density posterior contours for the four-parameter fits including the different four-quark Wilson coefficients and C_ϕ. The numbers above the plots show the 95% CI bounds while the correlations are given on the top-right side. The correlation between each pair of the Wilson coefficients is highlighted as a heatmap. The upper panel shows the fit including up to $\mathcal{O}(1/\Lambda^2)$ in δR_{λ_3} while the lower one shows the fit with including also $\mathcal{O}(1/\Lambda^4)$. This figure has been published in [236].

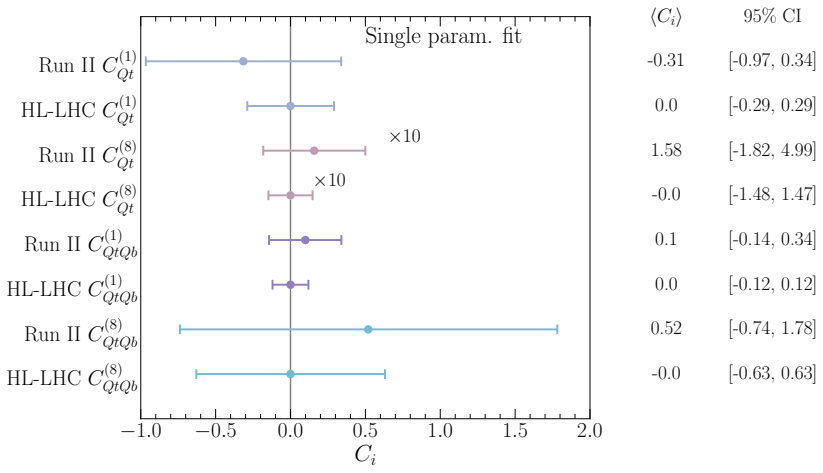

Figure 5.10. Results of a single parameter fit showing the improvement in constraining power of the HL-LHC over the current bounds from Run-2 data. This figure has been published in [236].

contain the aforementioned linear combination. The four-parameter fit also reveals that the Wilson coefficients $C_{Qt}^{(1),(8)}$ have a large correlation with C_{QtQb}^{+} because all of the four Wilson coefficients appear in a linear combination in the NLO corrections except for $h \to b\bar{b}$ and $t\bar{t}h$. However, this correlation is not as strong due to the large NLO correction of the Higgs decay $h \to b\bar{b}$ from $C_{QtQb}^{(1),(8)}$. Moreover, the correlation between the four-heavy-quark Wilson coefficients and C_ϕ depends on the δR_{λ_3} truncation.

5.2.2 Prospects for HL-LHC

Using the CMS Higgs signal strength measurement projections for the HL-LHC in refs. [93, 252] for a centre-of-mass energy of $\sqrt{s} = 14$ TeV and integrated luminosity of $3\,\text{ab}^{-1}$, it is possible to repeat the fits done for Run-II. The projections for the S2 scenario explained in [192] were used. These assume the improvement on the systematics that is expected to be attained by the end of the HL-LHC physics programme, and that theory uncertainties are improved by a factor of two with respect to current values. These projections are assumed to have their central values in the SM prediction with the total uncertainties summarised in table 2.1 in Appendix **??**.

In Figure 5.10 I show the comparison between the fit results of Run-II data and the projections for the HL-LHC for single parameter fits. For the operators $\mathcal{O}_{Qt}^{(1),(8)}$ the constraining power of the HL-LHC is roughly a factor two better as the current bounds we could set from single Higgs data, while for the operators $\mathcal{O}_{QtQb}^{(1),(8)}$ the improvement is a little less. While in Figure 5.11 the limits on C_ϕ in a single parameter fit for Run-2 and the projections for the HL-LHC are shown. including in δR_{λ_3} up to order $\mathcal{O}(1/\Lambda^2)$ or $\mathcal{O}(1/\Lambda^4)$. While for Run-II data the inclusion of $\mathcal{O}(1/\Lambda^4)$ made a significant difference, this is less pronounced for the HL-LHC projections. These results are very similar to

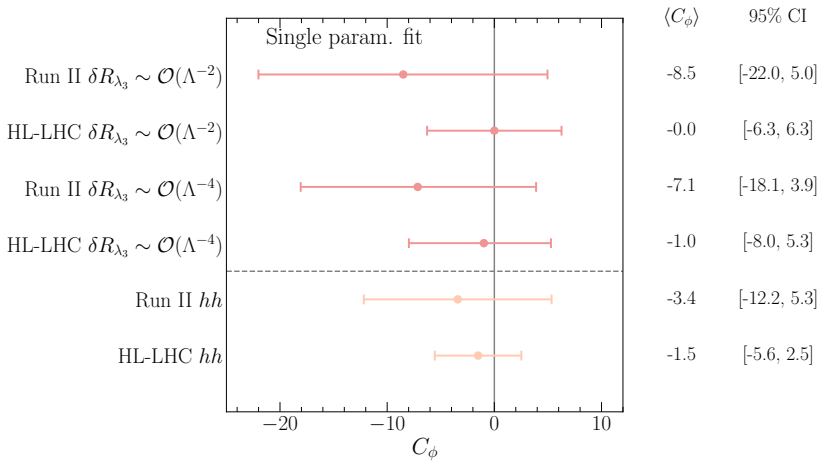

Figure 5.11. A forest plot illustrating the means and 95% CI's of the posteriors built from the C_ϕ in a single-parameter fit, showing also the differences in including terms of $\mathcal{O}(1/\Lambda^2)$ or up to $\mathcal{O}(1/\Lambda^4)$ in the definition of δR_{λ_3}. For comparison, also the limits and projections from searches for Higgs pair production are shown. This figure has been published in [236].

the projections presented in a κ_λ fit in [260]. The results were also confronted with data from searches for Higgs pair production 139 fb^{-1} [258] and HL-LHC projections [261] on Higgs pair production, showing that Higgs pair production will still allow to set stronger limits on C_ϕ.

5.3 Conclusion

In this chapter, the calculations of the NLO corrections depending on four-heavy-quark operators to single Higgs rates have been calculated. We have seen that operators both homogenous and heterogeneous chirality structures contribute to Higgs rates at NLO. Though, the operators with heterogeneous chirality structure have more sizeable effects as they would contribute to $hf\overline{f}$ vertex renormalisation in SMEFT and therefore appear in more channels compared to the operators baring homogenous chirality structure. Using the calculation results, fits using Higgs data have been preformed. The operators with the same chirality structure will not be constrained strongly by the Higgs data, and hence their results were not included. This applies to the operators that contribute only via beauty quarks loops, like $\mathcal{O}_{Qb}^{(1),(8)}$.
Two processes stood out in this calculation in terms of their sensitivity to these operators. The decay of the Higgs to beauty quarks, which had strong sensitivity to $\mathcal{O}_{QtQb}^{(1),(8)}$, Moreover, the associated production of the Higgs with top pair $t\bar{t}h$, which had large finite corrections coming from $\mathcal{O}_{Qt}^{(1),(8)}$. These corrections were depending on the colour factor and thus broke the degeneracy between the singlet and octet operators.
Using these calculations combined Higgs measurements using complete Run-II data as

well as HL-LHC projections, fits for constraining these operators have been preformed. These fits also included the SMEFT operator modifying the Higgs self-coupling C_ϕ which is weakly constrained, and only appears at NLO in single Higgs rates; like the group of four-heavy-quark operators considered. One can observe from the fits, that the constrains on C_ϕ from single Higgs data will become significantly diluted compared to the fits preformed with this operator alone, or even with ones that enter at LO [115–118, 120]. This is due to the strong correlation patters amongst C_ϕ and the four-fermion operators in question. On the contrary, The fits yielded overall stronger bounds on the four-heavy-quark operators than the ones obtained from top data [141, 234]. Comparable bounds can be also seen when EWPO data is considered [143], which these operators also enter at NLO in these observables. Additionally, the authors of ref. [262] have shown that these operators could also be constrained from flavour observables involving $\Delta F = 2$, in particular $B_s - -\overline{B}_s$ mixing. Although these bounds depend on the flavour ansatz of the New Physics, and not completely model independent.
The results of these calculations and consequent fits further emphasize the interconnectivity of SMEFT operators and experimental observables, which was discussed inchapter 3. Then remains the question: *How this interconnectivity would manifest in a NP model ?*. Particularly, one might wonder if the strong correlation between these four-fermion operators and $\mathcal{O}_\phi$ could appear in a UV complete model. In fact, large effective couplings involving four top quarks are expected in many NP models, for example partial compositness [263]. These models would also generate sizeable modifications to the Higgs self-interaction. Similar effects could be obtained from models containing new scalars such as an additional Higgs doublet $\varphi \sim (1,2)_{\frac{1}{2}}$, or other scalars with non-singlet representation under $SU(3)_c$ like $(6,1)_{\frac{1}{3}}$ and $(8,2)_{\frac{1}{2}}$. For further details on these models and their matching see [264]. In addition, for NLO matching to SMEFT see [265].

6 Virtual two-loop calculation of Zh production via gluon fusion

As we have seen in section 2.3, Higgs couplings to the weak vector bosons, i.e. Z and W is approaching the precision level. For their measurements both VBF and Vh channels are used, the associated Higgs production with the vector bosons are not only important for measuring the VVh coupling but also other couplings and properties as discussed in subsection 4.1.3. The most notable example emphasising the importance of this channel is the measurement of the Higgs decaying to beauty quarks $h \to b\bar{b}$ by both ATLAS and CMS [266, 267]. Hence, the Vh Higgs production is an important channel to look for in the future runs of the LHC. As the statistical and systematic uncertainties coming from the experimental setup of the LHC will be eventually reduced in the future runs, due to higher integrated luminosity, upgraded detectors and improved analysis techniques. There is an exigency to reduce theoretical uncertainties emerging from the perturbative calculations of cross-sections. In order to accomplish that, one should include higher order terms to the theoretical prediction. Since Wh production has no gluon fusion channel, and the main source of Zh uncertainties actually come from its gluon fusion part. Higher order correction to the $gg \to Zh$ is the key to improve the theoretical modelling for Vh.
It should be noted that the Zh channel can receive contributions from new particles [268], particularly at the large invariant-mass region where the gluon fusion contribution becomes more important, and HTL approximation would typically fail. Therefore, better understanding of the SM prediction of the Zh gluon fusion channel is crucial for both the SM precision measurements of Higgs production within the SM and for testing NP in this channel, e.g. new vector-like leptons.
This chapter aims to demonstrate the use of p_T–expansion technique, developed in [204] as an approach to compute the two-loop virtual corrections to $gg \to Zh$ analytically, including top mass effects. This method also allows for the use of Padé approximants, in order to extend the range of validity of this calculation.cite the paper once it is out

This chapter is structured as follows : In section 6.1 contains the general notation we have used for the gluon fusion Zh process calculation. Then, in subsection 6.1.1 the transverse momentum expansion method is discussed. Calculation of the LO form-factors in the transverse momentum expansion is illustrated in section 6.2 as a proof of concept for the p_T-expansion technique. Outline of the two-loop calculation is discussed in section 6.3. Finally, in section 6.4, the results of our calculation are shown with concluding remarks at the end. This chapter is based on the work my collaborators and I have published in [1].

6.1 General notation

The amplitude $g_a^\mu(p_1)g_b^\nu(p_2) \to Z^\rho(p_3)h(p_4)$ can be written as

$$\mathcal{A} = i\sqrt{2}\frac{m_Z G_F \frac{\alpha_s^0}{4\pi}(\mu_R)}{\pi}\delta_{ab}\epsilon_\mu^a(p_1)\epsilon_\nu^b(p_2)\epsilon_\rho(p_3)\hat{\mathcal{A}}^{\mu\nu\rho}(p_1,p_2,p_3), \tag{6.1}$$

$$\hat{\mathcal{A}}^{\mu\nu\rho}(p_1,p_2,p_3) = \sum_{i=1}^{6}\mathcal{P}_i^{\mu\nu\rho}(p_1,p_2,p_3)\mathcal{A}_i(\hat{s},\hat{t},\hat{u},m_t,m_h,m_Z), \tag{6.2}$$

where μ_R is the renormalisation scale and $\epsilon_\mu^a(p_1)\epsilon_\nu^b(p_2)\epsilon_\rho(p_3)$ are the polarization vectors of the gluons and the Z boson, respectively. It is possible to decompose the amplitude into a maximum of 6 Lorentz structures encapsulated by the tensors $\mathcal{P}_i^{\mu\nu\rho}$. Due to the presence of the γ_5 these projectors are proportional to the Levi-Civita total anti-symmetric tensor $\epsilon^{\alpha\beta\gamma\delta}$. One can choose to an orthogonal basis explicitly shown in **??**, such that

$$\mathcal{P}_i^{\mu\nu\rho}\mathcal{P}_{j\,\mu\nu\rho} = 0, \quad \text{for } i \neq j \tag{6.3}$$

By this choice one obtains unique form factors corresponding to each projector

$$\mathcal{A}_i(\hat{s},\hat{t},\hat{u},m_t,m_h,m_Z), \tag{6.4}$$

that are multivariate complex functions of the top (m_t), Higgs (m_h) and Z (m_Z) bosons masses, and of the partonic Mandelstam variables

$$\hat{s} = (p_1+p_2)^2, \quad \hat{t} = (p_1+p_3)^2, \quad \hat{u} = (p_2+p_3)^2, \tag{6.5}$$

where $\hat{s}+\hat{t}+\hat{u} = m_Z^2 + m_h^2$ and all the momenta are considered to be incoming. The form-factors $\mathcal{A}_i$ can be perturbatively expanded in orders of α_s,

$$\mathcal{A}_i = \sum_{k=0}\left(\frac{\alpha_s}{\pi}\right)^k \mathcal{A}_i^{(k)} \tag{6.6}$$

Where $\mathcal{A}_i^{(0)}$ and $\mathcal{A}_i^{(1)}$ are the LO and NLO terms, respectively. Using Fermi's Golden Rule, we can write thee Born partonic cross-section as

$$\hat{\sigma}^{(0)}(\hat{s}) = \frac{m_Z^2 G_F^2 \alpha_s(\mu_R)^2}{64\hat{s}^2(2\pi)^3}\int_{\hat{t}^-}^{\hat{t}^+} d\hat{t}\sum_i \left|\mathcal{A}_i^{(0)}\right|^2, \tag{6.7}$$

where $\hat{t}^\pm = [-\hat{s}+m_h^2+m_Z^2 \pm \sqrt{(\hat{s}-m_h^2-m_Z^2)^2-4m_h^2m_Z^2}\,]/2$.

The LO has two sets of diagrams, the triangle, and box diagrams shown in Figure 6.1. In (a), the triangle diagrams contains a neutral Goldstone boson G^0, instead in (b) the Z boson is mediated. The interplay between these two diagram types depends on the ξ gauge. Moreover, the Z boson is strictly off-shell, due to Furry's theorem. In the Landau gauge the Z- mediated diagrams will also vanish, this can be seen by considering the

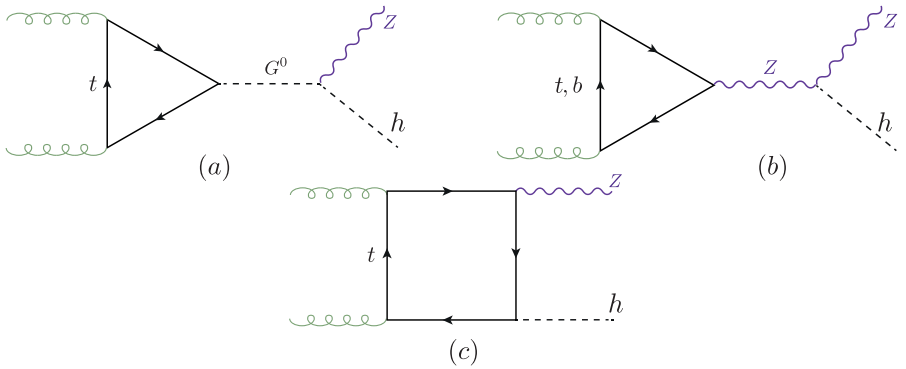

Figure 6.1. Feynman diagrams type for the LO $gg \to Zh$ process. The triangle diagrams in a general ξ gauge involve Z and the neutral Goldstone G^0 propagators.

subamplitude ggZ^* which in the Landau gauge can be related to the decay of a massive vector boson with mass $\sqrt{\hat{s}}$ into two massless ones, a process that is forbidden by the Landau-Yang theorem [269, 270]. The triangle diagrams are also proportional to the mass difference between the up and down type quarks. In this calculation, the first and second generation quarks are assumed to be massless, as well as the b quark, hence light quarks loops do not contribute to this process. The same would apply to the box diagrams (c), as they are proportional to the quark Yukawa coupling, and vanish in the massless quarks case. Moreover, triangle diagrams with $b-$ quark loops contribute to $\sim 1\%$ of the total amplitude, computed in the limit $m_b \to 0$.

6.1.1 The transverse momentum expansion

Choosing to expand in small p_T of the Z boson, the first step is expressing p_T in terms of the Mandelstam variables and masses

$$p_T^2 = \frac{\hat{t}\hat{u} - m_Z^2 m_h^2}{\hat{s}}. \tag{6.8}$$

From eq.(6.8), together with the relation between the Mandelstam variables, one finds

$$p_T^2 + \frac{m_h^2 + m_Z^2}{2} \leq \frac{\hat{s}}{4} + \frac{\Delta_m^2}{\hat{s}}, \tag{6.9}$$

where $\Delta_m = (m_h^2 - m_Z^2)/2$. Eq.(6.9) implies $p_T^2/\hat{s} < 1$ that, together with the kinematical constraints $m_h^2/\hat{s} < 1$ and $m_Z^2/\hat{s} < 1$. With these relations in mind, one can expand the amplitudes in terms of small $p_T^2/\hat{s}$, $m_h^2/\hat{s}$ and $m_Z^2/\hat{s}$, which is technically valid throughout the whole phase space, contrary to the LME and HE limits. The caveat for this expansion is that, the amplitude does not depend on p_T explicitly. Instead, one would expand in

the reduced Mandelstam variables $t'/s' \ll 1$ or $u'/s' \ll 1$, defined as

$$s' = p_1 \cdot p_2 = \frac{\hat{s}}{2}, \quad t' = p_1 \cdot p_3 = \frac{\hat{t} - m_Z^2}{2}, \quad u' = p_2 \cdot p_3 = \frac{\hat{u} - m_Z^2}{2} \tag{6.10}$$

and satisfy

$$s' + t' + u' = \Delta_m. \tag{6.11}$$

The choice of the expansion parameter t' or u' depends whether one expands in the forward or backwards kinematics. Because the process $gg \to Zh$, has two particles in the final states with different masses, the amplitude is not symmetric under the their exchange. One therefore cannot compute the cross-section by integrating only the forward-expanded amplitude [1], contrary what has been done for the Higgs pair [204]. In order to overcome this issue, one could further examine the projectors in **??** and observe that they can be split into symmetric and anti-symmetric parts with respect to the exchange $t' \leftrightarrow u'$. Then, expand the symmetric part in the forward kinematics, like the Higgs pair case. As for the anti-symmetric part, the antisymmetric factor is simply extracted by multiplying the form-factors by $1/(\hat{t} - \hat{u})$, written as $1/(2s' - 4t' - 2\Delta_m)$, then perform the expansion in the forward kinematics and finally multiply back by $(\hat{t} - \hat{u})$.

In order to implement the p_T-expansion at the Feynman diagrams level we start by splitting the momenta into longitudinal and transverse with respect to the beam direction, by introducing the vector [204],

$$r^\mu = p_1^\mu + p_3^\mu, \tag{6.12}$$

which satisfies

$$r^2 = \hat{t}, \quad r \cdot p_1 = \frac{\hat{t} - m_Z^2}{2}, \quad r \cdot p_2 = -\frac{\hat{t} - m_h^2}{2}, \tag{6.13}$$

and hence can be also written as

$$r^\mu = -\frac{\hat{t} - m_h^2}{\hat{s}} p_1^\mu + \frac{\hat{t} - m_Z^2}{\hat{s}} p_2^\mu + r_\perp^\mu = \frac{t'}{s'}(p_2^\mu - p_1^\mu) - \frac{\Delta_m}{s'} p_1^\mu + r_\perp^\mu, \tag{6.14}$$

where

$$r_\perp^2 = -p_T^2. \tag{6.15}$$

substituting the definition of p_T from eq.(6.8) one obtains

$$t' = -\frac{s'}{2}\left\{1 - \frac{\Delta_m}{s'} \pm \sqrt{\left(1 - \frac{\Delta_m}{s'}\right)^2 - 2\frac{p_T^2 + m_Z^2}{s'}}\right\} \tag{6.16}$$

implying that the expansion in small p_T (the minus sign case in eq.(6.16)) can be realized at the level of Feynman diagrams, by expanding the propagators in terms of the vector r^μ around $r^\mu \sim 0$ or, equivalently, $p_3^\mu \sim -p_1^\mu$, see eq.(6.14).

6.2 Born cross-section in the p_T-expansion

As a baseline test for the validity and convergence behaviour of the p_T expansion we start by computing the LO amplitude, and consequently the Born partonic cross-section in the p_T expansion then compare it with the exact results found in [195, 196] .
Starting by defining the one-loop functions appearing in the similar calculation of the Born cross-section for $gg \to hh$ in the same expansion carried out in ref. [204]

$$B_0[\hat{s}, m_t^2, m_t^2] \equiv B_0^+, \qquad B_0[-\hat{s}, m_t^2, m_t^2] \equiv B_0^-, \tag{6.17}$$

$$C_0[0, 0, \hat{s}, m_t^2, m_t^2, m_t^2] \equiv C_0^+, \qquad C_0[0, 0, -\hat{s}, m_t^2, m_t^2, m_t^2] \equiv C_0^- \tag{6.18}$$

$$B_0[q^2, m_1^2, m_2^2] = \frac{1}{i\pi^2} \int \frac{d^n k}{\mu^{n-4}} \frac{1}{(k^2 - m_1^2)((k+q)^2 - m_2^2)}, \tag{6.19}$$

$$C_0[q_a^2, q_b^2, (q_a + q_b)^2, m_1^2, m_2^2, m_3^2] = \frac{1}{i\pi^2} \int \frac{d^d k}{\mu^{d-4}} \frac{1}{[k^2 - m_1^2][(k+q_a)^2 - m_2^2][(k-q_b)^2 - m_3^2]} \tag{6.20}$$

are the Passarino-Veltman functions [271], with d the dimension of spacetime and μ the 't Hooft mass. There are only two non-vanishing form-factors at LO, one is symmetric $\mathcal{A}_2$, and the other is antisymmetric $\mathcal{A}_6$, in the p_T-expansion, these form-factors are give by,

up to order $\mathcal{O}(p_T^2)$

$$\mathcal{A}_2^{(0,\triangle)} = -\frac{p_T}{\sqrt{2}\,(m_Z^2+p_T^2)}(\hat{s}-\Delta_m)\,m_t^2 C_0^+, \tag{6.21}$$

$$\begin{aligned}
\mathcal{A}_2^{(0,\square)} = {} & \frac{p_T}{\sqrt{2}\,(m_Z^2+p_T^2)}\Bigg\{ \\
& \left(m_t^2 - m_Z^2\frac{\hat{s}-6m_t^2}{4\hat{s}} - p_T^2\frac{12m_t^4-16m_t^2\hat{s}+\hat{s}^2}{12\hat{s}^2}\right)B_0^+ \\
- & \left(m_t^2 - \Delta_m\frac{m_t^2}{(4m_t^2+\hat{s})} + m_Z^2\frac{24m_t^4-6m_t^2\hat{s}-\hat{s}^2}{4\hat{s}\,(4m_t^2+\hat{s})} - \right. \\
& \qquad \left. p_T^2\frac{48m_t^6-68m_t^4\hat{s}-4m_t^2\hat{s}^2+\hat{s}^3}{12\hat{s}^2\,(4m_t^2+\hat{s})}\right)B_0^- \\
+ & \left(2m_t^2 - \Delta_m + m_Z^2\frac{3m_t^2-\hat{s}}{\hat{s}} + p_T^2\frac{3m_t^2\hat{s}-2m_t^4}{\hat{s}^2}\right)m_t^2\,C_0^- \\
+ & \left(\hat{s} - 2m_t^2 + m_Z^2\frac{\hat{s}-3m_t^2}{\hat{s}} + p_T^2\frac{2m_t^4-3m_t^2\hat{s}+\hat{s}^2}{\hat{s}^2}\right)m_t^2\,C_0^+ \\
+ & \log\left(\frac{m_t^2}{\mu^2}\right)\frac{m_t^2}{(4m_t^2+\hat{s})}\left(\Delta_m + 2m_Z^2 + p_T^2\frac{2\hat{s}-2m_t^2}{3\hat{s}}\right) \\
- & \Delta_m\frac{2m_t^2}{(4m_t^2+\hat{s})} + m_Z^2\frac{\hat{s}-12m_t^2}{4\,(4m_t^2+\hat{s})} + p_T^2\frac{8m_t^4-2m_t^2\hat{s}+\hat{s}^2}{4\hat{s}(4m_t^2+\hat{s})}\Bigg\},
\end{aligned} \tag{6.22}$$

and

$$\mathcal{A}_6^{(0,\triangle)} = 0, \tag{6.23}$$

$$\begin{aligned}
\mathcal{A}_6^{(0,\square)} = {} & \frac{\hat{t}-\hat{u}}{\hat{s}^2}\,p_T\left[\frac{m_t^2}{2}\Big(B_0^- - B_0^+\Big) - \frac{\hat{s}}{4}\right. \\
& \left. - \frac{2m_t^2+\hat{s}}{2}m_t^2\,C_0^- + \frac{2m_t^2-\hat{s}}{2}m_t^2\,C_0^+\right],
\end{aligned} \tag{6.24}$$

where these form-factors were divided into triangle ($\triangle$) and box ($\square$) contributions, and B_0 functions are understood as the finite part of the integrals on the right hand side of eq.(6.19).

Using several truncations of the p_T-expansion, and comparing it to the exact LO result, one can see in Figure 6.2 the exact Born partonic LO cross section (red line) as a function of the invariant mass of the Zj system, M_{Zh}, in comparison to the p_T-expansions. For the numerical evaluation of the cross section here and in the following, we used as SM

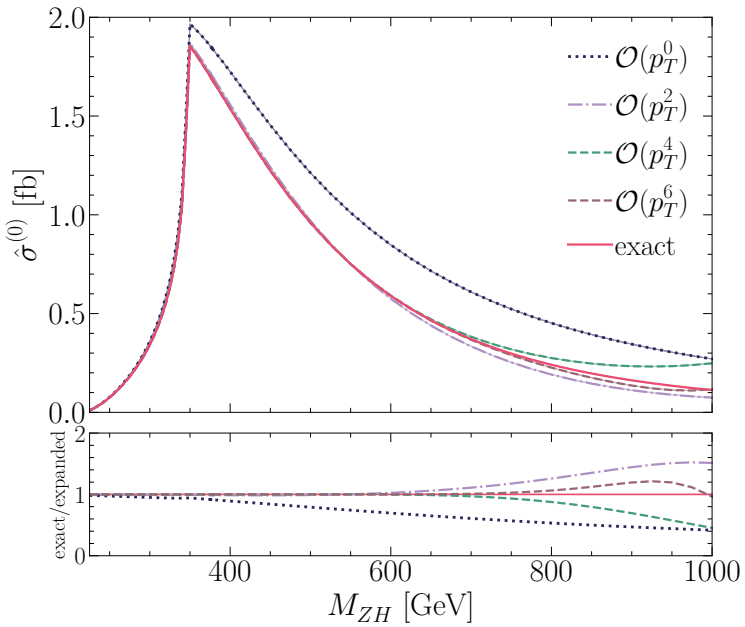

Figure 6.2. The Born partonic cross-section as a function of the invariant mass M_{Zh}. The exact (red line) is plotted together with results at different orders in the p_T-expansion (dashed lines). In the bottom part, the ratio of the full result over the p_T-expanded one at various orders is shown. This plot has been already published in [1]

input parameters

$$m_Z = 91.1876 \text{ GeV}, \quad m_h = 125.1 \text{ GeV}, \quad m_t = 173.21 \text{ GeV},$$
$$m_b = 0 \text{ GeV}, \quad G_F = 1.16637 \text{ GeV}^{-2}, \quad \alpha_s(m_Z) = 0.118.$$

From the ratio plotted in the lower panel of Figure 6.2 , we observe that the $\mathcal{O}(p_T^0)$ expansion is in good agreement with the exact result when $M_{Zh} \lesssim 2m_t$. Inclusion of higher order terms up tp $\mathcal{O}(p_T^6)$ extended the validity of the expansion to reach $M_{Zh} \lesssim 750\,\text{GeV}$. This is the similar behaviour seen in [204] for Higgs pair. Therefore, one would expect the p_T-expanded two-loop virtual correction to be an accurate approximation with the exact (numerical) result for the region of the invariant mass of $M_{Zh} \sim 700 - 750\,\text{GeV}$. Similar conclusions can be seen more explicitly in Table 6.1, where it is shown that the partonic cross-section at $\mathcal{O}(p_T^4)$ agrees with the full result for $M_{ZH} \lesssim 600\,\text{GeV}$ on the permille level and the agreement further improves when $\mathcal{O}(p_T^6)$ terms are included.

M_{Zh} [GeV]	$\mathcal{O}(p_T^0)$	$\mathcal{O}(p_T^2)$	$\mathcal{O}(p_T^4)$	$\mathcal{O}(p_T^6)$	full
300	0.3547	0.3393	0.3373	0.3371	0.3371
350	1.9385	1.8413	1.8292	1.8279	1.8278
400	1.6990	1.5347	1.5161	1.5143	1.5142
600	0.8328	0.5653	0.5804	0.5792	0.5794
750	0.5129	0.2482	0.3129	0.2841	0.2919

Table 6.1. The partonic cross section $\hat{\sigma}^{(0)}$ at various orders in p_T and the full computation for several values of M_{Zh}, This table has been already published in [1].

6.3 NLO calculation

The virtual two-loop corrections to $gg \to Zh$ are shown in Figure 6.3, which involve corrections to the triangle topology in (a) and (b). The corrections to the box topology in (c) and a new topology , dented by double triangle in (d). Both two-loop corrections to the triangles, and the double triangle diagrams can be computed exactly analytically. However, the two-loop box diagrams contain master-integrals (MI's) that have no analytic solutions, so far. The two-loop box diagrams will be computed in the p_T-expansion.

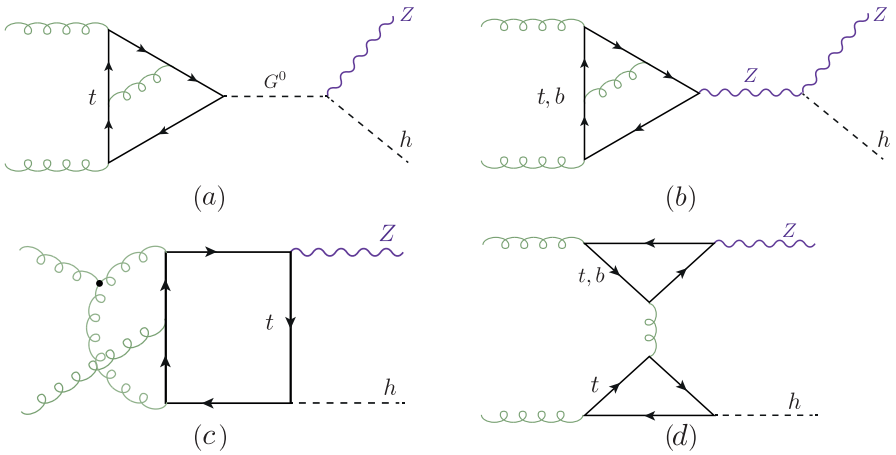

Figure 6.3. Feynman diagrams types for the virtual NLO corrections to the $gg \to Zh$ process.

6.3.1 Renormalisation

The two-loop corrections to the triangle and box diagrams contain both UV and IR divergences. The first emerges from UV divergent sub-diagrams, such as top mass renormalisation and QCD vertex correction. While the lR divergences come from massless

loops. In order to remove these divergences, one introduces adequate counter-terms. On the other hand, the double triangle is both UV and IR finite.

We start by the gluon wavefunction renormalisation of the incoming gluons (external legs) such that the amplitude is renormalised by $Z_A^{1/2}$ for each gluon.

$$Z_A = 1 + \frac{\alpha_s^0}{4\pi}\frac{2}{3\epsilon}\left(\frac{\mu_R^2}{m_t^2}\right)^{\epsilon}. \tag{6.25}$$

The on-shell scheme for the top mass renormalisation has been used, in which the bare mass is replaced by the renormalised one $m_0 = Z_m m$ in the propagators this gives the $\overline{\text{MS}}$ renormalised mass.

$$Z_m = 1 + C_F\frac{3}{\epsilon}. \tag{6.26}$$

In order to convert the mass definition to the on-shell scheme we add the finite renormalisation term

$$Z_m^{OS} = 1 - 2C_F, \tag{6.27}$$

here $C_F = (N_c^2-1)/2N_c$ is one of the two Casimir invariants of QCD along with $C_A = N_c$. The $q\bar{q}g$ vertex correction involves a renormalisation of the strong couplings constant α_s which is done via replacing the bare constant α_s^0 with the renormalised one, hence it becomes $\alpha_s^0 = \frac{\mu_R^{2\epsilon}}{S_\epsilon} Z_{\alpha_s}\alpha_s$, where

$$Z_{\alpha_s} = 1 - \frac{\alpha_s}{4\pi}\frac{1}{\epsilon}\left(\beta_0 - \frac{2}{3}\right)\left(\frac{\mu_R^2}{m_t^2}\right)^{\epsilon}, \tag{6.28}$$

and the constant $\beta_0 = \frac{11}{3}C_A - \frac{2}{3}N_f$, where N_f is the number of "active" flavours. The 5-flavour scheme $N_f = 5$ is adopted here.

The loop integrals were evaluated via dimensional regularisation in $d = 4 - 2\epsilon$ dimensions. Which requires some caution when γ_5 is present in the amplitude. We let γ_5 naively anti-commute with all d-dimensional γ_μ's and then correct that with the finite renormalisation constant known as **Larin counter-term** [272]

$$Z_5 = 1 - 2\,C_F. \tag{6.29}$$

The renormalised amplitude is written as

$$\mathcal{M}(\alpha_s, m, \mu_R) = Z_A\mathcal{M}(\alpha_s^0, m^0). \tag{6.30}$$

Putting all the above substitutions together, we get the renormalised two-loop form-

factor:

$$(\mathcal{A}^{(1)})^R = \mathcal{A}^{(1)} - \mathcal{A}^{(0)}_{UV} - \mathcal{A}^{(0)}_{UV,m} + \mathcal{A}^{(0)}_{\text{Larin}} \tag{6.31}$$

$$\begin{aligned}
\mathcal{A}^{(0)}_{UV} &= \frac{\alpha_s}{4\pi}\frac{\beta_0}{\epsilon}\left(\frac{\mu_R^2}{\hat{s}}\right)^{-\epsilon}\mathcal{A}^{(0)}. \\
\mathcal{A}^{(0)}_{UV,m} &= \frac{\alpha_s}{4\pi}\left(\frac{3}{\epsilon}-2\right)C_F\left(\frac{\mu_R^2}{\hat{s}}\right)^{-\epsilon} m^0\partial_m\mathcal{A}^{(0)}.
\end{aligned} \tag{6.32}$$

$$\mathcal{A}^{(0)}_{\text{Larin}} = -\frac{\alpha_s}{4\pi}C_F\mathcal{A}^{(0)}.$$

The following IR-counter-term is used in order to cancel the IR divergences.

$$\mathcal{A}^{(0)}_{IR} = \frac{e^{\gamma_E\epsilon}}{\Gamma(1-\epsilon)}\frac{\alpha_s}{4\pi}\left(\frac{\beta_0}{\epsilon}+\frac{C_A}{\epsilon^2}\right)\left(\frac{\mu_R^2}{\hat{s}}\right)^{2\epsilon}\mathcal{A}^{(0)} \tag{6.33}$$

The one-loop form-factors, need to be expanded up to order $\mathcal{O}(\epsilon^2)$, for the UV and IR counter-terms.

6.3.2 Calculation of the exact virtual corrections

The two-loop calculations of the triangle digrams involves the diagrams of with virtual Z^* and G^0, depending on the gauge of choice. Observations found in ref.[197] shows that due to Landau-Yang theorem in the Landau gauge the diagrams with the Z^* exchange vanishes. Therefore, the part of the top triangle diagrams can be obtained from the decay amplitude of a pseudoscalar boson into two gluons which is known in the literature in the full mass dependence up to NLO terms [273, 274]. On the contrary, in the unitary gauge, the NLO calculation needs to be done with the Z^* exchange diagrams only. The calculations result in apparently different Lorentz structures, that are linked via the Schouten identity

$$q^\alpha\epsilon^{\beta\gamma\delta\phi} + q^\beta\epsilon^{\gamma\delta\phi\alpha} + q^\gamma\epsilon^{\delta\phi\alpha\beta} + q^\gamma\epsilon^{\delta\phi\alpha\beta} + q^\delta\epsilon^{\phi\alpha\beta\gamma} + q^\phi\epsilon^{\alpha\beta\gamma\delta} = 0 \tag{6.34}$$

A cross-check has been preformed in order to ensure that the NLO calculation introduces no new Lorentz structures, and gives the same result in a general R_ξ gauge as the results in [273, 274]. The two-loop calculation has been carried out in R_ξ gauge. The amplitudes have been automatically generated by `FeynArts` [240] and contracted with the projectors as defined in **??** using `FeynCalc` [275, 276] and `Package X` [277] and in-house Mathematica routines. The two-loop integrals were reduced to a set of master integrals MI, illustrated graphically in Figure 6.4 using `Kira` [278]. These MI's are either products of one-loop functions (a)-(c), (e),(f),(h) and (l) or can be found in the literature [274, 279]. Their implementation in our calculation has been validated numerically using `SecDec` [280, 281]. The virtual correction for the triangle diagrams

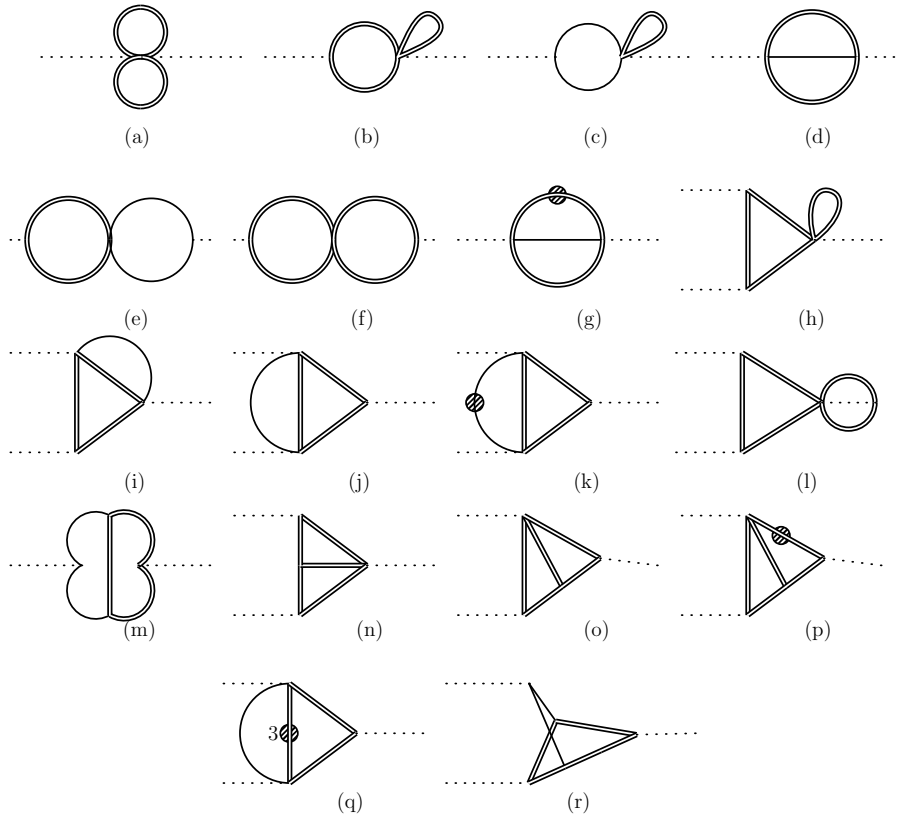

Figure 6.4. The list of two-loop master integrals (MI's) resulting from the reduction of the two-loop triangle corrections, and the product of one-loop MI's appearing in this list also appear in the calculation of the double-triangle diagrams. A single line denotes a massless propagator, while a double line denotes a massive one. The dot denotes a squared propagator, unless the number of the exponent is indicated, here only 3 appears in diagram (q).

can be separated according to their colour factors into

$$\mathcal{A}^{(1)} = C_F \mathcal{A}^{(1)}_{CF} + C_A \mathcal{A}^{(1)}_{CA}, \tag{6.35}$$

The C_A part contains a double pole $\mathcal{O}(1/\epsilon^2)$ and a single pole $\mathcal{O}(1/\epsilon)$, both coming from the IR divergence. Whilst the C_F part contains a UV divergent pole that needs to be cured via mass renormalisation. The poles do not have a dependence on the renormalisation scale μ_R. However, there is a dependence on that scale in the finite part, as well. No new Lorentz structures appeared, and the final result in R_ξ matched the one found in [273, 274] for the Landau gauge. The explicit results are shown in **??**

The calculation of the double triangle diagrams (d) of Figure 6.3 is fairly straightforward, all of the integrals can be rewritten in terms of products of one-loop functions. All of the Lorentz structures appear in the double triangle except for $\mathcal{P}_6$, analogous to the triangle case. The explicit forms of form-factors corresponding to these structures are presented in **??**. Although we write the amplitude using a different tensorial structure with respect to ref.[202] we have checked, using the relations between the two tensorial structures reported in **??**, that our result is in agreement with the one presented in ref.[199].

6.3.3 Calculation of the p_T-expanded virtual corrections

The two-loop triangle diagrams can also be interpreted as an expansion in p_T, but this expansion terminates at $\mathcal{O}(p_T^2)$, rather being an infinite series. Hence, in this section we concentrate on the two-loop box diagrams p_T-expansion [1].
Similar to the two-loop triangle diagrams, the box diagrams amplitudes were generated projected through the same pipeline. After the contraction of the epsilon tensors the diagrams were expanded as described in subsection 6.1.1, keeping only $\mathcal{O}(p_T^4)$ terms. They were reduced to MI's using `FIRE` [282] and `LiteRed` [283]. The resulting MI's were identical to the one for Higgs pair production [204]. Nearly all of them are expressed in terms of generalised harmonic polylogarithms with the exception of two elliptic integrals [284, 285]. The renormalisation and IR pole subtraction procedure was carried out like prescribed subsection 6.3.1.
As a control, the two-loop box diagrams were also computed in the LME up to $\mathcal{O}(1/m_t^6)$. Since this expansion should be included within the p_T-expansion. We have retained the LME analytic expression by further expanding the p_T-expanded amplitude in small $\hat{s}/m_t^2$. Providing an additional cross-check for the validity of the p_T-expansion.

6.4 Results and conclusions

The virtual corrections to the gluon fusion Zh production have been implemented in a `FORTRAN` code using `handyG` [286], for the evaluation of generalised harmonic polylogarithms, `Chaplin` [287] for the harmonic polylogarithms appearing in the triangle two-loop

[1] The calculation of the box diagrams has been done mainly by my collaborators, the co-authors of [1]

$\hat{s}/m_t^2$	$\hat{t}/m_t^2$	ref.[203]	$\mathcal{O}(p_T^6)$
1.707133657190554	-0.441203767016323	35.429092(6)	35.430479
3.876056604162662	-1.616287256345735	4339.045(1)	4340.754
4.130574250302561	-1.750372271104745	6912.361(3)	6915.797
4.130574250302561	-2.595461551488002	6981.09(2)	6984.20

Table 6.2. Comparison of $\mathcal{V}_{fin}4/(\alpha_s^2\alpha^2)$ with the numerical results of ref.[203]. This plot has been already published in [1].

functions while the elliptic integrals are evaluated using the routines of ref.[285]. Since the result is analytic, the code is significantly faster than the numerical evaluation of the two-loop amplitude [203], with evalution time of ca. 0.5 min per one phase space point on a personal laptop.
In order to facilitate the comparison of our results with the ones presented in the literature, we define the finite part of the virtual corrections as in ref.[202][2]

$$\begin{aligned}\mathcal{V}_{fin} = \frac{G_F^2 m_Z^2}{16}\left(\frac{\alpha_s}{\pi}\right)^2 \Bigg[\sum_i \left|\mathcal{A}_i^{(0)}\right|^2 \frac{C_A}{2}\left(\pi^2 - \log^2\left(\frac{\mu_R^2}{\hat{s}}\right)\right) \\ +2\sum_i \mathrm{Re}\left[\mathcal{A}_i^{(0)}\left(\mathcal{A}_i^{(1)}\right)^*\right]\Bigg]\end{aligned} \tag{6.36}$$

and in the numerical evaluation of eq.(6.36) we fixed $\mu_R = \sqrt{\hat{s}}$. Triangle and LME box toopologies were validated against the results of refs.[199, 202] finding perfect agreement at the form-factor level, i,.e.$\mathcal{A}_i^{(1)}$.

The virtual part of the partonic cross-section from the finite part of the virtual corrections in eq.(6.36) is defined by

$$\Delta\hat{\sigma}_{virt} = \int_{\hat{t}^-}^{\hat{t}^+} d\hat{t}\frac{\alpha_s}{16\pi^2}\frac{1}{\hat{s}^2}\mathcal{V}_{fin} \tag{6.37}$$

This function is used to confront p_T-expanded results. Starting with low M_{Zh} we have compared the p_T-expanded with the LME $\mathcal{V}_{fin}$, finding a good numerical agreement. It is important to note that, at the same order in the expansion, the p_T-expanded terms are more accurate than the LME ones, although computationally more demanding. Additional checks have been done using the numerical evaluation of the NLO amplitude by [203], where they have evaluated the exact two-loop MI's using `pySecDec` [288, 289]. Table 6.2 shows a comparison between our p_T-expanded $\mathcal{V}_{fin}4/(\frac{\alpha_s^0}{4\pi}^2\alpha^2)$ versus the exact numerical result of [203] for several phase space points. As can be seen from the table the relative difference between the two results is less than half a permille.

In Figure 6.5, the dashed lines show the different orders of the expansion. For all

[2]The definition of the matrix elements here differs by a factor of $\frac{1}{\hat{s}}$ from ref.[202], *cf.* also **??**.

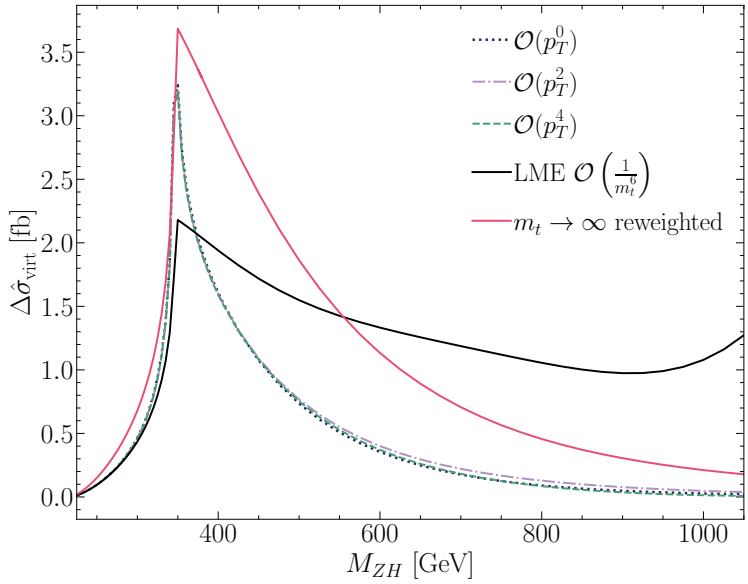

Figure 6.5. $\Delta\hat{\sigma}_{virt}$ defined by eq.(6.37), shown as a function of M_{ZH}. The various orders of the p_T-expansion are plotted as dashed lines, while the black and red continuous lines stand for the LME and reweighted $m_t \to \infty$ results, respectively.This plot has been already published in [1].

parts of the matrix elements the best results available, i.e. both $\mathcal{A}^{(0)}$ were used and the double-triangle contribution are evaluated exactly, while for $\mathcal{A}^{(1)}$ we use the various orders in the p_T-expansion. For comparison, the results are shown were $\mathcal{A}^{(1)}$ is replaced by the one computed in LME up to $\mathcal{O}(1/m_t^6)$ (full black line), which as mentioned before is valid up to $M_{ZhH} < 2m_t$. We observe that within the validity of the LME our results agree well with it. Furthermore, the results in the infinite top mass limit reweighted by the full amplitudes squared can be seen as the full red line in the plot, corresponding to the approach of ref.[197], keeping though the double triangle contribution in full top mass dependence. Differently from the LME line, the $m_t \to \infty$ reweighted one shows a behaviour, for $M_{Zh} \gtrsim 400\,\text{GeV}$, similar to the behaviour of the p_T lines. Still, the difference between the reweighted result and the p_T-expanded ones is significant. The p_T-expanded results show very good convergence. The zero order in our expansion agrees extremely well with the higher orders in the expansion, and all the three results are very close up to $M_{Zh} \sim 500\,\text{GeV}$.

The calculation of the virtual two-loop corrections to the $gg \to Zh$ is done using exact results for the triangle and double-triangle topologies, and in the p_T-expansion for the box one. The result of the calculation showed that we get the exact same MI's that was found for Higgs pair production [204] , mostly these MI's are expressed in terms of generalised harmonic polylogarithms with the exception of two elliptic integrals. Using the LO calculation, we have shown the validity of the p_T-expansion covering the invariant mass interval $M_{Zh} \lesssim 750$ GeV which covers $\sim 98\%$ of the total phase space for $13 - 14$

TeV energies.
The p_T-expansion agrees with per mill level with the numerical results found in [203]. However, it allows for fast computation of the amplitude with circa one second per phase space point using a modern laptop with mid-range specifications. Additionally. the integration over the $\hat{t}$ variable in eq.(6.37) converges very well. The flexibility of our analytic results, an application to beyond-the-Standard Model is certainly possible.
Finally, it should be noted that this calculation complements nicely the results obtained in ref.[202] using a high-energy expansion, that according to the authors provides precise results for $p_T \gtrsim 200\,\text{GeV}$. The merging of the two analyses is going to provide a result that covers the whole phase space, can be easily implemented into a Monte Carlo code using v which is currently a work in progress in Cite the new paper here-later

Part III

Higgs Pair Production

7 Overview of Higgs pair production at colliders

The determination of the shape of the Higgs potential is an essential part of the LHC physics programme. Unlike the determination of most properties of the Higgs and its couplings to heavy particles, the light Yukawa and Higgs-self couplings are exceptionally hard to probe. This is particularly evident from the conclusion of chapter 5. When we have seen that the effectiveness of the utilisation of single Higgs signals in order to probe the Higgs trilinear coupling is challenged with the fact that other weakly constrained operators also affect these signals. Thus, Higgs pair production remains as thee only direct way to access this elusive interaction.
The production of Higgs in pairs has roughly 10^{-4} the signal of producing a single Higgs at the LHC. The Higgs pair production with Higgs pair decays considered have a cross-section of $\sim$ 1fb, in the SM. This would make it inaccessible from Run-II or Run-III data, but should be accessed using the whole luminosity of the HL-LHC [66, 192, 290]. As for the quartic coupling, which would require NLO corrections to Higgs pair, which are currently unknown, or triple Higgs production, both of which are beyond the sensitivity of the LHC [291]. The measurement potentials for the light Yukawa couplings shall be discussed in the Next chapter. The main advantages for Higgs pair production in determining the Higgs trilinear self-coupling comes from the dependence of the cross-section of λ_3 at the LO level, as well as the fact that the rest of SMEFT operators entering in this process (see eq (3.11)) can be strongly constraint from other processes, breaking any potential correlations that might appear between them and the trilinear coupling using only di-Higgs data. However, the inclusion of light quark Yukawa couplings modifiers e.g.$C_{u\phi}$ and $C_{d\phi}$ would complicate things as we shall see in **??**.
This chapter will start by reviewing the theoretical status of the dominant process for Higgs pair production, the gluon fusion, in section 7.1. Then, the other subdominant channels will be briefly reviewed in section 7.2. I will afterwards overview the experimental efforts in probing this rare yet fascinating processes in section 7.3. Finally, I will present in section 7.4 a summery of the trilinear Higgs-self coupling constraints.

7.1 Higgs pair production by gluon fusion

The dominant process for Higgs pair production at the LHC (and hadron colliders in general) is the gluon gluon fusion (ggF) via a heavy quark loop Q, mainly the top and beauty quark, with the latter contributing only to about 1%, as shown in Figure 7.1. This process is well-studied at leading order (LO) analytically [292–295]. The higher or-

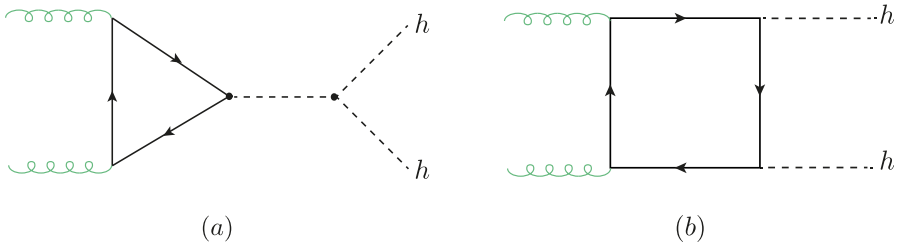

Figure 7.1. Feynman diagrams for the ggF process of Higgs pair production in the SM.

der computations are significantly more complicated to preform compared to the gluon fusion production of a single Higgs. This is due to the fact that multi-scale amplitudes at two-loops (and more) cannot be always computed analytically using the current computational techniques. The first attempt to compute the NLO corrections to di-Higgs were via the infinite top limit (HTL/LME) approximation [112, 197, 296] and implemented in `HPAIR`. These corrections were found to be large, with a K-factor of ~ 2. This prompted more calculations with inclusion of top mass effects [178, 297–300], which improved the stability of the LME expansion as well as corrected the cross-section by $\sim 10\%$. In addition, the threshold resummation effects of the LME has been included in [301]. This approach, however, is not sufficient to produce corrections to the differential cross-section, as the LME fails for $m_{hh}^2/4m_t^2 \lesssim 1$. Using numerical evaluation of the two-loop integrals, it is possible to obtain exact results with full top mass dependence, see refs. [302–304]. But this comes at the cost of computational power required to evaluate the cross-section. Hence, approximation methods were imperative in obtaining more flexible results for use at simulations and BSM Higgs pair production predictions. These approximations methods are analogous, and sometimes connected to the ones used for Zh production discussed in chapter 6. This includes, small final particle transverse momentum [204], and high energy (HE) expansions [305**?**]. In addition to a method developed in refs. [306, 307] which considers both $\hat{s}, \hat{t}$ and m_t as large quantities while keeping the Higgs mass as small one. This method has a wide coverage of the m_{hh} spectrum. The use of Padé approximation to improve the p_T–expanded amplitude coverage as well as to obtain a description for the three-loop (NNLO) form factors was demonstrated in [308]. The NNLO cross section with top mass effects has been computed numerically in [309] and also at differential level [310], and analytically only in the LME [311]. Also, NLO+ NNL analytic results have been obtained by [312]. Parton shower matching for NLO Higgs pair production has been computed in [313, 314], which was essential for the `POWHEG` implementation for di-Higgs, with NLO corrections computed from a grid has been made available by [158, 314, 315]. Figure 7.2 shows the Higgs pair virtual partonic cross-section defined in eq.(6.37) vs the p_T and HE expansions bridged using Padé approximants [316]. The matching between the results across low and high energy intervals of m_{hh} shows the strength of Padé approximants technique. This is the most recent analytic higher order correction result for Higgs pair production.
The LO Higgs pair production with SMEFT operators is available in `SMEFTatNLO` mode [227] for `MadGraph`.

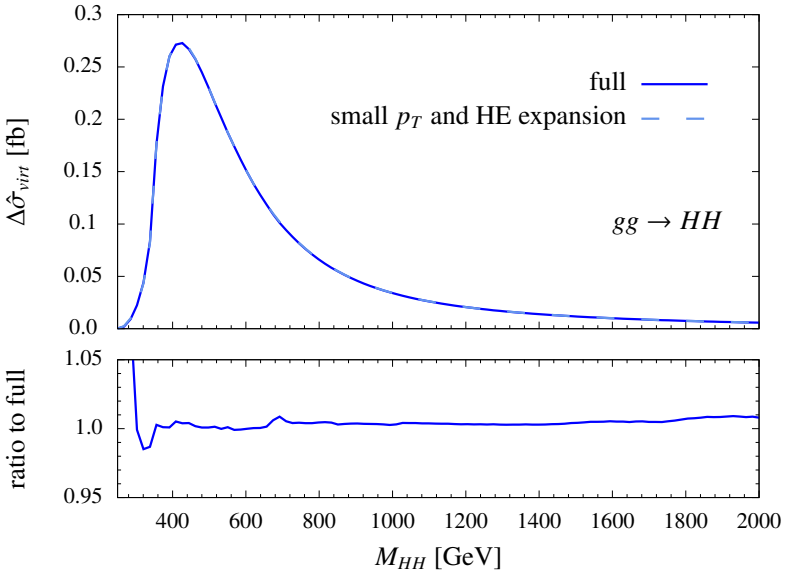

Figure 7.2. Combination of the HE and p_T expansions of the virtual two-loop NLO corrections using Padé approximants, confronted with the NLO results from a numerical grid. This plot is taken from [316].

Calculation of LO in addition to Higher order corrections to Higgs pair production in EFT, MSSM and composite Higgs models can be found in [149, 155, 317–319].
The NNLO correction were used according to the Higgs cross section working group recommended values [320, 321]:

$$K = \frac{\sigma_{NNLO}}{\sigma_{LO}}, \qquad K_{14\text{TeV}} \approx 1.71. \tag{7.1}$$

7.1.1 Theoretical uncertainties

There are four main sources of theoretical uncertainties for Higgs pair production:

1. Scale uncertainty: coming form the arbitrariness of scales choice.
2. PDF uncertainties : coming form the uncertainty in the PDF fitting and model.
3. α_s running uncertainty: originating from the initial value (i.e. $\alpha_s(M_Z)$).
4. Top mass renormalisation scheme, which involves m_t appearing in the loop propagators and in the top Yukawa.

The computation of the uncertainties is described in [322, 323]. for PDF and α_s uncertainties. In order to calculate the scale uncertainties, the cross-section was computed

	σ [fb]	Scale [fb]	PDF+α_s [fb]	Total [fb]
SM HEFT (LO)	18.10	–	–	–
SM running mass (LO)	16.96	–	–	–
SM (LO)	21.45	$^{+4.29}_{-3.43}$	± 1.46	$^{+4.53}_{-3.73}$
SM (NLO) [327]	33.89	$^{+6.17}_{-4.98}$	$^{+2.37}_{-2.01}$	$^{+6.61}_{-5.37}$
SM (NNLO) [309]	36.69	$^{+0.77}_{-1.83}$	± 1.10	$^{+1.66}_{-6.43}$ (incl. m_t uncertainty [324])

Table 7.1. Gluon fusion (ggF) Higgs pair production cross-section at 14 TeV with theoretical uncertainties, the HTL/LME is computed using (SM HEFT), top running mass, LO, NLO and NNLO QCD corrections. The NLO and NNLO results are taken from the references cited in the table. The LO results are computed via a FORTRAN code.

with different μ_R and μ_F values ranging between:

$$\frac{M_{hh}}{4} \leq \mu_R/\mu_F \leq M_{hh} \tag{7.2}$$

As for the m_t renormalisation uncertainty, one uses the $\overline{\text{MS}}$ running of the top mass formula at N^{3}LO [324]

$$\overline{m_t}(m_t^{pole}) = m_t^{pole}\left(1 + \frac{4}{3\pi}\alpha_s(m_t^{pole}) + 10.9\frac{\alpha_s^2(m_t^{pole})}{\pi^2} + 107.11\frac{\alpha_s^3(m_t^{pole})}{\pi^3}\right)^{-3} \tag{7.3}$$

The total 14 TeV ggF hh, cross-section at different orders in computation with its uncertainties are shown in Table 7.1, which indicates that the uncertainties are dominated by the m_t renormalisation scheme of $\sim -18\%$ uncertainty in the lower envelope. This is significant part of the uncertainty budget and needs to be resolved by including N^{3}LO corrections to ggF hh, such corrections are available in the HTL [325, 326].

7.2 Other processes

Like the single Higgs production at hadron colliders, the production of Higgs pairs has the same subdominant channels VBF, di-Higgsstrahlung Vhh and associates production of Higgs pair with tops $t\bar{t}hh/tjhh$. Their cross-sections and uncertainties at 14 TeV are shown in Table 7.2, while in Figure 7.3 their cross-sections as a function of the centre-of-mass energy $\sqrt{s}$ is shown [260].

7.2.1 VBF hh

Vector boson fusion hh production has the second largest cross-section after ggF hh, which is calculated up to N^{3}LO [327–329] inclusively and differentially at NNLO [330]. The dominant diagrams are analigious to the single Higgs VBF, which involve the W/Z bosons exchanged in the $t-$channel. The process has the same topology as the -off shell-

Process	Cross-section 14 TeV (fb)	Theo. accuracy	Theo. uncertainty (%)	Contribution (%)
1. ggF hh	36.690	NNLO QCD	12.3	90.1
2. VBF hh	2.050	N³LO QCD	2.1	5.0
3. Zhh	0.415	NNLO QCD	3.6	1.0
4. W^+hh	0.369	NNLO QCD	2.1	0.9
5. W^-hh	0.198	NNLO QCD	3.0	0.5
6. tthh & tjhh	0.986	NLO QCD	5.1	2.4

Table 7.2. Summery of the Higgs pair production processes at 14 TeV LHC.

single Higgs VBF, with the off-shell Higgs giving two final states ones via the trilinear self-coupling.

7.2.2 Di-Higgsstrahlung

The associated production of Higgs pair with W and Z bosons has a small cross-section compared to ggF and VBF, this process is known up to NNLO QCD accuracy, which includes the gluon-fusion component in the full computation [331**?** , 332].

7.2.3 Associated Higgs pair production with t-quarks

Sometimes called the di-Higgs bremsstrahlung off top quarks [260], this channel has a steeper dependence on $\sqrt{s}$ than the single Higgs bremsstrahlung $t\bar{t}h$. One can see, for example, from Figure 7.3 that its cross-section becomes at roughly the same values as the VBF's. Only NLO computations for this channels have been carried out [333].
All of the three channels have a relatively small NLO correction, compared to gluon fusion. Which ranges from 10-30%.

7.3 Experimental overview for Higgs pair production

The search for Higgs pair production can be divided into two categories, resonant and non-resonant searches. The first searches for a heavy scalar or spin-2 resonance that decays into a Higgs pair. While the latter is concerned about the SM or if the new particle has a mass beyond the reach of the LHC, i.e. when the EFT limit is valid. In this review, I shall focus on the non-resonant searches, as these are the ones relevant to focus of this thesis, for detailed overview of the resonant searches, and non-resonant ones, see [260].
Figure 7.4 shows the current searches for non-resonant Higgs pair production by both ATLAS and CMS. The searches are summarised according to the final state:

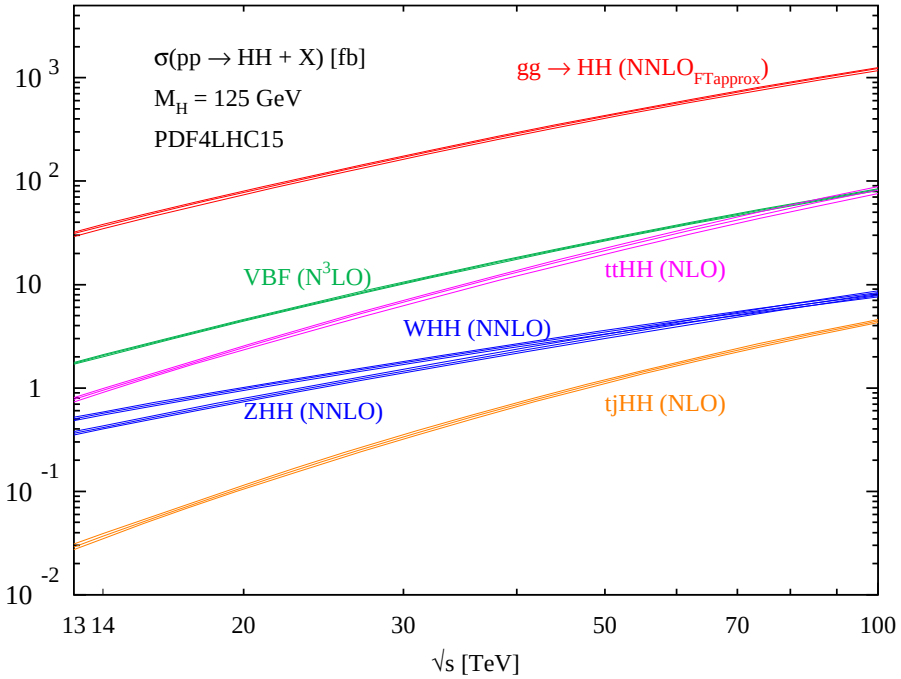

Figure 7.3. The cross-section of all di-Higgs processes at the highest available perturbation order as a function of centre-of-mass energy $\sqrt{s}$.The bands show the uncertainties without the top-mass renormalisation scheme. This plot is taken from [260].

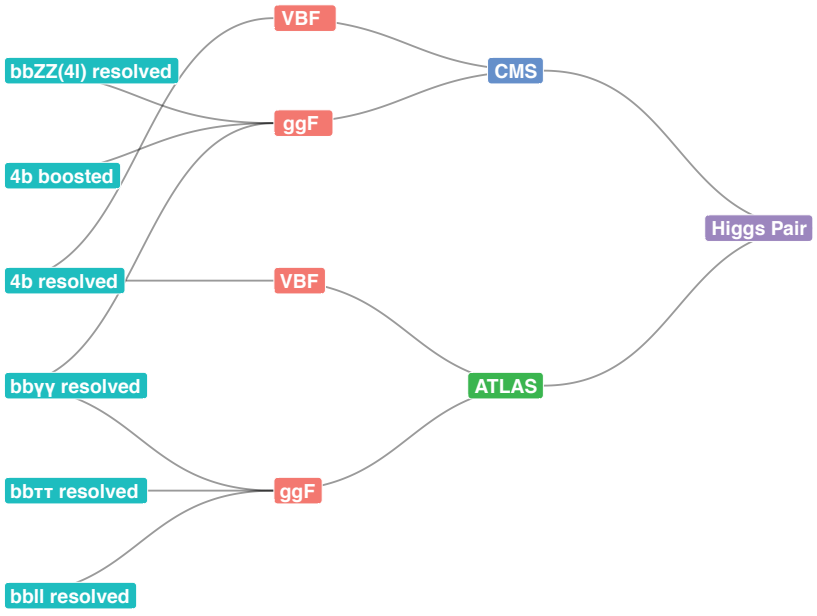

Figure 7.4. The non-resonant Higgs pair searches conducted by ATLAS and CMS using the full Run-II data.

$hh \to b\bar{b}b\bar{b}$

The final state $hh \to b\bar{b}b\bar{b}$ has the highest cross-section possible for Higgs pair, but poses a difficulty due to the large QCD background coming from production of 4 b-tagged jets. CMS [334] has used Boosted decision trees (BDT) for studying this final state for ggF and VBF channels, separated. This allowed for sinsitivity for the trilinear and $hhVV$ coupling. This analysis lead to 95% CL bounds on $\kappa_\lambda \in [-2.3; 9.4]$ and $\kappa_{2V} \in [-0.1; 2.2]$. They have also preformed boosted analysis for the VBF channel, by defining two large jets with jet radius of $\Delta R = 0.8$. This analysis is not sensitive to the trilinear self-coupling, but it is sensitive to both κ_V and κ_{2V}, which leads to the most stringent bound on the latter coupling modifier so far $\kappa_{2V} \in [0.6; 1.4]$. The $\kappa_{2V} = 0$ hypothesis is excluded with $p < 0.001$ [335]. On the other hand, ATLAS has preformed only a resolved analysis for this final state and only for the VBF production channel [336], hence they were able to only report bounds on $hhVV$ coupling $\kappa_{2V} \in [-0.43; 2.56]$.

$hh \to b\bar{b}VV$

ATLAS has considered the gluon fusion final state $hh \to b\bar{b}\ell\ell$, with the leptons coming from WW/ZZ decays [337]. This states covers around 90% of the total $hh \to b\bar{b}VV$ signal. Their analysis was divided into two categorise, same-flavour and different-flavour leptons. The observed signal strength were higher than the expected one. Hence, no bounds on the self-coupling could be extracted from this search. Similar analysis has been carried out by CMS, but with a requirement to observe four leptons instead of two, hence they searched for the final state$hh \to b\bar{b}(ZZ^* \to 4\ell)$. The 95% CL upper limit on the signal strength was 30 times the SM one, with bounds on Higgs self-coupling of $\kappa_\lambda \in [-9; 14]$ [338].

$hh \to b\bar{b}\tau\tau$

This channel has backgrounds coming from real τ's, such as $t\bar{t}$ and Zj with heavy jets. Also, fake τ's coming from QCD multijet process. A neural network has been used by ATLAS [339] for this channel's search, using resolved b jets. The extracted bounds on κ_λ are $[-2.4; 9.2]$.

$hh \to b\bar{b}\gamma\gamma$

This final is the most promising for Higgs pair searches and observation. Despite having a lower cross-section that the previous final states with BR of 0.27% in the SM, it has the highest selection efficiency. This is due to the low backgrounds and the ability to fully reconstruct the photons. The dominant non-reducible background is $b\bar{b}\gamma\gamma$ which has a cross-section of ~ 13fb at the 14 TeV LHC, more details about the backgrounds of this final states are stated in Table 7.3.

Both ATLAS and CMS have published searches of this channel using resolved b-jets and BDT and neural networks [258, 340]. With ATLAS reporting the strongest 95% CL

Channel	LO σ [fb]	NLO K-fact	$6\,\text{ab}^{-1}$ [#evt @ NLO]
$b\bar{b}h, y_b^2$	0.0648	1.5	583
$b\bar{b}h, y_b y_t$	-0.00829	1.9	-95
$b\bar{b}h, y_t^2$	0.123	2.5	1,840
Zh	0.0827	1.3	645
$\sum b\bar{b}h$	0.262	-	2,970
$b\bar{b}\gamma\gamma$	12.9	1.5	116,000
$t\bar{t}h$	1.156	1.2	6,938

Table 7.3. SM cross-section for the main background processes at 14 TeV with $6\,\text{ab}^{-1}$ data at the HL-LHC. For $b\bar{b}h$ production, the Higgs boson is decayed to a pair of photons. The total production of Higgs associated with $b\bar{b}$ is denoted by $\sum b\bar{b}h$ and is the sum of the top four channels.

bound on κ_λ yet, which was used in the comparisons in Figure 5.11. While CMS has reported bounds on κ_λ and κ_{2V} : $\kappa_\lambda \in [-3.3; 8.5]$ and $\kappa_{2V} \in [-1.3; 3.5]$.

7.3.1 Prospects for the HL-LHC

The highlight of the HL-LHC programme is the search for the Higgs pair production. It is projected that the Higgs pair signal to be observed at $\sim 4 - 4.5\sigma$ level. The use of machine learning techniques in the event analysis of hh searches will be a key factor in the potential discovery of this process [192]. In **??** the interpretable machine learning technology will be exploited in improving the sensitivity for hh signals at the HL-LHC. With the main focus on the $b\bar{b}\gamma\gamma$ final state. As this channel has the highest potential for discovery of di-Higgs production [327, 341–346]. The expected bounds on κ_λ at the HL-LHC for combined ATLAS and CMS is $\kappa_\lambda \in [0.1, 2.3]$ [192, 260]

7.4 Summary

The Higgs pair production is a missing key measurement of the SM, it is essential for the determination of the Higgs potential by directly constraining the Higgs trilinear self-coupling. Moreover, this channel is sensitive to non-linear couplings with the Higgs, like $hhVV$ and $hhf\overline{f}$. Due to the small cross-section of this channel, current searches obtain rather weak bounds on κ_λ that are comparable with the perturbative unitarity bounds [55]. Hence, the need for higher luminosity is imperative. Consequently, the HL-LHC is expected to result in an observation or even discovery of this process. Particularly with the help of advanced machine learning techniques.
The observation of Higgs pair production is expected to provide a direct measurement on one of the two " difficult" couplings of the Higgs, which is the trilinear self-coupling. However, as we shall explore in the upcoming chapters, it could also provide a window for observing the second difficult coupling discussed in the first chapter; the coupling between the Higgs and light quarks.

8 Higgs pair as a probe for light Yukawa couplings

The vast hierarchy of quark (and lepton) masses that we have seen in section 1.3 is one of the unsolved mysteries of the SM. One might wonder whether the Higgs is actually responsible for the light quarks masses or there exist other physics that interplays with the Higgs in generating the light quark mass terms. In fact, one of Weinberg's last papers was exactly addressing this question [347], in this paper he proposed that only the third generation fermions obtain their masses from Yukawa coupling, while the rest acquire theirs via loop-level interactions. Despite his models being only illustrative, his paper is a proof that even the pioneers of the SM theory still reflect upon this mystery. The pragmatic approach to unravelling this puzzle, is to directly measure the Higgs interaction with light fermions. Ideally, this would be via Higgs decay to first and second generation fermions. This is feasible for the muon case [104, 105] and rather challenging for the charm quarks [106–108] but almost impossible with the current technologies for the electron [348], strange and first generation quarks. Although, lepton colliders might have potential for *strange tagging* [349]. The difficulties here is twofold, first, the SM predicts that these couplings to be extremely small effectually making these decay channels vanishing even at few ab^{-1} luminosity. Additionally, even if NP would enhance the Higgs coupling to these fermions, the resolution of the LHC, would not be sufficient for reconstructing the Higgs from electron pairs, and it is not possible to distinguish up, down or gluon jets at the LHC form an overwhelming QCD background . This means that the search for these couplings ought to take a non-trivial path. Enhancements of light quark Yukawa couplings would open the tree-level quark anti-quark inhalation Higgs production channel $q\bar{q}$A, which is enhanced by the presence of light quarks in the PDF's. Moreover breaking the degeneracy amongst the strange up and down quarks, by having a *production tagging* coming form the different distributions of the PDF's amongst quark flavours. For sufficiently large enhancement of the light quark Yukawa couplings, this channel would even become dominant over the loop-induced gluon fusion, as seen in Figure 8.2. Working strictly in the SMEFT paradigm, the $q\bar{q}$A channel would contain a $hhq\bar{q}$ contact interaction illustrated in Figure 8.1, this interaction enhances the Higgs pair production more than the single Higgs $q\bar{q}$A, thus making Higgs pair production more sensitive to light quark Yukawa enhancement, as Figure 8.2 indicates.
Although the ggF Higgs pair production channel in SMEFT contains diagrams with contact $hhq\bar{q}$ interaction shown in Figure 8.3, the contribution of this diagram topology is suppressed by the kinematic mass of the quarks appearing inside the loops, hence the ggF channel is not affected by enhanced light quark Yukawa couplings in a significant way.

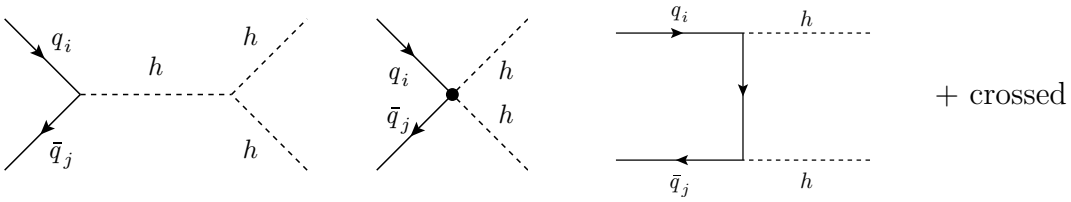

Figure 8.1. Feynman diagrams for the $q\bar{q}$A Higgs pair production in the SMEFT paradigm. The middle diagram shows a contact $hhq\bar{q}$ interaction, that contributes to significant enhancement of this channel compared to its single Higgs counterpart.

This chapter aims to exploit the potential for Higgs pair production as a direct measurement channel for light quark Yukawa. Focusing on the first generation quarks. I will start by introducing the inclusion of light quark couplings to the Higgs in the SMEFT framework in section 8.1. Then the NLO QCD calculation of the $q\bar{q}$A channel will be shown in section 8.2. section 8.4 will outline a cut-based analysis of the di-Higgs final state $b\bar{b}\gamma\gamma$ in order to estimate the sensitivity of this channel for the HL-LHC. Later, in section 8.5 an optimised approach for enhancing the sensitivity based on multi-variant analysis and interpretable machine learning will be showcased. The results of both analysis techniques will be discussed and compared in section 8.6 While in section 8.7 I will overview the other searches for light Yukawa couplings comparing it the Higgs pair production expected sensitivity. This chapter will be concluded in section 8.8.
The cut-based analysis has been published in [2], while the interpretable machine-learning one is an undergoing project with R. Gröber, C. Grojean, A. Paul, and Z. Qian.

8.1 SMEFT and light Yukawa couplings

Including the flavour indices ij of the SMEFT operators introduced in refs. [128, 133] and chapter 3, we would get light quark -Higgs coupling enhancement from the operators

$$\Delta\mathcal{L}_y = \frac{\phi^\dagger\phi}{\Lambda^2}\left(C^{ij}_{u\phi}\overline{Q}^i_L\tilde{\phi}u^j_R + C^{ij}_{d\phi}\overline{Q}^i_L\phi d^j_R + h.c.\right), \tag{8.1}$$

The mass matrices of the up- and down-type quarks obtained from the Yukawa and the new SMEFT coupling are

$$\begin{aligned} M^u_{ij} &= \frac{v}{\sqrt{2}}\left(y^u_{ij} - \frac{1}{2}(C_{u\phi})_{ij}\frac{v^2}{\Lambda^2}\right), \\ M^d_{ij} &= \frac{v}{\sqrt{2}}\left(y^d_{ij} - \frac{1}{2}(C_{d\phi})_{ij}\frac{v^2}{\Lambda^2}\right), \end{aligned} \tag{8.2}$$

where y^q_{ij} are the SM Yukawa matrix elements introduced in eq. (1.22). Since the quark masses are measured quantities, one would naturally rotate to the mass basis using bi-

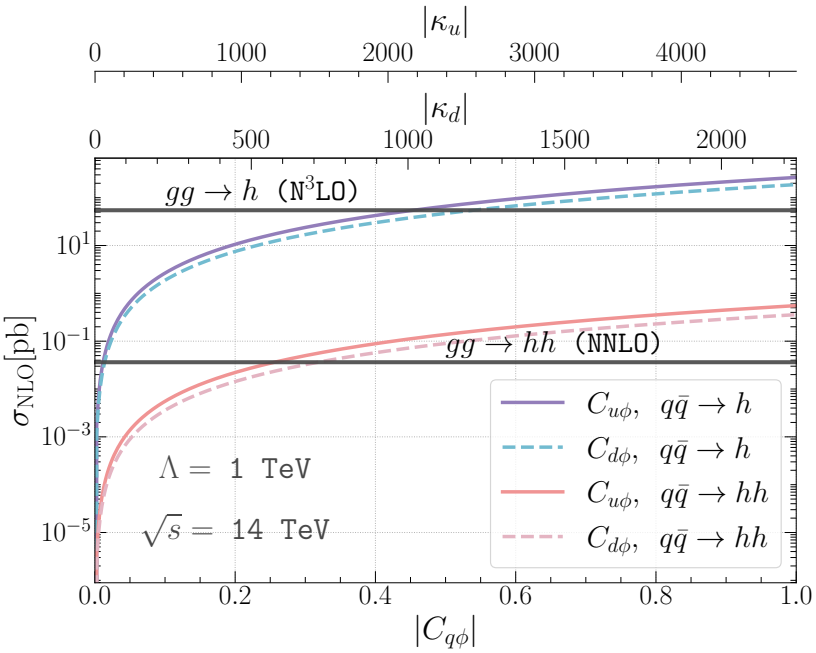

Figure 8.2. *The production cross-section of single Higgs and di-Higgs at* 14 *TeV from the quark anti-quark annihilation* $q\bar{q}A$ *as a function of the Wilson coefficients* $C_{u\phi}$ *and* $C_{d\phi}$ *versus the SM gluon fusion cross-sections (the horizontal solid line for* $gg \to h$ *and the dashed-dotted one for* $gg \to hh$*). One can observe that for values of* $C_{u\phi} = 0.22\,(0.43)$ *and* $C_{d\phi} = 0.26\,(0.47)$ *the* $q\bar{q}A$ *channel becomes the dominant di-Higgs (single Higgs) production channel. The UV scale is set to* $\Lambda = 1$ *TeV.*

unitary transformation represented by the matrices $\mathcal{V}_q, \mathcal{U}_q$, like in the SM. The Wilson coefficients matrix elements in the flavour space in the mass basis can be written as

$$\tilde{C}^{ij}_{q\phi} = (\mathcal{V}_q)^*_{ni}\, C^{nm}_{q\phi}\, (\mathcal{U}_q)_{mj}\,, \quad \text{with} \quad q = u, d\,. \tag{8.3}$$

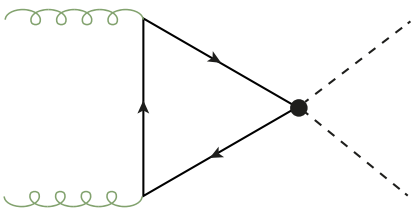

Figure 8.3. The new diagram for ggF emerging from the $hhq\bar{q}$ coupling stemming from an effective dim-6 operator.

n order to match these Wilson coefficients to Higgs couplings to quarks, we use the Lagrangian operator describing these couplings

$$\mathcal{L} \supset g_{h\bar{q}_i q_j}\bar{q}_i q_j h + g_{h\bar{q}_i q_j}\bar{q}_i q_j h^2 \tag{8.4}$$

Then the matching results in identifying the SMEFT couplings of Higgs and quarks

$$g_{h\bar{q}_i q_j} := \quad \frac{m_{q_i}}{v}\delta_{ij} - \frac{v^2}{\Lambda^2}\frac{\tilde{C}^{ij}_{q\phi}}{\sqrt{2}}, \qquad\qquad g_{hh\bar{q}_i q_j} := \quad -\frac{3}{2\sqrt{2}}\frac{v}{\Lambda^2}\tilde{C}^{ij}_{q\phi}. \tag{8.5}$$

We observe that, in the general case, we will be having non-diagonal couplings. However, such couplings are strongly constraint by flavour observables , particularly neutral meson mixing [350].

$$|\tilde{C}^{12}_{q\phi}| \lesssim 10^{-5}\Lambda^2/v^2| \qquad\qquad |\tilde{C}^{13/23}_{d\phi}| \lesssim 10^{-4}\Lambda^2/v^2 \tag{8.6}$$

Due to these strong constraints, it is typical to consider SMEFT with minimal flavour violation (MFV) [351], in which the SM Yukawa matrices y_q^{ij} are the only spurions breaking the global $SU(3)_Q \otimes SU(3)_U \otimes SU(3)_D \to U^6(1)$ flavour symmetry. This implies that the Wilson coefficients matrices in the mass basis are simultaneously diagonalisable with the SM Yukawa matrices. This make the Wilson coefficients maintain the hierarchy of the couplings seen in the SM, thus MFV is not a viable scheme when one wants to consider significant enhancements to the couplings for first and second generations, but keep the third generation couplings unchanged.

In order to bypass the constraints of MFV and yet avoid flavour changing neutral currents (FCNC) that are prohibited by flavour observables, one needs to turn to flavour alignment [352, 353] or its generalisation aligned flavour violation (AFV) [354] .

With flavour alignment, the NP flavour parameters (here the Wilson coefficients) are aligned with the SM Yukawa, such that both can be simultaneously diagonalised, hence preventing tree-level FCNCs. But unlike MFV, the constraint on making these new parameters proportional to the SM Yukawas is lifted. This would induce radiative FCNCs, as this formalism in unstable under quantum corrections [355–357]. This alignment breaking would not be seen in the SMEFT, but rather when UV-complete models are considered. AFV resolves this instability, by ensuring that any NP Spurion breaking the flavour symmetry will transform trivially under the quark phases transformations $U^6(1)$, keeping the CKM matrix as the only flavour object that has non-trivial transformations. Thereby the CKM will have physical flavour changing currents as well as a $\mathcal{CP}$-violating phase. This constraint on the NP flavour spurions k_q, allows them to be written as a series in powers of the CKM matrix, known as the alignment expansion

$$k_u = K_{0,u} + K_{1,u}V^*_{CKM}K_{2,u}V^T_{CKM}K_{3,u} + \mathcal{O}(V^4_{CKM}) + \dots, \tag{8.7}$$

$$(k_d)^\dagger = K_{0,d} + K_{1,d}V^T_{CKM}K_{2,d}V^*_{CKM}K_{3,d} + \mathcal{O}(V^4_{CKM}) + \dots, \tag{8.8}$$

where $K_{i,u}$ and $K_{i,d}$ are complex 3×3 diagonal matrices invariant under flavour transformations. This formalism is stable under renormalisation group evolution as any linear

combinations or tensor product of the spurions will remain flavour aligned.
For simplicity, I shall only consider the first term in the alignment expansion, such that only diagonal $C_{q\phi}$ are investigated, as the other terms are already CKM-suppressed and not of particular phenomenological interest. With this in mind, and using the translation between SMEFT and κ-formalism discussed in subsection 3.2.2, it is possible to identify the couplings in SMEFT with the κ's

$$g_{h\bar{q}_i q_i} = \kappa_q g^{\text{SM}}_{h\bar{q}_i q_i}\,, \qquad\qquad g_{hh\bar{q}_i q_i} = -\frac{3}{2}\frac{1-\kappa_q}{v} g^{\text{SM}}_{h\bar{q}_i q_i}\,, \tag{8.9}$$

in a slight abuse of language of the κ-framework used often in experimental analyses, as the $hhq\bar{q}$ coupling also depends on the light quarks coupling modifier κ_q.

Higgs pair production offers an extra advantage for probing light Yukawa interactions, as it is particularly sensitive to the $hhq\bar{q}$ interaction, one could also consider the non-linear HEFT, by extending it to include Wilson coefficients c_q and c_{qq} for the first and second generation quarks, in analogy to ones defined for the top quark in eq. (3.14) [358]. The analysis preformed on these HEFT parameters is published in [2].

8.2 Higgs pair production and Higgs decays with modified light Yukawa couplings

As we have briefly discussed in the introduction, the gluon fusion channel Higgs pair production is affected by enhanced light Yukawa couplings in two ways. First, the inclusion of light quark loops in the triangle and box diagrams. Second, the new diagrams introduced by the contact $hhq\bar{q}$ coupling shown in Figure 8.3. However, these effects are negligible, due to the mass-suppression of these diagrams by the light quark appearing in the loops. Therefore, effectively, one could consider the ggF channel as purely derived by third generation quarks, and only affected by the trilinear coupling C_ϕ as far as this analysis is concerned.

8.2.1 Higgs pair production via quark anti-quark annihilation

Contrary to the ggF, the $q\bar{q}$A channel does not exist in the SM, except for $b\bar{b} \to hh$, following the assumptions of 4(or 5)-flavour scheme, that the these quarks are massless. This channel contains four-diagrams shown in Figure 8.1, and its differential partonic cross-section is given by

$$\frac{d\hat{\sigma}_{q_i\bar{q}_j}}{d\hat{t}} = \frac{1}{16\pi}\frac{1}{12\hat{s}}\left[\left|2g_{hhq_i\bar{q}_j} + \frac{g_{hhh}\, g_{hq_i\bar{q}_j}}{\hat{s} - m_h^2 - i m_h \Gamma_h}\right|^2 + \mathcal{O}(g^4_{hq_i\bar{q}_j})\right], \tag{8.10}$$

where the $\mathcal{O}(g^4_{hq_i\bar{q}_j})$ terms stem from the $\hat{t}$ and $\hat{u}$ channel diagrams, and their contribution is typically only $\sim 0.1\%$ of the total cross-section. The hadronic cross section is then

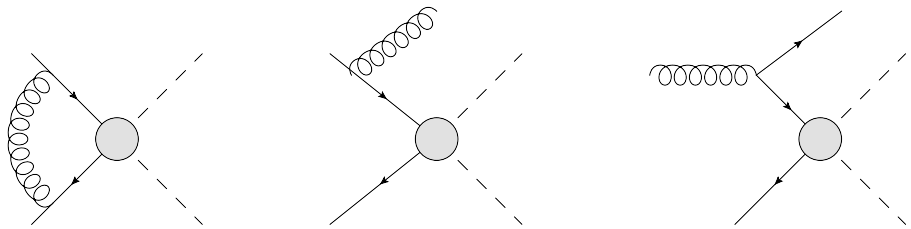

Figure 8.4. Generic form of the QCD corrections of order $\mathcal{O}(\alpha_s)$ to the $q\bar{q}$A Higgs pair production.

obtained by

$$\sigma_{\text{hadronic}} = \int_{\tau_0}^{1} d\tau \int_{\hat{t}_-}^{\hat{t}_+} d\hat{t} \sum_{i,j} \frac{d\mathcal{L}^{q_i\bar{q}_j}}{d\tau} \frac{d\hat{\sigma}_{q_i\bar{q}_j}}{d\hat{t}} \,, \tag{8.11}$$

with $\tau_0 = 4\,m_h^2/s$, $\hat{s} = \tau s$ and

$$\hat{t}_\pm = m_h^2 - \frac{\hat{s}(1 \mp \beta)}{2} \qquad \text{and} \qquad \beta = \sqrt{1 - \frac{4m_h^2}{\hat{s}}} \,. \tag{8.12}$$

The parton luminosity is given by

$$\frac{d\mathcal{L}^{q_i\bar{q}_j}}{d\tau} = \int_{\tau}^{1} \frac{dx}{x} \left[f_{q_i}(x/\tau, \mu_F^2) f_{\bar{q}_j}(x, \mu_F^2) + f_{\bar{q}_j}(x/\tau, \mu_F^2) f_{q_i}(x, \mu_F^2) \right] . \tag{8.13}$$

All the kinematic masses were neglected, in accordance with the 5-flavour scheme of the PDF's while the coupling of the Higgs boson to the light quarks (for flavour diagonal couplings) is

$$g_{hq_i\bar{q}_j} = \frac{m_q^{\overline{MS}}(\mu_R)}{v} \kappa_q \delta_{ij} \,, \tag{8.14}$$

and analogously for the $g_{hhq_i\bar{q}_j}$ coupling. It is worth noting that there is no inconsistency with such an assumption since in scenarios of modified Yukawa couplings, the masses of the quarks need not to be generated by electroweak symmetry breaking.

NLO QCD correction

Since the ggF NLO QCD corrections are sizeable, it is reasonable to assume that the same would apply to the $q\bar{q}$A. Computing the NLO QCD corrections to this channel is a relatively straight-forward task, as they are only one-loop. More simplifications can be made by neglecting the NLO corrections of the $\hat{t}$ and $\hat{u}$ channels because they are strongly suppressed. This enables us to use the NLO QCD corrections results from $b\bar{b} \to h$ in the 5-flavour scheme [359–361][1] by some adjustments taking into account the modified LO cross section and the different kinematics of the process. The Feynman diagrams at NLO QCD are shown in fig. 8.4. For convenience and in order to make our

[1] Note that the NLO and NNLO QCD corrections for $b\bar{b}hh$ have been given in [362, 363].

adjustments explicit we report here the formulae from [364]

$$\sigma(q\bar{q} \to h) = \sigma_{LO} + \Delta\sigma_{q\bar{q}} + \Delta\sigma_{qg} \tag{8.15a}$$

$$\Delta\sigma_{q\bar{q}} = \frac{\alpha_s(\mu_R)}{\pi} \int_{\tau_0}^1 d\tau \sum_q \frac{d\mathcal{L}^{q\bar{q}}}{d\tau} \int_\tau^1 dz\ \hat{\sigma}_{LO}(Q^2 = z\tau s)\ \omega_{q\bar{q}}(z) \tag{8.15b}$$

$$\Delta\sigma_{qg} = \frac{\alpha_s(\mu_R)}{\pi} \int_{\tau_0}^1 d\tau \sum_{q,\bar{q}} \frac{d\mathcal{L}^{qg}}{d\tau} \int_\tau^1 dz\ \hat{\sigma}_{LO}(Q^2 = z\tau s)\ \omega_{qg}(z) \tag{8.15c}$$

and

$$\hat{\sigma}_{LO}(Q^2) = \int_{\hat{t}_-}^{\hat{t}_+} \frac{d\hat{\sigma}_{q_i\bar{q}_j}}{d\hat{t}} \tag{8.16}$$

with $z = \tau_0/\tau$, $\sigma_{LO} = \sigma_{\text{hadronic}}$ of eq. (8.11), and the ω factors are given by

$$\omega_{q\bar{q}}(z) = -P_{qq}(z) \ln\frac{\mu_F^2}{\tau s} + \frac{4}{3}\left\{\left(2\zeta_2 - 1 + \frac{3}{2}\ln\frac{\mu_R^2}{M_{hh}^2}\right)\delta(1-z)\right. \tag{8.17a}$$
$$\left. + (1+z^2)\left[2\mathcal{D}_1(z) - \frac{\ln z}{1-z}\right] + 1 - z\right\},$$

$$\omega_{qg}(z) = -\frac{1}{2}P_{qg}(z)\ln\left(\frac{\mu_F^2}{(1-z)^2\tau s}\right) - \frac{1}{8}(1-z)(3-7z), \tag{8.17b}$$

with $\zeta_2 = \frac{\pi^2}{6}$. The Altarelli Parisi splitting functions $P_{qq}(z)$ and $P_{qg}(z)$ [365–367] are given by

$$P_{qq}(z) = \frac{4}{3}\left[2\mathcal{D}_0(z) - 1 - z + \frac{3}{2}\delta(1-z)\right], \tag{8.18a}$$

$$P_{qg} = \frac{1}{2}\left[z^2 + (1-z)^2\right], \tag{8.18b}$$

and the 'plus' distribution is

$$\mathcal{D}_n(z) := \left(\frac{\ln(1-z)^n}{1-z}\right)_+. \tag{8.19}$$

The renormalisation scale $\mu_R = M_{hh}$ and the factorisation scale $\mu_F = M_{hh}/4$, were chosen as central values.
The NLO $q\bar{q}$A cross-section as well as the LO ggF were implemented in a private FORTRAN code utilising the `VEGAS` integration algorithm, and NNPDF30 parton distribution functions (PDF's)[368] implemented via the `LHAPDF-6` package [369]. For the one-loop integrals appearing in the form factors of the box and triangle diagrams, we have used the Collier library [370] to ensure numerical stability of the loop integral calculation

for massless quarks inside the loops [2]. The resulting NLO K-factor was found to be

$$K_{NLO} = \frac{\sigma_{NLO}}{\sigma_{LO}} = 1.28 \pm 0.02\,, \tag{8.20}$$

with the error denoting the theoretical uncertainty. The K-factor does not depend on the scaling of the couplings, nor the flavour of the initial $q\bar{q}$ since the LO cross section factors out (with exception of the different integration in the real contributions).
The $q\bar{q}$A channel will enhance the overall Higgs pair production cross-section, but if one considers the ggF as a SM background for the Yukawa enhancement "signal" $q\bar{q}$A channel, it would be interesting to estimate qualitatively when this signal becomes dominant. This estimates how sensitive is Higgs pair to enhanced light Yukawa couplings as **??** demonstrates. The dominant term for $q\bar{q}$A comes from the $hhq\bar{q}$ vertex diagram, such that the $q\bar{q}$A cross-section behaves for large values of κ as (assuming that $\sigma_{SM}^{qqA} \sim 0$)

$$(\sigma^{qqA} - \sigma_{SM}^{qqA}) \sim g_{hhq\bar{q}}^2 \sim v^{-4}\, m_q^2\, \kappa_q^2. \tag{8.21}$$

The ggF cross-section instead gets contributions from light quark loops interfering with top quark loops in the triangle SM diagram, leading to a scaling of

$$(\sigma^{ggF} - \sigma_{SM}^{ggF}) \sim \kappa_q\, \frac{m_q^2}{v^2\, M_{hh}^2}\, \ln^2\left(\frac{M_{hh}}{m_q}\right). \tag{8.22}$$

Taking the ratio we get

$$\frac{(\sigma^{qqA} - \sigma_{SM}^{qqA})}{(\sigma^{ggF} - \sigma_{SM}^{ggF})} \sim \frac{\kappa_q}{v^2\left(\frac{\ln^2\left(\frac{M_{hh}}{m_q}\right)}{M_{hh}^2}\right)}. \tag{8.23}$$

This ratio approaches one (neglecting effects from different PDFs) when

$$\kappa_q^{qqA=ggF} \sim \frac{v^2\, \ln^2\left(\frac{M_{hh}}{m_q}\right)}{M_{hh}^2}\,. \tag{8.24}$$

Using this order of magnitude estimate, we see that the two cross sections are roughly equal if $\kappa_c^{qqA=ggF} \sim 1$, $\kappa_s^{qqA=ggF} \sim 10$ and $\kappa_u^{qqA=ggF} \sim \kappa_d^{qqA=ggF} \sim 10^3$. The actual values of $\kappa_q^{qqA=ggF}$ for the first generation quarks can be read from fig. **??**.It is interesting to point out to the pact that these κ_q values are not yet excluded.

8.2.2 Higgs decays

The same way hh production squires additional channels due to enhanced Yukawa couplings, also Higgs decays to light quarks will become significant compared to the SM

[2] I have expanded code to include other SMEFT operators, and it can be found in the `GitHub` repository `https://github.com/alasfar-lina/HH_XS_in_SMEFT`

case with Higgs decays to first generation BR'S being $< \mathcal{O}(10^{-9})$ [321]. In addition to the contribution of light quarks in the loop-level decays $h \to \gamma\gamma/Z\gamma$ and $h \to gg$, though this effect is small. Since the $h \to q\bar{q}$ decay are near impossible to detect with the current technologies, the effect of opening these decay channels is reduction in the branching ratios of the Higgs final states that are typically sought after, like $h \to b\bar{b}$ and $h \to \gamma\gamma$.
In order to compute the Higgs partial widths and branching ratios (BR) at higher orders in QCD, I have modified the FORTRAN programme `HDECAY` [371, 372] to include the light fermion decay channels and loops in the above-mentioned decays [3]. The overall change of the Higgs total width is given by

$$\Gamma_H \approx \Gamma_{\text{SM}} + \sum_{q=c,s,u,d} \frac{g^2_{h\bar{q}_i q_i}}{(g^{\text{SM}}_{h\bar{q}_i q_i})^2} \Gamma_q \,, \tag{8.25}$$

where Γ_q can be obtained at NLO QCD from the modified `HDECAY` code. Detailed results for the Branching ratios for the final states of interest have been published in [2]. In order to have a preliminary estimate about the sensitivity of Higgs pair production to light Yukawa enhancements, it is important to consider both production and decay effects in terms of signal strength

$$\mu_i := \frac{\sigma \, \text{BR}_i}{\sigma^{\text{SM}} \, \text{BR}^{\text{SM}}_i}. \tag{8.26}$$

Comparing the production of single Higgs vs. Higgs pair signal strengths, for any final state of interest, we could see in Figure 8.5 that for first generation $C_{q\phi} \lesssim 0.8$ Higgs pair production has a higher signal strength than single-Higgs production despite having double the reduction in the signal strength from the decays of two Higgs bosons as opposed to a single one. In fact, and as we shall see in section 8.7, values of $C_{q\phi} > 0.4$ have been already excluded by multiple searches.

8.3 Event generation for the final state $hh \to b\bar{b}\gamma\gamma$

For this study, the final state $b\bar{b}\gamma\gamma$ is considered, as this channel has the most potential for Higgs pair searches [192]. It has the "clean" $h \to \gamma\gamma$ decay, but also the other Higgs decay to b-quark pair is a channel with large branching ratio $\sim 58\%$ and b-tagging capabilities for ATLAS and CMS are continuously improving.

For the cut-based analysis, the FORTRAN codes used to compute the hh cross-section and decay have been interfaced with `Pythia` 6.4 [373], where the $q\bar{q}$A process was generated at NLO and the ggF at NLO, then multiplied with the NLO k-factor. The generated events were written to a ROOT file via `RootTuple` tool [374] for further

[3] The modified `HDECAY` code can be found in the `GitHub` repository `https://github.com/alasfar-lina/hdecay_lightflavour`

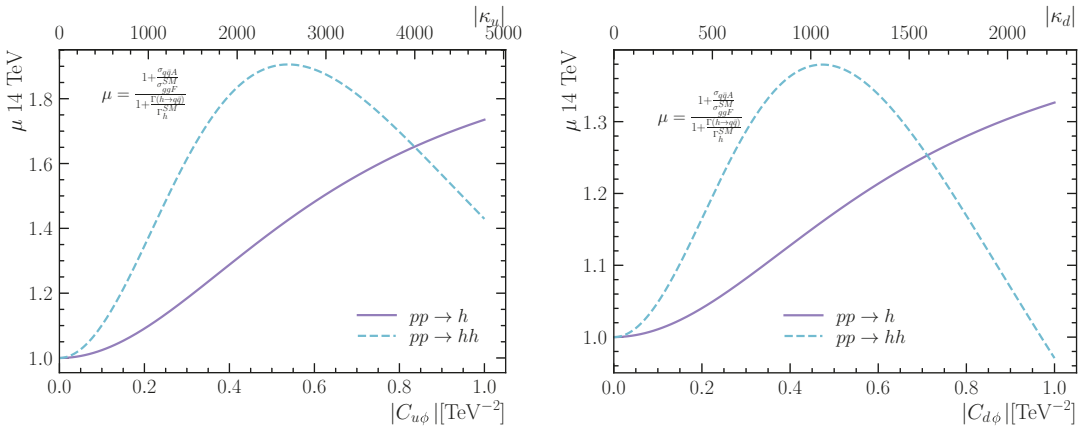

Figure 8.5. Signal strength at 14 TeV LHC, of the single Higgs (purple solid line) vs. Higgs pair (blue dashed line) as functions of $C_{u\phi}$ (left) and $C_{d\phi}$ (right). Both plots show that for $C_{q\phi} \lesssim 0.8$ the signal strength of Higgs pair production is higher than the single Higgs one. This implies that Higgs pair production is more sensitive to enhancements of light quark Yukawa in SMEFT. This is independent of the final state (except for $h \to q\bar{q}$).

analysis.
The backgrounds were not simulated for this analysis, rather, the results from [341] were used, because we have used the same cuts as this reference.

For the improved analysis which is based on interpretable BDT, the backgrounds and signal events needed to be generated. The backgrounds described in Table 7.3 were generated using `MadGraph_aMC@NLO` [225], then showered via `Pythia 8.3` [375] and a detector simulation is done using `Delphes 3` [376], the QED/QCD background $b\bar{b}\gamma\gamma$, Zh and $b\bar{b}h$ events were taken from the analysis data of Ref. [377], while $t\bar{t}h$ events were generated specifically for this analysis.In order to obtain the NLO cross-section for these process, the events were multiplied by their respective K-factors that have been obtained from $t\bar{t}h$ [378], $b\bar{b}\gamma\gamma$ [379], Zh [380] and the remaining part of the $b\bar{b}h$ processes from [381].
The Higgs pair signals were generated in a slightly different pipeline, the ggF channel events were simulated first using `POWHEG` [158, 314, 315], which has been modified to separate the individual contributions from the box, triangle and their interference individually. This is done in order to easily scale by κ_λ (or C_ϕ), as the box does not depend on it, while the triangle and the interference have quadratic and linear dependence on the trilinear coupling, respectively. The $q\bar{q}$A channel events were generated via `MadGraph_aMC@NLO` using a UFO model created with `FeynRules` [241]. Samples for both up- and down-quark initiated $q\bar{q}$A processes have been generated. Parton showering and fast detector simulation for both Higgs pair processes were run thorough the same pipeline as the backgrounds, this also goes for the scaling by the NLO of $q\bar{q}$A and NNLO for ggF K-factors after the event generation. The Higgs bosons were decayed with the assumption of narrow width approximation, and the BR values were computed

Channel	LO σ [fb]	K-fact.	Order	$6\,\text{ab}^{-1}$ [#evt @ order]
$hh^{gg\text{F}}_{\text{tri}}$	$7.288 \cdot 10^{-3}$	2.28	NNLO	96
$hh^{gg\text{F}}_{\text{box}}$	0.054	1.98		680
$hh^{gg\text{F}}_{\text{int}}$	-0.036	2.15		-460
$u\bar{u}\text{A}$ $(C_{d\phi} = 0.1)$	2.753	1.29	NLO	28
$d\bar{d}\text{A}$ $(C_{u\phi} = 0.1)$	4.270	1.30		43

Table 8.1. The LO cross-section for Higgs pair production processes (including the decay $hh \to b\bar{b}\gamma\gamma$) for $6\,\text{ab}^{-1}$ 14 TeV HL-LHC.

in the modified `HDECAY` code.
To be inclusive and to explore the capabilities and importance of the full detector coverage, no generator-level cuts were applied on these processes except for the $b\bar{b}\gamma\gamma$ processes to avoid divergences. These minimal generator-level cuts for $b\bar{b}\gamma\gamma$ are

$$\text{generator level cuts:} \quad \begin{aligned} & Xp_T^b > 20 \text{ GeV}, \\ & \eta_\gamma < 4.2,\ \Delta R_{b\gamma} > 0.2, \\ & 100 < m_{\gamma\gamma}\,(\text{GeV}) < 150. \end{aligned} \tag{8.27}$$

Here Xp_T implies a minimum p_T cut for at least one b-jet. After the showering and detector simulation, further basic selection cuts were applied to select events with

$$\text{basic cuts:} \quad \begin{aligned} & n_{\text{eff}}^{bjet} \geq 1,\ n_{eff}^{\gamma jet} \geq 2, \\ & p_T^{bjet} > 30 \text{ GeV},\ p_T^{\gamma jet} > 5 \text{ GeV}, \\ & \eta_{bjet,\gamma jet} < 4,\ 110 \text{ GeV} < m_{\gamma_1\gamma_2} < 140 \text{ GeV}, \end{aligned} \tag{8.28}$$

and $n_{eff}^{b/\gamma jet}$ representing the number of b/γ-jets that pass the basic selection. The cross-section, K-factors, number of events with 6ab^{-1} luminosity at 14 TeV are given in Table 7.3 for the background and in Table 8.1 for the Higgs pair signals. Both analysis methods included sensitivity analysis for the HL-LHC, i.e. 14 TeV and $6\,\text{ab}^{-1}$ [4] luminosity and projections for a future hadron circular collider (FCC-hh), with 100 TeV and the luminosity of 30 ab^{-1} has been done for the ML based analysis, the results for the FCC can be foun in the **??**

8.4 Cut-based analysis

A cut and count analysis has been preformed mainly as a "proof of concept", in order to demonstrate the sensitivity of Higgs pair production for probing light quark Yukawa couplings. The analysis used the same cuts and m_{hh} binning as ref. [341] such that their

[4] In the published cut-based analysis [2] $3\,\text{ab}^{-1}$ luminosity for the HL-LHC was used. However, here I used $6\,\text{ab}^{-1}$ when reporting fit results

background events counts can be used.

8.4.1 Analysis strategy

In order to derive sensitivity bounds, the number of expected background N_b and signal N_s events needs to be estimated from simulated events. Since N_b is taken from [341], the task is to estimate N_s for the $q\bar{q}$A process as a function of $C_{q\phi}$, and to reproduce N_s of the ggF SM process published in the reference as a cross-check.
Since the cross-section, branching fraction and the integrated luminosity, it is only needed to estimate the selection efficiency ϵ_{SEL} from the applied cuts appearing in eq (2.1) to obtain the number of signal events.
The basic cuts of trigger-level selection are jets and photons with minimal p_T and maximal η.

$$p_T(\gamma/j) > 25\,\text{GeV}\,, \quad |\eta(\gamma/j)| < 2.5\,. \tag{8.29}$$

Additionally, a veto on the events with hard leptons is applied

$$p_T(\ell) > 20\,\text{GeV}, \quad |\eta(\ell)| < 2.5\,, \tag{8.30}$$

Jets were clustered using `fastjet` [382] with the anti-kt algorithm with a radius parameter of $R = 0.5$.
The b-tagging efficiency of $\epsilon_b = 0.7$, as well as the photon identification efficiency $\epsilon_\gamma = 0.8$ have been simulated, in accordance with the ATLAS and CMS performance [383–385, 385, 386]. The selection cuts we used are the same ones as in [341], starting with the cuts of the transverse momentum p_T of the photons and b-tagged jets. The two hardest photons/b-tagged jets, with transverse momentum $p_{T>}$, and the softer ones with $p_{T<}$ are selected to satisfy

$$p_{T>}(b/\gamma) > 50\,\text{GeV}, \quad \text{and} \quad p_{T<}(b/\gamma) > 30\,\text{GeV}\,. \tag{8.31}$$

In order to ensure well-separation of the photons and b-jets, we require the following cuts on the jet radius,

$$\Delta R(b,b) < 2, \quad \Delta R(\gamma,\gamma) < 2, \quad \Delta R(b,\gamma) > 1.5\,. \tag{8.32}$$

The mass windows used used are about three times the photon resolution of ATLAS and CMS [385, 386], such wide windows were used in order to avoid significant signal loss.

$$105\,\text{GeV} < m_{b\bar{b}} < 145\,\text{GeV}, \quad 123\,\text{GeV} < m_{\gamma\gamma} < 130\,\text{GeV}\,. \tag{8.33}$$

The selection cuts are summarised in table Table 8.2 with their corresponding efficiency. The total selection efficiency for the ggF channel was found to be $\epsilon_{ggF} = 0.044$, consistent with the results of [341], while the $q\bar{q}$A channel efficiency is slightly higher $\epsilon_{qq} = 0.05 \pm 0.001$ for the up and down quark initiated $q\bar{q}$A, results for second generation quarks can be found in [2].

cut	ϵ_{cut}	$\delta\epsilon_{\text{cut}}$
Trigger-level in eq. (8.29) and (8.30)	0.71	0.04
p_T cuts in eq. (8.31)	0.35	0.07
ΔR cuts in eq. (8.32)	0.69	0.21
total	0.11	0.06

Table 8.2. The cuts used in the analysis with their efficiency ϵ_{cut} and uncertainties on these efficiencies $\delta\epsilon_{\text{cut}} = \sqrt{\epsilon(1-\epsilon)\,N}$, where N is the total number of events. The analysis was performed on 100K SM simulated events. This table is published in [2].

8.4.2 Statistical analysis

The likelihood ratio test statistic q_μ was used in order to estimate the HL-LHC sensitivity, and set projected limits on the SMEFT Wilson coefficients $C_{q\phi}$, with and without the modifier of the trilinear coupling C_ϕ. Additionally to the HEFT parameters c_q and c_{qq}. The likelihood function was constructed from the signal and background events in each bin of the m_{hh} distribution described in [341]

$$-\ln \mathscr{L}(\mu) = \sum_{i\in\text{bins}} (N_{bi} + \mu\, N_{si}) - n_i \,\ln(N_{bi} + \mu\, N_{si}), \tag{8.34}$$

with N_{bi} and N_{si} being the number of background and signal events in the ith m_{hh} distribution, respectively. In order to include the theoretical uncertainties on the expected number of signal events, the above likelihood was extended by a Gaussian distribution for N_{si} in which the mean equals to the central value of the bin values and standard deviation σ equals to its theoretical uncertainty. The signal strength μ was then estimated by minimising $-\ln \mathscr{L}(\mu)$ to obtain the estimator for $\hat{\mu}$ by injecting SM signal + background events n_i. The test statistic is then given by

$$q_\mu = 2(\ln \mathscr{L}(\mu) - \ln \mathscr{L}(\hat{\mu})), \tag{8.35}$$

following the procedure described in [387], and using the Python package `pyhf` [388, 389]. The expected 6 ab^{-1}HL-LHC sensitivity for the signal strength at 95% (68 %) CL is found to be $\mu = 1.5(1.1)$.

8.5 Optimised search for Higgs pair via Interpretable machine learning

When dealing with a multi-variate problem, such as the separation of the Higgs pair signal from its backgrounds, the use of "simple" cuts is not the most efficient method for accomplishing this task. This is mainly due to the fact that in multivariate analysis, the various features used in the classification correlate with each other. This is not captured with the cut and count method. With boasted decision tree (BDT) classifier,

it is possible to capture these correlations and introduce highly non-trivial cuts .

8.5.1 Constructing features

The simulated events of the signal and background described in the event selection section are required to contain at least two reconstructed photons and at a b-tagged jet. From these events, the following high-level features were constructed

- $p_T^{b_1}$, $p_T^{b_2}$, $p_T^{\gamma_1}$, $p_T^{\gamma\gamma}$,
- $\eta_{b_{j1}}$, $\eta_{b_{j2}}$, η_{γ_1}, $\eta_{\gamma\gamma}$,
- n_{bjet}, n_{jet}, $\Delta R^{b\gamma}_{\text{min}}$, $\Delta\varphi^{bb}_{\text{min}}$,
- $m_{\gamma\gamma}$, m_{bb}, $m_{b_1 h}$, $m_{b\bar{b}h}$, H_T.

$p_T^{b/\gamma_{1,2}}$ and $\eta^{b/\gamma_{1,2}}$ are the p_T and pseudorapidity for the tagged leading and sub-leading b/γ-jets (in our definition the subleading b-jet could be a null four-vector since we require one b-jet inclusive), n_{bj} is the number of tagged and passed b-jets. $\Delta R^{b\gamma}_{\text{min}}$ and $\Delta\varphi^{bb}_{\text{min}}$ are the minimum R-distance and φ-angle between a tagged b-jet and a photon jet. The remaining variables are the invariant masses and H_T is the scalar sum of the transverse mass of the system.
These features are the same as the ones studied in ref.. [377] for $b\bar{b}h$. However, they are, by no means, unique. It is possible to run the analysis with another set of features and obtain the same results, as long as these features are independent and highly correlated. Figure 8.6 shows the distributions four most important features from this list, the $m_{\gamma\gamma}$ is very important in distinguishing the large $b\bar{b}\gamma\gamma$ background from the signal and $t\bar{t}h$ (or other background that contain $h \to \gamma\gamma$). While the rest, particularly H_T distinguishes the different hh channels and also hh from other Higgs channels backgrounds.

8.5.2 Exploratory network analysis

The aim of this analysis is to explore how the kinematic variables constructed in the previous section are related to each other. Moreover, we are interested in examining their variation from channel to channel. This can be achieved by calculating the intra-feature correlations stratified according to the signal channels (ggF, $u\bar{u}$A, ddA) and background. Then draw them as network diagrams that can be seen in (a) of Figure 8.7. The Pearson's correlation networks show some differences amongst the different signal strata.[5]. These differences can be further investigated by a post-hoc hypothesis test, based on a linear mixed effects model for each pair of the features X_i, X_j stratified according to the processes (ggF, $u\bar{u}$A, $d\bar{d}$A and background) S_k, given as follows

$$X_i = \beta_{ij} X_j + \beta_k S_k + \beta_0, \tag{8.36}$$

[5] for network plots of the backgrounds see [377]

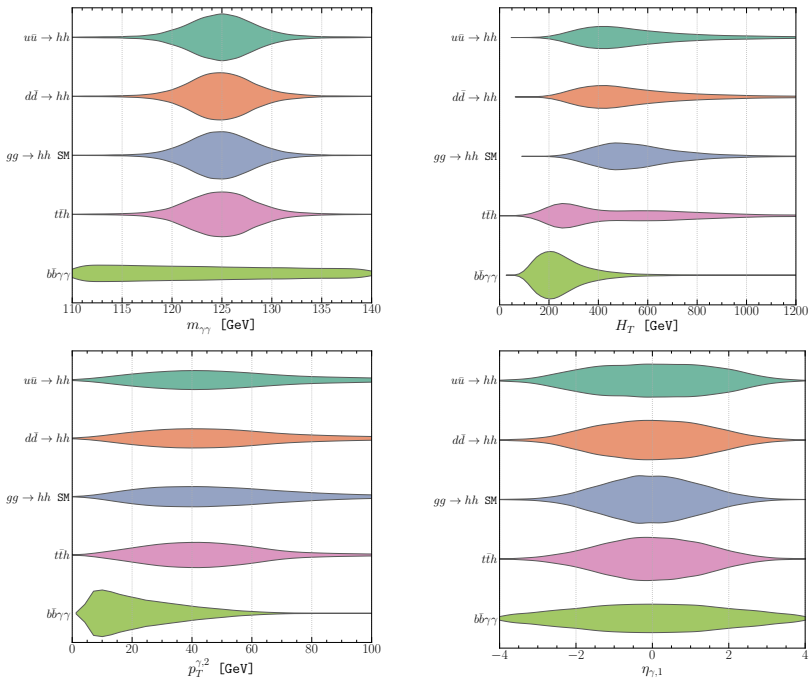

Figure 8.6. violin plots of the most significant features used by the BDT classifier for the signal channels, and the two most significant backgrounds $b\bar{b}\gamma\gamma$.

where β_{ij}, β_k and β_0 are the constants for the fit . The hypothesis test is therefore preformed by taking the ratio of log likelihood for the linear model of eq. (8.36), defined as

$$t = \frac{\mathscr{L}(\beta_{ij}, \beta_k, \beta_0)}{\mathscr{L}(\beta_{ij}, \beta_k = 0, \beta_0)}. \tag{8.37}$$

This analysis of variation (ANOVA) yields a p-value for each feature pair, these p-values are false discovery rate (FDR)-corrected, and the correlation difference amongst the strata is considered significant if the FDR-corrected p-values pass the threshold $p < 0.001$ or $p > 0.01$ when comparing $u\bar{u}$A against $d\bar{d}$A [6]. The result of these comparisons can be seen in sub-figures (b). We can see that many of the features do not have significant variation across the strata.This indicates that these features are not important in the separation of the signal from the background. The most significant variation is between the ggF (equivalently $q\bar{q}$A) and the background. While for the $q\bar{q}$A channels, the correlation patters are almost identical except for the correlation between the observables related to the PDF's, which is expected since the only kinematic difference between the up- and down- initiated $q\bar{q}$A emerges from the PDF's of the up and down quarks.

[6] The threshold for this comparison is related due to the high degree of similarity between the two channels.

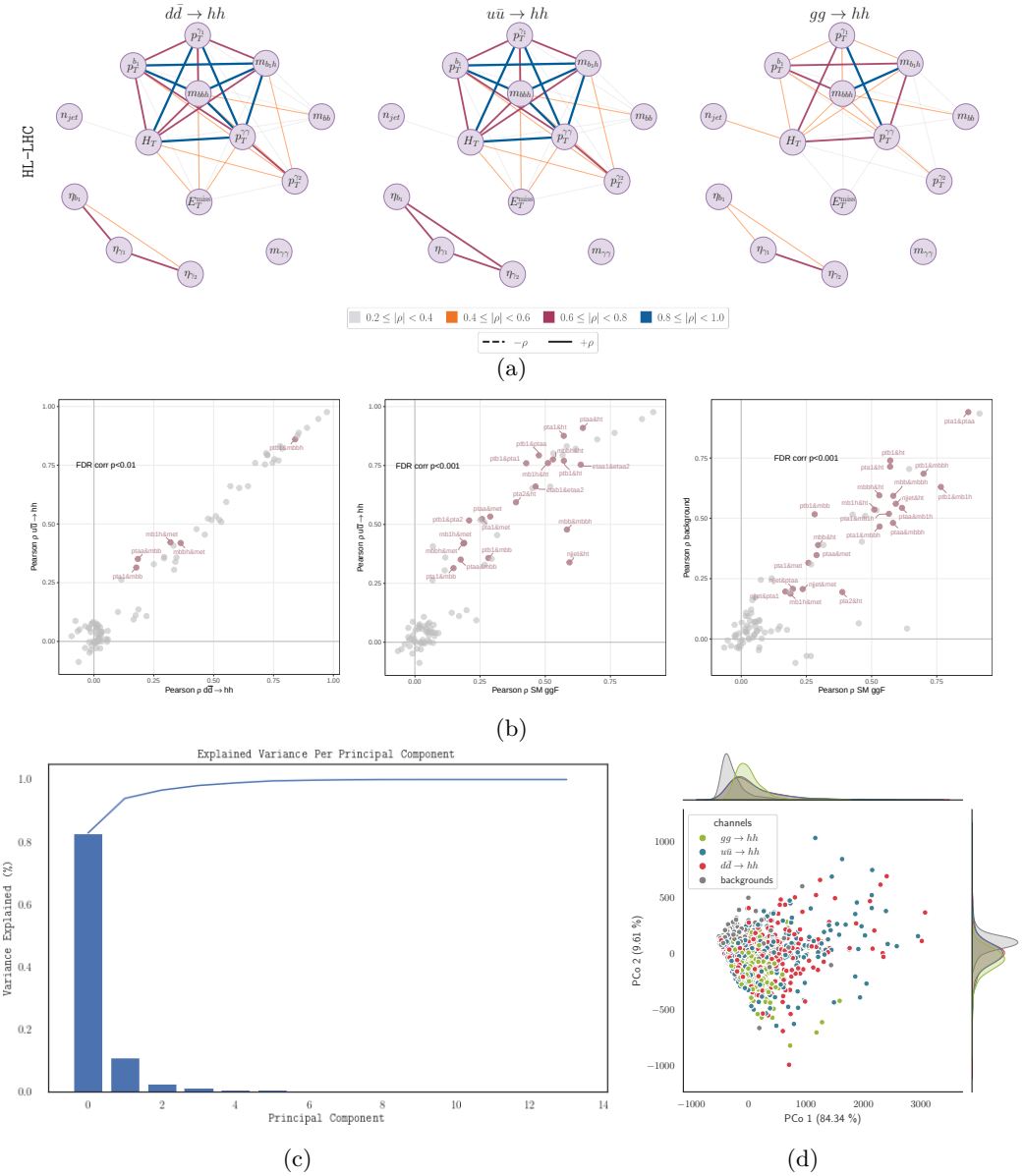

Figure 8.7. (a) Network diagrams of the signal channels of their Pearson correlation ρ between the features, showing slightly different patterns of correlation amongst these channels. (b) The same Pearson correlations of figure (a) plotted against each other for the different signals, with the colouring indicating whether the difference between the correlation passes the hypothesis testing (ANOVA) passes the threshold FDR-corrected p-value indicated at each figure. (c) Scree plot of the Principal-component clustering (PCo) of the the signal channels and the backgrounds, almost full variance coverage is obtained by the first four PCo's .(d) The clustering in the first two PCo's, one can see that even with unsupervised clustering the di-Higgs signals have a significantly different distribution than the background. However, it is hard to see an marked clustering for the different signal channels.

This network analysis allows for better understanding of the feature set at hand. When considering that many intra-feature correlations do not vary much across the channels as seen in (b) of Figure 8.7 and the features themselves cluster into four groups according to their correlations, it is tempting to further reduce the dimensionality of the feature space by preforming an unsupervised clustering via Principle Component analysis (PCoA). Panel (c) in Figure 8.7 contains a scree plot showing that the variance explained by the first few PCo's is very high, thus reducing the dimensionality of our feature space significantly. When the first two PCo's are plotted (d), the clustering of signal and the background channels can be seen. The distinction between the signals vs. backgrounds is visible, but less marked between the signal channel themselves, in particular $u\overline{u}$A against $d\overline{d}$A . The first PCo contains, from highest weight to lowest, $m_{\gamma\gamma}, H_T, n_{jet}, m_{bb}$ and $p_T^{\gamma_1}$. The rest of the of features have a negligible weight.
It is not surprising to see these feature contribute the most in the clustering of events given how they are distributed as we have seen in Figure 8.6. In the next step of the analysis we will see then appear once more.

8.5.3 Classification analysis

The unsupervised clustering and network analysis merely offers a method to explore how the Higgs pair signal is different from the backgrounds. It is useful to reduce the dimensionality of the feature space and offer "hints" on which subset of features has the highest discriminant power. However, for analysis of the sensitivity and full resolution of the signal against backgrounds, the gold standard is rule-based machine learning. The use of BDT's and random forests in particle physics analysis has been explored since early LHC era, nowadays it became widespread, their popularity becomes evident when one examines the literature-review of this thesis for instance. Many of the recent Higgs experimental analyses were preformed using some rule-based ML algorithm. [7]
In this analysis, the EXtreme gradient BDT (XGBoost), with its Python implementation [390], has been used as the classifier algorithm. The standard procedure for training and testing the classifier was followed, starting with the complete list of features listed in subsection 8.5.1 and then the most important features were shortlisted to improve the efficiency and performance of the classifier. This was possible due to the introduction of interpretability to the ML analysis, which provided variable importance measures, by which features with low importance index can be removed.
Interpretability is achieved by incorporating a mathematically robust measure from game theory known as **Shapley values** [391]. This measure formulate an axiomatic prescription for fairly distributing the payoff of a game amongst the players in a n-player cooperative game. When applied to ML, Shapley values estimate the significance of the features used in the classification. The process naturally and mathematically lends itself to examining the correlations amongst the features used in the classification, since all possible combinations of variables can be taken out of the game to check the outcome.

[7] Rule-based ML algorithms outperform deep neural networks in terms of simplicity of implementation and computational requirements. In addition, rule-based algorithms, such as decision trees, are more transparent as far as the signal vs. background separation is concerned

Actual no. of events	Predicted no. of events at HL-LHC					
Channel	hh^{ggF}_{tri}	hh^{ggF}_{tri}	hh^{ggF}_{box}	$Q\overline{Q}h$	$b\bar{b}\gamma\gamma$	total
hh^{ggF}_{tri}	28	14	18	38	10	108
hh^{ggF}_{int}	89	80	129	178	41	517
hh^{ggF}_{box}	77	105	266	265	50	763
$Q\overline{Q}h$	177	98	191	5,457	1,835	7,758
$b\bar{b}\gamma\gamma$	1,743	845	1,074	30,849	287,280	321,791

Table 8.3. The confusion matrix output of the trained BDT five-channel classifier. The separation between the ggF topologies allows for setting constraints on C_ϕ. The number of events shown are for the HL-LHC at 14 TeV and integrated luminosity of 6 ab^{-1}, assuming the SM signal.

Further information regarding the application of Shapley values in particle physics analysis can be found in refs. [377, 392, 393]. For Higgs pair production study presented here, the same procedure described in [377] was followed, The importance of a variable in determining the outcome of a classification will be quantified by the mean of the absolute Shapley value, $\overline{|S_v|}$, larger values signifying higher importance. The SHAP (SHapley Additive exPlanations) [394] package implemented in Python was used. This package computes the feature importance using Shapley values calculated exactly from tree-explainers [395, 396].

Classifier output

The trained BDT's outputs are extracted in terms of confusion matrices, with number of events as entries. The diagonal elements of these matrices represent the true positive (TP) identification of the signal and true negative (TN) rejection of the background, while the upper triangular part represents the signal loss, or false negative counts (FN) . Finally the lower triangular part shows the remaining background contamination of the signal, or the false positive counts (FP). Using these counts it is possible to estimate the accuracy score ACC of the classifiers

$$ACC = \frac{TP + TN}{TP + TN + FP + FN} \approx 0.7, \tag{8.38}$$

And the sensitivity $TP/P \approx 0.2$, which corresponds to the ϵ_{SEL} of the cut-based analysis. Here we see that the ML- based analysis yielded a four- to five-fold increase in ϵ_{SEL} compared to the cut and count method. Table 8.3 shows one of these matrices from the classification of the ggF SM signal separated into the topologies according to their dependence on C_ϕ. For up- and down-quark $q\bar{q}$A, the same matrices were constructed, and sense the number of events for these processes scale with $C^2_{q\phi}$ it is only required to produce one matrices for each classification procedure, like the case of the ggF channel. For the fitting procedure, a Bayesian framework based on an MCMC method was used, analogous to the procedure described in section 5.2
The full analysis code, including the BDT training and fits as well as the confusion ma-

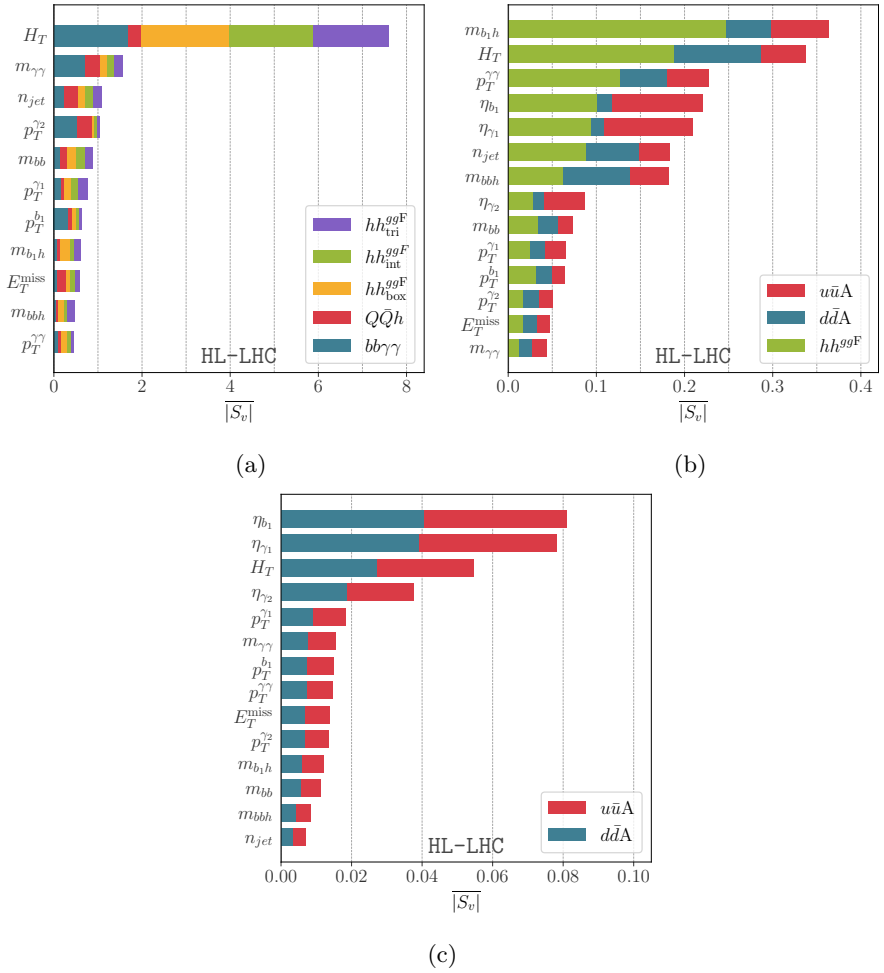

Figure 8.8. The feature importance output in terms of $\overline{|S_v|}$. The higher the value of $\overline{|S_v|}$, the more important the kinematic variable is in separating the different channels : (a) The hierarchy of variables important for the separation of hh^{ggF}_{tri} from hh^{ggF}_{int} events from hh^{ggF}_{box}, $Q\overline{Q}h$ and $b\bar{b}\gamma\gamma$ QCD-QED background (b) The hierarchy of variables important for the separation of hh^{ggF}, $u\bar{u}$A and $d\bar{d}$A events. (c) The hierarchy of variables important for the separation of $u\bar{u}$A from $d\bar{d}$A events.

trices for the classification procedures preformed can be found in the `Github` repository: https://github.com/talismanbrandi/IML-diHiggs.git.

Feature importance and Shapley values

Another output of the interpretable BDT is the SHAP scores for the features used in the classification. The $\overline{|S_v|}$ values are used to order the features used for the classification. The most important features in different classifiers used in this analysis is seen in Figure 8.8. Panel (a) shows the hierarchy of the features used for the separation of the SM ggF signal from the backgrounds, the same features that showed the most

significant change in the network analysis and unsupervised clustering appear in the top of the list. However, the BDT was able to distinguish between the the different signals, a task the unsupervised clustering was unable to fulfil. Figure (b) shows the list of feature importance for the ggF vs $q\bar{q}$A classification, while (c) demonstrates the full strength of the BDT in distinguishing $u\bar{u}$A from $d\bar{d}$A despite having very little variation of their kinematic distributions. As expected, $u\bar{u}$A vs $d\bar{d}$A classification, the features appeared on top of the list, are related to the different PDF's but their ranking was unintuitive because this classification is a truly a multivariate problem, where the intra-variable correlations and differences have been fully extorted.

8.6 Fit results

The fit from the cut-bases analysis was originally made for $3\,\text{ab}^{-1}$ and published in [2], but for a better comparison with the optimised multi-variate analysis the fit for this thesis was carried out again for $6\,\text{ab}^{-1}$, and with SMEFT Wilson coefficient parametrisation. Thus harmonising it with the results of the rest of the thesis. The fits were done in the $C_\phi - C_{q\phi}$ plane shown the top plots of Figure 8.9. As well as the $C_{u\phi} - C_{d\phi}$ one in the low panel of the same figure. We see that even with the traditional technique, two-parameter fits were possible. However, the bounds obtained on the trilinear self-coupling modifier are weaker than the projected bounds for the HL-LHC, made by ATLAS and CMS [93, 290, 397], which is expected due to the dilution of these bounds by adding Light Yukawa coupling modifiers and the loss of some signal due to the analysis technique. For the $C_{u\phi} - C_{d\phi}$ combined fit, no correlation between the two parameters is seen.
To demonstrate the power of multi-variate (MV) analysis, we compare the fit results from single parameter fits of this analysis to the cut-and count technique (CC) for both up and down quark coupling modifiers at 68% CL/CI

$$\begin{aligned} C_{u\phi}^{MV}\left(\kappa_u^{MV}\right) &= [-0.09, 0.10]\ ([-466, 454]), \quad C_{u\phi}^{CC}(\kappa_u^{CC}) = [-0.18, 0.17]\ ([-841, 820]), \\ C_{d\phi}^{MV}(\kappa_d^{MV}) &= [-0.16, 0.16]\ ([-360, 360]), \quad C_{d\phi}^{CC}(\kappa_d^{CC}) = [-0.18, 0.18]\ ([-405, 405]). \end{aligned} \tag{8.39}$$

A significant improvement of the bounds from using MV analysis over CC one of two-fold for $C_{u\phi}$, but a mild one for $C_{d\phi}$ with $\mathcal{O}(10\%)$ improvement.

In order to compare the ML multi-variate analysis used to other sensitivity projections, the projections on the trilinear coupling modifier C_ϕ are shown in Figure 8.10. These bounds are obtained by using the we pe BDT classification showcased in Table 8.3. These bounds are similar or slightly better than the results quoted by the experimental sensitivity analysis quoted before. This was achieved by optimising the BDT with spearating the signal and background channels, as well as the exclusion of less-important features. The projected 1σ bound on C_ϕ is $[-1.57, 1.00]$ at HL-LHC. Another advantage of the optimised multi-variate analysis is the ability to preform two-parameter fits in the

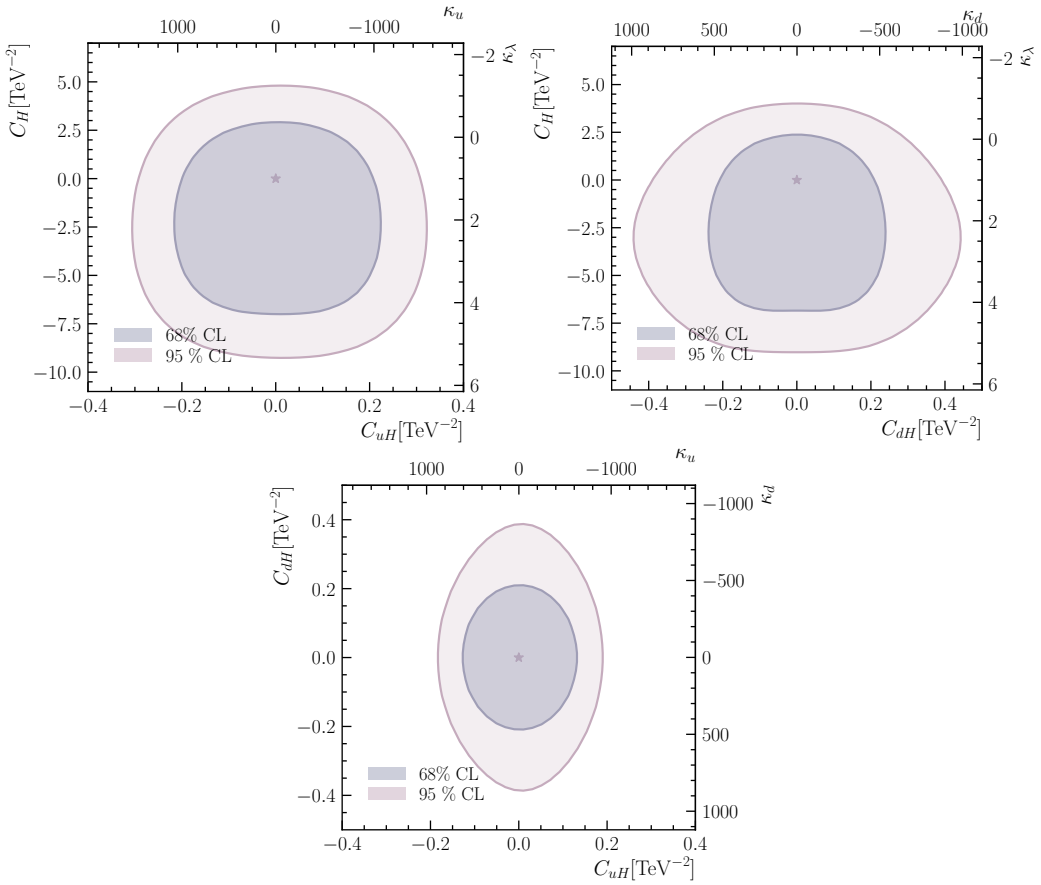

Figure 8.9. The 68% and 95% CL contours of the constraints on up and down Yukawa coupling modifiers as well as C_ϕ from two-parameter fits using the results of the cut-based analysis for the HL-LHC at 14 TeV and $6\mathrm{ab}^{-1}$ integrated luminosity.

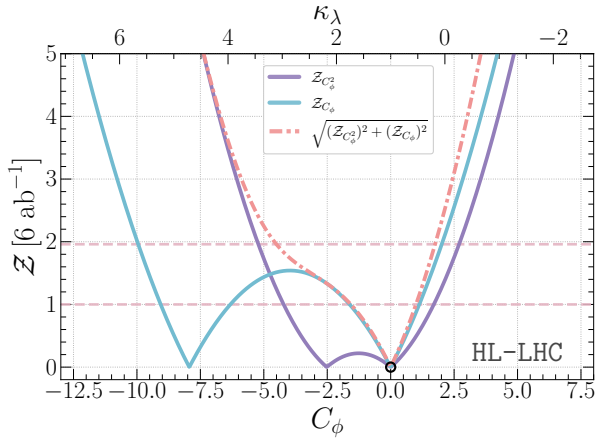

Figure 8.10. Bounds on C_ϕ (or κ_λ) at the HL-LHC from single parameter fit. The solid blue lines are the constraints coming from the hh^{ggF}_{int} contribution which scales linearly with the modified coupling and the solid purple line is that from the hh^{ggF}_{tri} contribution that scales quadratically with the modified coupling. The red dashed line is the combination of the quadratic and linear channel. The horizontal light red dashed lines marks the 68% and 95%CI's.

same planes described above, shown in Figure 8.11 while maintaining the improvement over the cut-based one. Since the BDT training was able to achieve sufficient accuracy for seven-channel classifier, including up and down $q\bar{q}$A, the three ggF topologies and the backgrounds. It was possible to resolve all of the signal channels strata and their parametric dependence on the three Wilson coefficients $C_{u\phi}$, $C_{d\phi}$ and C_ϕ. A three-parameter fit is possible without degeneracies, as seen in Figure 8.12. However, the posterior distribution of the three-parameter fit show no marked correlations amongst the Wilson coefficients. In both two- and three-parameter fits degeneracy in the $C_{d\phi}$ direction is observed at 99.7$ CI. This due to the reduction of the Higgs pair signal when the $h \to d\bar{d}$ decay channel is opened, particularly for high values of this Wilson coefficient as highlighted by Figure 8.5. In fact, when this analysis is applied for the strange quark, the overall effect of enhanced strange quark is a reduction in the $b\bar{b}\gamma\gamma$ signal, making this Higgs pair final state insensitive to strange Yukawa enhancements, more details on this were discussed in [2]. Comparing with the constraints on C_ϕ from a single parameter fit in Figure 8.10, it can be seen from the two- and three-parameter fits in Figure 8.11 and Figure 8.12, respectively, that, the constraints on C_ϕ become diluted when the light-quark Yukawa coupling modifiers $C_{q\phi}$ are taken into an account. This effect is somewhat more prominent for $C_{d\phi}$ than for $C_{u\phi}$ and stems from the fact that away from $C_{u\phi,d\phi} = 0$ larger negative values of C_ϕ are allowed by the crescent shaped curves of the HDP contours. The bounds on $C_{u\phi}$ and $C_{d\phi}$ from the fit with two-parameters including C_ϕ remain the same as the bounds on these Wilson coefficient from the single parameter $C_{u\phi,d\phi}$ fits. The fit results are summarised in Table 8.4.

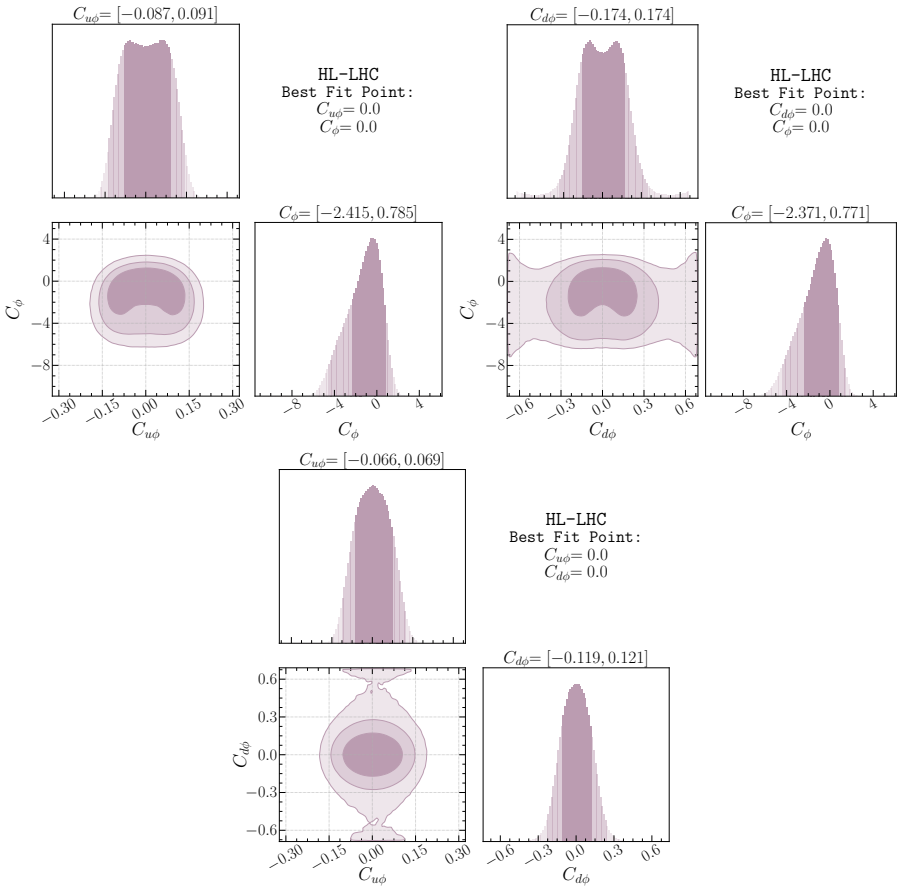

Figure 8.11. The 68%, 95% and 99.7% HDP contours, for Bayesian fits preformed on pairs of Wilson coefficients for C_ϕ, $C_{u\phi}$ and $C_{d\phi}$ form the multi-variate analysis output.

Operators	$C_{u\phi}$	$C_{d\phi}$	C_ϕ	κ_u	κ_d	κ_λ
HL-LHC 14 TeV 6 ab^{-1} @ 68% CI						
$\mathcal{O}_\phi$	–	–	[-1.57, 1.00]	–	–	[0.53, 1.73]
$\mathcal{O}_{u\phi}$	[-0.09, 0.10]	–	–	[-477, 431]	–	–
$\mathcal{O}_{d\phi}$	–	[-0.16, 0.16]	–	–	[-360, 360]	–
$\mathcal{O}_{u\phi}$ & $\mathcal{O}_\phi$	[-0.087, 0.091]	–	[-2.42, 0.79]	[-434, 417]	–	[0.63, 2.13]
$\mathcal{O}_{d\phi}$ & $\mathcal{O}_\phi$	–	[-0.17, 0.17]	[-2.73, 0.77]	–	[-381, 379]	[0.63, 2.27]
$\mathcal{O}_{u\phi}$ & $\mathcal{O}_{d\phi}$	[-0.065, 0.069]	[-0.12, 0.12]	–	[-331, 312]	[-268, 272]	–
All	[-0.077, 0.084]	[-0.160, 0.162]	[-2.77, 0.43]	[-400, 369]	[-362, 359]	[0.79, 2.30]

Table 8.4. Summary of the 68% projected bounds on $C_{u\phi}$, $C_{d\phi}$ and C_ϕ from single-, two- and three-parameter fits for HL-LHC with 6 ab^{-1} of data and FCC-hh with 30 ab^{-1} of data. The corresponding bounds on the rescaling of the effective couplings, κ_u, κ_d and κ_λ are presented on the right side of the table.

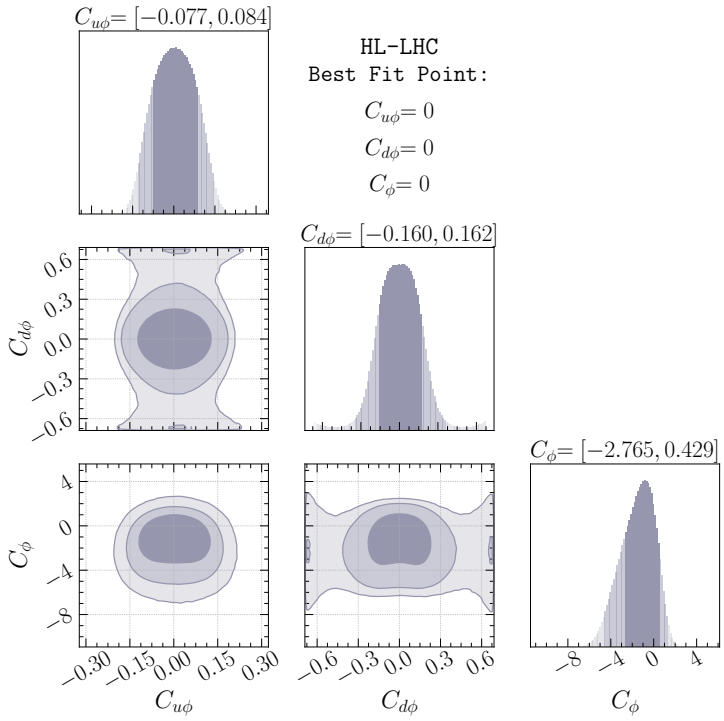

Figure 8.12. Three parameter Bayesian fits with $C_{u\phi}$, $C_{d\phi}$ and C_{ϕ}, the HDP contours are the same as Figure 8.11 .

8.7 Overview of Light Yukawa searches

There are additional measurements of the light-quark Yukawa couplings that might become relevant at HL-LHC or FCC-hh, a careful study of which is beyond the scope of the current work. Yet we attempt to include a discussion here, so as to provide a comparison with our study and to put it into proper context, or to serve as proposal for further studies. The channel $pp \to h+j$ has been suggested as a probe for charm Yukawa coupling [398] with charm-tagged jet having a potential bound of $\kappa_c \sim 1$ for the HL-LHC, depending on the charm-tagging scheme. This process could be used for the first and second generations Yukawa couplings by looking at the shapes of kinematic distributions, the most important one being the p_T distribution [399–401]. The expected HL-LHC 95% CL bounds are $\kappa_c \in [-0.6, 3.0]$, $|\kappa_u| \lesssim 170$ and $|\kappa_d| \lesssim 990$. The use of $h + j$ process along with other single Higgs processes have also been suggested as indirect probes for Higgs self coupling [114–118, 120], due to the contribution of the trilinear coupling to NLO electroweak corrections to these processes. In addition, experimental fits have been carried out for the trilinear coupling from single Higgs observables [148, 402].

It seems that for the HL-LHC, an optimal bound for the trilinear coupling can be obtained by combing both the data from single-Higgs process as well as Higgs pair production [147], with 68% CL bound on $\kappa_\lambda \in [0.1, 2.3]$, compared to the expected

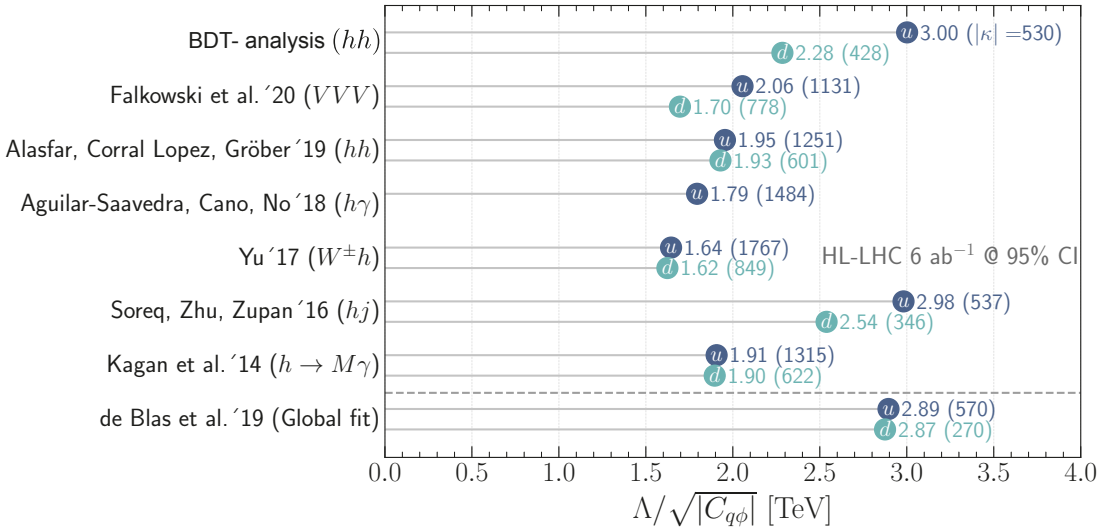

Figure 8.13. Summary of the 95% CI/CL sensitivity bounds on the SMEFT Wilson coefficients $C_{u\phi}$ (blue), and $C_{d\phi}$ (green). The bounds are interpreted in terms of the NP scale Λ that can be reached through the measurements of the Wilson coefficient at the HL-LHC at 6 ab^{-1}, the corresponding κ_q's are shown inside the parentheses. Single parameter fit 95% CI bounds are used from this analysis for comparison with previous studies.

bound of $\kappa_\lambda \in [0.0, 2.5] \cup [4.9, 7.4]$ coming from using di-Higgs measurements alone. Moreover, single Higgs processes, namely Zh and $W^{\pm}h$ production, could also be useful in probing charm-Yukawa coupling using a mixture of b- and c-tagging schemes leveraging the mistagging probability of c-jets as b-jets in b-tagging working points, and vice-versa, in order to break the degeneracy in the signal strength [403]. The use of this technique could probe $\kappa_c \sim 1$ in the FCC-hh. Of course, for the charm-Yukawa coupling, the constraints are set to improve significantly, as there has been recent direct observation of $h \to c\bar{c}$ [106]. Therefore, from here on, we will mainly concentrate on the process with more potential for constraining Yukawa couplings of the first generation quarks.

Rare Higgs decays to mesons, $h \to M + V$, $M = \Upsilon, J/\Psi, \phi \ldots$, were also suggested as a probe for light-quark Yukawa couplings [404–406], and there have been experimental searches for these decays [106, 407] with bounds on the branching ratios, $\mathcal{B}(h \to X, \gamma,\ X = \Upsilon, J/\Psi,) \sim 10^{-4} - 10^{-6}$ at 95% CL. It was shown in Ref. [408], that the charge asymmetry of the process $pp \to hW^+$ vs $pp \to hW^-$ can be used as a probe for light-quark Yukawa couplings as well as to break the degeneracy amongst quark flavours. Moreover, the rare process $pp \to h\gamma$ is also a possible way to distinguish between enhancements of the up- and down-Yukawa couplings [409] where the authors have estimated the bounds on the up-Yukawa coupling of $\kappa_u \sim 2000$ at the HL-LHC. Despite some processes appearing more sensitive than others, one should think of these processes as complementary to each other.

One of the main features of the effective couplings $hhq\bar{q}$ and $hhhq\bar{q}$ emerging from SMEFT operator $\mathcal{O}_{q\phi}$, or the Chiral Lagrangian for that matter, is that these couplings

are either free from propagator suppression for $hhq\bar{q}$ or scale with energy for $hhhq\bar{q}$ while being safe from strong unitarity constraints. This feature gives processes with multiple Higgs and/or vector bosons $V = W^{\pm}, Z$ an advantage in constraining $\mathcal{O}_{q\phi}$. The latter constrains come from the longitudinal degrees of freedom of the gauge bosons which can be understood from the Goldstone boson equivalence theorem. The use of the final state VV as a probe for $\mathcal{O}_{q\phi}$ is difficult due to the large SM background. However, the three-boson final state VVV was shown to give strong projected bounds for light-quark Yukawa couplings for HL-LHC with 95% CL bounds on $\kappa_u \sim 1600$, and $\kappa_d \sim 1100$. A ten fold improvement is expected at FCC-hh [410] with bounds of order $\kappa_d \sim 30$. Higgs pair production has a smaller SM background compared to VV production, but it has a significantly smaller cross section too, even when compared to VVV, as the latter process has already been observed at the LHC [411, 412].

On the contrary, Higgs pair production is inaccessible with the runs I-III of the LHC, but it is potentially accessible at the HL-LHC [413] having a $\sigma \cdot BR \sim 1\text{fb}^{-1}$. However, Higgs pair production, particularly the channel $h \to b\bar{b}\gamma\gamma$, is of significant interest as it has unique features. The first being the ability to constrain the trilinear and light-quark Yukawa couplings simultaneously, as we have already seen in the previous sections. Secondly, Higgs pair production could probe non-linear relations between Yukawa interaction and $hhq\bar{q}$ couplings [414]. Lastly, Higgs pair production is expected to be significant enhanced in certain models involving modification of light-quark Yukawa couplings (cf. [415–417])

For future colliders, like the FCC-hh at 100 TeV, in addition to Higgs pair production triple Higgs production might be an interesting channel for constraining the operators with Wilson coefficient $C_{u\phi}$ and $C_{d\phi}$ due to the energy increase of a Feynman diagram coupling the quarks to three Higgs bosons. In this case, a similar study to ours should be performed to see whether also in this case it will be important to do a combined fit on the light quark Yukawa couplings together with the trilinear and quartic Higgs self-couplings.[8] Finally, it should be noted that there are also non collider signatures for enhanced light-quark Yukawa couplings, manifesting in frequency shifts in atomic clocks from Higgs forces at the atomic level [419].

8.8 Discussion and conclusion

In this work we walk through an analysis of how kinematic shapes can be used to glean information about the nuances of various production modes with the same final states but deformed differentially by the existence of degrees of freedom beyond the Standard Model. We show that this information can be extracted by using an interpretable machine learning framework which is not only very effective separating these differences in kinematic shapes, but also yields itself to interpretations in terms of physics that is know and well understood. The example we chose is Higgs pair production in the $b\bar{b}\gamma\gamma$ final state.

[8] In [418], it was shown that $\sim \mathcal{O}(1)$ bounds on the quartic Higgs self-coupling can be reached at the FCC-hh.

We emphasized that probing Higgs pair production is an important next step for an understanding of the model underlying the fundamental interactions of particles and hence a potential gateway to new physics. We show that even beyond the trilinear Higgs couplings, the light-quark Yukawa couplings can be probed through this production mode. In fact, the $q\bar{q}$A channel opens up only in the presence of BSM physics and well motivated models of new dynamics bring about the simultaneous modification of the trilinear Higgs coupling and the light-quark Yukawa couplings. Indeed, we motivated our study by showing that in different frameworks large modifications of the light quark Yukawa couplings can be obtained. Knowing the difficulty of measuring these couplings we propose an interpretable machine learning framework that significantly outperforms traditional cut-based analyses.

As opposed to using black-box models, the interpretable framework allows us to gain physics insights into how signal and background separation can be brought into effect, pointing to kinematic variables like H_T and $m_{\gamma\gamma}$ as being important variables that instrument this separation. As a result we find enhanced sensitivities to C_ϕ or κ_λ that quantify the modification to the Higgs trilinear coupling. Furthermore, we see that the measurement of the light-quark Yukawa couplings is aided by using the methods we advocate bringing about far greater sensitivities than would be possible with a cut-based analysis at the HL-LHC and the FCC-hh. The advantage of using an interpretable framework using Shapley values is that it provides added confidence to the robustness of the multivariate analyses that we perform using simulated data.

The salient results of this work are:

- The modification of the Higgs trilinear coupling can be measures at $\mathcal{O}(1)$ precision at the HL-LHC and at $\mathcal{O}(1\%)$ precision at the FCC-hh.
- The rescaling of the light-quark Yukawa couplings, κ_u and κ_d, can be measured to $\mathcal{O}(100)$ at the HL-LHC and $\mathcal{O}(10)$ at FCC-hh. This translated to $C_{u\phi}$ and $C_{d\phi}$ constrained at $\mathcal{O}(10\%)$ at the HL-LHC and $\mathcal{O}(1\%)$ at FCC-hh.
- The measurement of C_ϕ, or κ_λ, is significantly diluted once the light-quark Yukawa couplings are allowed to vary. Hence, in a joint fit, the bounds on C_ϕ are much weaker.
- There are theoretical models that motivate the simultaneous modification of the trilinear Higgs coupling and the light-quark Yukawa couplings. Hence, the dilution of the bounds on C_ϕ due to the presence of NP in the light-quark Yukawa sector should be taken into consideration in future phenomenological extraction of C_ϕ.
- The bounds obtained with the interpretable machine learning framework that we use not only outperforms cut-based analyses by far, but also allows for physics insights into kinematic distributions of the various channels that helps distinguish them in an experiment.

In conclusion, we stress that the interplay between the Yukawa sector and the Higgs trilinear coupling is non-trivial and requires careful consideration. Future experiments at the HL-LHC and FCC-hh will bring significant improvements in the sensitivities to

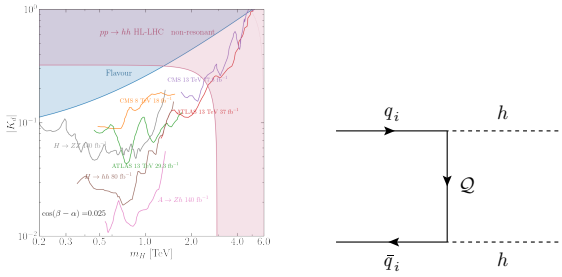

Figure 8.14. Examples of potential UV-complete models leading to a $hhf\overline{f}$ coupling. The left Feynman diagram shows a heavy Higgs H, the right diagram a vector-like quark $\mathcal{Q}$.

C_ϕ, $C_{u\phi}$ and $C_{d\phi}$ through the Higgs pair production channel. In particular, the bounds on the light-quark Yukawa couplings from Higgs pair production can possibly be the most stringent bounds amongst all other experimental probes of the light quark Yukawa couplings.

Part IV

Flavour physics

9 Flavour anomalies and Electroweak precision tests

9.1 Introduction

In the era of the Large Hadron Collider (LHC) an intense program aimed at probing the Standard Model (SM) at the TeV scale has been established. At the same time, one of the most valuable sources for the study of new physics (NP) above the electroweak (EW) scale is provided by indirect tests of the SM via the so-called the EW precision observables (EWPO). These include, in particular, the very precise measurements at the Z pole performed at the Large Electron-Positron (LEP) collider and the Stanford Linear Collider (SLC). In corroboration with the Higgs-boson discovery and the experimental information collected at LHC and Tevatron, they provide strong constraints on theories beyond the SM (BSM) that lead to important deformations of the standard EW sector [29, 140, 142, 235, 420–425]. Intriguingly, the interplay between the TeV region under scrutiny at the LHC and the NP probes represented by EW precision tests may be of fundamental importance for the study of the *B-physics anomalies* [426–433].

The outcome of LHCb and Belle analyses in the study of semileptonic B decays points to the possible presence of NP in the measured ratios $R_{K^{(*)}} \equiv Br(B \to K^{(*)}\mu^+\mu^-)/Br(B \to K^{(*)}e^+e^-)$ at low dilepton mass [434–437]. The averaged experimental values deviate from unity at the $\sim 2.5\sigma$ level, hinting at lepton universality violation (LUV). A statistically significant inference of LUV in $b \to s\ell\ell$ ($\ell = e, \mu$) transitions can be translated into a strong case for the evidence of BSM physics [438–440].

The interpretation of these experimental results as an imprint of heavy new dynamics has primarily been assessed in a model-independent fashion via the language of effective field theories (EFT) in [441–445] and more recently revisited in refs. [431, 432, 446–450]. Furthermore, the NP picture depicted by these global analyses could also accommodate a set of tensions related to the well-measured muonic channel of these B decays, in particular, to the angular analysis of $B \to K^*\mu^+\mu^-$ [451, 452]. These measurements have very recently been updated by the LHCb collaboration [453].

The set of tensions not related to LUV tests would specifically connect NP effects to muon-flavoured couplings. However, long-distant effects present in the amplitude of these processes [454–458] – involving hadronic contributions that are theoretically difficult to handle [459–462] – make such a conclusion debatable, see, e.g. [463, 464]. From this point of view, the LUV information extracted from ratios of branching ratios and from observables like the ones considered in [465–468] remain the most promising avenue in the future for a more precise assessment of the overall tension seen in $b \to s\ell\ell$ measurements [469]. Eventually, while a tighter upper limit has been recently obtained

by LHCb on the branching ratio of $B_s \to e^+e^-$ [470], the combined experimental average for the $Br(B_s \to \mu^+\mu^-)$ [471–473] also shows some tension with the SM prediction [474] as can be seen from the findings in [431, 432].

A broader discussion on B-physics anomalies should also include the LUV information stemming from another class of rare B decays, namely $b \to c$ semileptonic transitions [475–478]. Indeed, a combined resolution of $R_{K^{(*)}}$ anomalies with the long-standing deviations observed in $R_{D^{(*)}} \equiv Br(B \to D^{(*)}\tau\nu)/Br(B \to D^{(*)}\ell\nu)$ originally found at Babar [479] and subsequently measured at Belle [480] and LHCb [481], has triggered a lot of interest in the theory community. In particular, in order for NP effects to simultaneously account for a $\sim 20\%$ deviation in tree-level charged-weak decays and in loop-level flavour-changing neutral currents (FCNC), models with a highly non-trivial flavour structure are required [482–491], often being at the edge of flavour physics constraints [262, 492] and collider bounds [493, 494]. So far, model building has been mainly put forward in the direction of UV-completing low-energy leptoquark benchmarks identified, for instance, in refs. [429, 430, 433, 495, 496].

It is important to acknowledge that the most up-to-date measurements of $R_{D^{(*)}}$ from the Belle collaboration – obtained by fully reconstructing the τ particle via the hadronic [497] and, more notably, leptonic [498] decay modes – turns out to be in good agreement with the SM [499–502]. This fact may cast some doubt on the effective role one should really attribute to $b \to c$ transitions in the interpretation of the depicted *B-physics crisis*.

Therefore, in light of the recent results from Belle and LHCb, it is timely for us to focus again on the $b \to s\ell\ell$ conundrum and reassess the solutions to B-physics anomalies that can be realized at one loop without any new source of flavour violation. The simplest resolution of these anomalies has been proposed in ref. [503], extending the SM with a single new Abelian gauge group, together with the presence of top- and muon-partners, resulting in a top-philic Z' boson capable of evading present collider constraints [504] and responsible for the required LUV signatures.

Such a minimal model actually falls into a larger category pointed out in ref. [428] through the language of the Standard Model Effective Field Theory (SMEFT), and subsequently elaborated upon in greater detail in the phenomenological study of ref. [505].

At the basis of this class of proposals, the notable attempt is twofold:

i) Addressing the deviations in these FCNC processes with NP effects entering at one-loop level, as for SM amplitudes. This reduces the original multi-TeV domain of NP for B anomalies [506] to energies closer to present and future collider reach.

ii) Avoiding the introduction of new sources of flavour violation beyond the SM Yukawa couplings, relaxing in this way, any restrictive flavour probe of NP in a fashion similar to what is predicted in Minimal Flavour Violation (MFV) [351, 507, 508].

The aforementioned proposal shows a strong tension with Z-pole precision observables [505, 509]. In ref. [431] it has been shown that even in the presence of large hadronic effects in the amplitude of $B \to K^*\mu^+\mu^-$, a tension of at the 3σ level at least

would persist between B data and EWPO for muonic LUV effects, and an even stronger tension would be found in the case of LUV scenarios involving electron couplings.

This fact has been brought to light recently [510] to abandon *ii)*, and reformulate the original proposal addressing B anomalies at one loop adding specific BSM sources of flavour violation in order to reconcile B data with EW precision tests in this context. However, as briefly advertised in ref. [431], an important caveat of this EW tension versus B anomalies concerns the assumption of no tree-level NP contributions to EWPO.

In this work, we attempt, for the first time, to provide a broad exploration of the possible cross-talk of NP in the EW sector and in the flavour playground for $b \to s\ell\ell$ transitions. Firstly, we revisit the standard EW analysis in the presence of leading-log one-loop contributions from the renormalization group equations (RGE) evolution of the operators in the SMEFT [244, 245]. Then, we perform a joint fit to the comprehensive experimental set that includes EWPO in conjugation with the state-of-the-art measurements of semileptonic B decays. Our EFT analysis targets heavy new dynamics that contributes to $b \to s\ell\ell$ at the loop level only through SMEFT RGE, involving the SM Yukawa couplings as the only sources of flavour violation in the resolution of B anomalies.

Within our study, we systematically review novel correlations among gauge-invariant dimension-six operators that help us shed new light on the one-loop solutions to B anomalies. Continuing in the spirit of the previous work done by some of us [431, 444, 460, 463, 511–513], we shall furnish our results in both a conservative and optimistic approach to the non-perturbative hadronic contributions which can significantly affect the conclusions on the NP effects at hand.

On the basis of the SMEFT picture obtained from our combined inspection of EW and flavour data, we proceed to refine simple UV models already considered in the literature [428, 503, 504]. We corner the interesting parameter space of this refined class of models where EWPO are respected while B anomalies can be addressed at one loop without introducing new sources of flavour violation. Eventually, we go on to discuss the complementary probes offered by collider searches.

The paper is organized as follows: in section 9.2 we review the ingredients of our EFT analysis; in section 9.3 we detail the strategy adopted for our combined EW+flavour fit in the SMEFT, the results from which are collected in section 9.4; in section 9.5 we discuss the most economic viable Z' model in relation to our EFT results and also mention possible alternative leptoquark scenarios. Our conclusions are summarized in section 9.6.

9.2 Theoretical preamble

Previous global analyses of $b \to s\ell\ell$ anomalies have highlighted the appearance of new dynamics at a scale of $\mathcal{O}(10)$ TeV for $\mathcal{O}(1)$ effective couplings encoding NP effects at the tree level [441–445]. The mass gap with the weak scale, characterized by the Higgs vacuum expectation value (VEV) $v \approx 246$ GeV, justifies the BSM translation of these results in the gauge-invariant formalism of the SMEFT [128, 514]. At dimension six, in

an operator product expansion in inverse powers of the NP scale Λ, and working in the Warsaw basis [128], the operators of interest for the explanation of these B anomalies are [428, 431, 432]:

$$\begin{aligned} O_{\ell\ell 23}^{LQ^{(1)}} &= \overline{L}_\ell \gamma_\mu L_\ell \, \overline{Q}_2 \gamma^\mu Q_3 \ , \\ O_{\ell\ell 23}^{LQ^{(3)}} &= \overline{L}_\ell \gamma_\mu \tau^A L_\ell \, \overline{Q}_2 \gamma^\mu \tau^A Q_3 \ , \\ O_{23\ell\ell}^{Qe} &= \overline{Q}_2 \gamma_\mu Q_3 \, \overline{e}_\ell \gamma^\mu e_\ell \ , \\ O_{\ell\ell 23}^{Ld} &= \overline{L}_\ell \gamma_\mu L \, \overline{d}_2 \gamma^\mu d_3 \ , \\ O_{\ell\ell 23}^{ed} &= \overline{d}_2 \gamma_\mu d_3 \, \overline{e}_\ell \gamma^\mu e_\ell \ , \end{aligned} \tag{9.1}$$

where weak doublets are represented in upper case, $SU(2)_{\rm L}$ singlets in lower case, and Pauli matrices τ^A characterize $SU(2)_{\rm L}$ triplet currents. Within available light-cone sum-rule results on long-distance effects in $B \to K^* \mu^+ \mu^-$ [454, 458], data point to the presence of both the operators with $b \to s$ left-handed and right-handed currents with muonic flavour ($\ell = 2$) in eq. (9.1) [431, 446–448]. However, it is important to observe that:

- The current statistical significance for the need of right-handed $b \to s$ couplings remain small, hinted only by the ratio $R_{K^*}/R_K \neq 1$ at the 1σ level [431, 445]. Hence, the present B anomalies can be essentially addressed by $O_{2223}^{LQ^{(1,3)}}$ and O_{2322}^{Qe}.

- Within a conservative approach to hadronic uncertainties [459–461], the preference for muonic NP effects in global analyses gets mitigated to a large extent and electro-phillic scenarios become viable too [444]; moreover, the fully left-handed operator(s)[1] $O_{\ell\ell 23}^{LQ^{(1,3)}}$ offers the minimal model-independent resolution to $b \to s$ anomalies [431].

Interestingly, with a leading expansion in the top-quark Yukawa coupling of the RGE computed in [244, 245], the Wilson coefficients associated to O_{2223}^{LQ} and O_{2322}^{Qe} can be generated at one loop by two distinct sets of dimension-six operators [428] that can lead to LUV effects in $b \to s\ell\ell$ amplitudes without flavour violation in the quark current. A first set involves operators built of Higgs and leptonic currents:

$$\begin{aligned} O_{\ell\ell}^{HL^{(1)}} &= (H^\dagger i \overset{\leftrightarrow}{D}_\mu H)(\overline{L}_\ell \gamma^\mu L_\ell) \, , \\ O_{\ell\ell}^{HL^{(3)}} &= (H^\dagger i \overset{\leftrightarrow}{D}{}^A_\mu H)(\overline{L}_\ell \gamma^\mu \tau^A L_\ell) \, , \\ O_{\ell\ell}^{He} &= (H^\dagger i \overset{\leftrightarrow}{D}_\mu H)(\overline{e}_\ell \gamma^\mu e_\ell) \, . \end{aligned} \tag{9.2}$$

A second one corresponds to semileptonic four-fermion (SL-4F) operators with right-

[1] The most promising observables that will allow to genuinely disentangle NP effects in the future in the fully left-handed operator $O_{\ell\ell 23}^{LQ^{(3)}}$ from the ones of $O_{\ell\ell 23}^{LQ^{(1)}}$, are $B \to K^{(*)} \nu\overline{\nu}$ decays [515–517].

handed top-quark currents:

$$\begin{aligned} O^{Lu}_{\ell\ell 33} &= (\overline{L}_\ell \gamma_\mu L_\ell)(\overline{u}_3 \gamma^\mu u_3)\,, \\ O^{eu}_{\ell\ell 33} &= (\overline{e}_\ell \gamma_\mu e_\ell)(\overline{u}_3 \gamma^\mu u_3)\,. \end{aligned} \tag{9.3}$$

Solving the RGE in a leading-logarithmic approximation, the matching conditions for the left-handed quark-current operators in eq. (9.1) at the scale $\mu_{\rm EW} \sim v$ are:[2]

$$\begin{aligned} C^{LQ^{(1)}}_{\ell\ell 23} &= V^*_{ts} V_{tb} \left(\frac{y_t}{4\pi}\right)^2 \log\left(\frac{\Lambda}{\mu_{\rm EW}}\right) \left(C^{Lu}_{\ell\ell 33} - C^{HL^{(1)}}_{\ell\ell}\right)\,, \\ C^{LQ^{(3)}}_{\ell\ell 23} &= V^*_{ts} V_{tb} \left(\frac{y_t}{4\pi}\right)^2 \log\left(\frac{\Lambda}{\mu_{\rm EW}}\right) C^{HL^{(3)}}_{\ell\ell}\,, \\ C^{Qe}_{23\ell\ell} &= V^*_{ts} V_{tb} \left(\frac{y_t}{4\pi}\right)^2 \log\left(\frac{\Lambda}{\mu_{\rm EW}}\right) \left(C^{eu}_{\ell\ell 33} - C^{He}_{\ell\ell}\right)\,. \end{aligned} \tag{9.4}$$

In terms of vectorial and axial currents typically discussed in the context of the weak effective theory at low energies [520–522], the operators in eq. (9.4) are matched to

$$\begin{aligned} O_{9V,\ell} &= \frac{\alpha_e}{8\pi}(\overline{s}\gamma_\mu(1-\gamma_5)b)(\overline{\ell}\gamma^\mu \ell)\,, \\ O_{10A,\ell} &= \frac{\alpha_e}{8\pi}(\overline{s}\gamma_\mu(1-\gamma_5)b)(\overline{\ell}\gamma^\mu\gamma_5 \ell)\,, \end{aligned} \tag{9.5}$$

so that the matching conditions at the scale $\mu_{\rm EW}$ for the set of operators in eq. (9.2) - (9.3) follow:

$$\begin{aligned} C^{\rm NP}_{9,\ell} &= \frac{\pi v^2}{\alpha_e \Lambda^2}\left(\frac{y_t}{4\pi}\right)^2 \log\left(\frac{\Lambda}{\mu_{\rm EW}}\right) \left(C^{HL^{(3)}}_{\ell\ell} - C^{HL^{(1)}}_{\ell\ell} - C^{He}_{\ell\ell} + C^{Lu}_{\ell\ell 33} + C^{eu}_{\ell\ell 33}\right)\,, \\ C^{\rm NP}_{10,\ell} &= \frac{\pi v^2}{\alpha_e \Lambda^2}\left(\frac{y_t}{4\pi}\right)^2 \log\left(\frac{\Lambda}{\mu_{\rm EW}}\right) \left(C^{HL^{(1)}}_{\ell\ell} - C^{HL^{(3)}}_{\ell\ell} - C^{He}_{\ell\ell} - C^{Lu}_{\ell\ell 33} + C^{eu}_{\ell\ell 33}\right)\,, \end{aligned} \tag{9.6}$$

where $\alpha_e \equiv e^2/(4\pi)$, e being the electric charge, and the overall normalization in the weak Hamiltonian follows the standard conventions adopted in refs. [431, 444, 460].

As anticipated in the Introduction, the set of operators of interest for the study of $R_{K^{(*)}}$ in eq. (9.4) is also probed by EW precision data. Indeed, operators involving the Higgs field and lepton bilinears in the SMEFT induce modifications to EW-boson couplings that have been precisely measured at LEP/SLC, providing also an important test bed for lepton universality [423, 509]. Modifications of the Z couplings to the leptons can be induced also at loop level through the top-loop contribution [235]. In the leading-log approximation and at the leading order in the top Yukawa coupling, LUV effects can

[2] In this work, for one-loop effects, we assume the NP scale to be $\Lambda = 1$ TeV. We also set $\mu_{\rm EW} = m_t \simeq v/\sqrt{2}$ to minimize the matching-scale dependence with the inclusion of next-to-leading corrections [518, 519].

be generated by:

$$\begin{aligned}\Delta g^{\ell\ell}_{Z,L}\Big|_{\rm LUV} &= -\frac{1}{2}\left(C^{HL^{(1)}}_{\ell\ell}+C^{HL^{(3)}}_{\ell\ell}\right)\frac{v^2}{\Lambda^2}-3\left(\frac{y_t\,v}{4\pi\Lambda}\right)^2\log\left(\frac{\Lambda}{\mu_{\rm EW}}\right)C^{Lu}_{\ell\ell 33}\,, \\ \Delta g^{\ell\ell}_{Z,R}\Big|_{\rm LUV} &= -\frac{1}{2}C^{He}_{\ell\ell}\frac{v^2}{\Lambda^2}-3\left(\frac{y_t\,v}{4\pi\Lambda}\right)^2\log\left(\frac{\Lambda}{\mu_{\rm EW}}\right)C^{eu}_{\ell\ell 33}\,,\end{aligned} \tag{9.7}$$

where $\Delta g^{\ell\ell}_{Z,L(R)} \equiv g^{\ell\ell}_{Z,L(R)} - g^{\ell\ell,\rm SM}_{Z,L(R)}$ is the deviation with respect to the left-handed (right-handed) leptonic couplings to the Z boson in the SM theory.

Motivated by the previous observations, we would like to perform an EFT analysis of new physics models that can explain the flavour anomalies in the above-mentioned fashion, but exploring more generally the interplay of such SM extensions with EWPO. For that purpose, we consider an EFT analysis of new physics with the following assumptions:

- The solution to the flavour anomalies is obtained via radiative effects, such as those described in eq. (9.6).
- Such NP can also contribute to EWPO at tree-level, in a flavour non-universal way.
- Other effects that could enter in the previous observables via renormalization group (RG) mixing are either small or can be constrained better via other processes.

As we will see in section 9.5, and can also be deduced using the results in [264], it is not difficult to construct minimal BSM models where the previous conditions are satisfied. From an EFT point of view, fulfilling these considerations requires the enlarging of the set of operators considered in eq. (9.2) and also including the corresponding dimension-six interactions modifying the neutral and charged quark currents:

$$\begin{aligned}O^{HQ^{(1)}}_{qq} &= (H^\dagger i\overleftrightarrow{D}_\mu H)(\overline{Q}_q\gamma^\mu Q_q)\,, \\ O^{HQ^{(3)}}_{qq} &= (H^\dagger i\overleftrightarrow{D}^A_\mu H)(\overline{Q}_q\gamma^\mu \tau^A Q_q)\,, \\ O^{Hu}_{qq} &= (H^\dagger i\overleftrightarrow{D}_\mu H)(\overline{u}_q\gamma^\mu u_q)\,, \\ O^{Hd}_{qq} &= (H^\dagger i\overleftrightarrow{D}_\mu H)(\overline{d}_q\gamma^\mu d_q)\,,\end{aligned} \tag{9.8}$$

where $q = 1,2,3$ identifies quark generations.[3] In this regard, we note that EWPO cannot separate in a clean way contributions from the first family quarks, in particular in the d sector. Therefore, and analogously to what was done in ref. [523], we identify deviations in the couplings of the EW bosons to the first and second family of the quarks via $C^{HQ^{(1,3)}}_{11} = C^{HQ^{(1,3)}}_{22}$, $C^{Hu}_{11} = C^{Hu}_{22}$, and $C^{Hd}_{11} = C^{Hd}_{22}$. This implicit $U(2)^3$ symmetry

[3] In our SMEFT analysis we require these quark operators to be diagonal in a basis that is aligned, as much as possible, with the down-quark physical basis. This will be convenient to avoid possible dangerous tree-level FCNC effects [262]. Similarly, we also assume lepton-flavour alignment with the charged-lepton mass basis.

in the quark sector would in general also help to mitigate large contributions to FCNC. Note that, even in this situation, not all the Wilson coefficients related to eq. (9.8) can be well constrained with the EWPO. This is the case for the Wilson coefficient of O_{33}^{Hu}, which modifies the right-handed top quark coupling to the Z. This cannot be probed at tree level by Z-pole measurements.

Introducing eq. (9.8) also modifies the EW couplings of the Z to all fermions at the one-loop level, and in particular the leptonic couplings, $g_{Z,L(R)}^{\ell\ell}$. These are, however, flavour-universal effects. In our study, we propagate the leading y_t effects of this kind, coming from the RG mixing with $O_{33}^{HQ^{(1)}}$. As we will see, given the comparatively weaker bound on the Wilson coefficient of that operator compared to the leptonic ones, these effects can be sizeable in the fit. It must be noted that, at the same order in the perturbative expansions we are considering, similar effects from O_{33}^{Hu} could also have a non-negligible phenomenological impact. However, as explained before, C_{33}^{Hu} cannot be directly bound in the EWPO fit. Hence, to avoid flat directions in our EFT analysis, we assume the RGE boundary condition $C_{33}^{Hu} = 0$ to hold true. Excluding $\mathcal{O}_{33}^{Hu}$ and taking into account the aforementioned assumptions in the quark sector, eq. (9.8) adds a total of 7 new degrees of freedom into our EFT analysis.

Finally, for completeness, we also consider the effects of the four-lepton operator:

$$O_{1221}^{LL} = (\overline{L}_1\gamma^\mu L_2)(\overline{L}_2\gamma_\mu L_1) \ , \tag{9.9}$$

which contributes to the muon decay amplitude, and therefore alters the extraction of the value of the Fermi constant, G_F, which is one of the inputs of the SM EW sector.

The operators in eqs. (9.2), (9.8) and (9.9), with the assumptions mentioned before, saturate all the 17 degrees of freedom, i.e. combinations of operators, that can be constrained in a fit to EWPO in the dimension-six SMEFT framework [4], while keeping flavour changing neutral currents in the light quark sector under control. Together with the 4 four-fermion operators from eq. (9.3), this completes a total of 21 operators, which we include in the fit setup described in the next section.

9.3 Analysis strategy

We now proceed to discuss in more detail our EFT analysis. Our aim is to pin down the picture that should address the present B anomalies via one-loop SM RGE effects of flavour-conserving dimension-six operators, and respect at the same time the constraints from EW precision. We can achieve this goal with a comprehensive global analysis that

[4] In this regard, we should mention that at dimension six, in the Warsaw basis, EW observables are also affected by two more operators not discussed so far: $O_{HWB} = (H^\dagger\tau^A H)W^A_{\mu\nu}B^{\mu\nu}$ and $O_{HD} = \left|H^\dagger D_\mu H\right|^2$. Contrary to the set in eqs. (9.2) and (9.8), these operators only induce oblique, and therefore flavour-universal, corrections in EW observables. Given our focus on LUV effects, we assume for O_{HWB} and O_{HD} that the corresponding Wilson coefficients are not generated by the NP at the scale Λ.

aims at combining EWPO and $b \to s\ell\ell$ data.[5]

We perform a Bayesian analysis on the most recent set of $b \to s\ell\ell$ measurements together with the state-of-the-art theoretical information already implemented and described in ref. [431]. We include in our study EW physics following what originally done in ref. [421] and, more recently, in ref. [423]. In particular, we adopt the list of observables reported in Table 1 of this reference, and allow for lepton non-universal contributions from heavy BSM physics in EWPO [509, 523] within the framework described in section 9.2.

For this purpose we adopt the publicly available `HEPfit` [255] package, a Markov Chain Monte Carlo (MCMC) framework built using the Bayesian Analysis Toolkit [527].[6] In our analyses we vary $\mathcal{O}(100)$ parameters including nuisance parameters. The data that we use for the fits can be categorized as follows:

- The set of EWPO including the Z-pole measurements from LEP/SLD, the measurements of the W properties at LEP-II, as well as several related inputs from the Tevatron and LHC measurements of the properties of the EW bosons [14, 16, 528–532]. The following lists the bulk of the EWPO included in the fits:

$$M_H,\ m_t,\ \alpha_S(M_Z),\ \Delta\alpha^{(5)}_{\rm had}(M_Z),$$
$$M_Z,\ \Gamma_Z,\ R_{e,\mu,\tau},\ \sigma_{\rm had},\ A_{FB}^{e,\mu,\tau},\ A_{e,\mu,\tau},\ A_{e,\tau}(P_\tau),\ R_{c,b},\ A_{FB}^{c,b},\ A_{s,c,b},\ R_{u+c},$$
$$M_W, \Gamma_W,\ {\rm BR}_{W\to e\nu,\mu\nu,\tau\nu},\ \Gamma_{W\to cs}/\Gamma_{W\to ud+cs},\ |V_{tb}|\,;$$

- The angular distribution of $B \to K^{(*)}\ell^+\ell^-$ decays for both μ and e final states in the large-recoil region.[7] These include data from ATLAS [533], Belle [467], CMS [534, 535] and LHCb [453, 536]; we also include the branching fractions from LHCb [537], and of $B \to K^*\gamma$[8] for which we use the HFLAV average [539];
- Branching ratios for $B^{(+)} \to K^{(+)}\mu^+\mu^-$ decays in the large-recoil region measured by LHCb [540];
- The angular distribution of $B_s \to \phi\mu^+\mu^-$ [541] and the branching ratio of the decay $B_s \to \phi\gamma$ [542], measured by LHCb;
- The lepton universality violating ratios R_K [436] and R_{K^*} [435] from LHCb and Belle [437];
- Branching ratio of $B_{(s)} \to \mu^+\mu^-$ measured by LHCb [472], CMS [471], and ATLAS [473]; we also use the upper limit on $B_s \to e^+e^-$ decay reported recently by

[5] See ref. [524] for another recent analysis where $b \to s\ell\ell$ data and EW measurements have been combined, with the different scope of resolving tensions in the determination of the Cabibbo angle [525, 526].

[6] All code and configuration files can be made available upon request.

[7] We do not consider in this work low-recoil data, plagued by broad charmonium resonances, implying very large hadronic uncertainties. For analogous reasoning, we do not attempt to study here the baryon rare decay $\Lambda_b \to \Lambda\,\mu^+\mu^-$ as well.

[8] NP effects from dipole operators are strongly constrained as extensively investigated in ref. [538]. However, radiative exclusive B decays still provide relevant information about hadronic effects [463].

LHCb [470].

For the $B \to K^* \ell^+ \ell^-$ channel, as in previous works [431, 444, 463, 511–513], we consider two different scenarios for hadronic contributions stemming from long-distance effects [454, 455, 459]. We take into account a conservative approach (Phenomenological Data Driven or PDD) as originally proposed in [460], and refined in ref. [463], and a more optimistic approach based on the results in [454] (Phenomenological Model Driven or PMD). For the PDD model, a quite generic model of hadronic contributions is simultaneously fitted to $b \to s\ell\ell$ data together with the effects coming from NP. Within this approach, a net assessment of the presence of BSM physics is only possible via observables sensitive to LUV effects. See the discussion in ref. [431] for more details. For the PMD approach we use the dispersion relations specified in [454] to constrain the hadronic contributions in the entire large-recoil region considered in the analysis. This leads to much smaller hadronic effects in the $B \to K^* \ell^+ \ell^-$ amplitudes [511], which significantly affects NP results of global analysis [431].

We have characterized our study by considering several different scenarios for the SMEFT fit. In particular, we would like to clarify the sets of data and operators used in each of these fit scenarios, which are organized as follows:

- **EW**: In this fit we simultaneously vary the Wilson coefficients of the *17 operators* in eqs. (9.2), (9.8), and (9.9), as presented in section 9.2. This fit includes EW precision measurements only, and it is performed under the assumptions listed in section 9.2.
- **EW (SL-4F Only)**: This refers to a fit done with the Wilson coefficients of the *SL-4F operators* involving the right-handed top current, reported in eq. (9.3). This scenario incorporates the assumption that BSM enters the modifications of the Z couplings to muons and electrons through top-quark loops only.
- **EW & Flavour**: In these fits we vary the Wilson coefficients of all the *21 operators* given in eq. (9.2), (9.8), and eq. (9.9), together with eq. (9.3). We use all the EW data and include all the flavour observables listed at the beginning of this section. This scenario comes in two varieties, PDD and PMD, as explained above.
- **Flavour**: These fits exclusively include the Wilson coefficients of the *4 operators* (both electrons and muons) appearing in eq. (9.3), and are done including only flavour data, i.e. excluding EW measurements. Results are again distinguished for the PDD and PMD cases.

9.4 Results from the SMEFT

9.4.1 Analysis of EW and $b \to s\ell\ell$ data

As a first step in our analysis, we reproduced the outcome of the EW fit originally obtained in ref. [509] using `HEPfit`. Then, we expanded upon the standard EW results through the study of the **EW** scenario introduced in the previous section, yielding

constraints on the Wilson coefficients of the SMEFT operators involving, in particular, dimension-six operators with a Higgs-doublet current, and including also leading-loop effects under the working hypotheses stated in section 9.2. The subset of these operators containing leptonic currents can give rise to non-universal modifications of EW gauge-boson couplings. Assuming NP integrated out at the heavy scale $\Lambda > v$, these operators also contribute via RGE flow to $b \to s\ell\ell$ observables at one loop, see eq. (9.4).

On the left side of Figure 9.1, we show in orange the bounds from the **EW** fit on the Wilson coefficients of the operators with leptonic currents in terms of mean and standard deviation of the marginalized posterior probability density function. We observe compatibility with the SM within the 2σ level. Note that EW data strongly correlate the operators under consideration among themselves, as can be seen in the correlation matrix presented in Figure 9.2.

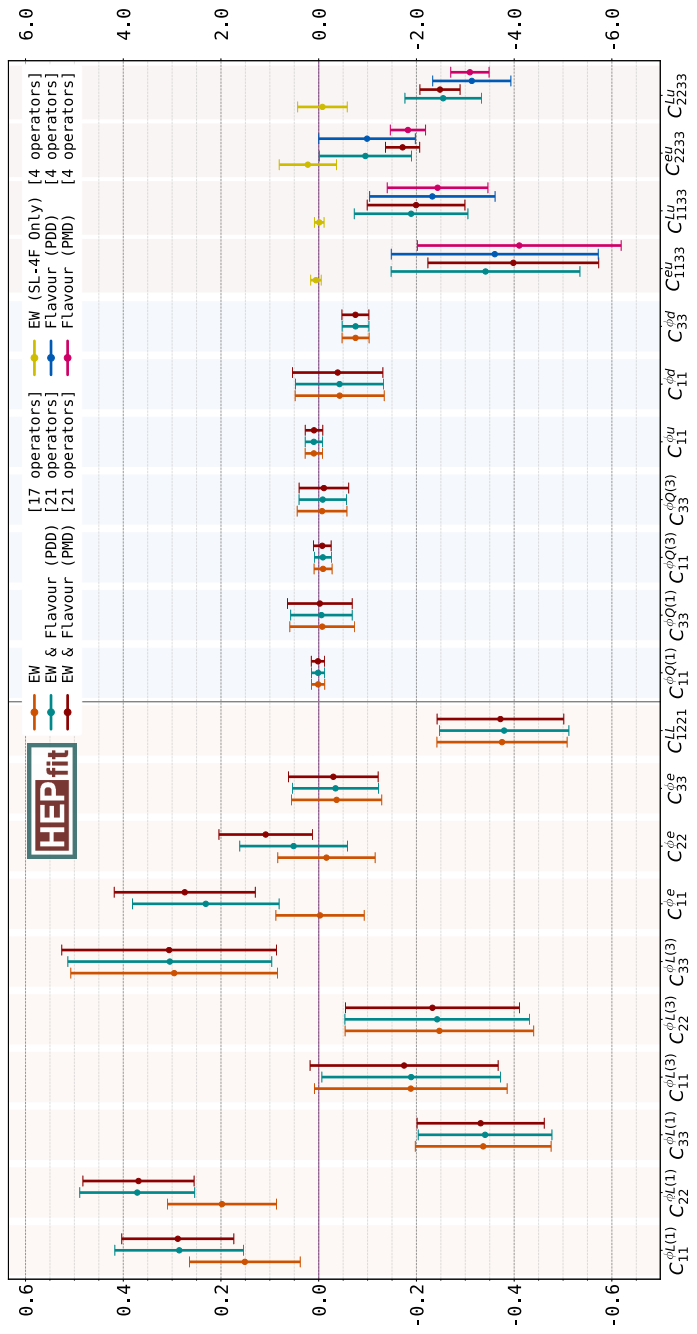

Figure 9.1. Mean and standard deviation of the marginalized posterior distributions for each of the Wilson coefficients (in TeV^{-2}) considered in the different fits described in section 9.3. Note that each fit assumes a different set of non-zero operators: EW – 17 operators presented in eqs. (9.2), (9.8) and (9.9); EW(SL-4F Only) – four-fermion operators in eq.(9.3); Flavour (PDD) and (PMD) are the fits with the operators in eq.(9.3), where (PDD) and (PMD) refer to the various assumptions on the hadronic long-distance effects in the flavour sector; EW & Flavour (PDD) and (PMD) stand for the fits including the 21 operators in eqs. (9.2), (9.3), (9.8) and (9.9). (Note the different scaling in the axes quantifying the size of the bounds presented in each half of the figure.)

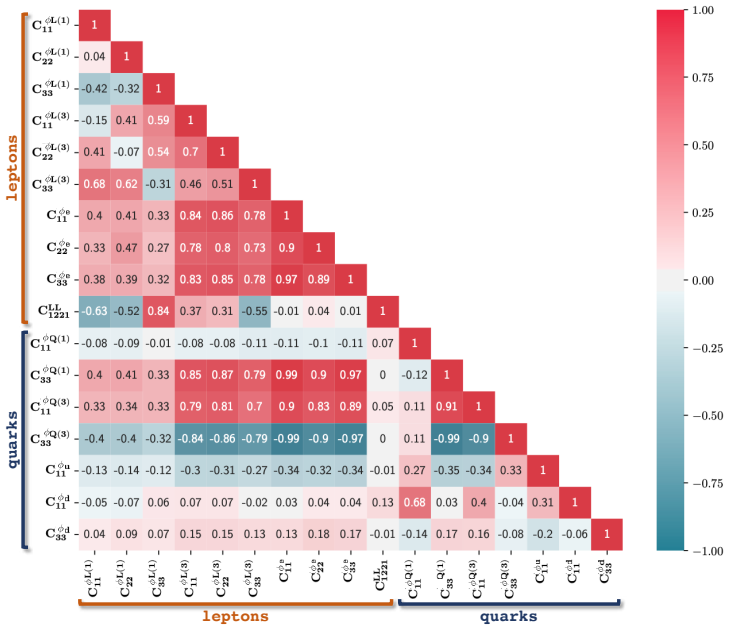

Figure 9.2. *The correlation matrix extracted from the SMEFT analysis of the set of independent operators in eqs. (9.2), (9.8), (9.9) in the **EW** scenario introduced in section 9.3. The two distinct groups of Wilson coefficients associated to leptonic and quark interactions are remarked as "leptons" and "quarks", respectively.*

where away from the photon pole, $R^{\rm SM}_{K^{(*)}}$ are predicted to be unity at percent level [440].

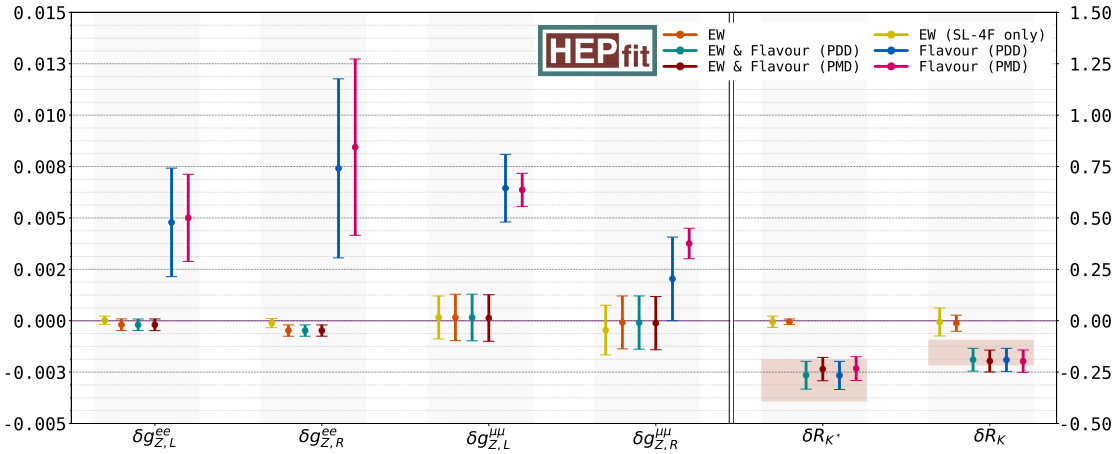

Figure 9.3. *Mean and standard deviation of the marginalized posterior of the key set of observables for this work, in relation to the tension between $b \to s\ell\ell$ anomalies and LEP/SLD measurements. In particular, the left panel shows the deviations in the effective $Z\ell\ell$ couplings, normalized by SM values. The right panel, on the other hand, shows the deviation from the nominal SM values of the lepton universality violating ratios, see eq. (9.10), with the red boxes indicating the region selected by the experimental measurements of $R_{K,(K^*)}$.*

In particular, the strong correlation between the operators with quarks and leptons is introduced by the non-negligible one-loop universal contribution of the operator $\mathcal{O}_{33}^{HQ^{(1)}}$ to all the EW couplings, as anticipated at the end of section 9.4. With the direct bound on $C_{33}^{HQ^{(1)}}$ being relatively weak compared to the limits on the leptonic operators, such effects in the leptonic couplings can be sizable.

This leads to a relaxation of the naive bounds on $C_{\ell\ell}^{HL^{(1)}}$, $C_{\ell\ell}^{HL^{(3)}}$ and $C_{\ell\ell}^{He}$ that one would obtain in a tree-level analysis. To illustrate this, we present in section 9.7 a comparison with the results from such a tree level analysis of the EW fit. The results in Figure 9.2 can then be compared to those in Figure 9.8 where, as it is apparent, there is a substantial decoupling between the dimension-six operators made of Higgs doublets and quark bilinears from the leptonic ones.

The impact of these operators on the key observables for the present discussion is reported in Figure 9.3. There, we collect mean and standard deviation on the shift in the Z coupling to light leptons (normalized to the corresponding SM value),and on the effect on $R_{K^{(*)}}$ in the dilepton-mass range $[1.0, 6.0]$ GeV^2:

$$\delta g_{Z,L(R)}^{ee(\mu\mu)} \equiv g_{Z,L(R)}^{ee(\mu\mu)} / g_{Z,L(R)}^{ee(\mu\mu),\mathrm{SM}} - 1 \ , \ \delta R_{K^{(*)}} \equiv R_{K^{(*)}} - R_{K^{(*)}}^{\mathrm{SM}} \ , \tag{9.10}$$

Note that EW measurements tightly constrain NP effects modifying the EW gauge boson couplings to electrons, and also forbid deviations beyond the per-mille level in the case of couplings to muons. This translates into strong bounds on the Wilson coefficients $C_{\ell\ell}^{HL^{(1,3)},He}$. Hence, the one-loop contribution to $R_{K^{(*)}}$ from $O_{\ell\ell}^{HL^{(1,3)},He}$ comes out to be tiny. We can then move our attention to the **EW (SL-4F Only)** scenario, reported in yellow in Figure 9.1 and Figure 9.3, and find a similar conclusion. Indeed, EW data once again strongly constrain the NP Wilson coefficients related to $O_{\ell\ell 33}^{eu,Lu}$ – the SL-4F operators – implying all the four NP Wilson coefficients to be compatible with 0. However, note that unlike the previous case, $C_{\ell\ell 33}^{Lu,eu}$ only contribute at one loop to $\delta g_{Z,L(R)}^{\ell\ell}$ and $\delta R_{K^{(*)}}$ in eq. (9.10). Consequently, the resulting impact on $b \to s\ell\ell$ flavour observables can be larger than the one in the **EW** scenario. As depicted in Figure 9.3, however, there is still an overall tension between EWPO bounds (in yellow) and the experimental measurements of R_K and R_{K^*} (indicated by the shaded red boxes in the right side of the figure) at the 3σ level.

To frame this tension from a different perspective, let us now focus on the set of flavour measurements as previously done in ref. [431]. In Figure 9.1 we also show the constraints on the four Wilson coefficients of eq. (9.3) coming from $b \to s\ell\ell$ data, in what we dubbed as the **Flavour** scenario. We present the PMD case, corresponding to an optimistic approach to QCD power corrections, in pink, while the more conservative PDD case is shown in blue. We observe that in both cases a muonic solution to B anomalies stands out, with C_{2233}^{Lu} different from 0 at more than 3σ in the PDD case, and at roughly 6σ in the PMD one.

We stress that the difference between the results obtained in the PMD and in the PDD case is substantially driven by the angular analysis of $B \to K^*\mu\mu$. In particular, only within the PDD approach the fully left-handed solution to B anomalies, $C_{9,\ell} = -C_{10,\ell}$,

is favoured by data (signalled here by the Wilson coefficient of $O^{eu}_{\ell\ell 33}$ being compatible with 0 at 1σ, see the results in blue in Figure 9.1). In addition, an electron resolution of B anomalies is, once again, viable only within PDD [431, 444].

In the **Flavour** scenario one can also predict the induced shift in the Z-boson couplings according to eq. (9.7), and these are shown in Figure 9.3. As can be seen, $\delta g^{\ell\ell}_{Z,L,R}$ would receive large contributions at one loop from $O^{Lu,eu}_{\ell\ell 33}$ in correspondence to the one-loop MFV-like resolution of B anomalies. Such contribution would be, however, now in tension with the results from EW precision tests. In particular, as a reflection of the main role played by O^{Lu}_{2233} in the **Flavour** fit to the four NP Wilson coefficients considered, $g^{\mu\mu}_{Z,L}$ shows the most important deviation from the SM value. Also, the prediction of $g^{\mu\mu}_{Z,L(R)}$ becomes indirectly sensitive to the underlying treatment of hadronic uncertainties adopted for the study of $b \to s$ data. Therefore, we observe that within the PMD approach, the inconsistency between what is needed to address B anomalies and what is required by EW measurements is even more severe than the 3σ established in the **EW (SL-4F Only)** scenario, and imprinted also in the **Flavour** fit with the PDD approach. In fact, we stress once again that adopting light-cone sum-rule results [454] for the long-distant effects in $B \to K^*\ell\ell$ decay, the tension between B anomalies and EW data reaches the 6σ level.

So, how do we reach a consensus between $b \to s\ell\ell$ measurements and EWPO? Succinctly, an obvious solution which satisfies these constraints is a class of models where $R_{K^{(*)}}$ anomalies are addressed at tree level and where modifications to Z-lepton-lepton vertices are at the same time suppressed. However, these models would not offer a solution to B anomalies of the MFV type envisaged so far, namely they would rely on the existence of sizeable new sources of flavour violation. At this point, we would like to emphasize that a combined fit of EW and flavour observables offers a new insight into this matter: it highlights strong correlations between the dimension-six operators $O^{Lu(eu)}_{\ell\ell 33}$ and $O^{HL^{(1)}(He)}_{\ell\ell}$ as is evident from Figure 9.4. This figure presents a pictorial representation of the correlations between the leptonic operators included in the different fits.

Apart from the fits introduced in the previous section, for illustration purposes we also show in Figure 9.4 the correlations obtained in a variant of the **EW** fit including also the four-fermion operators $O^{Lu(eu)}_{\ell\ell 33}$, labelled as **EW (including SL-4F operators)**. This is shown in the upper-right corner of the figure. As can be seen in that panel, and one could deduce from the relations in eq. (9.7), in a pure EW fit adding the four-fermion operators would simply introduce 4 flat directions. These are illustrated by the links connecting the $C^{eu}_{\ell\ell 33}$ ($C^{Lu}_{\ell\ell 33}$) and $C^{He}_{\ell\ell}$ ($C^{HL^{(1)}}_{\ell\ell}$) operators, corresponding to 100% anti-correlation. Such flat directions are lifted upon the introduction of the flavour measurements of R_K and R_{K^*}, as can be seen in the lower panels of Figure 9.4 for the **EW & Flavour** fits. Even then, due again to relations in eq. (9.4) and (9.7) and the comparatively different precision of the EW and flavour measurements, sizable correlations remain.

In Figure 9.1 the imprint of these correlations is a shift of central values and an increase on the bounds on the corresponding Wilson coefficients, with red and green bars representing the outcome of the fit in the **EW & Flavour** scenario within the **PMD** and

PDD approaches, respectively. The interplay between $O_{\ell\ell 33}^{Lu(eu)}$ and $O_{\ell\ell}^{HL^{(1)}(He)}$ is evident when comparing the reported red and green bounds versus the orange EW constraints on $C_{\ell\ell}^{HL^{(1)}(He)}$, and the yellow ones for $C_{\ell\ell 33}^{Lu(eu)}$. Consequently, as clearly depicted in Figure 9.3, looking at the red and green ranges reported for the **EW & Flavour** scenario, $R_{K^{(*)}}$ puzzles are solved with EW precision being respected. It is important to emphasize that, despite the significant correlation between quark and lepton operators introduced by the one-loop effects of $C_{33}^{HQ^{(1)}}$, quark operators play no significant role in reconciling the EWPO constraints with the solution to B anomalies. This will become clearer in the next section, but can be easily understood from the fact that, as mentioned before, quark and lepton constraints are somewhat uncorrelated in the tree-level EW fit, and the fact that the one-loop corrections effect induced by $C_{33}^{HQ^{(1)}}$ are flavour universal.

9.4.2 A minimal EFT picture

Finally, let us draw what would be the minimal picture for NP out of the general analysis obtained with the 21 operators considered in the **EW & Flavour** scenario. Indeed, a simpler picture will serve as a guideline for the UV models discussed in section 9.5. As mentioned before, given the hadronic uncertainties at hand, the most economic explanation addressing in particular $R_{K^{(*)}}$ anomalies resides in the NP contribution from the fully left-handed operator, $O_{\ell\ell 23}^{LQ}$. In the present context this operator is generated at one loop by $O_{\ell\ell 33}^{Lu}$, according to eq. (9.4).

Then, in Figure 9.5 we show in orange the overall constraint from $b \to s\ell\ell$ data on $C_{\ell\ell 33}^{Lu}$ within the most conservative approach to long-distance effects, i.e. the PDD one. In particular, in the left (right) panel we report the constraint on the muonic (electronic) scenario. In the same figure, we highlight with the vertical gray band the bound derived from the full correlated set of EWPO on the same operator. From the comparison of the orange and gray single-operator bounds, the tension between flavour and EW measurements is manifest at the 3σ level in the left panel of Figure 9.5. It gets even more pronounced in the right panel due to the precise probe of NP that EW gauge-boson couplings to electrons provide. In the same Figure 9.5, we also show with the horizontal gray band the result of the EWPO constraints applied this time on the NP contribution coming exclusively from the operator $C_{\ell\ell}^{HL^{(1)}}$. Note that this operator would also contribute to $R_{K^{(*)}}$ at one loop, but the size needed would be $\mathcal{O}(1)$ and it is out of scale in the vertical axis of the plot.

Most importantly, in the same figure we display in (dashed) magenta the $1(2)\sigma$ contour where EW data are reconciled with the one-loop MFV explanation of B anomalies when a combined fit of the NP contributions from these two operators is performed. Therefore, heavy BSM degrees of freedom that, once integrated out, generate sizeable contributions both to the Wilson coefficient of $O_{\ell\ell}^{HL^{(1)}}$ and of $C_{\ell\ell 33}^{Lu}$ are the key aspect of this scenario that addresses B anomalies without requiring sources of flavour violation beyond SM ones.

Finally, note that the role played here by $O_{\ell\ell 33}^{Lu}$ could be shared, in part, with $O_{\ell\ell 33}^{eu}$, depending on how much departure is actually required from the fully left-handed solution

to B anomalies. As already noted, this fact critically depends on the information stemming from $B \to K^* \mu\mu$ [431]. On general grounds, to relieve the bounds from EWPO, the presence of $O^{eu}_{\ell\ell 33}$ would also necessitate sizeable NP effects from $O^{He}_{\ell\ell}$.

As a last comment of this section we would also like to highlight that in the class of models considered the prediction for the LUV observable R_K is always close to the one for R_{K^*}: any hint of NP coming from $R_{K^*}/R_K \neq 1$ [438, 439, 445, 543] would not be addressed within the NP models considered here, mainly involving the operators in eq. (9.2) and (9.3). In the following sections we will put our focus on the economic EFT scenario captured in Figure 9.5 to build up simple UV scenarios realizing the EFT picture here delineated.

9.5 Directions for UV models

In this section we discuss how the lesson derived from the SMEFT picture illustrated, in particular, in Figure 9.5, can be realized in a minimal extension of the SM. Here, we explicitly show how models involving a new Z' gauge boson around the TeV scale provide the most economic example of the correlations advertised in the previous section. This can be achieved if we have a Z' coupled both to top and lepton SM fields. These couplings can be obtained introducing vector-like top and muon/electron partners reasonably close to the EW scale [503, 504], making this class of models potentially interesting also from the point of view of naturalness in the Higgs sector. Finally, we will also briefly comment on possible alternative scenarios that can be obtained with leptoquarks.

9.5.1 Z′ with vector-like partners

Let us start with the baseline presented originally in ref. [503]. A simple extension of the SM, able to address B anomalies, and that does not introduce any explicit new source of flavour violation, can be conceived as follows:

- The SM gauge group, $SU(3)_c \otimes SU(2)_L \otimes U(1)_Y$, is extended by a new Abelian gauge group, $U(1)_X$, under which SM fields are neutral;
- There is a new complex scalar field $\mathcal{S}$ that spontaneously breaks $U(1)_X$, giving a mass to the gauge boson X_μ equal to $m_{Z'} = g_X \langle \mathcal{S} \rangle$;
- A coloured vector-like top partner, $\mathcal{T}$, properly charged under $U(1)_X$ and $U(1)_Y$ can mix with the right-handed top-quark field u_3 via a Yukawa interaction with $\mathcal{S}$;
- A vector-like muonic partner, $\mathcal{M}$, doublet of $SU(2)_L$ and charged under $U(1)_{X,Y}$, can mix with the muonic doublet L_2 via another Yukawa coupling of $\mathcal{S}$;
- The couplings controlling the kinetic-mixing term, $X_{\mu\nu} B^{\mu\nu}$, and the quadratic scalar mixing, $\mathcal{S}^\dagger \mathcal{S} H^\dagger H$, are set to be phenomenologically negligible.[9]

[9] Using naive dimensional analysis, both kinetic and scalar quadratic mixing should appear beyond the tree level suppressed at least by a loop factor and the corresponding SM-partner rotation angles.

Then, the UV model is completely characterized by eight new parameters: the gauge coupling g_X, the mass $\mu_{\mathcal{S}}$ and quartic $\lambda_{\mathcal{S}}$ of the renormalizable potential of $\mathcal{S}$, the new Yukawa couplings $Y_{\mathcal{T},\mathcal{M}}$, here taken to be real, and the vector-like mass-term parameters $M_{\mathcal{T},\mathcal{M}}$. In particular, the Lagrangian of the model contains the following terms:

$$M_{\mathcal{T}}\overline{\mathcal{T}_R}\mathcal{T}_L+M_{\mathcal{M}}\overline{\mathcal{M}}_R\mathcal{M}_L+Y_t\overline{u}_3\tilde{H}^\dagger Q_3+Y_{\mathcal{T}}\overline{u}_3\mathcal{T}_L\mathcal{S}+Y_\mu\overline{e}_2H^\dagger L_2+Y_{\mathcal{M}}\overline{\mathcal{M}}_R L_2\mathcal{S}+\text{h.c.}\,, \quad (9.11)$$

that characterize the mixing pattern of SM fields and vector-like partners.[10] Symmetry breaking of $U(1)_X$ is triggered by $\langle\mathcal{S}\rangle^2=-\mu_{\mathcal{S}}^2/(2\lambda_{\mathcal{S}})\equiv\eta^2\neq 0$, that implies the following fermionic mixing patterns:

$$\text{top sector:}\quad \begin{pmatrix}\overline{u}_3 & \overline{\mathcal{T}}_R\end{pmatrix}\begin{pmatrix}\frac{Y_t\,v}{\sqrt{2}} & \frac{Y_{\mathcal{T}}\eta}{\sqrt{2}}\\ 0 & M_{\mathcal{T}}\end{pmatrix}\begin{pmatrix}U_3\\ \mathcal{T}_L\end{pmatrix}+\text{h.c.}\,, \quad (9.12)$$

$$\text{muon sector:}\quad \begin{pmatrix}\overline{e}_2 & \overline{\mathcal{M}}_R\end{pmatrix}\begin{pmatrix}\frac{Y_\mu v}{\sqrt{2}} & 0\\ \frac{Y_{\mathcal{M}}\eta}{\sqrt{2}} & M_{\mathcal{M}}\end{pmatrix}\begin{pmatrix}E_2\\ \mathcal{M}_L\end{pmatrix}+\text{h.c.}\,,$$

where U_i (E_i) indicates the Q_i-component (L_i-component) with weak isospin 1/2 (-1/2). Using the determinant and trace of the squared mass matrices, one can easily show that the eigenvalues $m_{t,\mathcal{T}}$ and $m_{\mu,\mathcal{M}}$ must satisfy [503]:

$$\begin{aligned} m_{t,\mu}\,m_{\mathcal{T},\mathcal{M}} &= \frac{1}{\sqrt{2}}Y_{t,\mu}vM_{\mathcal{T},\mathcal{M}}\,, \quad (9.13)\\ m_{t,\mu}^2+m_{\mathcal{T},\mathcal{M}}^2 &= M_{\mathcal{T},\mathcal{M}}^2+\frac{1}{2}(Y_{t,\mu}\,v)^2+\frac{1}{2}(Y_{\mathcal{T},\mathcal{M}}\,\eta)^2\,, \end{aligned}$$

that in the decoupling limit clearly yield: $m_{t,\mu}\simeq Y_{t,\mu}v/\sqrt{2}$, $m_{\mathcal{T},\mathcal{M}}\simeq M_{\mathcal{T},\mathcal{M}}$.

Defining for the top sector the rotation matrix from the interaction to the mass basis following the convention:

$$\begin{pmatrix}t_{R(L)}\\ \mathcal{T}'_{R(L)}\end{pmatrix}=\begin{pmatrix}\cos\theta^t_{R(L)} & -\sin\theta^t_{R(L)}\\ \sin\theta^t_{R(L)} & \cos\theta^t_{R(L)}\end{pmatrix}\begin{pmatrix}u_3(U_3)\\ \mathcal{T}_{R(L)}\end{pmatrix}\,, \quad (9.14)$$

and doing similarly for the muonic sector, the mixing angles between SM fields, t and μ, and their partner mass eigenstates, $\mathcal{T}'$ and $\mathcal{M}'$, can be conveniently expressed in terms of the dimensionless ratios $\xi_{\mathcal{T},\mathcal{M}}$ and $\varepsilon_{t,\mu}$:

$$\begin{aligned} &\tan 2\theta^t_R=\tfrac{2\xi_{\mathcal{T}}}{\xi_{\mathcal{T}}^2-\varepsilon_t^2-1}\,,\quad \tan 2\theta^t_L=\tfrac{2\varepsilon_t}{\xi_{\mathcal{T}}^2-\varepsilon_t^2+1}\,,\ \text{with}\ \varepsilon_t\equiv\tfrac{Y_t v}{Y_{\mathcal{T}}\eta},\ \xi_{\mathcal{T}}\equiv\tfrac{\sqrt{2}M_{\mathcal{T}}}{\eta Y_{\mathcal{T}}}\,; \quad (9.15)\\ &\tan 2\theta^\mu_R=\tfrac{2\varepsilon_\mu}{\xi_{\mathcal{M}}^2-\varepsilon_\mu^2+1}\,,\ \tan 2\theta^t_L=\tfrac{2\xi_{\mathcal{M}}}{\xi_{\mathcal{M}}^2-\varepsilon_\mu^2-1}\,,\ \text{with}\ \varepsilon_\mu\equiv\tfrac{Y_\mu v}{Y_{\mathcal{M}}\eta},\ \xi_{\mathcal{M}}\equiv\tfrac{\sqrt{2}M_{\mathcal{M}}}{\eta Y_{\mathcal{M}}}\,. \end{aligned}$$

In a perturbative expansion in $\varepsilon_{t,\mu}$, eq. (9.15) clearly shows that the mixing in the top sector proceeds mainly through $\tan\theta^t_R\simeq 1/\xi_{\mathcal{T}}$, while in the muonic sector one has

[10] Note that upon an opposite $U(1)_X$ charge assignment for the vector-like fermionic partners than the one implicitly assumed, one should replace in eq. (9.11) $\mathcal{S}$ with $S^\dagger$.

$\tan\theta_L^\mu \simeq 1/\xi_{\mathcal{M}}$ and very tiny $\tan\theta_R^\mu$.

Hence, for $\varepsilon_{t,\mu}/\xi_{\mathcal{T},\mathcal{M}} = Y_{t,\mu}v/\sqrt{2}M_{\mathcal{T},\mathcal{M}} < 1$, the leading couplings of the Z' boson to the SM fields correspond to right-handed tops and to left-handed muons as well as neutrinos according to:[11]

$$g_{Z't_R} = g_X \sin^2\theta_R^t = \frac{g_X}{1+\xi_{\mathcal{T}}^2} + \mathcal{O}\left(\varepsilon_t^2/\xi_{\mathcal{T}}^2\right) , \tag{9.16}$$

$$g_{Z'\mu_L(\nu)} = g_X \sin^2\theta_L^\mu = \frac{g_X}{1+\xi_{\mathcal{M}}^2} + \mathcal{O}\left(\varepsilon_\mu^2/\xi_{\mathcal{M}}^2\right) , \tag{9.17}$$

with $g_{Z't_L(\mu_R)}$ being non-negligible only at order $\varepsilon_{t(\mu)}^2/\xi_{\mathcal{T}(\mathcal{M})}^2$. Consequently, integrating out the Z' relevantly generates the operator O_{2233}^{Lu} with Wilson coefficient:

$$C_{2233}^{Lu} = -\frac{g_{Z't_R}g_{Z'\mu_L}}{m_{Z'}^2} \simeq -\frac{1}{(1+\xi_{\mathcal{T}}^2)(1+\xi_{\mathcal{M}}^2)\,\eta^2} , \tag{9.18}$$

together with four-fermion operators built of t_R or μ_L, ν fields that can be potentially probed at collider and by experimental signatures like ν-trident production.

From eq. (9.18) it is clear that in order to have $|C_{2233}^{Lu}| \sim 2$ TeV^{-2} as highlighted in Figure 9.5, one needs to rely on a relatively low symmetry-breaking scale $\eta \lesssim$ TeV;[12] for $m_{Z'} \sim$ TeV this implies $g_X \gtrsim 1$. In Figure 9.6 we show the 1σ region corresponding to the explanation of B anomalies via eq. (9.18) in the parameter space $\xi_{\mathcal{T},\mathcal{M}}$, fixing the gauge coupling $g_X = m_{Z'}/\eta$ for a tentative Z' gauge boson at the TeV scale and the VEV of the new scalar field $\mathcal{S}$ set to $\eta = 250$ GeV and $\eta = 500$ GeV in the left and right panel, respectively. In the same plot, we re-interpret in our scenario the most relevant collider constraints originally identified in ref. [505].

For small values of $\xi_{\mathcal{M}}$, the measurement of neutrino-trident production performed in [544] is effective, and its constraint is reported at the 2σ level with the orange vertical band. Under the reasonable assumption that the Z' boson is mainly produced at tree level in association with the $t\bar{t}$ pair, in the blue region we show the 95% high-p_T constraint stemming from the recasting of the $pp \to \mu^-\mu^+t\bar{t}$ search at ATLAS [545], while in cyan we report the expected constraint on the model from the 4-tops analysis of CMS [546], see ref. [505] for further details. From the same work, we also adopt the expected collider constraints for future projected luminosity corresponding to 300 fb^{-1}, shown with dashed lines. Note that these projections become of fundamental importance when it comes to probe the interesting 1σ region connected to B anomalies. In particular, the right panel in Figure 9.6 captures the benchmark for a promising discovery at the High-Luminosity LHC.

Finally, in the same figure, fixing the partner Yukawa coupling to $\mathcal{O}(1)$ values as reported in the two panels, we mark in gray the region corresponding to the bound on the mass of the vector-like partner expected from collider, taken to be $m_{\mathcal{T}} = 1.4$ TeV

[11] In what follows, for $\eta \sim \mathcal{O}(v)$ we will have $\xi_T \sim \mathcal{O}(1)$; consequently, $\varepsilon_t \sim \mathcal{O}(v/M_{\mathcal{T}})$.

[12] Note that even for masses as low as $\mu_{\mathcal{S}} \sim \mathcal{O}(v)$, for $\eta \simeq v$ and $\lambda_{\mathcal{S}} \sim \mathcal{O}(1)$, the interactions of $\mathcal{S}$ do not alter the phenomenology discussed here since the largest $\mathcal{S}$-generated effects are still suppressed as $\mathcal{O}(\varepsilon_t^2/\xi_{\mathcal{T}}^2)$.

from the search at ATLAS in ref. [547], and $m_{\mathcal{M}} = 0.8$ TeV from the CMS analysis of ref. [548].

As already discussed, the scenario depicted in Figure 9.6 remains viable under the lens of EW precision as long as we also have some heavy new dynamics yielding at the EW scale an imprint of $O_{22}^{HL^{(1)}}$ consistently with the correlation obtained in the left panel of Figure 9.5.

A simple way to obtain such NP contribution would be to consider the joint effect that the leptonic mixing of the vector-like partner would have together with the kinetic mixing of the Z', so far neglected. The Z-Z' mixing could also originate from charging the new scalar field $\mathcal{S}$ under both Abelian gauge groups, introducing a small misalignment with the standard hypercharge $U(1)_Y$ in the UV. However, the required mixing of the Z' would end up mediating light-quark pair annihilation into muons: the typical size of the Wilson coefficient of this four-fermion operator would be $\mathcal{O}(g_Y^2/m_{Z'}^2)$, in net tension with the di-muon bound from ATLAS [545], probing NP scales as high as 20 - 40 TeV for $\mathcal{O}(1)$ (dimensionless) couplings. Hence, we rule out here this possibility.

Interestingly, it is still possible to generate $O_{22}^{HL^{(1)}}$ without relying on the Z-Z' mixing, but rather invoking the presence in the UV theory of additional new vector-like leptonic states [549, 550]. These ones may be phenomenologically interesting in relation to the problem of the origin of neutrino masses as well as for the prediction of the anomalous magnetic moment $(g-2)_\mu$ [551], and may give peculiar multi-lepton signatures at colliders [552, 553].

In the most economic scenario, we may consider the presence in the UV theory of a pair of new vector-like muonic partners: a singlet of $SU(2)_L$, S_Y, and a triplet of $SU(2)_L$, T_Y, where in both cases the subscript Y denotes the hypercharge of the fermion. These fields would have their own mass terms controlled by the parameters M_{S_Y,T_Y}, and interact with the SM doublet L_2 via the Yukawa couplings $\mathcal{Y}_{S_Y,T_Y}$ according to:

$$\mathcal{Y}_{S_0}\overline{S}_{0,R}\tilde{H}^\dagger L_2 + \mathcal{Y}_{T_0}\overline{T}^A_{0,R}\tau^A\tilde{H}^\dagger L_2 + \text{h.c.}\ , \tag{9.19}$$

where we have reported the case of vector-like muonic partners with hypercharge $Y = 0$. We assume the new Yukawa couplings to be real. Another possibility of interest may be the one of replacing in eq. (9.19) $\tilde{H} = i\tau^2 H^*$ with the Higgs doublet, H, and involve then the pair of vector-like partners with hypercharge $Y = 1$.

Integrating out these vector-like states from the theory would generate contributions related to $\mathcal{O}^{HL^{(1,3)}}$ [550, 551] of the form:

$$\begin{aligned} C_{22}^{HL^{(1)}} &= \frac{\mathcal{Y}_{S_0}^2}{4M_{S_0}^2} - \frac{\mathcal{Y}_{S_1}^2}{4M_{S_1}^2} + \frac{3\mathcal{Y}_{T_0}^2}{4M_{T_0}^2} - \frac{3\mathcal{Y}_{T_1}^2}{4M_{T_1}^2}\ , \\ C_{22}^{HL^{(3)}} &= -\frac{\mathcal{Y}_{S_0}^2}{4M_{S_0}^2} - \frac{\mathcal{Y}_{S_1}^2}{4M_{S_1}^2} + \frac{\mathcal{Y}_{T_0}^2}{4M_{T_0}^2} + \frac{\mathcal{Y}_{T_1}^2}{4M_{T_1}^2}\ . \end{aligned} \tag{9.20}$$

Clearly, in order to have $C_{22}^{HL^{(1)}} \sim 0.1$ and negligible $C_{22}^{HL^{(3)}}$[13], one would need to rely on a tuning of the $Y = 0$ triplet Wilson coefficient with one of the contributions coming from the singlet vector-like muonic partner. However, once generated at the NP scale $\Lambda \sim \mathcal{O}(M_{T_0}) \gg v$, we observe that the relation established between the triplet and singlet contributions to $O^{HL^{(1,3)}}$ would be stable under the RG flow of the SMEFT.

A final comment is needed for the electron scenario reported in the right panel of Figure 9.5, that involves opposite signs for the Wilson coefficients of O^{Lu} and $O^{HL^{(1)}}$ discussed so far. For the former, we note that the sign highlighted in the matching in eq. (9.18) follows from having assumed the same sign for the charge of the vector-like top and muon partners under $U(1)_X$. Hence, assuming the vector-like electron partner to have the opposite $U(1)_X$ charge of the top-partner one would be sufficient to accomplish $C_{1133}^{Lu} > 0$. (Of course, this would also imply a distinct use in eq. (9.11) of $\mathcal{S}$ and $\mathcal{S}^\dagger$ couplings in the Yukawa terms of the vector-like partners involved to keep the theory invariant under $U(1)_X$.) For what concerns the generation of $C_{11}^{HL^{(1)}} < 0$, according to eq. (9.20) one needs to correlate once again the contribution stemming from S_0, or from S_1, with the effect coming from a $SU(2)_L$ triplet, that now needs to be identified with T_1, namely the triplet of hypercharge $Y = 1$.

Eventually, we wish also to comment on the possible role of the O^{eu} operator, so far neglected in this discussion, but of potential relevance more in general. In fact, as mentioned earlier, the presence of O^{eu} would be particularly needed in the case where hadronic corrections entering in the amplitude of $B \to K^* \ell\ell$ would be of the size originally estimated in [454]. In that case, a solution to flavour anomalies would be preferred in the muonic channel with NP Wilson coefficient C_{2233}^{eu} also substantially deviating from 0, as already discussed in subsection 9.4.1. Then, one would need to involve also the operator C_{22}^{He} to relieve possible tensions with EW precision. In a general picture, the required NP effects from $O_{11,22}^{He}$ can be obtained integrating out heavy vector-like $SU(2)_L$ leptonic doublets.

9.5.2 Leptoquark scenarios

An alternative way to reproduce the minimal EFT scenario of Figure 9.5 would be via *leptoquarks* (LQ), particles generically predicted in grand unified theories (GUTs) [554, 555]. Notoriously, LQ-induced dimension-six operators could be potentially dangerous as they would lead to proton decay at tree level, forcing to push their scale up to the GUT scale. However, the outcome may drastically change in models where the couplings of the LQs would be non-universal with respect to lepton and/or quark flavours. In such a case their mass could be much lower than what typically expected in GUTs and their signatures may actually be probed at present colliders. Interestingly, such LQs are candidates that could explain the lepton flavour universality violation – even at the loop level here considered [505, 510] – hinted in the recent LHCb and Belle data. However,

[13] We have indeed verified that a scenario involving at the same time C^{Lu} and $C^{HL^{(1,3)}}$ would not alter what already highlighted in Figure 9.5, with the best-fit value for $|C^{HL^{(3)}}|$ turning out to be of $\mathcal{O}(10^{-2})$.

this would imply generically a rather non-trivial flavour structure in the theory [556]. For a comprehensive survey of LQ models, see for instance [264, 496, 557–559].

Here, we limit ourselves to the case of toy models that specifically generate the operators of interest, namely $C^{Lu}_{\ell\ell 33}$ and $C^{eu}_{\ell\ell 33}$, for $\ell = 1$ (electron) or $\ell = 2$ (muon). In these peculiar LQ models we then assume that couplings between right-handed top quarks and light leptons are the only ones that actually matter for TeV phenomenology.

In Table 9.1 we list the vector and scalar LQs that constitute the potential LQ candidates able to generate the solutions for $b \to s\ell\ell$ anomalies at one loop under scrutiny.

Vector LQ: $\mathcal{V}^\mu$	$SU(3)_c \otimes SU(2)_L \otimes U(1)_Y$	Comments
$\overline{L}_\ell \gamma_\mu (\tau^A) Q_3 \, \mathcal{V}^{\mu(A)}$	$(\overline{\mathbf{3}}, \mathbf{1} \text{ or } \mathbf{3}, -2/3)$	not of interest
$(\mathcal{V}^\mu)^\dagger \, \overline{e}^c_\ell \gamma_\mu Q_3$	$(\overline{\mathbf{3}}, \mathbf{2}, 5/6)$	not of interest
$\overline{L}^c_\ell \gamma_\mu u_3 \, i\tau^2 \, \mathcal{V}^\mu$	$(\overline{\mathbf{3}}, \mathbf{2}, -1/6)$	generates $C^{Lu}_{\ell\ell 33} > 0$
$\overline{e}_\ell \gamma_\mu u_3 \, \mathcal{V}^\mu$	$(\overline{\mathbf{3}}, \mathbf{1}, -5/3)$	generates $C^{eu}_{\ell\ell 33} < 0$
Scalar LQ: $\mathcal{S}$		
$\overline{L}_\ell (\tau^A)(i\tau^2) \, Q^c_3 \, \mathcal{S}^{\dagger(A)}$	$(\overline{\mathbf{3}}, \mathbf{1} \text{ or } \mathbf{3}, 1/3)$	not of interest
$\overline{e}_\ell Q_3 \, i\tau^2 \mathcal{S}$	$(\overline{\mathbf{3}}, \mathbf{2}, -7/6)$	not of interest
$\overline{L}_\ell u_3 \, \mathcal{S}$	$(\overline{\mathbf{3}}, \mathbf{2}, -7/6)$	generates $C^{Lu}_{\ell\ell 33} < 0$
$\overline{e}^c_\ell u_3 \, \mathcal{S}$	$(\overline{\mathbf{3}}, \mathbf{1}, 1/3)$	generates $C^{eu}_{\ell\ell 33} > 0$

Table 9.1. Scalar and vector LQ interactions under scrutiny: LQs of interest for our analysis have to generate the dimension-six operators $O^{Lu,eu}_{\ell\ell 33}$.

Looking back at Figure 9.5, from the table above we recognize as the most economic LQ scenario for the resolution of B anomalies at one loop, the case of the vector LQ $\mathcal{V}^\mu \sim (\overline{\mathbf{3}}, \mathbf{2}, -1/6)$ for LUV effects originating from electron couplings, and the scalar $\mathcal{S} \sim (\overline{\mathbf{3}}, \mathbf{2}, -7/6)$ for the ones associated to muons. The interaction terms of interest are:

$$\mathcal{L}_{\mathcal{V}\overline{f}f} = \tilde{\lambda}_{te} \, \overline{L}^c_1 \gamma_\mu u_3 \, i\tau^2 \mathcal{V}^\mu + \text{h.c.} \quad , \quad \mathcal{L}_{\mathcal{S}\overline{f}f} = \lambda_{t\mu} \, \overline{L}_2 u_3 \mathcal{S} + \text{h.c.}, \tag{9.21}$$

leading to the corresponding matching condition:

$$C^{Lu}_{1133} = + \frac{|\tilde{\lambda}_{te}|^2}{M^2_{\mathcal{V}}} \quad , \quad C^{Lu}_{2233} = - \frac{|\lambda_{t\mu}|^2}{2M^2_{\mathcal{S}}} \, . \tag{9.22}$$

In Figure 9.7 we report in (lighter) magenta the underlying $1(2)\sigma$ region where B anomalies are addressed in concordance with the minimal EFT picture of Figure 9.5. In the same plot, we also show a conservative estimate of the present LHC constraint on the mass of the LQ states considered, based on the dedicated collider study of ref. [560].

We conclude noting that from the point of view of realizing the economic EFT result in Figure 9.5, these leptoquark models should again be supplied by the combination of a singlet and a triplet $SU(2)_L$ muon/electron partners. Otherwise, in these models the leading contribution to $C^{HL^{(1)}}_{\ell\ell}$ would appear only at the loop level, in net distinction

with the Z' scenario, where the Z-Z' mixing could be a priori exploited.

9.6 Summary

In this work we have revisited the analysis of $b \to s\ell\ell$ anomalies looking for NP solutions that generate these FCNC processes at one loop and do not involve any new source of flavour violation beyond the SM ones. To this end, we have performed a broad analysis with dimension-six operators in the SMEFT, combining the experimental data on B-physics with measurements of EWPO. The general outcome of our study is summarized in Figure 9.1 and, supported with Figure 9.3, shows that a resolution of B anomalies of the MFV nature can be made fully compatible with EW precision.

From the SMEFT results derived we have then proceeded to identifying a minimal EFT scenario as captured in Figure 9.5, that served as a simple guidance for SM UV completions. In this regard, we have explored in some detail the top-phillic and muon/electron-phillic Z', interesting for direct searches at collider as highlighted in Figure 9.6. We have also commented on the viable leptoquark scenarios, collected in Table 9.1. For both Z' and leptoquark solutions we have found that additional contributions were necessary in order to maintain Z coupling measurements under control: in particular, we have shown that a correlated pair of vector-like leptons, a $SU(2)_L$ singlet and a triplet, can realize the minimal EFT scenario depicted on Figure 9.5. We observe that the existence of these particles may be independently motivated by the heavy new dynamics underlying the origin of neutrino masses and/or by a tentative explanation of the $(g-2)_\mu$ anomaly [551].

We conclude by noting that the measurement of B decays at the scale of a few GeV is expected to reach a precision regime with the completion of the future runs at LHC and SuperKEKB. Hence, better measurements of the LUV observables and angular distributions of $b \to s\ell\ell$ will be available in the next few years from Belle II [469] and LHCb [561]. These will add a fundamental verification of the current interpretation of B anomalies and of the direction in our search for NP signatures. Along these lines, should these signals of LUV persist, their interplay with EW precision measurements could be further tested at future e^+e^- colliders. In particular, circular e^+e^- colliders running at the Z pole, such as the FCC-ee [562, 563] or CEPC [564], could test deviations in the lepton universality of neutral weak currents with more than one order of magnitude improvement in precision compared to current data. At linear colliders, like the ILC [565] or CLIC [566], where there is no proposed run at the Z pole, it would still be possible to obtain a significant improvement in the measurements of EWPO via radiative return to the Z [567]. Furthermore, the high-energy regime achievable at linear colliders would allow, after crossing the $t\bar{t}$ threshold, to directly test the effects of the interactions $O_{1133}^{Lu,eu}$ via $e^+e^- \to t\bar{t}$. For the muon case, on the other hand, to test $O_{2233}^{Lu,eu}$ one would still need to rely on more complicated signals, such as $t\bar{t}\mu^+\mu^-$, which would be in any case cleaner than at the LHC. (However, ideal optimal tests of these 4-fermion operators in 2-to-2 scattering processes would require a high-energy muon collider.) All of these could represent valuable additions from a "flavour" perspective in the interpretation of EW (and Higgs) measurements at these future machines within the EFT framework [523,

568].

9.7 Discussions on EW fits

Here we revisit the constraints set by EWPO on the parameter space of the SMEFT. We make minimal flavour assumptions and include all quark and lepton operators described in the **EW** fit presented in section 9.3. Measurements of EWPO have been extensively studied in the literature [142, 421, 422, 424, 509, 569–574] within the SMEFT framework. The purpose here is to provide further details on the correlation between quark and lepton sectors constrained by EWPO, illustrating some of the effects when going beyond the tree-level analysis.

The experimental inputs are the same considered for the **EW** fit in section 9.3, and include, in particular, the full set measurements taken at LEP/SLD at the Z pole, as well as the measurements of the W boson obtained at LEP II, the Tevatron and the LHC (e.g. mass, width, branching ratios as well as the determination of $|V_{tb}|$ at the LHC [14]). For these fits we use the `HEPfit`package [255] as for the rest of the work.

We first consider the case of the **EW** fit at the tree level. In this case, the results of the fit reveal that while there is sizable correlation between the left-handed leptonic operators, as well as between the different quark operators, both sector are however decoupled to a good extent in the fit as can be seen from Figure 9.8.

For the main fits presented in section 9.4, however, we also consider the leading logarithmically enhanced contributions at one-loop level via RG running. For our purposes, and considering the size of the bounds on the different operators from the EW fit, the most important contribution comes from $C_{33}^{HQ^{(1)}}$. This induces an universal contribution that propagates into all EWPO. As a result of this, and similar to what was seen between the leptonic operators and the 4-fermion operators due to their interplay in eqs. (9.7), a non-trivial pattern of correlations between the lepton and quark operator sectors in the **EW** fit arises, as shown in Figure 9.2. Similar to the change in the bounds on the leptonic operators in the **EW+Flavour** fit once we included the RG effects of the four-fermion operators, the bounds on the leptonic operators also relax in the EW fit once we include the RG effects from $C_{33}^{HQ^{(1)}}$. This is shown in Figure 9.9. However, unlike in the **EW+Flavour** fit, such effects do not induce a significant shift in the central values of the Wilson coefficients, which is simply due to the fact that the data selects $C_{33}^{HQ^{(1)}}$ to be centered around zero.

As can be seen in Figure 9.9, the relaxation of the bounds can be in some cases rather dramatic, which brings about the question of what could be the impact of further effects not included in our analysis. We estimated that including the main RG effects for all the other operators in the EW fit amounts to changes of at most $\sim 25\%$. One should

[14] The extraction of $|V_{tb}|$ could be, a priori, affected by other SMEFT effects entering in single-top production, e.g. 4-fermion operators. Such effects are neglected in our analysis. The only effect of this input in the EW fits in this paper is to lift a flat direction that would otherwise appear between $C_{33}^{HQ^{(1)}}$ and $C_{33}^{HQ^{(3)}}$, had we excluded this measurement. Even with this input, these two coefficients are nearly 100% correlated, as can be seen in Figure 9.8.

also note that finite terms involving the Wilson coefficients of the quark coupling may become relevant at this point. As can be deduced from the full NLO results presented in [574], these are not expected to significantly change the picture. In any case, the overall conclusions on this paper regarding the reconciliation between EW data and B anomalies hold true.

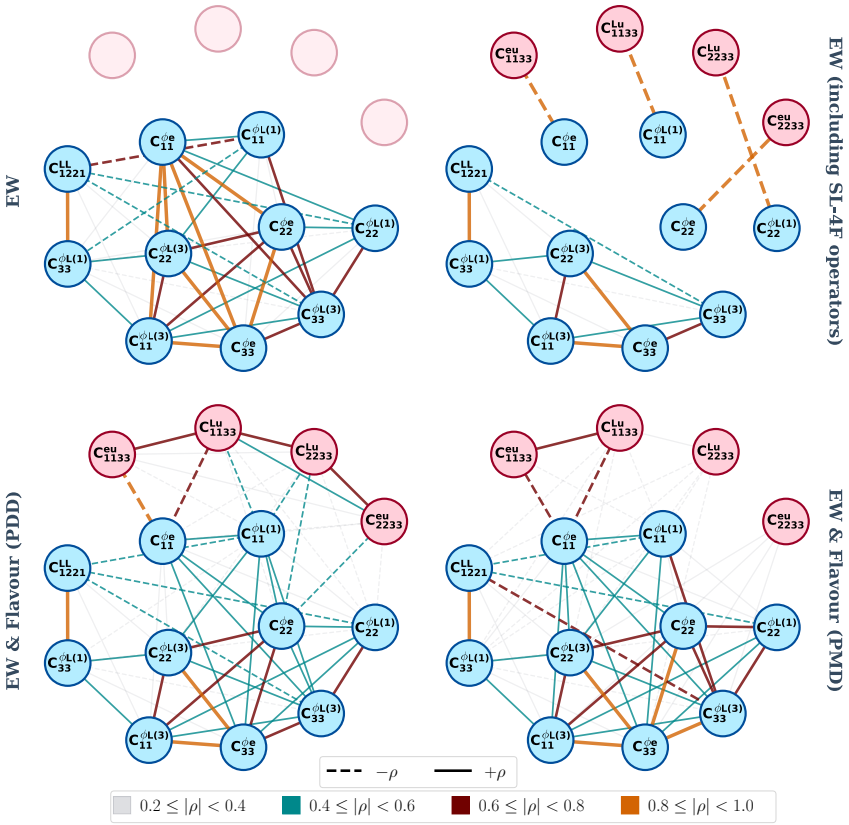

Figure 9.4. *Correlations among dimension-six operators involving leptonic currents in different scenarios. In the upper side we show the* ***EW*** *fit (upper-left panel), and the scenario where in the same setup the SL-4F operators are also included (upper-right panel), highlighting the anti-correlation among the set of Wilson coefficients* $C_{\ell\ell}^{HL^{(1)}}, C_{\ell\ell}^{He}$ *and* $C_{\ell\ell 33}^{Lu,eu}$*. In the lower-side panels we show how* $b \to s\ell\ell$ *measurements break these degeneracies, showing the* ***Flavour*** *fit for the PDD case (lower-left panel), and the PMD one (lower-right panel).*

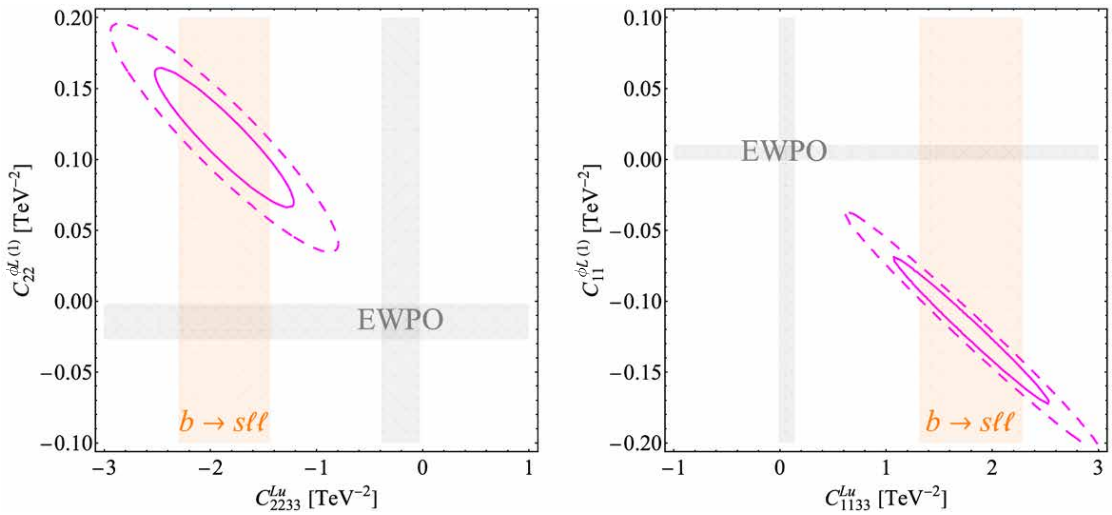

Figure 9.5. *The most economic EFT picture where B anomalies can be reconciled at one loop with EWPO. In (dashed) magenta the 1(2)σ correlation between the Wilson coefficients of the operators responsible of addressing B anomalies without any source of flavour violation beyond the Yukawa couplings of the SM. The minimal scenario involves LUV effects in the (electron) muon sector as highlighted by the 1σ orange band in the (right) left panel, originated from* $b \to s\ell\ell$ *data analyzed with a conservative approach to hadronic uncertainties. In same figure, the 1σ region allowed by EWPO within a single-operator analysis, horizontal and vertical grey bands.*

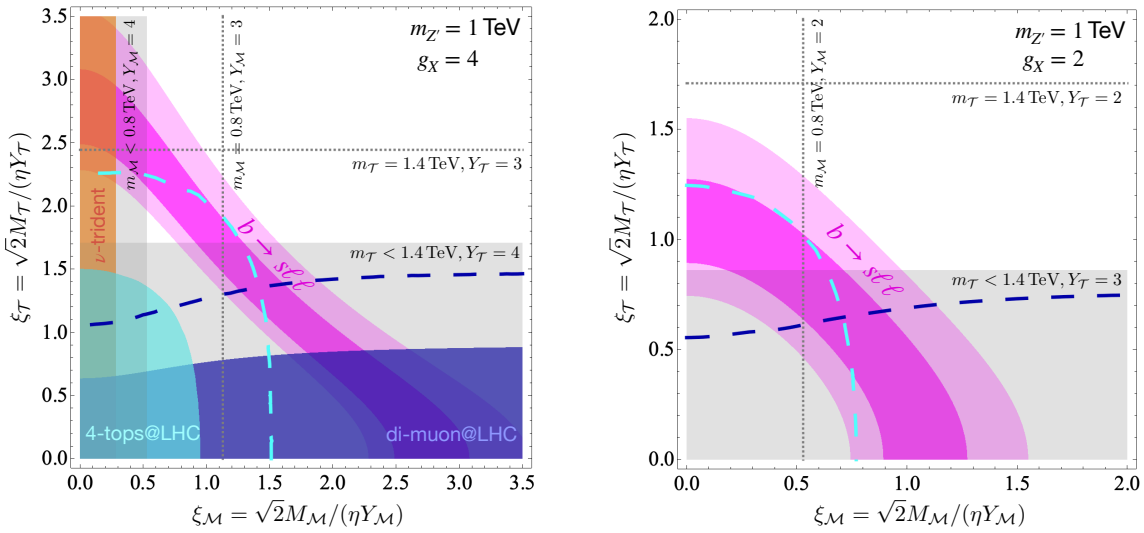

Figure 9.6. *68% (95%) probability region in (lighter) magenta for the minimal Z' model that addresses B anomalies in the parameter space identified by eq. (9.18), with $\eta = m_{Z'}/4$ (left panel), and $\eta = m_{Z'}/2$ (right panel), for $m_{Z'} = 1$ TeV. Relevant LHC constraints are reported in blue and cyan regions according to the analysis originally performed in ref. [505], together with the corresponding collider projections at 300 fb^{-1}. Finally, the gray regions underlie the parameter space where the mass of the vector-like partner lies below current collider limits for a fixed Yukawa coupling as explicitly reported, while dashed lines show the corresponding shift of the limit due to a smaller value of the same type of Yukawa coupling.*

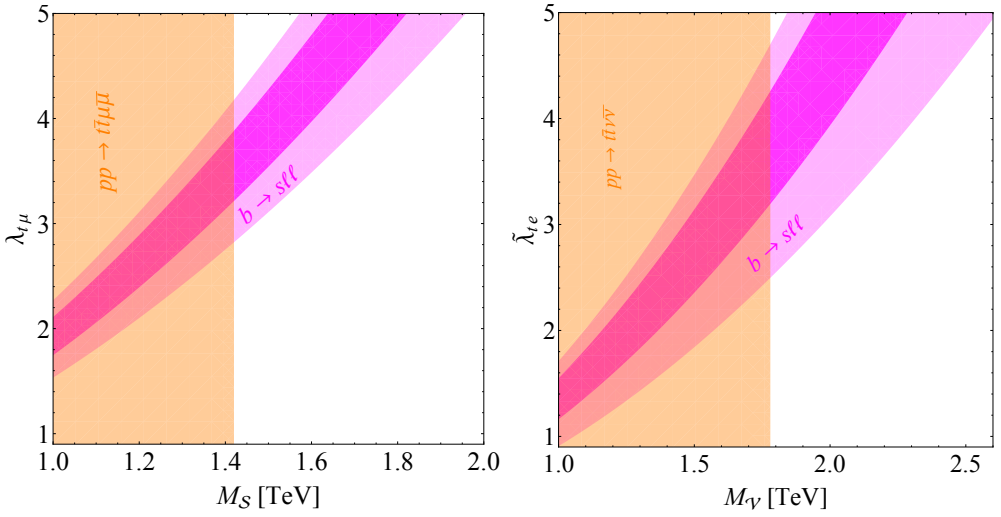

Figure 9.7. 68% (95%) probability region in magenta for the LQ candidates addressing $b \to s\ell\ell$ anomalies at one loop. The scalar (vector) LQ corresponds to a solution with LUV effects related to muon (electron) couplings. A conservative bound on the corresponding LQ mass is reported according to the analysis of ref. [560].

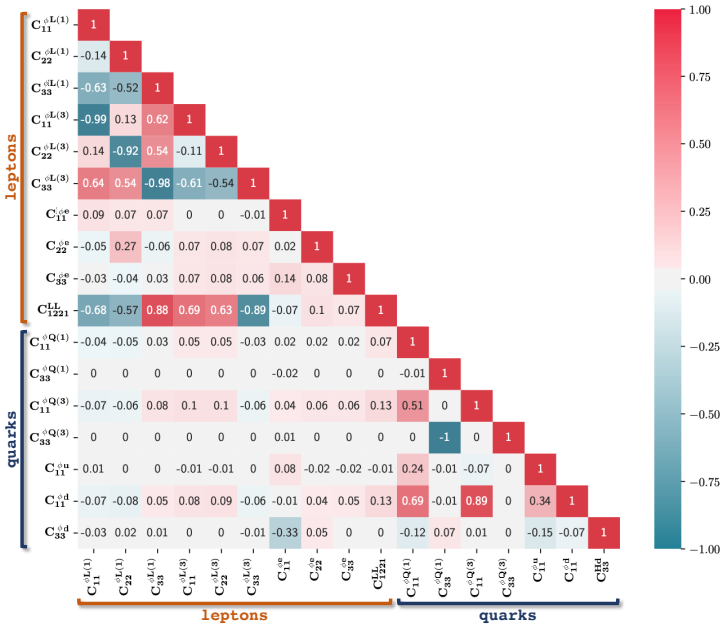

Figure 9.8. *The correlation matrix extracted from the SMEFT analysis of the set of independent operators in eqs. (9.2), (9.8), (9.9), including only their effects at tree-level. The two distinct groups of correlated Wilson coefficients associated to leptonic and quark interactions are remarked as "leptons" and "quarks", respectively. Note that, compared to Figure 9.2, in this tree-level analysis there is a significant decorrelation between the constraints on quarks and lepton operators.*

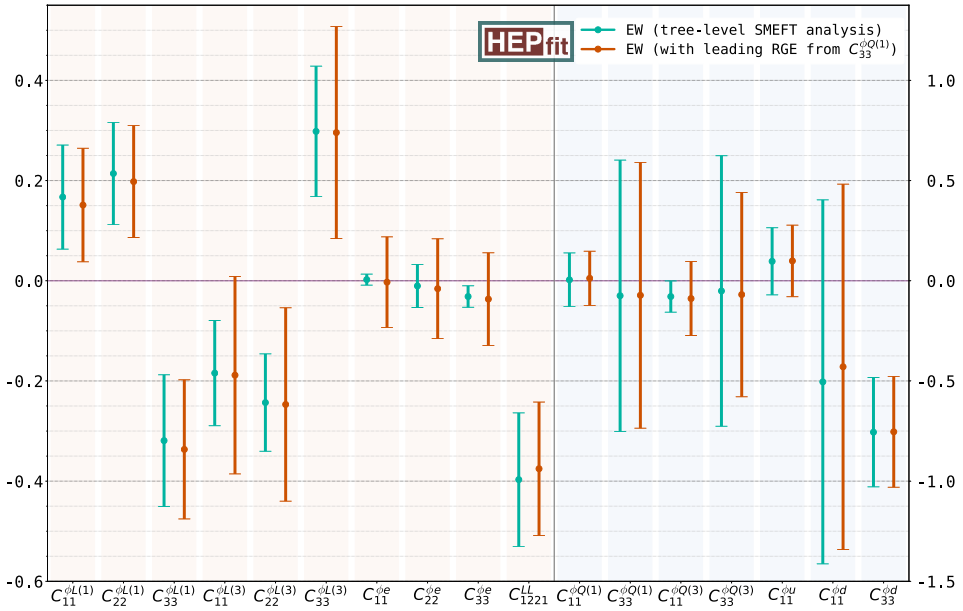

Figure 9.9. *Comparison of the mean and standard deviation of the marginalized posterior for the Wilson coefficients (in TeV^{-2}) of the operators included in the* **EW** *fit under two different approximations: in green the results from a pure tree-level analysis; in orange we show the result including the dominant log-enhanced one-loop terms. See text for details.*

Bibliography

[1] L. Alasfar, G. Degrassi, P. P. Giardino, R. Gröber, and M. Vitti, "Virtual corrections to $gg \to ZH$ via a transverse momentum expansion," *JHEP* **05** (2021) 168, arXiv:2103.06225 [hep-ph].

[2] L. Alasfar, R. Corral Lopez, and R. Gröber, "Probing Higgs couplings to light quarks via Higgs pair production," *JHEP* **11** (2019) 088, arXiv:1909.05279 [hep-ph].

[3] L. Alasfar, A. Azatov, J. de Blas, A. Paul, and M. Valli, "B anomalies under the lens of electroweak precision," *JHEP* **12** (2020) 016, arXiv:2007.04400 [hep-ph].

[4] R. A. Minlos, *Introduction to mathematical statistical physics*. No. 19. American Mathematical Soc., 2000.

[5] M. Gell-Mann, "The eightfold way: A theory of strong interaction symmetry,". https://www.osti.gov/biblio/4008239.

[6] C. N. Yang and R. L. Mills, "Conservation of isotopic spin and isotopic gauge invariance," *Phys. Rev.* **96** (Oct, 1954) 191–195. https://link.aps.org/doi/10.1103/PhysRev.96.191.

[7] **Particle Data Group** Collaboration, P. Zyla *et al.*, "Review of Particle Physics," *PTEP* **2020** no. 8, (2020) 083C01.

[8] D. S. Freed, "Lectures on topological quantum field theory," 1993.

[9] R. Dijkgraaf and E. Witten, "Topological gauge theories and group cohomology," *Communications in Mathematical Physics* **129** no. 2, (1990) 393–429.

[10] A. Salam and J. C. Ward, "On a gauge theory of elementary interactions," *Il Nuovo Cimento (1955-1965)* **19** no. 1, (1961) 165–170. https://doi.org/10.1007/BF02812723.

[11] A. Salam and J. C. Ward, "Weak and electromagnetic interactions," *Il Nuovo Cimento (1955-1965)* **11** no. 4, (1959) 568–577. https://doi.org/10.1007/BF02726525.

[12] S. Weinberg, "A model of leptons," *Phys. Rev. Lett.* **19** (Nov, 1967) 1264–1266. https://link.aps.org/doi/10.1103/PhysRevLett.19.1264.

[13] F. Capozzi, E. Lisi, A. Marrone, D. Montanino, and A. Palazzo, "Neutrino masses and mixings: Status of known and unknown 3ν parameters," *Nucl. Phys. B* **908** (2016) 218–234, arXiv:1601.07777 [hep-ph].

[14] **ALEPH, DELPHI, L3, OPAL, SLD, LEP Electroweak Working Group, SLD Electroweak Group, SLD Heavy Flavour Group** Collaboration, S. Schael *et al.*, "Precision electroweak measurements on the Z resonance," *Phys. Rept.* **427** (2006) 257–454, arXiv:hep-ex/0509008 [hep-ex].

[15] **SLD** Collaboration, K. Abe *et al.*, "First direct measurement of the parity violating coupling of the Z0 to the s quark," *Phys. Rev. Lett.* **85** (2000) 5059–5063, arXiv:hep-ex/0006019.

[16] **CDF, D0** Collaboration, T. E. W. Group, "2012 Update of the Combination of CDF and D0 Results for the Mass of the W Boson," arXiv:1204.0042 [hep-ex].

[17] **ALEPH, DELPHI, L3, OPAL, LEP Electroweak** Collaboration, S. Schael *et al.*, "Electroweak Measurements in Electron-Positron Collisions at W-Boson-Pair Energies at LEP," *Phys. Rept.* **532** (2013) 119–244, arXiv:1302.3415 [hep-ex].

[18] **DØ** Collaboration, V. M. Abazov *et al.*, "Measurement of $\sin^2\theta^{\ell}_{\text{eff}}$ and Z-light quark couplings using the forward-backward charge asymmetry in $p\overline{p} \to Z/\gamma^* \to e^+e^-$ events with $\mathcal{L} = 5.0$ fb^{-1} at $\sqrt{s} = 1.96$ TeV," *Phys. Rev. D* **84** (2011) 012007, arXiv:1104.4590 [hep-ex].

[19] **CMS** Collaboration, V. Khachatryan *et al.*, "Measurement of the t-channel single-top-quark production cross section and of the $| V_{tb} |$ CKM matrix element in pp collisions at $\sqrt{s}$= 8 TeV," *JHEP* **06** (2014) 090, arXiv:1403.7366 [hep-ex].

[20] **ATLAS** Collaboration, M. Aaboud *et al.*, "Measurement of the W-boson mass in pp collisions at $\sqrt{s} = 7$ TeV with the ATLAS detector," *Eur. Phys. J. C* **78** no. 2, (2018) 110, arXiv:1701.07240 [hep-ex]. [Erratum: Eur.Phys.J.C 78, 898 (2018)].

[21] Y. Nambu, "Quasi-particles and gauge invariance in the theory of superconductivity," *Phys. Rev.* **117** (Feb, 1960) 648–663. https://link.aps.org/doi/10.1103/PhysRev.117.648.

[22] J. Goldstone, "Field theories with superconductor solutions," *Il Nuovo Cimento (1955-1965)* **19** no. 1, (1961) 154–164.

[23] J. Goldstone, A. Salam, and S. Weinberg, "Broken symmetries," *Phys. Rev.* **127** (Aug, 1962) 965–970. https://link.aps.org/doi/10.1103/PhysRev.127.965.

[24] P. W. Anderson, "Plasmons, gauge invariance, and mass," *Phys. Rev.* **130** (Apr, 1963) 439–442. https://link.aps.org/doi/10.1103/PhysRev.130.439.

[25] F. Englert and R. Brout, "Broken symmetry and the mass of gauge vector mesons," *Phys. Rev. Lett.* **13** (Aug, 1964) 321–323. https://link.aps.org/doi/10.1103/PhysRevLett.13.321.

[26] P. W. Higgs, "Broken symmetries and the masses of gauge bosons," *Phys. Rev. Lett.* **13** (Oct, 1964) 508–509. https://link.aps.org/doi/10.1103/PhysRevLett.13.508.

[27] G. S. Guralnik, C. R. Hagen, and T. W. B. Kibble, "Global conservation laws and massless particles," *Phys. Rev. Lett.* **13** (Nov, 1964) 585–587. https://link.aps.org/doi/10.1103/PhysRevLett.13.585.

[28] G. S. Guralnik, "The History of the Guralnik, Hagen and Kibble development of the Theory of Spontaneous Symmetry Breaking and Gauge Particles," *Int. J. Mod. Phys. A* **24** (2009) 2601–2627, arXiv:0907.3466 [physics.hist-ph].

[29] J. Erler and M. Schott, "Electroweak Precision Tests of the Standard Model after the Discovery of the Higgs Boson," *Prog. Part. Nucl. Phys.* **106** (2019) 68–119, arXiv:1902.05142 [hep-ph].

[30] **CMS** Collaboration, S. Chatrchyan *et al.*, "Observation of a New Boson at a Mass of 125 GeV with the CMS Experiment at the LHC," *Phys. Lett. B* **716** (2012) 30–61, arXiv:1207.7235 [hep-ex].

[31] **ATLAS** Collaboration, G. Aad *et al.*, "Observation of a new particle in the search for the Standard Model Higgs boson with the ATLAS detector at the LHC," *Phys. Lett. B* **716** (2012) 1–29, arXiv:1207.7214 [hep-ex].

[32] N. Cabibbo, "Unitary symmetry and leptonic decays," *Phys. Rev. Lett.* **10** (Jun, 1963) 531–533. https://link.aps.org/doi/10.1103/PhysRevLett.10.531.

[33] M. Kobayashi and T. Maskawa, "CP-Violation in the Renormalizable Theory of Weak Interaction," *Progress of Theoretical Physics* **49** no. 2, (02, 1973) 652–657, https://academic.oup.com/ptp/article-pdf/49/2/652/5257692/49-2-652.pdf. https://doi.org/10.1143/PTP.49.652.

[34] R. E. Behrends, R. J. Finkelstein, and A. Sirlin, "Radiative corrections to decay processes," *Phys. Rev.* **101** (Jan, 1956) 866–873. https://link.aps.org/doi/10.1103/PhysRev.101.866.

[35] T. Kinoshita and A. Sirlin, "Radiative corrections to fermi interactions," *Phys. Rev.* **113** (Mar, 1959) 1652–1660. https://link.aps.org/doi/10.1103/PhysRev.113.1652.

[36] I. Mohammad and A. Donnachie, "Radiative Corrections to Radiative Muon Decay,".

[37] T. van Ritbergen and R. G. Stuart, "Complete 2-loop quantum electrodynamic contributions to the muon lifetime in the fermi model," *Phys. Rev. Lett.* **82** (Jan, 1999) 488–491. https://link.aps.org/doi/10.1103/PhysRevLett.82.488.

[38] D. Ross and M. Veltman, "Neutral currents and the higgs mechanism," *Nuclear Physics B* **95** no. 1, (1975) 135–147. https://www.sciencedirect.com/science/article/pii/055032137590485X.

[39] A. Djouadi, "The Anatomy of electro-weak symmetry breaking. I: The Higgs boson in the standard model," *Phys. Rept.* **457** (2008) 1–216, arXiv:hep-ph/0503172.

[40] M. J. Dugan, H. Georgi, and D. B. Kaplan, "Anatomy of a composite higgs model," *Nuclear Physics* **254** (1985) 299–326.

[41] C. T. Hill and E. H. Simmons, "Strong Dynamics and Electroweak Symmetry Breaking," *Phys. Rept.* **381** (2003) 235–402, arXiv:hep-ph/0203079. [Erratum: Phys.Rept. 390, 553–554 (2004)].

[42] M. Schwartz, *Quantum Field Theory and the Standard Model*. Quantum Field Theory and the Standard Model. Cambridge University Press, 2014. https://books.google.nl/books?id=HbdEAgAAQBAJ.

[43] M. Peskin and D. Schroeder, *An Introduction To Quantum Field Theory*. Frontiers in Physics. Avalon Publishing, 1995. https://books.google.de/books?id=EVeNNcslvX0C.

[44] M. Einhorn, D. Jones, and M. Veltman, "Heavy particles and the rho parameter in the standard model," *Nuclear Physics B* **191** no. 1, (1981) 146–172. https://www.sciencedirect.com/science/article/pii/0550321381902923.

[45] W. J. Marciano and J. L. Rosner, "Atomic parity violation as a probe of new physics," *Phys. Rev. Lett.* **65** (Dec, 1990) 2963–2966. https://link.aps.org/doi/10.1103/PhysRevLett.65.2963.

[46] M. E. Peskin and T. Takeuchi, "New constraint on a strongly interacting higgs sector," *Phys. Rev. Lett.* **65** (Aug, 1990) 964–967. https://link.aps.org/doi/10.1103/PhysRevLett.65.964.

[47] D. C. Kennedy and P. Langacker, "Erratum: "precision electroweak experiments and heavy physics: A global analysis [phys. rev. lett. 65, 2967 (1990)]," *Phys. Rev. Lett.* **66** (Jan, 1991) 395–395. https://link.aps.org/doi/10.1103/PhysRevLett.66.395.2.

[48] M. E. Peskin and T. Takeuchi, "Estimation of oblique electroweak corrections," 1991.

[49] M. Golden and L. Randall, "Radiative corrections to electroweak parameters in technicolor theories," *Nuclear Physics B* **361** no. 1, (1991) 3–23. https://www.sciencedirect.com/science/article/pii/0550321391906144.

[50] B. Holdom and J. Terning, "Large corrections to electroweak parameters in technicolor theories," *Physics Letters B* **247** no. 1, (1990) 88–92. https://www.sciencedirect.com/science/article/pii/037026939091054F.

[51] G. Altarelli, R. Barbieri, and S. Jadach, "Toward a model-independent analysis of electroweak data," *Nuclear Physics B* **369** no. 1, (1992) 3–32. https://www.sciencedirect.com/science/article/pii/055032139290376M.

[52] R. S. Chivukula, S. B. Selipsky, and E. H. Simmons, "Nonoblique effects in the zbb^{-} vertex from extended technicolor dynamics," *Phys. Rev. Lett.* **69** (Jul, 1992) 575–577. https://link.aps.org/doi/10.1103/PhysRevLett.69.575.

[53] E. H. Simmons, R. S. Chivukula, and J. Terning, "Testing extended technicolor with R(b)," *Prog. Theor. Phys. Suppl.* **123** (1996) 87–96, arXiv:hep-ph/9509392.

[54] G. Valencia and S. Willenbrock, "Goldstone-boson equivalence theorem and the higgs resonance," *Phys. Rev. D* **42** (Aug, 1990) 853–859. https://link.aps.org/doi/10.1103/PhysRevD.42.853.

[55] L. Di Luzio, R. Gröber, and M. Spannowsky, "Maxi-sizing the trilinear Higgs self-coupling: how large could it be?," *Eur. Phys. J. C* **77** no. 11, (2017) 788, arXiv:1704.02311 [hep-ph].

[56] M. Lindner, "Implications of Triviality for the Standard Model," *Z. Phys. C* **31** (1986) 295.

[57] M. Sher, "Electroweak Higgs Potentials and Vacuum Stability," *Phys. Rept.* **179** (1989) 273–418.

[58] J. A. Casas, J. R. Espinosa, and M. Quiros, "Standard model stability bounds for new physics within LHC reach," *Phys. Lett. B* **382** (1996) 374–382, arXiv:hep-ph/9603227.

[59] G. Isidori, G. Ridolfi, and A. Strumia, "On the metastability of the standard model vacuum," *Nucl. Phys. B* **609** (2001) 387–409, arXiv:hep-ph/0104016.

[60] G. Degrassi, S. Di Vita, J. Elias-Miro, J. R. Espinosa, G. F. Giudice, G. Isidori, and A. Strumia, "Higgs mass and vacuum stability in the Standard Model at NNLO," *JHEP* **08** (2012) 098, arXiv:1205.6497 [hep-ph].

[61] J. Ellis, "Physics goals of the next century@ cern," in *AIP Conference Proceedings*, vol. 542, pp. 267–292, American Institute of Physics. 2000.

[62] "LHC-facts." http://www.lhc-facts.ch.

[63] "Weltmaschine- CERN und LHC." https://www.weltmaschine.de/cern_und_lhc/lhc/.

[64] "LHC Design Report Vol.1: The LHC Main Ring,".

[65] "LHC lomg term schedule ." https://lhc-commissioning.web.cern.ch/schedule/LHC-long-term.htm.

[66] "High-Luminosity Large Hadron Collider (HL-LHC) : Preliminary Design Report,".

[67] "LHC preformance tracking." https://bpt.web.cern.ch/lhc/.

[68] "Taking a look at the LHC." https://www.lhc-closer.de/taking_a_closer_look_at_lhc/0.luminosity.

[69] "ATLAS Run 2 luminosity public results ." https://twiki.cern.ch/twiki/bin/view/AtlasPublic/LuminosityPublicResults.

[70] "CMS luminosity public results ." https://twiki.cern.ch/twiki/bin/view/CMSPublic/LumiPublicResults.

[71] "ATLAS Run 2 luminosity public results ." https://twiki.cern.ch/twiki/bin/view/AtlasPublic/LuminosityPublicResultsRun2.

[72] S. Fartoukh *et al.*, "LHC Configuration and Operational Scenario for Run 3," tech. rep., CERN, Geneva, Nov, 2021. https://cds.cern.ch/record/2790409.

[73] **CMS** Collaboration, A. M. Sirunyan *et al.*, "A measurement of the Higgs boson mass in the diphoton decay channel," *Phys. Lett. B* **805** (2020) 135425, arXiv:2002.06398 [hep-ex].

[74] **ATLAS** Collaboration, M. Aaboud *et al.*, "Measurement of the Higgs boson mass in the $H \to ZZ^* \to 4\ell$ and $H \to \gamma\gamma$ channels with $\sqrt{s} = 13$ TeV pp collisions using the ATLAS detector," *Phys. Lett. B* **784** (2018) 345–366, arXiv:1806.00242 [hep-ex].

[75] **ATLAS, CMS** Collaboration, G. Aad *et al.*, "Combined Measurement of the Higgs Boson Mass in pp Collisions at $\sqrt{s} = 7$ and 8 TeV with the ATLAS and CMS Experiments," *Phys. Rev. Lett.* **114** (2015) 191803, arXiv:1503.07589 [hep-ex].

[76] **CMS** Collaboration, A. M. Sirunyan *et al.*, "Measurements of properties of the Higgs boson decaying into the four-lepton final state in pp collisions at $\sqrt{s} = 13$ TeV," *JHEP* **11** (2017) 047, arXiv:1706.09936 [hep-ex].

[77] P. M. Aronow and B. T. Miller, *Foundations of Agnostic Statistics*. Cambridge University Press, 2019.

[78] J. De Blas, G. Durieux, C. Grojean, J. Gu, and A. Paul, "On the future of Higgs, electroweak and diboson measurements at lepton colliders," *JHEP* **12** (2019) 117, arXiv:1907.04311 [hep-ph].

[79] S. Banerjee, R. S. Gupta, O. Ochoa-Valeriano, and M. Spannowsky, "High energy lepton colliders as the ultimate Higgs microscopes," arXiv:2109.14634 [hep-ph].

[80] **ATLAS** Collaboration, M. Aaboud *et al.*, "Constraints on off-shell Higgs boson production and the Higgs boson total width in $ZZ \to 4\ell$ and $ZZ \to 2\ell 2\nu$ final states with the ATLAS detector," *Phys. Lett. B* **786** (2018) 223–244, arXiv:1808.01191 [hep-ex].

[81] **CMS** Collaboration, A. M. Sirunyan *et al.*, "Measurements of the Higgs boson width and anomalous HVV couplings from on-shell and off-shell production in the four-lepton final state," *Phys. Rev. D* **99** no. 11, (2019) 112003, arXiv:1901.00174 [hep-ex].

[82] **ATLAS** Collaboration, G. Aad *et al.*, "Study of the spin and parity of the Higgs boson in diboson decays with the ATLAS detector," *Eur. Phys. J. C* **75** no. 10, (2015) 476, arXiv:1506.05669 [hep-ex]. [Erratum: Eur.Phys.J.C 76, 152 (2016)].

[83] **CMS** Collaboration, V. Khachatryan *et al.*, "Constraints on the spin-parity and anomalous HVV couplings of the Higgs boson in proton collisions at 7 and 8 TeV," *Phys. Rev. D* **92** no. 1, (2015) 012004, arXiv:1411.3441 [hep-ex].

[84] **CMS** Collaboration, V. Khachatryan *et al.*, "Measurement of differential and integrated fiducial cross sections for Higgs boson production in the four-lepton decay channel in pp collisions at $\sqrt{s} = 7$ and 8 TeV," *JHEP* **04** (2016) 005, arXiv:1512.08377 [hep-ex].

[85] "Measurements of the total cross sections for Higgs boson production combining the $H \to \gamma\gamma$ and $H \to ZZ^* \to 4\ell$ decay channels at 7, 8 and 13 TeV center-of-mass energies with the ATLAS detector,".

[86] **CMS** Collaboration, A. M. Sirunyan *et al.*, "Measurement and interpretation of differential cross sections for Higgs boson production at $\sqrt{s} = 13$ TeV," *Phys. Lett. B* **792** (2019) 369–396, arXiv:1812.06504 [hep-ex].

[87] **ATLAS** Collaboration, "Combined measurement of the total and differential cross sections in the $H \to \gamma\gamma$ and the $H \to ZZ^* \to 4\ell$ decay channels at $\sqrt{s}$ =13 TeV with the ATLAS detector,".

[88] **ATLAS** Collaboration, "Measurements and interpretations of Higgs-boson fiducial cross sections in the diphoton decay channel using 139 fb^{-}1 of pp collision data at $\sqrt{s} = 13$ TeV with the ATLAS detector,".

[89] **CMS** Collaboration, "Measurements of properties of the Higgs boson in the four-lepton final state in proton-proton collisions at $\sqrt{s} = 13$ TeV,".

[90] N. Berger *et al.*, "Simplified Template Cross Sections - Stage 1.1," arXiv:1906.02754 [hep-ph].

[91] **ATLAS** Collaboration, "A combination of measurements of Higgs boson production and decay using up to 139 fb^{-1} of proton–proton collision data at $\sqrt{s} = 13$ TeV collected with the ATLAS experiment," Tech. Rep. ATLAS-CONF-2020-027, 2020.

[92] **CMS** Collaboration, A. M. Sirunyan *et al.*, "Measurements of Higgs boson production cross sections and couplings in the diphoton decay channel at $\sqrt{s} =$ 13 TeV," *JHEP* **07** (2021) 027, arXiv:2103.06956 [hep-ex].

[93] **CMS Collaboration** Collaboration, "Sensitivity projections for Higgs boson properties measurements at the HL-LHC," tech. rep., CERN, Geneva, 2018. https://cds.cern.ch/record/2647699.

[94] **CMS** Collaboration, "Combined Higgs boson production and decay measurements with up to 137 fb-1 of proton-proton collision data at sqrts = 13 TeV," Tech. Rep. CMS-PAS-HIG-19-005, 2020.

[95] **CMS** Collaboration, "Measurement of Higgs boson production in association with a W or Z boson in the H $\rightarrow$ WW decay channel," Tech. Rep. CMS-PAS-HIG-19-017, 2021.

[96] **ATLAS** Collaboration, "Combined measurements of Higgs boson production and decay using up to 139 fb^{-1} of proton-proton collision data at $\sqrt{s} = 13$ TeV collected with the ATLAS experiment,".

[97] H. Cooper, L. Hedges, and J. Valentine, *The handbook of research synthesis and meta-analysis 2nd edition*, pp. 1–615. Russell Sage Foundation, Dec., 2009.

[98] **CMS** Collaboration, A. M. Sirunyan *et al.*, "Search for associated production of a Higgs boson and a single top quark in proton-proton collisions at $\sqrt{s} = 13$ TeV," *Phys. Rev. D* **99** no. 9, (2019) 092005, arXiv:1811.09696 [hep-ex].

[99] **CMS** Collaboration, A. M. Sirunyan *et al.*, "Observation of Higgs boson decay to bottom quarks," *Phys. Rev. Lett.* **121** no. 12, (2018) 121801, arXiv:1808.08242 [hep-ex].

[100] **ATLAS** Collaboration, M. Aaboud *et al.*, "Observation of $H \rightarrow b\bar{b}$ decays and VH production with the ATLAS detector," *Phys. Lett. B* **786** (2018) 59–86, arXiv:1808.08238 [hep-ex].

[101] **ATLAS** Collaboration, M. Aaboud *et al.*, "Measurement of VH, H $\to$ b$\bar{\text{b}}$ production as a function of the vector-boson transverse momentum in 13 TeV pp collisions with the ATLAS detector," *JHEP* **05** (2019) 141, arXiv:1903.04618 [hep-ex].

[102] **ATLAS** Collaboration, M. Aaboud *et al.*, "Cross-section measurements of the Higgs boson decaying into a pair of τ-leptons in proton-proton collisions at $\sqrt{s} = 13$ TeV with the ATLAS detector," *Phys. Rev. D* **99** (2019) 072001, arXiv:1811.08856 [hep-ex].

[103] **CMS** Collaboration, "Measurement of Higgs boson production and decay to the $\tau\tau$ final state,".

[104] **ATLAS** Collaboration, G. Aad *et al.*, "A search for the dimuon decay of the Standard Model Higgs boson with the ATLAS detector," *Phys. Lett. B* **812** (2021) 135980, arXiv:2007.07830 [hep-ex].

[105] **CMS** Collaboration, A. M. Sirunyan *et al.*, "Evidence for Higgs boson decay to a pair of muons," *JHEP* **01** (2021) 148, arXiv:2009.04363 [hep-ex].

[106] **ATLAS** Collaboration, "Direct constraint on the Higgs-charm coupling from a search for Higgs boson decays to charm quarks with the ATLAS detector,".

[107] **ATLAS** Collaboration, G. Aad *et al.*, "Direct constraint on the Higgs-charm coupling from a search for Higgs boson decays into charm quarks with the ATLAS detector," arXiv:2201.11428 [hep-ex].

[108] **CMS** Collaboration, A. M. Sirunyan *et al.*, "A search for the standard model Higgs boson decaying to charm quarks," *JHEP* **03** (2020) 131, arXiv:1912.01662 [hep-ex].

[109] **ATLAS Collaboration** Collaboration, C. Bernius, "HL-LHC prospects from ATLAS and CMS," tech. rep., CERN, Geneva, Mar, 2019. https://cds.cern.ch/record/2666331.

[110] **ATLAS** Collaboration, "Prospects for $H \to c\bar{c}$ using Charm Tagging with the ATLAS Experiment at the HL-LHC," Tech. Rep. ATL-PHYS-PUB-2018-016, CERN, Geneva, Aug, 2018. http://cds.cern.ch/record/2633635.

[111] **ATLAS** Collaboration, G. Aad *et al.*, "A search for the $Z\gamma$ decay mode of the Higgs boson in pp collisions at $\sqrt{s} = 13$ TeV with the ATLAS detector," *Phys. Lett. B* **809** (2020) 135754, arXiv:2005.05382 [hep-ex].

[112] S. Dawson, S. Dittmaier, and M. Spira, "Neutral Higgs boson pair production at hadron colliders: QCD corrections," *Phys. Rev. D* **58** (1998) 115012, arXiv:hep-ph/9805244.

[113] A. Papaefstathiou and K. Sakurai, "Triple Higgs boson production at a 100 TeV proton-proton collider," *JHEP* **02** (2016) 006, arXiv:1508.06524 [hep-ph].

[114] M. McCullough, "An Indirect Model-Dependent Probe of the Higgs Self-Coupling," *Phys. Rev. D* **90** no. 1, (2014) 015001, arXiv:1312.3322 [hep-ph]. [Erratum: Phys.Rev.D 92, 039903 (2015)].

[115] M. Gorbahn and U. Haisch, "Indirect probes of the trilinear Higgs coupling: $gg \to h$ and $h \to \gamma\gamma$," *JHEP* **10** (2016) 094, arXiv:1607.03773 [hep-ph].

[116] G. Degrassi, P. P. Giardino, F. Maltoni, and D. Pagani, "Probing the Higgs self coupling via single Higgs production at the LHC," *JHEP* **12** (2016) 080, arXiv:1607.04251 [hep-ph].

[117] W. Bizon, M. Gorbahn, U. Haisch, and G. Zanderighi, "Constraints on the trilinear Higgs coupling from vector boson fusion and associated Higgs production at the LHC," *JHEP* **07** (2017) 083, arXiv:1610.05771 [hep-ph].

[118] F. Maltoni, D. Pagani, A. Shivaji, and X. Zhao, "Trilinear Higgs coupling determination via single-Higgs differential measurements at the LHC," *Eur. Phys. J. C* **77** no. 12, (2017) 887, arXiv:1709.08649 [hep-ph].

[119] G. Degrassi and M. Vitti, "The effect of an anomalous Higgs trilinear self-coupling on the $h \to \gamma Z$ decay," *Eur. Phys. J. C* **80** no. 4, (2020) 307, arXiv:1912.06429 [hep-ph].

[120] G. Degrassi, B. Di Micco, P. P. Giardino, and E. Rossi, "Higgs boson self-coupling constraints from single Higgs, double Higgs and Electroweak measurements," *Phys. Lett. B* **817** (2021) 136307, arXiv:2102.07651 [hep-ph].

[121] U. Haisch and G. Koole, "Off-shell Higgs production at the LHC as a probe of the trilinear Higgs coupling," arXiv:2111.12589 [hep-ph].

[122] S. Weinberg, "Phenomenological lagrangians," *Physica A: Statistical Mechanics and its Applications* **96** no. 1, (1979) 327–340. https://www.sciencedirect.com/science/article/pii/0378437179902231.

[123] S. Weinberg, "Baryon- and lepton-nonconserving processes," *Phys. Rev. Lett.* **43** (Nov, 1979) 1566–1570. https://link.aps.org/doi/10.1103/PhysRevLett.43.1566.

[124] L. Lehman, "Extending the Standard Model Effective Field Theory with the Complete Set of Dimension-7 Operators," *Phys. Rev. D* **90** no. 12, (2014) 125023, arXiv:1410.4193 [hep-ph].

[125] L. Lehman and A. Martin, "Low-derivative operators of the Standard Model effective field theory via Hilbert series methods," *JHEP* **02** (2016) 081, arXiv:1510.00372 [hep-ph].

[126] B. Henning, X. Lu, T. Melia, and H. Murayama, "2, 84, 30, 993, 560, 15456, 11962, 261485, ...: Higher dimension operators in the SM EFT," *JHEP* **08** (2017) 016, arXiv:1512.03433 [hep-ph]. [Erratum: JHEP 09, 019 (2019)].

[127] J. A. Aguilar-Saavedra, "Effective four-fermion operators in top physics: A Roadmap," *Nucl. Phys. B* **843** (2011) 638–672, arXiv:1008.3562 [hep-ph]. [Erratum: Nucl.Phys.B 851, 443–444 (2011)].

[128] B. Grzadkowski, M. Iskrzynski, M. Misiak, and J. Rosiek, "Dimension-Six Terms in the Standard Model Lagrangian," *JHEP* **10** (2010) 085, arXiv:1008.4884 [hep-ph].

[129] W. Buchmüller and D. Wyler, "Effective lagrangian analysis of new interactions and flavour conservation," *Nuclear Physics B* **268** no. 3, (1986) 621–653. https://www.sciencedirect.com/science/article/pii/0550321386902622.

[130] K. Hagiwara, S. Ishihara, R. Szalapski, and D. Zeppenfeld, "Low-energy effects of new interactions in the electroweak boson sector," *Phys. Rev. D* **48** (1993) 2182–2203.

[131] R. Alonso, E. E. Jenkins, A. V. Manohar, and M. Trott, "Renormalization Group Evolution of the Standard Model Dimension Six Operators III: Gauge Coupling Dependence and Phenomenology," *JHEP* **04** (2014) 159, arXiv:1312.2014 [hep-ph].

[132] G. F. Giudice, C. Grojean, A. Pomarol, and R. Rattazzi, "The Strongly-Interacting Light Higgs," *JHEP* **06** (2007) 045, arXiv:hep-ph/0703164.

[133] R. Contino, M. Ghezzi, C. Grojean, M. Muhlleitner, and M. Spira, "Effective Lagrangian for a light Higgs-like scalar," *JHEP* **07** (2013) 035, arXiv:1303.3876 [hep-ph].

[134] J. Elias-Miró, C. Grojean, R. S. Gupta, and D. Marzocca, "Scaling and tuning of EW and Higgs observables," *JHEP* **05** (2014) 019, arXiv:1312.2928 [hep-ph].

[135] R. S. Gupta, A. Pomarol, and F. Riva, "BSM Primary Effects," *Phys. Rev. D* **91** no. 3, (2015) 035001, arXiv:1405.0181 [hep-ph].

[136] M. Carena and H. Haber, "Higgs boson theory and phenomenology," *Progress in Particle and Nuclear Physics* **50** no. 1, (2003) 63–152. https://www.sciencedirect.com/science/article/pii/S0146641002001771.

[137] R. Contino, "The Higgs as a Composite Nambu-Goldstone Boson," in *Theoretical Advanced Study Institute in Elementary Particle Physics: Physics of the Large and the Small*, pp. 235–306. 2011. arXiv:1005.4269 [hep-ph].

[138] G. Panico and A. Wulzer, *The Composite Nambu-Goldstone Higgs*, vol. 913. Springer, 2016. arXiv:1506.01961 [hep-ph].

[139] **ATLAS** Collaboration, "Methodology for EFT interpretation of Higgs boson Simplified Template Cross-section results in ATLAS,".

[140] S. Dawson, S. Homiller, and S. D. Lane, "Putting SMEFT Fits to Work," arXiv:2007.01296 [hep-ph].

[141] **SMEFiT** Collaboration, J. J. Ethier, G. Magni, F. Maltoni, L. Mantani, E. R. Nocera, J. Rojo, E. Slade, E. Vryonidou, and C. Zhang, "Combined SMEFT interpretation of Higgs, diboson, and top quark data from the LHC," *JHEP* **11** (2021) 089, arXiv:2105.00006 [hep-ph].

[142] J. Ellis, C. W. Murphy, V. Sanz, and T. You, "Updated Global SMEFT Fit to Higgs, Diboson and Electroweak Data," *JHEP* **06** (2018) 146, arXiv:1803.03252 [hep-ph].

[143] S. Dawson and P. P. Giardino, "Flavorful Electroweak Precision Observables in the Standard Model Effective Field Theory," arXiv:2201.09887 [hep-ph].

[144] J. Ellis, M. Madigan, K. Mimasu, V. Sanz, and T. You, "Top, Higgs, Diboson and Electroweak Fit to the Standard Model Effective Field Theory," *JHEP* **04** (2021) 279, arXiv:2012.02779 [hep-ph].

[145] G. Degrassi, P. Gambino, and P. P. Giardino, "The $m_W - m_Z$ interdependence in the Standard Model: a new scrutiny," *JHEP* **05** (2015) 154, arXiv:1411.7040 [hep-ph].

[146] G. D. Kribs, A. Maier, H. Rzehak, M. Spannowsky, and P. Waite, "Electroweak oblique parameters as a probe of the trilinear Higgs boson self-interaction," *Phys. Rev. D* **95** no. 9, (2017) 093004, arXiv:1702.07678 [hep-ph].

[147] S. Di Vita, C. Grojean, G. Panico, M. Riembau, and T. Vantalon, "A global view on the Higgs self-coupling," *JHEP* **09** (2017) 069, arXiv:1704.01953 [hep-ph].

[148] **ATLAS** Collaboration, "Constraints on the Higgs boson self-coupling from the combination of single-Higgs and double-Higgs production analyses performed with the ATLAS experiment," Tech. Rep. ATLAS-CONF-2019-049, 2019.

[149] R. Grober, M. Muhlleitner, and M. Spira, "Higgs Pair Production at NLO QCD for CP-violating Higgs Sectors," *Nucl. Phys. B* **925** (2017) 1–27, arXiv:1705.05314 [hep-ph].

[150] J. Gasser and H. Leutwyler, "Chiral perturbation theory to one loop," *Annals of Physics* **158** no. 1, (1984) 142–210. https://www.sciencedirect.com/science/article/pii/0003491684902422.

[151] J. Gasser and H. Leutwyler, "Chiral perturbation theory: Expansions in the mass of the strange quark," *Nuclear Physics B* **250** no. 1, (1985) 465–516. https://www.sciencedirect.com/science/article/pii/0550321385904924.

[152] G. Buchalla, O. Catà, and C. Krause, "Complete Electroweak Chiral Lagrangian with a Light Higgs at NLO," *Nucl. Phys. B* **880** (2014) 552–573, arXiv:1307.5017 [hep-ph]. [Erratum: Nucl.Phys.B 913, 475–478 (2016)].

[153] G. Buchalla, O. Cata, A. Celis, and C. Krause, "Note on Anomalous Higgs-Boson Couplings in Effective Field Theory," *Phys. Lett. B* **750** (2015) 298–301, arXiv:1504.01707 [hep-ph].

[154] **LHC Higgs Cross Section Working Group** Collaboration, D. de Florian *et al.*, "Handbook of LHC Higgs Cross Sections: 4. Deciphering the Nature of the Higgs Sector," arXiv:1610.07922 [hep-ph].

[155] G. Buchalla, M. Capozi, A. Celis, G. Heinrich, and L. Scyboz, "Higgs boson pair production in non-linear Effective Field Theory with full m_t-dependence at NLO QCD," *JHEP* **09** (2018) 057, arXiv:1806.05162 [hep-ph].

[156] M. Capozi and G. Heinrich, "Exploring anomalous couplings in Higgs boson pair production through shape analysis," *JHEP* **03** (2020) 091, arXiv:1908.08923 [hep-ph].

[157] D. de Florian, I. Fabre, G. Heinrich, J. Mazzitelli, and L. Scyboz, "Anomalous couplings in Higgs-boson pair production at approximate NNLO QCD," arXiv:2106.14050 [hep-ph].

[158] G. Heinrich, S. P. Jones, M. Kerner, and L. Scyboz, "A non-linear EFT description of $gg \to HH$ at NLO interfaced to POWHEG," *JHEP* **10** (2020) 021, arXiv:2006.16877 [hep-ph].

[159] K. Agashe, R. Contino, and A. Pomarol, "The minimal composite higgs model," *Nuclear Physics B* **719** no. 1, (2005) 165–187. https://www.sciencedirect.com/science/article/pii/S0550321305003445.

[160] W. D. Goldberger, B. Grinstein, and W. Skiba, "Distinguishing the higgs boson from the dilaton at the large hadron collider," *Phys. Rev. Lett.* **100** (Mar, 2008) 111802. https://link.aps.org/doi/10.1103/PhysRevLett.100.111802.

[161] K. Habaa, S. Matsuzaki, and K. Yamawaki, "Holographic Techni-dilaton, or Conformal Higgs," in *International Workshop on Strong Coupling Gauge Theories in LHC Era: SCGT 09*, pp. 401–403. 2011. arXiv:1003.2841 [hep-ph].

[162] A. Delgado, K. Lane, and A. Martin, "A Light Scalar in Low-Scale Technicolor," *Phys. Lett. B* **696** (2011) 482–486, arXiv:1011.0745 [hep-ph].

[163] J. Galloway, M. A. Luty, Y. Tsai, and Y. Zhao, "Induced Electroweak Symmetry Breaking and Supersymmetric Naturalness," *Phys. Rev. D* **89** no. 7, (2014) 075003, arXiv:1306.6354 [hep-ph].

[164] S. Chang, J. Galloway, M. Luty, E. Salvioni, and Y. Tsai, "Phenomenology of Induced Electroweak Symmetry Breaking," *JHEP* **03** (2015) 017, arXiv:1411.6023 [hep-ph].

[165] C. Hartmann and M. Trott, "Higgs Decay to Two Photons at One Loop in the Standard Model Effective Field Theory," *Phys. Rev. Lett.* **115** no. 19, (2015) 191801, arXiv:1507.03568 [hep-ph].

[166] A. Falkowski, B. Fuks, K. Mawatari, K. Mimasu, F. Riva, and V. Sanz, "Rosetta: an operator basis translator for Standard Model effective field theory," *Eur. Phys. J. C* **75** no. 12, (2015) 583, arXiv:1508.05895 [hep-ph].

[167] M. Gonzalez-Alonso, A. Greljo, G. Isidori, and D. Marzocca, "Pseudo-observables in Higgs decays," *Eur. Phys. J. C* **75** (2015) 128, arXiv:1412.6038 [hep-ph].

[168] A. Falkowski and R. Rattazzi, "Which EFT," arXiv:1902.05936 [hep-ph].

[169] S. Di Vita, G. Durieux, C. Grojean, J. Gu, Z. Liu, G. Panico, M. Riembau, and T. Vantalon, "A global view on the Higgs self-coupling at lepton colliders," *JHEP* **02** (2018) 178, arXiv:1711.03978 [hep-ph].

[170] M. Bonetti, K. Melnikov, and L. Tancredi, "Higher order corrections to mixed QCD-EW contributions to Higgs boson production in gluon fusion," *Phys. Rev. D* **97** no. 5, (2018) 056017, arXiv:1801.10403 [hep-ph]. [Erratum: Phys.Rev.D 97, 099906 (2018)].

[171] X. Chen, T. Gehrmann, E. W. N. Glover, A. Huss, B. Mistlberger, and A. Pelloni, "Fully Differential Higgs Boson Production to Third Order in QCD," *Phys. Rev. Lett.* **127** no. 7, (2021) 072002, arXiv:2102.07607 [hep-ph].

[172] G. Billis, B. Dehnadi, M. A. Ebert, J. K. L. Michel, and F. J. Tackmann, "Higgs pT Spectrum and Total Cross Section with Fiducial Cuts at Third Resummed and Fixed Order in QCD," *Phys. Rev. Lett.* **127** no. 7, (2021) 072001, arXiv:2102.08039 [hep-ph].

[173] M. Bonetti, K. Melnikov, and L. Tancredi, "Three-loop mixed QCD-electroweak corrections to Higgs boson gluon fusion," *Phys. Rev. D* **97** no. 3, (2018) 034004, arXiv:1711.11113 [hep-ph].

[174] M. Bonetti, E. Panzer, V. A. Smirnov, and L. Tancredi, "Two-loop mixed QCD-EW corrections to $gg \to Hg$," *JHEP* **11** (2020) 045, arXiv:2007.09813 [hep-ph].

[175] M. Becchetti, R. Bonciani, V. Del Duca, V. Hirschi, F. Moriello, and A. Schweitzer, "Next-to-leading order corrections to light-quark mixed QCD-EW contributions to Higgs boson production," *Phys. Rev. D* **103** no. 5, (2021) 054037, arXiv:2010.09451 [hep-ph].

[176] M. L. Czakon and M. Niggetiedt, "Exact quark-mass dependence of the Higgs-gluon form factor at three loops in QCD," *JHEP* **05** (2020) 149, arXiv:2001.03008 [hep-ph].

[177] M. Czakon, R. V. Harlander, J. Klappert, and M. Niggetiedt, "Exact Top-Quark Mass Dependence in Hadronic Higgs Production," *Phys. Rev. Lett.* **127** no. 16, (2021) 162002, arXiv:2105.04436 [hep-ph].

[178] F. Maltoni, E. Vryonidou, and M. Zaro, "Top-quark mass effects in double and triple Higgs production in gluon-gluon fusion at NLO," *JHEP* **11** (2014) 079, arXiv:1408.6542 [hep-ph].

[179] K. Kudashkin, K. Melnikov, and C. Wever, "Two-loop amplitudes for processes $gg \to Hg, qg \to Hq$ and $q\bar{q} \to Hg$ at large Higgs transverse momentum," *JHEP* **02** (2018) 135, arXiv:1712.06549 [hep-ph].

[180] J. M. Lindert, K. Kudashkin, K. Melnikov, and C. Wever, "Higgs bosons with large transverse momentum at the LHC," *Phys. Lett. B* **782** (2018) 210–214, arXiv:1801.08226 [hep-ph].

[181] S. P. Jones, M. Kerner, and G. Luisoni, "Next-to-leading-order qcd corrections to higgs boson plus jet production with full top-quark mass dependence," *Phys. Rev. Lett.* **120** (Apr, 2018) 162001. https://link.aps.org/doi/10.1103/PhysRevLett.120.162001.

[182] V. Hankele, G. Klämke, D. Zeppenfeld, and T. Figy, "Anomalous higgs boson couplings in vector boson fusion at the cern lhc," *Physical Review D* **74** no. 9, (2006) 095001.

[183] T. Han, G. Valencia, and S. Willenbrock, "Structure function approach to vector boson scattering in p p collisions," *Phys. Rev. Lett.* **69** (1992) 3274–3277, arXiv:hep-ph/9206246.

[184] T. Figy, C. Oleari, and D. Zeppenfeld, "Next-to-leading order jet distributions for Higgs boson production via weak boson fusion," *Phys. Rev. D* **68** (2003) 073005, arXiv:hep-ph/0306109.

[185] E. L. Berger and J. M. Campbell, "Higgs boson production in weak boson fusion at next-to-leading order," *Phys. Rev. D* **70** (2004) 073011, arXiv:hep-ph/0403194.

[186] M. Gomez-Bock, M. Mondragon, M. Muhlleitner, M. Spira, and P. M. Zerwas, "Concepts of Electroweak Symmetry Breaking and Higgs Physics," in *4th CERN-CLAF School of High-Energy Physics*, pp. 177–238. 12, 2007. arXiv:0712.2419 [hep-ph].

[187] P. Bolzoni, F. Maltoni, S.-O. Moch, and M. Zaro, "Higgs production via vector-boson fusion at NNLO in QCD," *Phys. Rev. Lett.* **105** (2010) 011801, arXiv:1003.4451 [hep-ph].

[188] A. Denner, S. Dittmaier, S. Kallweit, and A. Mück, "HAWK 2.0: A Monte Carlo program for Higgs production in vector-boson fusion and Higgs strahlung at hadron colliders," *Comput. Phys. Commun.* **195** (2015) 161–171, arXiv:1412.5390 [hep-ph].

[189] T. Han and S. Willenbrock, "QCD correction to the p p —> W H and Z H total cross-sections," *Phys. Lett. B* **273** (1991) 167–172.

[190] O. Brein, A. Djouadi, and R. Harlander, "NNLO QCD corrections to the Higgs-strahlung processes at hadron colliders," *Phys. Lett. B* **579** (2004) 149–156, arXiv:hep-ph/0307206.

[191] S. Amoroso *et al.*, "Les Houches 2019: Physics at TeV Colliders: Standard Model Working Group Report," in *11th Les Houches Workshop on Physics at TeV Colliders: PhysTeV Les Houches*. 3, 2020. arXiv:2003.01700 [hep-ph].

[192] M. Cepeda *et al.*, "Report from Working Group 2: Higgs Physics at the HL-LHC and HE-LHC," *CERN Yellow Rep. Monogr.* **7** (2019) 221–584, arXiv:1902.00134 [hep-ph].

[193] C. Englert, M. McCullough, and M. Spannowsky, "Gluon-initiated associated production boosts Higgs physics," *Phys. Rev. D* **89** no. 1, (2014) 013013, arXiv:1310.4828 [hep-ph].

[194] C. Englert, R. Rosenfeld, M. Spannowsky, and A. Tonero, "New physics and signal-background interference in associated $pp \to HZ$ production," *EPL* **114** no. 3, (2016) 31001, arXiv:1603.05304 [hep-ph].

[195] B. A. Kniehl, "Associated Production of Higgs and Z Bosons From Gluon Fusion in Hadron Collisions," *Phys. Rev. D* **42** (1990) 2253–2258.

[196] D. A. Dicus and C. Kao, "Higgs Boson - Z^0 Production From Gluon Fusion," *Phys. Rev. D* **38** (1988) 1008. [Erratum: Phys.Rev.D 42, 2412 (1990)].

[197] L. Altenkamp, S. Dittmaier, R. V. Harlander, H. Rzehak, and T. J. Zirke, "Gluon-induced Higgs-strahlung at next-to-leading order QCD," *JHEP* **02** (2013) 078, arXiv:1211.5015 [hep-ph].

[198] R. V. Harlander, A. Kulesza, V. Theeuwes, and T. Zirke, "Soft gluon resummation for gluon-induced Higgs Strahlung," *JHEP* **11** (2014) 082, arXiv:1410.0217 [hep-ph].

[199] A. Hasselhuhn, T. Luthe, and M. Steinhauser, "On top quark mass effects to $gg \to ZH$ at NLO," *JHEP* **01** (2017) 073, arXiv:1611.05881 [hep-ph].

[200] R. Harlander, J. Klappert, C. Pandini, and A. Papaefstathiou, "Exploiting the WH/ZH symmetry in the search for New Physics," *Eur. Phys. J. C* **78** no. 9, (2018) 760, arXiv:1804.02299 [hep-ph].

[201] B. Hespel, F. Maltoni, and E. Vryonidou, "Higgs and Z boson associated production via gluon fusion in the SM and the 2HDM," *JHEP* **06** (2015) 065, arXiv:1503.01656 [hep-ph].

[202] J. Davies, G. Mishima, and M. Steinhauser, "Virtual corrections to $gg \to ZH$ in the high-energy and large-m_t limits," arXiv:2011.12314 [hep-ph].

[203] L. Chen, G. Heinrich, S. P. Jones, M. Kerner, J. Klappert, and J. Schlenk, "ZH production in gluon fusion: two-loop amplitudes with full top quark mass dependence," arXiv:2011.12325 [hep-ph].

[204] R. Bonciani, G. Degrassi, P. P. Giardino, and R. Gröber, "Analytical Method for Next-to-Leading-Order QCD Corrections to Double-Higgs Production," *Phys. Rev. Lett.* **121** no. 16, (2018) 162003, arXiv:1806.11564 [hep-ph].

[205] A. Broggio, A. Ferroglia, R. Frederix, D. Pagani, B. D. Pecjak, and I. Tsinikos, "Top-quark pair hadroproduction in association with a heavy boson at NLO+NNLL including EW corrections," *JHEP* **08** (2019) 039, arXiv:1907.04343 [hep-ph].

[206] A. Kulesza, L. Motyka, D. Schwartländer, T. Stebel, and V. Theeuwes, "Associated top quark pair production with a heavy boson: differential cross sections at NLO+NNLL accuracy," *Eur. Phys. J. C* **80** no. 5, (2020) 428, arXiv:2001.03031 [hep-ph].

[207] G. Bevilacqua, H.-Y. Bi, H. B. Hartanto, M. Kraus, and M. Worek, "The simplest of them all: $t\bar{t}W^{\pm}$ at NLO accuracy in QCD," *JHEP* **08** (2020) 043, arXiv:2005.09427 [hep-ph].

[208] A. Denner and G. Pelliccioli, "NLO QCD corrections to off-shell $\mathrm{t\bar{t}W^{+}}$ production at the LHC," *JHEP* **11** (2020) 069, arXiv:2007.12089 [hep-ph].

[209] G. Bevilacqua, H.-Y. Bi, H. B. Hartanto, M. Kraus, J. Nasufi, and M. Worek, "NLO QCD corrections to off-shell $t\bar{t}W^{\pm}$ production at the LHC: correlations and asymmetries," *Eur. Phys. J. C* **81** no. 7, (2021) 675, arXiv:2012.01363 [hep-ph].

[210] A. Denner and G. Pelliccioli, "Combined NLO EW and QCD corrections to off-shell $\mathrm{t\bar{t}W}$ production at the LHC," *Eur. Phys. J. C* **81** no. 4, (2021) 354, arXiv:2102.03246 [hep-ph].

[211] F. F. Cordero, M. Kraus, and L. Reina, "Top-quark pair production in association with a $W^{\pm}$ gauge boson in the POWHEG-BOX," *Phys. Rev. D* **103** no. 9, (2021) 094014, arXiv:2101.11808 [hep-ph].

[212] G. Bevilacqua, H. Y. Bi, F. Febres Cordero, H. B. Hartanto, M. Kraus, J. Nasufi, L. Reina, and M. Worek, "Modeling uncertainties of $t\bar{t}W^{\pm}$ multilepton signatures," *Phys. Rev. D* **105** no. 1, (2022) 014018, arXiv:2109.15181 [hep-ph].

[213] A. Denner, J.-N. Lang, and M. Pellen, "Full NLO QCD corrections to off-shell tt¯bb¯ production," *Phys. Rev. D* **104** no. 5, (2021) 056018, arXiv:2008.00918 [hep-ph].

[214] G. Bevilacqua, H.-Y. Bi, H. B. Hartanto, M. Kraus, M. Lupattelli, and M. Worek, "$t\bar{t}b\bar{b}$ at the LHC: on the size of corrections and b-jet definitions," *JHEP* **08** (2021) 008, arXiv:2105.08404 [hep-ph].

[215] A. Denner, J.-N. Lang, M. Pellen, and S. Uccirati, "NLO QCD + electroweak predictions for off-shell ttH production at the LHC," in *12th International Workshop on Top Quark Physics*. 12, 2019. arXiv:1912.08493 [hep-ph].

[216] F. Maltoni, E. Vryonidou, and C. Zhang, "Higgs production in association with a top-antitop pair in the Standard Model Effective Field Theory at NLO in QCD," *JHEP* **10** (2016) 123, arXiv:1607.05330 [hep-ph].

[217] F. Dulat, A. Lazopoulos, and B. Mistlberger, "iHixs 2 — Inclusive Higgs cross sections," *Comput. Phys. Commun.* **233** (2018) 243–260, arXiv:1802.00827 [hep-ph].

[218] S. Alioli, P. Nason, C. Oleari, and E. Re, "NLO Higgs boson production via gluon fusion matched with shower in POWHEG," *JHEP* **04** (2009) 002, arXiv:0812.0578 [hep-ph].

[219] P. Nason and C. Oleari, "NLO Higgs boson production via vector-boson fusion matched with shower in POWHEG," *JHEP* **02** (2010) 037, arXiv:0911.5299 [hep-ph].

[220] E. Bagnaschi, G. Degrassi, P. Slavich, and A. Vicini, "Higgs production via gluon fusion in the POWHEG approach in the SM and in the MSSM," *JHEP* **02** (2012) 088, arXiv:1111.2854 [hep-ph].

[221] J. M. Campbell, R. K. Ellis, R. Frederix, P. Nason, C. Oleari, and C. Williams, "NLO Higgs Boson Production Plus One and Two Jets Using the POWHEG BOX, MadGraph4 and MCFM," *JHEP* **07** (2012) 092, arXiv:1202.5475 [hep-ph].

[222] G. Luisoni, P. Nason, C. Oleari, and F. Tramontano, "$HW^{\pm}$/HZ + 0 and 1 jet at NLO with the POWHEG BOX interfaced to GoSam and their merging within MiNLO," *JHEP* **10** (2013) 083, arXiv:1306.2542 [hep-ph].

[223] B. Jäger, F. Schissler, and D. Zeppenfeld, "Parton-shower effects on Higgs boson production via vector-boson fusion in association with three jets," *JHEP* **07** (2014) 125, arXiv:1405.6950 [hep-ph].

[224] H. B. Hartanto, B. Jager, L. Reina, and D. Wackeroth, "Higgs boson production in association with top quarks in the POWHEG BOX," *Phys. Rev. D* **91** no. 9, (2015) 094003, arXiv:1501.04498 [hep-ph].

[225] J. Alwall, R. Frederix, S. Frixione, V. Hirschi, F. Maltoni, O. Mattelaer, H. S. Shao, T. Stelzer, P. Torrielli, and M. Zaro, "The automated computation of tree-level and next-to-leading order differential cross sections, and their matching to parton shower simulations," *JHEP* **07** (2014) 079, arXiv:1405.0301 [hep-ph].

[226] "Higgs corss-sections working group." https://twiki.cern.ch/twiki/bin/view/LHCPhysics/LHCHWG?redirectedfrom=LHCPhysics.LHCHXSWG.

[227] C. Degrande, G. Durieux, F. Maltoni, K. Mimasu, E. Vryonidou, and C. Zhang, "Automated one-loop computations in the standard model effective field theory," *Phys. Rev. D* **103** no. 9, (2021) 096024, arXiv:2008.11743 [hep-ph].

[228] R. Frederix, D. Pagani, and M. Zaro, "Large NLO corrections in $t\bar{t}W^{\pm}$ and $t\bar{t}t\bar{t}$ hadroproduction from supposedly subleading EW contributions," *JHEP* **02** (2018) 031, arXiv:1711.02116 [hep-ph].

[229] **CMS** Collaboration, A. M. Sirunyan *et al.*, "Search for the production of four top quarks in the single-lepton and opposite-sign dilepton final states in proton-proton collisions at $\sqrt{s} = 13$ TeV," *JHEP* **11** (2019) 082, arXiv:1906.02805 [hep-ex].

[230] **ATLAS** Collaboration, G. Aad *et al.*, "Evidence for $t\bar{t}t\bar{t}$ production in the multilepton final state in proton–proton collisions at $\sqrt{s} = 13$ TeV with the ATLAS detector," *Eur. Phys. J. C* **80** no. 11, (2020) 1085, arXiv:2007.14858 [hep-ex].

[231] **CMS** Collaboration, A. M. Sirunyan *et al.*, "Measurement of the cross section for $\mathrm{t\bar{t}}$ production with additional jets and b jets in pp collisions at $\sqrt{s} = 13$ TeV," *JHEP* **07** (2020) 125, arXiv:2003.06467 [hep-ex].

[232] **ATLAS** Collaboration, "Measurements of fiducial and differential cross-sections of $t\bar{t}$ production with additional heavy-flavour jets in proton-proton collisions at $\sqrt{s} = 13$ TeV with the ATLAS detector," Tech. Rep. ATLAS-CONF-2018-029, 2018.

[233] J. D'Hondt, A. Mariotti, K. Mimasu, S. Moortgat, and C. Zhang, "Learning to pinpoint effective operators at the LHC: a study of the $\mathrm{t\bar{t}b\bar{b}}$ signature," *JHEP* **11** (2018) 131, arXiv:1807.02130 [hep-ph].

[234] N. P. Hartland, F. Maltoni, E. R. Nocera, J. Rojo, E. Slade, E. Vryonidou, and C. Zhang, "A Monte Carlo global analysis of the Standard Model Effective Field Theory: the top quark sector," *JHEP* **04** (2019) 100, arXiv:1901.05965 [hep-ph].

[235] J. de Blas, M. Chala, and J. Santiago, "Renormalization Group Constraints on New Top Interactions from Electroweak Precision Data," *JHEP* **09** (2015) 189, arXiv:1507.00757 [hep-ph].

[236] L. Alasfar, J. de Blas, and R. Gröber, "Higgs probes of top quark contact interactions and their interplay with the Higgs self-coupling," arXiv:2202.02333 [hep-ph].

[237] A. Dedes, W. Materkowska, M. Paraskevas, J. Rosiek, and K. Suxho, "Feynman rules for the Standard Model Effective Field Theory in R_ξ -gauges," *JHEP* **06** (2017) 143, arXiv:1704.03888 [hep-ph].

[238] H. Patel, "Package-X: A Mathematica package for the analytic calculation of one-loop integrals," *Comput. Phys. Commun.* **197** (2015) 276–290, arXiv:1503.01469 [hep-ph].

[239] P. Maierhöfer, J. Usovitsch, and P. Uwer, "Kira—A Feynman integral reduction program," *Comput. Phys. Commun.* **230** (2018) 99–112, arXiv:1705.05610 [hep-ph].

[240] T. Hahn, "Generating Feynman diagrams and amplitudes with FeynArts 3," *Comput. Phys. Commun.* **140** (2001) 418–431, arXiv:hep-ph/0012260.

[241] A. Alloul, N. D. Christensen, C. Degrande, C. Duhr, and B. Fuks, "FeynRules 2.0 - A complete toolbox for tree-level phenomenology," *Comput. Phys. Commun.* **185** (2014) 2250–2300, arXiv:1310.1921 [hep-ph].

[242] A. Smirnov, "Algorithm FIRE – Feynman Integral REduction," *JHEP* **10** (2008) 107, arXiv:0807.3243 [hep-ph].

[243] S. Dawson and P. P. Giardino, "Higgs decays to ZZ and $Z\gamma$ in the standard model effective field theory: An NLO analysis," *Phys. Rev. D* **97** no. 9, (2018) 093003, arXiv:1801.01136 [hep-ph].

[244] E. E. Jenkins, A. V. Manohar, and M. Trott, "Renormalization Group Evolution of the Standard Model Dimension Six Operators I: Formalism and lambda Dependence," *JHEP* **10** (2013) 087, arXiv:1308.2627 [hep-ph].

[245] E. E. Jenkins, A. V. Manohar, and M. Trott, "Renormalization Group Evolution of the Standard Model Dimension Six Operators II: Yukawa Dependence," *JHEP* **01** (2014) 035, arXiv:1310.4838 [hep-ph].

[246] R. Gauld, B. D. Pecjak, and D. J. Scott, "One-loop corrections to $h \to b\bar{b}$ and $h \to \tau\overline{\tau}$ decays in the Standard Model Dimension-6 EFT: four-fermion operators and the large-m_t limit," *JHEP* **05** (2016) 080, arXiv:1512.02508 [hep-ph].

[247] G. Ossola, C. G. Papadopoulos, and R. Pittau, "Reducing full one-loop amplitudes to scalar integrals at the integrand level," *Nucl. Phys. B* **763** (2007) 147–169, arXiv:hep-ph/0609007.

[248] G. Ossola, C. G. Papadopoulos, and R. Pittau, "CutTools: A Program implementing the OPP reduction method to compute one-loop amplitudes," *JHEP* **03** (2008) 042, arXiv:0711.3596 [hep-ph].

[249] G. Ossola, C. G. Papadopoulos, and R. Pittau, "On the Rational Terms of the one-loop amplitudes," *JHEP* **05** (2008) 004, arXiv:0802.1876 [hep-ph].

[250] R. D. Ball *et al.*, "Parton distributions with LHC data," *Nucl. Phys. B* **867** (2013) 244–289, arXiv:1207.1303 [hep-ph].

[251] I. Brivio, Y. Jiang, and M. Trott, "The SMEFTsim package, theory and tools," *JHEP* **12** (2017) 070, arXiv:1709.06492 [hep-ph].

[252] "Guidelines for extrapolation of cms and atlas lhc/hl-lhc couplings projections to he-lhc." https://twiki.cern.ch/twiki/bin/view/LHCPhysics/GuidelinesCouplingProjections2018#Details%20of%20the%20CMS%20projections.

[253] J. Salvatier, T. V. Wiecki, and C. Fonnesbeck, "Probabilistic programming in python using PyMC3," *PeerJ Computer Science* **2** (Apr, 2016) e55. https://doi.org/10.7717/peerj-cs.55.

[254] R. Kumar, C. Carroll, A. Hartikainen, and O. Martin, "Arviz a unified library for exploratory analysis of bayesian models in python," *Journal of Open Source Software* **4** no. 33, (2019) 1143. https://doi.org/10.21105/joss.01143.

[255] J. de Blas *et al.*, "HEPfit: a Code for the Combination of Indirect and Direct Constraints on High Energy Physics Models," *Eur. Phys. J. C* **80** no. 5, (2020) 456, arXiv:1910.14012 [hep-ph].

[256] I. Brivio, S. Bruggisser, F. Maltoni, R. Moutafis, T. Plehn, E. Vryonidou, S. Westhoff, and C. Zhang, "O new physics, where art thou? A global search in the top sector," *JHEP* **02** (2020) 131, arXiv:1910.03606 [hep-ph].

[257] C. Zhang, "Constraining *qqtt* operators from four-top production: a case for enhanced EFT sensitivity," *Chin. Phys. C* **42** no. 2, (2018) 023104, arXiv:1708.05928 [hep-ph].

[258] **ATLAS** Collaboration, "Search for Higgs boson pair production in the two bottom quarks plus two photons final state in pp collisions at $\sqrt{s} = 13$ TeV with the ATLAS detector," Tech. Rep. ATLAS-CONF-2021-016, 2021.

[259] L. Alasfar, R. Gröber, C. Grojean, A. Paul, and Z. Qian, "Machine learning augmented probes of light-quark Yukawa and trilinear couplings from Higgs pair production," *In preparation* (2021) .

[260] J. Alison *et al.*, "Higgs boson potential at colliders: Status and perspectives," *Rev. Phys.* **5** (2020) 100045, arXiv:1910.00012 [hep-ph].

[261] **CMS** Collaboration, "Prospects for HH measurements at the HL-LHC," *CMS-PAS-FTR-18-019* (2018) .

[262] L. Silvestrini and M. Valli, "Model-independent Bounds on the Standard Model Effective Theory from Flavour Physics," *Phys. Lett. B* **799** (2019) 135062, arXiv:1812.10913 [hep-ph].

[263] G. Banelli, E. Salvioni, J. Serra, T. Theil, and A. Weiler, "The Present and Future of Four Top Operators," *JHEP* **02** (2021) 043, arXiv:2010.05915 [hep-ph].

[264] J. de Blas, J. C. Criado, M. Perez-Victoria, and J. Santiago, "Effective description of general extensions of the Standard Model: the complete tree-level dictionary," *JHEP* **03** (2018) 109, arXiv:1711.10391 [hep-ph].

[265] Anisha, S. D. Bakshi, S. Banerjee, A. Biekötter, J. Chakrabortty, S. K. Patra, and M. Spannowsky, "Effective limits on single scalar extensions in the light of recent LHC data," arXiv:2111.05876 [hep-ph].

[266] **ATLAS** Collaboration, M. Aaboud *et al.*, "Observation of $H \to b\bar{b}$ decays and VH production with the ATLAS detector," *Phys. Lett. B* **786** (2018) 59–86, arXiv:1808.08238 [hep-ex].

[267] **CMS** Collaboration, A. M. Sirunyan *et al.*, "Observation of Higgs boson decay to bottom quarks," *Phys. Rev. Lett.* **121** no. 12, (2018) 121801, arXiv:1808.08242 [hep-ex].

[268] R. V. Harlander, S. Liebler, and T. Zirke, "Higgs Strahlung at the Large Hadron Collider in the 2-Higgs-Doublet Model," *JHEP* **02** (2014) 023, arXiv:1307.8122 [hep-ph].

[269] L. D. Landau, "On the angular momentum of a system of two photons," *Dokl. Akad. Nauk SSSR* **60** no. 2, (1948) 207–209.

[270] C.-N. Yang, "Selection Rules for the Dematerialization of a Particle Into Two Photons," *Phys. Rev.* **77** (1950) 242–245.

[271] G. Passarino and M. J. G. Veltman, "One Loop corrections for e^+e^- annihilation into $\mu^+\mu^-$ in the Weinberg Model," *Nucl. Phys.* **B160** (1979) 151.

[272] S. Larin, "The Renormalization of the axial anomaly in dimensional regularization," *Phys. Lett. B* **303** (1993) 113–118, arXiv:hep-ph/9302240.

[273] M. Spira, A. Djouadi, D. Graudenz, and P. M. Zerwas, "Higgs boson production at the LHC," *Nucl. Phys. B* **453** (1995) 17–82, arXiv:hep-ph/9504378.

[274] U. Aglietti, R. Bonciani, G. Degrassi, and A. Vicini, "Analytic Results for Virtual QCD Corrections to Higgs Production and Decay," *JHEP* **01** (2007) 021, arXiv:hep-ph/0611266.

[275] R. Mertig, M. Bohm, and A. Denner, "FEYN CALC: Computer algebraic calculation of Feynman amplitudes," *Comput. Phys. Commun.* **64** (1991) 345–359.

[276] V. Shtabovenko, R. Mertig, and F. Orellana, "New Developments in FeynCalc 9.0," *Comput. Phys. Commun.* **207** (2016) 432–444, arXiv:1601.01167 [hep-ph].

[277] H. H. Patel, "Package-X 2.0: A Mathematica package for the analytic calculation of one-loop integrals," *Comput. Phys. Commun.* **218** (2017) 66–70, arXiv:1612.00009 [hep-ph].

[278] P. Maierhöfer, J. Usovitsch, and P. Uwer, "Kira—A Feynman integral reduction program," *Comput. Phys. Commun.* **230** (2018) 99–112, arXiv:1705.05610 [hep-ph].

[279] R. Bonciani, P. Mastrolia, and E. Remiddi, "Master integrals for the two loop QCD virtual corrections to the forward backward asymmetry," *Nucl. Phys. B* **690** (2004) 138–176, arXiv:hep-ph/0311145.

[280] S. Borowka and G. Heinrich, "Massive non-planar two-loop four-point integrals with SecDec 2.1," *Comput. Phys. Commun.* **184** (2013) 2552–2561, arXiv:1303.1157 [hep-ph].

[281] S. Borowka, G. Heinrich, S. P. Jones, M. Kerner, J. Schlenk, and T. Zirke, "SecDec-3.0: numerical evaluation of multi-scale integrals beyond one loop," *Comput. Phys. Commun.* **196** (2015) 470–491, arXiv:1502.06595 [hep-ph].

[282] A. V. Smirnov, "FIRE5: a C++ implementation of Feynman Integral REduction," *Comput. Phys. Commun.* **189** (2015) 182–191, arXiv:1408.2372 [hep-ph].

[283] R. N. Lee, "LiteRed 1.4: a powerful tool for reduction of multiloop integrals," *J. Phys. Conf. Ser.* **523** (2014) 012059, arXiv:1310.1145 [hep-ph].

[284] A. von Manteuffel and L. Tancredi, "A non-planar two-loop three-point function beyond multiple polylogarithms," *JHEP* **06** (2017) 127, arXiv:1701.05905 [hep-ph].

[285] R. Bonciani, G. Degrassi, P. P. Giardino, and R. Gröber, "A Numerical Routine for the Crossed Vertex Diagram with a Massive-Particle Loop," *Comput. Phys. Commun.* **241** (2019) 122–131, arXiv:1812.02698 [hep-ph].

[286] L. Naterop, A. Signer, and Y. Ulrich, "handyG —Rapid numerical evaluation of generalised polylogarithms in Fortran," *Comput. Phys. Commun.* **253** (2020) 107165, arXiv:1909.01656 [hep-ph].

[287] S. Buehler and C. Duhr, "CHAPLIN - Complex Harmonic Polylogarithms in Fortran," *Comput. Phys. Commun.* **185** (2014) 2703–2713, arXiv:1106.5739 [hep-ph].

[288] S. Borowka, G. Heinrich, S. Jahn, S. P. Jones, M. Kerner, J. Schlenk, and T. Zirke, "pySecDec: a toolbox for the numerical evaluation of multi-scale integrals," *Comput. Phys. Commun.* **222** (2018) 313–326, arXiv:1703.09692 [hep-ph].

[289] S. Borowka, G. Heinrich, S. Jahn, S. P. Jones, M. Kerner, and J. Schlenk, "A GPU compatible quasi-Monte Carlo integrator interfaced to pySecDec," *Comput. Phys. Commun.* **240** (2019) 120–137, arXiv:1811.11720 [physics.comp-ph].

[290] **ATLAS Collaboration** Collaboration, "Measurement prospects of the pair production and self-coupling of the Higgs boson with the ATLAS experiment at the HL-LHC,".

[291] T. Plehn and M. Rauch, "The quartic higgs coupling at hadron colliders," *Phys. Rev.* **D72** (2005) 053008, arXiv:hep-ph/0507321 [hep-ph].

[292] O. Eboli, G. Marques, S. Novaes, and A. Natale, "Twin higgs-boson production," *Physics Letters B* **197** no. 1, (1987) 269–272.

[293] E. Glover and J. van der Bij, "Higgs boson pair production via gluon fusion," *Nuclear Physics B* **309** no. 2, (1988) 282–294.

[294] D. A. Dicus, C. Kao, and S. S. D. Willenbrock, "Higgs Boson Pair Production From Gluon Fusion," *Phys. Lett.* **B203** (1988) 457–461.

[295] T. Plehn, M. Spira, and P. M. Zerwas, "Pair production of neutral Higgs particles in gluon-gluon collisions," *Nucl. Phys.* **B479** (1996) 46–64, arXiv:hep-ph/9603205 [hep-ph]. [Erratum: Nucl. Phys.B531,655(1998)].

[296] J. Grigo, K. Melnikov, and M. Steinhauser, "Virtual corrections to Higgs boson pair production in the large top quark mass limit," *Nucl. Phys.* **B888** (2014) 17–29, arXiv:1408.2422 [hep-ph].

[297] D. de Florian and J. Mazzitelli, "Two-loop virtual corrections to Higgs pair production," *Phys. Lett. B* **724** (2013) 306–309, arXiv:1305.5206 [hep-ph].

[298] J. Grigo, J. Hoff, K. Melnikov, and M. Steinhauser, "On the Higgs boson pair production at the LHC," *Nucl. Phys.* **B875** (2013) 1–17, arXiv:1305.7340 [hep-ph].

[299] J. Grigo, J. Hoff, and M. Steinhauser, "Higgs boson pair production: top quark mass effects at NLO and NNLO," *Nucl. Phys. B* **900** (2015) 412–430, arXiv:1508.00909 [hep-ph].

[300] G. Degrassi, P. P. Giardino, and R. Gröber, "On the two-loop virtual QCD corrections to Higgs boson pair production in the Standard Model," *Eur. Phys. J. C* **76** no. 7, (2016) 411, arXiv:1603.00385 [hep-ph].

[301] D. Y. Shao, C. S. Li, H. T. Li, and J. Wang, "Threshold resummation effects in Higgs boson pair production at the LHC," *JHEP* **07** (2013) 169, arXiv:1301.1245 [hep-ph].

[302] S. Borowka, N. Greiner, G. Heinrich, S. P. Jones, M. Kerner, J. Schlenk, and T. Zirke, "Full top quark mass dependence in Higgs boson pair production at NLO," *JHEP* **10** (2016) 107, arXiv:1608.04798 [hep-ph].

[303] S. Borowka, N. Greiner, G. Heinrich, S. P. Jones, M. Kerner, J. Schlenk, U. Schubert, and T. Zirke, "Higgs Boson Pair Production in Gluon Fusion at Next-to-Leading Order with Full Top-Quark Mass Dependence," *Phys. Rev. Lett.* **117** no. 1, (2016) 012001, arXiv:1604.06447 [hep-ph]. [Erratum: Phys. Rev. Lett.117,no.7,079901(2016)].

[304] J. Baglio, F. Campanario, S. Glaus, M. Mühlleitner, M. Spira, and J. Streicher, "Gluon fusion into Higgs pairs at NLO QCD and the top mass scheme," *Eur. Phys. J.* **C79** no. 6, (2019) 459, arXiv:1811.05692 [hep-ph].

[305] J. Davies, G. Mishima, M. Steinhauser, and D. Wellmann, "Double Higgs boson production at NLO in the high-energy limit: complete analytic results," *JHEP* **01** (2019) 176, arXiv:1811.05489 [hep-ph].

[306] X. Xu and L. L. Yang, "Towards a new approximation for pair-production and associated-production of the Higgs boson," *JHEP* **01** (2019) 211, arXiv:1810.12002 [hep-ph].

[307] G. Wang, Y. Wang, X. Xu, Y. Xu, and L. L. Yang, "Efficient computation of two-loop amplitudes for Higgs boson pair production," *Phys. Rev. D* **104** no. 5, (2021) L051901, arXiv:2010.15649 [hep-ph].

[308] J. Davies, R. Gröber, A. Maier, T. Rauh, and M. Steinhauser, "Top quark mass dependence of the Higgs boson-gluon form factor at three loops," *Phys. Rev.* **D100** no. 3, (2019) 034017, arXiv:1906.00982 [hep-ph].

[309] M. Grazzini, G. Heinrich, S. Jones, S. Kallweit, M. Kerner, J. M. Lindert, and J. Mazzitelli, "Higgs boson pair production at NNLO with top quark mass effects," *JHEP* **05** (2018) 059, arXiv:1803.02463 [hep-ph].

[310] D. de Florian, M. Grazzini, C. Hanga, S. Kallweit, J. M. Lindert, P. Maierhöfer, J. Mazzitelli, and D. Rathlev, "Differential Higgs Boson Pair Production at Next-to-Next-to-Leading Order in QCD," *JHEP* **09** (2016) 151, arXiv:1606.09519 [hep-ph].

[311] D. de Florian and J. Mazzitelli, "Higgs Boson Pair Production at Next-to-Next-to-Leading Order in QCD," *Phys. Rev. Lett.* **111** (2013) 201801, arXiv:1309.6594 [hep-ph].

[312] D. de Florian and J. Mazzitelli, "Higgs pair production at next-to-next-to-leading logarithmic accuracy at the LHC," *JHEP* **09** (2015) 053, arXiv:1505.07122 [hep-ph].

[313] S. Jones and S. Kuttimalai, "Parton Shower and NLO-Matching uncertainties in Higgs Boson Pair Production," *JHEP* **02** (2018) 176, arXiv:1711.03319 [hep-ph].

[314] G. Heinrich, S. P. Jones, M. Kerner, G. Luisoni, and L. Scyboz, "Probing the trilinear Higgs boson coupling in di-Higgs production at NLO QCD including parton shower effects," *JHEP* **06** (2019) 066, arXiv:1903.08137 [hep-ph].

[315] G. Heinrich, S. P. Jones, M. Kerner, G. Luisoni, and E. Vryonidou, "NLO predictions for Higgs boson pair production with full top quark mass dependence matched to parton showers," *JHEP* **08** (2017) 088, arXiv:1703.09252 [hep-ph].

[316] L. Bellafronte, G. Degrassi, P. P. Giardino, R. Gröber, and M. Vitti, "Gluon Fusion Production at NLO: Merging the Transverse Momentum and the High-Energy Expansions," arXiv:2202.12157 [hep-ph].

[317] R. Gröber and M. Mühlleitner, "Composite Higgs Boson Pair Production at the LHC," *JHEP* **06** (2011) 020, arXiv:1012.1562 [hep-ph].

[318] R. Grober, M. Muhlleitner, M. Spira, and J. Streicher, "NLO QCD Corrections to Higgs Pair Production including Dimension-6 Operators," *JHEP* **09** (2015) 092, arXiv:1504.06577 [hep-ph].

[319] D. de Florian, I. Fabre, and J. Mazzitelli, "Higgs boson pair production at NNLO in QCD including dimension 6 operators," *JHEP* **10** (2017) 215, arXiv:1704.05700 [hep-ph].

[320] S. Dittmaier *et al.*, "Handbook of LHC Higgs Cross Sections: 2. Differential Distributions," arXiv:1201.3084 [hep-ph].

[321] **LHC Higgs Cross Section Working Group** Collaboration, D. de Florian *et al.*, "Handbook of LHC Higgs Cross Sections: 4. Deciphering the Nature of the Higgs Sector," arXiv:1610.07922 [hep-ph].

[322] A. D. Martin, W. J. Stirling, R. S. Thorne, and G. Watt, "Uncertainties on alpha(S) in global PDF analyses and implications for predicted hadronic cross sections," *Eur. Phys. J.* **C64** (2009) 653–680, arXiv:0905.3531 [hep-ph].

[323] F. Demartin, S. Forte, E. Mariani, J. Rojo, and A. Vicini, "The impact of PDF and alphas uncertainties on Higgs Production in gluon fusion at hadron colliders," *Phys. Rev.* **D82** (2010) 014002, arXiv:1004.0962 [hep-ph].

[324] J. Baglio, F. Campanario, S. Glaus, M. Mühlleitner, J. Ronca, and M. Spira, "$gg \to HH$: Combined uncertainties," *Phys. Rev. D* **103** no. 5, (2021) 056002, arXiv:2008.11626 [hep-ph].

[325] L.-B. Chen, H. T. Li, H.-S. Shao, and J. Wang, "Higgs boson pair production via gluon fusion at N^{3}LO in QCD," *Phys. Lett. B* **803** (2020) 135292, arXiv:1909.06808 [hep-ph].

[326] L.-B. Chen, H. T. Li, H.-S. Shao, and J. Wang, "The gluon-fusion production of Higgs boson pair: N^{3}LO QCD corrections and top-quark mass effects," *JHEP* **03** (2020) 072, arXiv:1912.13001 [hep-ph].

[327] J. Baglio, A. Djouadi, R. Gröber, M. M. Mühlleitner, J. Quevillon, and M. Spira, "The measurement of the Higgs self-coupling at the LHC: theoretical status," *JHEP* **04** (2013) 151, arXiv:1212.5581 [hep-ph].

[328] L.-S. Ling, R.-Y. Zhang, W.-G. Ma, L. Guo, W.-H. Li, and X.-Z. Li, "NNLO QCD corrections to Higgs pair production via vector boson fusion at hadron colliders," *Phys. Rev. D* **89** no. 7, (2014) 073001, arXiv:1401.7754 [hep-ph].

[329] F. A. Dreyer and A. Karlberg, "Vector-Boson Fusion Higgs Pair Production at N^{3}LO," *Phys. Rev. D* **98** no. 11, (2018) 114016, arXiv:1811.07906 [hep-ph].

[330] F. A. Dreyer and A. Karlberg, "Fully differential Vector-Boson Fusion Higgs Pair Production at Next-to-Next-to-Leading Order," *Phys. Rev. D* **99** no. 7, (2019) 074028, arXiv:1811.07918 [hep-ph].

[331] H. T. Li and J. Wang, "Fully Differential Higgs Pair Production in Association With a W Boson at Next-to-Next-to-Leading Order in QCD," *Phys. Lett. B* **765** (2017) 265–271, arXiv:1607.06382 [hep-ph].

[332] H. T. Li, C. S. Li, and J. Wang, "Fully differential Higgs boson pair production in association with a Z boson at next-to-next-to-leading order in QCD," *Phys. Rev. D* **97** no. 7, (2018) 074026, arXiv:1710.02464 [hep-ph].

[333] R. Frederix, S. Frixione, V. Hirschi, F. Maltoni, O. Mattelaer, P. Torrielli, E. Vryonidou, and M. Zaro, "Higgs pair production at the LHC with NLO and parton-shower effects," *Phys. Lett. B* **732** (2014) 142–149, arXiv:1401.7340 [hep-ph].

[334] **CMS Collaboration** Collaboration, "Search for Higgs boson pair production in the four b quark final state," tech. rep., CERN, Geneva, 2021. https://cds.cern.ch/record/2771912.

[335] **CMS Collaboration** Collaboration, "Search for Higgs boson pair production via vector boson fusion with highly Lorentz-boosted Higgs bosons in the four b quark final state at $\sqrt{s} = 13$ TeV," tech. rep., CERN, Geneva, 2021. http://cds.cern.ch/record/2776802.

[336] **ATLAS** Collaboration, G. Aad *et al.*, "Search for the $HH \to b\bar{b}b\bar{b}$ process via vector-boson fusion production using proton-proton collisions at $\sqrt{s} = 13$ TeV with the ATLAS detector," *JHEP* **07** (2020) 108, arXiv:2001.05178 [hep-ex]. [Erratum: JHEP 01, 145 (2021), Erratum: JHEP 05, 207 (2021)].

[337] **ATLAS** Collaboration, G. Aad *et al.*, "Search for non-resonant Higgs boson pair production in the $bb\ell\nu\ell\nu$ final state with the ATLAS detector in pp collisions at $\sqrt{s} = 13$ TeV," *Phys. Lett. B* **801** (2020) 135145, arXiv:1908.06765 [hep-ex].

[338] **CMS Collaboration** Collaboration, "Search for nonresonant Higgs boson pair production in the 4 leptons plus 2 b jets final state in proton-proton collisions at $\sqrt{s} = 13$ TeV," tech. rep., CERN, Geneva, 2020. https://cds.cern.ch/record/2725691.

[339] **ATLAS Collaboration** Collaboration, "Combination of searches for non-resonant and resonant Higgs boson pair production in the $b\bar{b}\gamma\gamma$, $b\bar{b}\tau^+\tau^-$ and $b\bar{b}b\bar{b}$ decay channels using pp collisions at $\sqrt{s} = 13$ TeV with the ATLAS detector," tech. rep., CERN, Geneva, Oct, 2021. https://cds.cern.ch/record/2786865. All figures including auxiliary figures are available at https://atlas.web.cern.ch/Atlas/GROUPS/PHYSICS/CONFNOTES/ATLAS-CONF-2021-052.

[340] **CMS** Collaboration, A. M. Sirunyan *et al.*, "Search for nonresonant Higgs boson pair production in final states with two bottom quarks and two photons in proton-proton collisions at $\sqrt{s} = 13$ TeV," *JHEP* **03** (2021) 257, arXiv:2011.12373 [hep-ex].

[341] A. Azatov, R. Contino, G. Panico, and M. Son, "Effective field theory analysis of double Higgs boson production via gluon fusion," *Phys. Rev.* **D92** no. 3, (2015) 035001, arXiv:1502.00539 [hep-ph].

[342] U. Baur, T. Plehn, and D. L. Rainwater, "Probing the Higgs selfcoupling at hadron colliders using rare decays," *Phys. Rev.* **D69** (2004) 053004, arXiv:hep-ph/0310056 [hep-ph].

[343] F. Kling, T. Plehn, and P. Schichtel, "Maximizing the significance in Higgs boson pair analyses," *Phys. Rev.* **D95** no. 3, (2017) 035026, arXiv:1607.07441 [hep-ph].

[344] V. Barger, L. L. Everett, C. B. Jackson, and G. Shaughnessy, "Higgs-Pair Production and Measurement of the Triscalar Coupling at LHC(8,14)," *Phys. Lett.* **B728** (2014) 433–436, arXiv:1311.2931 [hep-ph].

[345] A. Adhikary, S. Banerjee, R. K. Barman, B. Bhattacherjee, and S. Niyogi, "Revisiting the non-resonant Higgs pair production at the HL-LHC," *JHEP* **07** (2018) 116, arXiv:1712.05346 [hep-ph].

[346] A. Alves, T. Ghosh, and K. Sinha, "Can We Discover Double Higgs Production at the LHC?," *Phys. Rev. D* **96** no. 3, (2017) 035022, arXiv:1704.07395 [hep-ph].

[347] S. Weinberg, "Models of Lepton and Quark Masses," *Phys. Rev. D* **101** no. 3, (2020) 035020, arXiv:2001.06582 [hep-th].

[348] **CMS** Collaboration, V. Khachatryan *et al.*, "Search for a standard model-like Higgs boson in the $\mu^+\mu^-$ and e^+e^- decay channels at the LHC," *Phys. Lett.* **B744** (2015) 184–207, arXiv:1410.6679 [hep-ex].

[349] Y. Nakai, D. Shih, and S. Thomas, "Strange Jet Tagging," arXiv:2003.09517 [hep-ph].

[350] G. Blankenburg, J. Ellis, and G. Isidori, "Flavour-Changing Decays of a 125 GeV Higgs-like Particle," *Phys. Lett.* **B712** (2012) 386–390, arXiv:1202.5704 [hep-ph].

[351] G. D'Ambrosio, G. F. Giudice, G. Isidori, and A. Strumia, "Minimal flavor violation: An Effective field theory approach," *Nucl. Phys.* **B645** (2002) 155–187, arXiv:hep-ph/0207036 [hep-ph].

[352] A. Pich and P. Tuzon, "Yukawa Alignment in the Two-Higgs-Doublet Model," *Phys. Rev. D* **80** (2009) 091702, arXiv:0908.1554 [hep-ph].

[353] A. Pich, "Flavour constraints on multi-Higgs-doublet models: Yukawa alignment," *Nucl. Phys. B Proc. Suppl.* **209** (2010) 182–187, arXiv:1010.5217 [hep-ph].

[354] D. Egana-Ugrinovic, S. Homiller, and P. Meade, "Aligned and Spontaneous Flavor Violation," *Phys. Rev. Lett.* **123** no. 3, (2019) 031802, arXiv:1811.00017 [hep-ph].

[355] P. M. Ferreira, L. Lavoura, and J. P. Silva, "Renormalization-group constraints on Yukawa alignment in multi-Higgs-doublet models," *Phys. Lett. B* **688** (2010) 341–344, arXiv:1001.2561 [hep-ph].

[356] M. Jung, A. Pich, and P. Tuzon, "Charged-Higgs phenomenology in the Aligned two-Higgs-doublet model," *JHEP* **11** (2010) 003, arXiv:1006.0470 [hep-ph].

[357] F. J. Botella, G. C. Branco, A. M. Coutinho, M. N. Rebelo, and J. I. Silva-Marcos, "Natural Quasi-Alignment with two Higgs Doublets and RGE Stability," *Eur. Phys. J. C* **75** (2015) 286, arXiv:1501.07435 [hep-ph].

[358] R. Contino, C. Grojean, M. Moretti, F. Piccinini, and R. Rattazzi, "Strong Double Higgs Production at the LHC," *JHEP* **05** (2010) 089, arXiv:1002.1011 [hep-ph].

[359] D. Dicus, T. Stelzer, Z. Sullivan, and S. Willenbrock, "Higgs boson production in association with bottom quarks at next-to-leading order," *Phys. Rev.* **D59** (1999) 094016, arXiv:hep-ph/9811492 [hep-ph].

[360] C. Balazs, H.-J. He, and C. P. Yuan, "QCD corrections to scalar production via heavy quark fusion at hadron colliders," *Phys. Rev.* **D60** (1999) 114001, arXiv:hep-ph/9812263 [hep-ph].

[361] R. V. Harlander and W. B. Kilgore, "Higgs boson production in bottom quark fusion at next-to-next-to leading order," *Phys. Rev.* **D68** (2003) 013001, arXiv:hep-ph/0304035 [hep-ph].

[362] S. Dawson, C. Kao, Y. Wang, and P. Williams, "QCD Corrections to Higgs Pair Production in Bottom Quark Fusion," *Phys. Rev.* **D75** (2007) 013007, arXiv:hep-ph/0610284 [hep-ph].

[363] A. H. Ajjath, P. Banerjee, A. Chakraborty, P. K. Dhani, P. Mukherjee, N. Rana, and V. Ravindran, "Higgs pair production from bottom quark annihilation to NNLO in QCD," *JHEP* **05** (2019) 030, arXiv:1811.01853 [hep-ph].

[364] M. Spira, "Higgs Boson Production and Decay at Hadron Colliders," *Prog. Part. Nucl. Phys.* **95** (2017) 98–159, arXiv:1612.07651 [hep-ph].

[365] V. N. Gribov and L. N. Lipatov, "Deep inelastic e p scattering in perturbation theory," *Sov. J. Nucl. Phys.* **15** (1972) 438–450. [Yad. Fiz.15,781(1972)].

[366] G. Altarelli and G. Parisi, "Asymptotic Freedom in Parton Language," *Nucl. Phys.* **B126** (1977) 298–318.

[367] Y. L. Dokshitzer, "Calculation of the Structure Functions for Deep Inelastic Scattering and e+ e- Annihilation by Perturbation Theory in Quantum Chromodynamics.," *Sov. Phys. JETP* **46** (1977) 641–653. [Zh. Eksp. Teor. Fiz.73,1216(1977)].

[368] **NNPDF** Collaboration, R. D. Ball *et al.*, "Parton distributions from high-precision collider data," *Eur. Phys. J.* **C77** no. 10, (2017) 663, arXiv:1706.00428 [hep-ph].

[369] A. Buckley, J. Ferrando, S. Lloyd, K. Nordström, B. Page, M. Rüfenacht, M. Schönherr, and G. Watt, "LHAPDF6: parton density access in the LHC precision era," *Eur. Phys. J.* **C75** (2015) 132, arXiv:1412.7420 [hep-ph].

[370] A. Denner, S. Dittmaier, and L. Hofer, "COLLIER - A fortran-library for one-loop integrals," *PoS* **LL2014** (2014) 071, arXiv:1407.0087 [hep-ph].

[371] A. Djouadi, J. Kalinowski, and M. Spira, "HDECAY: A Program for Higgs boson decays in the standard model and its supersymmetric extension," *Comput. Phys. Commun.* **108** (1998) 56–74, arXiv:hep-ph/9704448 [hep-ph].

[372] A. Djouadi, J. Kalinowski, M. Muehlleitner, and M. Spira, "HDECAY: Twenty$_{++}$ years after," *Comput. Phys. Commun.* **238** (2019) 214–231, arXiv:1801.09506 [hep-ph].

[373] T. Sjostrand, S. Mrenna, and P. Z. Skands, "PYTHIA 6.4 Physics and Manual," *JHEP* **05** (2006) 026, arXiv:hep-ph/0603175 [hep-ph].

[374] D. C. Hall, "RootTuple: A library enabling ROOT n-tuple output from FORTRAN HEP programs," http://roottuple.hepforge.org.

[375] T. Sjöstrand, S. Ask, J. R. Christiansen, R. Corke, N. Desai, P. Ilten, S. Mrenna, S. Prestel, C. O. Rasmussen, and P. Z. Skands, "An introduction to PYTHIA 8.2," *Comput. Phys. Commun.* **191** (2015) 159–177, arXiv:1410.3012 [hep-ph].

[376] **DELPHES 3** Collaboration, J. de Favereau, C. Delaere, P. Demin, A. Giammanco, V. Lemaître, A. Mertens, and M. Selvaggi, "DELPHES 3, A modular framework for fast simulation of a generic collider experiment," *JHEP* **02** (2014) 057, arXiv:1307.6346 [hep-ex].

[377] C. Grojean, A. Paul, and Z. Qian, "Resurrecting $b\bar{b}h$ with kinematic shapes," *JHEP* **04** (2021) 139, arXiv:2011.13945 [hep-ph].

[378] W. Beenakker, S. Dittmaier, M. Kramer, B. Plumper, M. Spira, and P. M. Zerwas, "Higgs radiation off top quarks at the Tevatron and the LHC," *Phys. Rev. Lett.* **87** (2001) 201805, arXiv:hep-ph/0107081.

[379] D. Fäh and N. Greiner, "Diphoton production in association with two bottom jets," *Eur. Phys. J. C* **77** no. 11, (2017) 750, arXiv:1706.08309 [hep-ph].

[380] F. Campanario, R. Roth, and D. Zeppenfeld, "QCD radiation in WH and WZ production and anomalous coupling measurements," *Phys. Rev. D* **91** (2015) 054039, arXiv:1410.4840 [hep-ph].

[381] S. Dawson, C. Jackson, L. Reina, and D. Wackeroth, "Higgs production in association with bottom quarks at hadron colliders," *Mod. Phys. Lett. A* **21** (2006) 89–110, arXiv:hep-ph/0508293.

[382] M. Cacciari, G. P. Salam, and G. Soyez, "FastJet User Manual," *Eur. Phys. J.* **C72** (2012) 1896, arXiv:1111.6097 [hep-ph].

[383] **CMS** Collaboration, S. Chatrchyan *et al.*, "Inclusive b-jet production in pp collisions at $\sqrt{s} = 7$ TeV," *JHEP* **04** (2012) 084, arXiv:1202.4617 [hep-ex].

[384] **CMS** Collaboration, "Performance of b tagging at sqrt(s)=8 TeV in multijet, ttbar and boosted topology events," Tech. Rep. CMS-PAS-BTV-13-001, CERN, Geneva, 2013. https://cds.cern.ch/record/1581306.

[385] **ATLAS** Collaboration, "Performance assumptions based on full simulation for an upgraded ATLAS detector at a High-Luminosity LHC," Tech. Rep. ATL-PHYS-PUB-2013-009, CERN, Geneva, 2013. http://cds.cern.ch/record/1604420.

[386] **CMS** Collaboration, "Photon ID performance with 19.6 fb^{-1} of data collected at $\sqrt{s} = 8$ TeV with the CMS detector," Tech. Rep. CMS-DP-2013-010, CERN, Geneva, 2013. http://cds.cern.ch/record/1542855.

[387] G. Cowan, K. Cranmer, E. Gross, and O. Vitells, "Asymptotic formulae for likelihood-based tests of new physics," *Eur. Phys. J.* **C71** (2011) 1554, arXiv:1007.1727 [physics.data-an]. [Erratum: Eur. Phys. J.C73,2501(2013)].

[388] L. Heinrich, M. Feickert, and G. Stark, "pyhf: v0.6.3." https://doi.org/10.5281/zenodo.1169739. https://github.com/scikit-hep/pyhf/releases/tag/v0.6.3.

[389] L. Heinrich, M. Feickert, G. Stark, and K. Cranmer, "pyhf: pure-python implementation of histfactory statistical models," *Journal of Open Source Software* **6** no. 58, (2021) 2823. https://doi.org/10.21105/joss.02823.

[390] T. Chen and C. Guestrin, "XGBoost: A Scalable Tree Boosting System," in *Proceedings of the 22nd ACM SIGKDD International Conference on Knowledge Discovery and Data Mining*, KDD '16, p. 785–794. Association for Computing Machinery, New York, NY, USA, 2016. https://dl.acm.org/doi/10.1145/2939672.2939785.

[391] L. S. Shapley, "Notes on the n-Person Game-II: The Value of an n-Person Game," *Rand Corporation* (1951) . https://www.rand.org/pubs/research_memoranda/RM0670.html.

[392] D. Alvestad, N. Fomin, J. Kersten, S. Maeland, and I. Strümke, "Beyond Cuts in Small Signal Scenarios - Enhanced Sneutrino Detectability Using Machine Learning," arXiv:2108.03125 [hep-ph].

[393] A. S. Cornell, W. Doorsamy, B. Fuks, G. Harmsen, and L. Mason, "Boosted decision trees in the era of new physics: a smuon analysis case study," arXiv:2109.11815 [hep-ph].

[394] S. M. Lundberg and S.-I. Lee, "A unified approach to interpreting model predictions," in *Advances in Neural Information Processing Systems*, I. Guyon, U. V. Luxburg, S. Bengio, H. Wallach, R. Fergus, S. Vishwanathan, and R. Garnett, eds., vol. 30, pp. 4765–4774. Curran Associates, Inc., 2017. 1705.07874. https://proceedings.neurips.cc/paper/2017/file/8a20a8621978632d76c43dfd28b67767-Paper.pdf.

[395] S. M. Lundberg, G. G. Erion, and S.-I. Lee, "Consistent Individualized Feature Attribution for Tree Ensembles," *arXiv e-prints* (Feb., 2018) , arXiv:1802.03888 [cs.LG].

[396] S. M. Lundberg, G. Erion, H. Chen, A. DeGrave, J. M. Prutkin, B. Nair, R. Katz, J. Himmelfarb, N. Bansal, and S.-I. Lee, "From local explanations to global understanding with explainable AI for trees," *Nature Machine Intelligence* **2** no. 1, (2020) 56–67. https://www.nature.com/articles/s42256-019-0138-9.

[397] **ATLAS** Collaboration, "Measurement prospects of the pair production and self-coupling of the Higgs boson with the ATLAS experiment at the HL-LHC,".

[398] I. Brivio, F. Goertz, and G. Isidori, "Probing the Charm Quark Yukawa Coupling in Higgs+Charm Production," *Phys. Rev. Lett.* **115** no. 21, (2015) 211801, arXiv:1507.02916 [hep-ph].

[399] Y. Soreq, H. X. Zhu, and J. Zupan, "Light quark Yukawa couplings from Higgs kinematics," *JHEP* **12** (2016) 045, arXiv:1606.09621 [hep-ph].

[400] F. Bishara, U. Haisch, P. F. Monni, and E. Re, "Constraining Light-Quark Yukawa Couplings from Higgs Distributions," *Phys. Rev. Lett.* **118** no. 12, (2017) 121801, arXiv:1606.09253 [hep-ph].

[401] G. Bonner and H. E. Logan, "Constraining the Higgs couplings to up and down quarks using production kinematics at the CERN Large Hadron Collider," arXiv:1608.04376 [hep-ph].

[402] **CMS** Collaboration, "Constraints on the Higgs boson self-coupling from ttH+tH, H to gamma gamma differential measurements at the HL-LHC," Tech. Rep. CMS-PAS-FTR-18-020, 2018.

[403] G. Perez, Y. Soreq, E. Stamou, and K. Tobioka, "Prospects for measuring the Higgs boson coupling to light quarks," *Phys. Rev.* **D93** no. 1, (2016) 013001, arXiv:1505.06689 [hep-ph].

[404] G. T. Bodwin, F. Petriello, S. Stoynev, and M. Velasco, "Higgs boson decays to quarkonia and the $H\bar{c}c$ coupling," *Phys. Rev.* **D88** no. 5, (2013) 053003, arXiv:1306.5770 [hep-ph].

[405] A. L. Kagan, G. Perez, F. Petriello, Y. Soreq, S. Stoynev, and J. Zupan, "Exclusive Window onto Higgs Yukawa Couplings," *Phys. Rev. Lett.* **114** no. 10, (2015) 101802, arXiv:1406.1722 [hep-ph].

[406] M. König and M. Neubert, "Exclusive Radiative Higgs Decays as Probes of Light-Quark Yukawa Couplings," *JHEP* **08** (2015) 012, arXiv:1505.03870 [hep-ph].

[407] **CMS** Collaboration, A. M. Sirunyan *et al.*, "Search for rare decays of Z and Higgs bosons to J/ψ and a photon in proton-proton collisions at $\sqrt{s} = 13$ TeV," *Eur. Phys. J. C* **79** no. 2, (2019) 94, arXiv:1810.10056 [hep-ex].

[408] F. Yu, "Light Quark Yukawa Couplings and the $W^{\pm}h$ Charge Asymmetry," *Nucl. Part. Phys. Proc.* **285-286** (2017) 123–125.

[409] J. A. Aguilar-Saavedra, J. M. Cano, and J. M. No, "More light on Higgs flavor at the LHC: Higgs boson couplings to light quarks through $h + \gamma$ production," *Phys. Rev. D* **103** no. 9, (2021) 095023, arXiv:2008.12538 [hep-ph].

[410] A. Falkowski, S. Ganguly, P. Gras, J. M. No, K. Tobioka, N. Vignaroli, and T. You, "Light quark Yukawas in triboson final states," *JHEP* **04** (2021) 023, arXiv:2011.09551 [hep-ph].

[411] **ATLAS** Collaboration, A. Sciandra, "Measurement of Triboson Production and aQGCs with the ATLAS detector,".

[412] **CMS** Collaboration, "Observation of heavy triboson production in leptonic final states in proton-proton collisions at $\sqrt{s} = 13$ TeV,".

[413] T. Binoth, S. Karg, N. Kauer, and R. Ruckl, "Multi-Higgs boson production in the Standard Model and beyond," *Phys. Rev.* **D74** (2006) 113008, arXiv:hep-ph/0608057 [hep-ph].

[414] R. Contino, M. Ghezzi, M. Moretti, G. Panico, F. Piccinini, and A. Wulzer, "Anomalous Couplings in Double Higgs Production," *JHEP* **08** (2012) 154, arXiv:1205.5444 [hep-ph].

[415] S. Bar-Shalom and A. Soni, "Universally enhanced light-quarks Yukawa couplings paradigm," *Phys. Rev.* **D98** no. 5, (2018) 055001, arXiv:1804.02400 [hep-ph].

[416] M. Bauer, M. Carena, and A. Carmona, "Higgs Pair Production as a Signal of Enhanced Yukawa Couplings," *Phys. Rev. Lett.* **121** no. 2, (2018) 021801, arXiv:1801.00363 [hep-ph].

[417] D. Egana-Ugrinovic, S. Homiller, and P. Meade, "Multi-Higgs Production Probes Higgs Flavor," *Phys. Rev. D* **103** (2021) 115005, arXiv:2101.04119 [hep-ph].

[418] A. Papaefstathiou and K. Sakurai, "Triple Higgs boson production at a 100 TeV proton-proton collider," *JHEP* **02** (Aug, 2015) 006. 10 p, arXiv:1508.06524. https://cds.cern.ch/record/2047255. Corrected version of Figure 6.

[419] C. Delaunay, R. Ozeri, G. Perez, and Y. Soreq, "Probing Atomic Higgs-like Forces at the Precision Frontier," *Phys. Rev.* **D96** no. 9, (2017) 093001, arXiv:1601.05087 [hep-ph].

[420] A. Falkowski, F. Riva, and A. Urbano, "Higgs at last," *JHEP* **11** (2013) 111, arXiv:1303.1812 [hep-ph].

[421] M. Ciuchini, E. Franco, S. Mishima, and L. Silvestrini, "Electroweak Precision Observables, New Physics and the Nature of a 126 GeV Higgs Boson," *JHEP* **08** (2013) 106, arXiv:1306.4644 [hep-ph].

[422] A. Falkowski and F. Riva, "Model-independent precision constraints on dimension-6 operators," *JHEP* **02** (2015) 039, arXiv:1411.0669 [hep-ph].

[423] J. de Blas, M. Ciuchini, E. Franco, S. Mishima, M. Pierini, L. Reina, and L. Silvestrini, "Electroweak precision observables and Higgs-boson signal strengths in the Standard Model and beyond: present and future," *JHEP* **12** (2016) 135, arXiv:1608.01509 [hep-ph].

[424] J. de Blas, M. Ciuchini, E. Franco, S. Mishima, M. Pierini, L. Reina, and L. Silvestrini, "The Global Electroweak and Higgs Fits in the LHC era," *PoS* **EPS-HEP2017** (2017) 467, arXiv:1710.05402 [hep-ph].

[425] J. Haller, A. Hoecker, R. Kogler, K. Mönig, T. Peiffer, and J. Stelzer, "Update of the global electroweak fit and constraints on two-Higgs-doublet models," *Eur. Phys. J. C* **78** no. 8, (2018) 675, arXiv:1803.01853 [hep-ph].

[426] B. Bhattacharya, A. Datta, D. London, and S. Shivashankara, "Simultaneous Explanation of the R_K and $R(D^{(*)})$ Puzzles," *Phys. Lett. B* **742** (2015) 370–374, arXiv:1412.7164 [hep-ph].

[427] F. Feruglio, P. Paradisi, and A. Pattori, "Revisiting Lepton Flavor Universality in B Decays," *Phys. Rev. Lett.* **118** no. 1, (2017) 011801, arXiv:1606.00524 [hep-ph].

[428] A. Celis, J. Fuentes-Martin, A. Vicente, and J. Virto, "Gauge-invariant implications of the LHCb measurements on lepton-flavor nonuniversality," *Phys. Rev. D* **96** no. 3, (2017) 035026, arXiv:1704.05672 [hep-ph].

[429] D. Buttazzo, A. Greljo, G. Isidori, and D. Marzocca, "B-physics anomalies: a guide to combined explanations," *JHEP* **11** (2017) 044, arXiv:1706.07808 [hep-ph].

[430] J. Kumar, D. London, and R. Watanabe, "Combined Explanations of the $b \to s\mu^+\mu^-$ and $b \to c\tau^-\overline{\nu}$ Anomalies: a General Model Analysis," *Phys. Rev.* **D99** no. 1, (2019) 015007, arXiv:1806.07403 [hep-ph].

[431] M. Ciuchini, A. M. Coutinho, M. Fedele, E. Franco, A. Paul, L. Silvestrini, and M. Valli, "New Physics in $b \to s\ell^+\ell^-$ confronts new data on Lepton Universality," *Eur. Phys. J.* **C79** no. 8, (2019) 719, arXiv:1903.09632 [hep-ph].

[432] J. Aebischer, W. Altmannshofer, D. Guadagnoli, M. Reboud, P. Stangl, and D. M. Straub, "B-decay discrepancies after Moriond 2019," *Eur. Phys. J.* **C80** no. 3, (2020) 252, arXiv:1903.10434 [hep-ph].

[433] C. Cornella, J. Fuentes-Martin, and G. Isidori, "Revisiting the vector leptoquark explanation of the B-physics anomalies," *JHEP* **07** (2019) 168, arXiv:1903.11517 [hep-ph].

[434] **LHCb** Collaboration, R. Aaij *et al.*, "Test of lepton universality using $B^+ \to K^+\ell^+\ell^-$ decays," *Phys. Rev. Lett.* **113** (2014) 151601, arXiv:1406.6482 [hep-ex].

[435] **LHCb** Collaboration, R. Aaij *et al.*, "Test of lepton universality with $B^0 \to K^{*0}\ell^+\ell^-$ decays," *JHEP* **08** (2017) 055, arXiv:1705.05802 [hep-ex].

[436] **LHCb** Collaboration, R. Aaij *et al.*, "Search for lepton-universality violation in $B^+ \to K^+\ell^+\ell^-$ decays," *Phys. Rev. Lett.* **122** no. 19, (2019) 191801, arXiv:1903.09252 [hep-ex].

[437] **Belle** Collaboration, A. Abdesselam *et al.*, "Test of lepton flavor universality in $B \to K^*\ell^+\ell^-$ decays at Belle," arXiv:1904.02440 [hep-ex].

[438] G. Hiller and M. Schmaltz, "R_K and future $b \to s\ell\ell$ physics beyond the standard model opportunities," *Phys. Rev.* **D90** (2014) 054014, arXiv:1408.1627 [hep-ph].

[439] G. Hiller and M. Schmaltz, "Diagnosing lepton-nonuniversality in $b \to s\ell\ell$," *JHEP* **02** (2015) 055, arXiv:1411.4773 [hep-ph].

[440] M. Bordone, G. Isidori, and A. Pattori, "On the Standard Model predictions for R_K and R_{K^*}," *Eur. Phys. J. C* **76** no. 8, (2016) 440, arXiv:1605.07633 [hep-ph].

[441] G. D'Amico, M. Nardecchia, P. Panci, F. Sannino, A. Strumia, R. Torre, and A. Urbano, "Flavour anomalies after the R_{K^*} measurement," *JHEP* **09** (2017) 010, arXiv:1704.05438 [hep-ph].

[442] L.-S. Geng, B. Grinstein, S. Jäger, J. Martin Camalich, X.-L. Ren, and R.-X. Shi, "Towards the discovery of new physics with lepton-universality ratios of $b \to s\ell\ell$ decays," *Phys. Rev. D* **96** no. 9, (2017) 093006, arXiv:1704.05446 [hep-ph].

[443] B. Capdevila, A. Crivellin, S. Descotes-Genon, J. Matias, and J. Virto, "Patterns of New Physics in $b \to s\ell^+\ell^-$ transitions in the light of recent data," *JHEP* **01** (2018) 093, arXiv:1704.05340 [hep-ph].

[444] M. Ciuchini, A. M. Coutinho, M. Fedele, E. Franco, A. Paul, L. Silvestrini, and M. Valli, "On Flavourful Easter eggs for New Physics hunger and Lepton Flavour Universality violation," *Eur. Phys. J.* **C77** no. 10, (2017) 688, arXiv:1704.05447 [hep-ph].

[445] G. Hiller and I. Nisandzic, "R_K and R_{K^*} beyond the standard model," *Phys. Rev. D* **96** no. 3, (2017) 035003, arXiv:1704.05444 [hep-ph].

[446] A. K. Alok, A. Dighe, S. Gangal, and D. Kumar, "Continuing search for new physics in $b \to s\mu\mu$ decays: two operators at a time," *JHEP* **06** (2019) 089, arXiv:1903.09617 [hep-ph].

[447] M. Algueró, B. Capdevila, A. Crivellin, S. Descotes-Genon, P. Masjuan, J. Matias, M. Novoa, and J. Virto, "Emerging patterns of New Physics with and without Lepton Flavour Universal contributions," *Eur. Phys. J. C* **79** no. 8, (2019) 714, arXiv:1903.09578 [hep-ph].

[448] K. Kowalska, D. Kumar, and E. M. Sessolo, "Implications for new physics in $b \to s\mu\mu$ transitions after recent measurements by Belle and LHCb," *Eur. Phys. J. C* **79** no. 10, (2019) 840, arXiv:1903.10932 [hep-ph].

[449] A. Arbey, T. Hurth, F. Mahmoudi, D. M. Santos, and S. Neshatpour, "Update on the b→s anomalies," *Phys. Rev. D* **100** no. 1, (2019) 015045, arXiv:1904.08399 [hep-ph].

[450] A. Datta, J. Kumar, and D. London, "The B anomalies and new physics in $b \to se^+e^-$," *Phys. Lett. B* **797** (2019) 134858, arXiv:1903.10086 [hep-ph].

[451] S. Descotes-Genon, J. Matias, and J. Virto, "Understanding the $B \to K^*\mu^+\mu^-$ Anomaly," *Phys. Rev.* **D88** (2013) 074002, arXiv:1307.5683 [hep-ph].

[452] S. Descotes-Genon, L. Hofer, J. Matias, and J. Virto, "Global analysis of $b \to s\ell\ell$ anomalies," *JHEP* **06** (2016) 092, arXiv:1510.04239 [hep-ph].

[453] **LHCb** Collaboration, R. Aaij *et al.*, "Measurement of *CP*-averaged observables in the $B^0 \to K^{*0}\mu^+\mu^-$ decay," arXiv:2003.04831 [hep-ex].

[454] A. Khodjamirian, T. Mannel, A. A. Pivovarov, and Y. M. Wang, "Charm-loop effect in $B \to K^{(*)}\ell^+\ell^-$ and $B \to K^*\gamma$," *JHEP* **09** (2010) 089, arXiv:1006.4945 [hep-ph].

[455] J. Lyon and R. Zwicky, "Resonances gone topsy turvy - the charm of QCD or new physics in $b \to s\ell^+\ell^-$?," arXiv:1406.0566 [hep-ph].

[456] V. Chobanova, T. Hurth, F. Mahmoudi, D. Martinez Santos, and S. Neshatpour, "Large hadronic power corrections or new physics in the rare decay $B \to K^* \mu^+ \mu^-$," *JHEP* **07** (2017) 025, arXiv:1702.02234 [hep-ph].

[457] T. Blake, U. Egede, P. Owen, K. A. Petridis, and G. Pomery, "An empirical model to determine the hadronic resonance contributions to $\overline{B}^0 \to \overline{K}^{*0} \mu^+ \mu^-$ transitions," *Eur. Phys. J. C* **78** no. 6, (2018) 453, arXiv:1709.03921 [hep-ph].

[458] C. Bobeth, M. Chrzaszcz, D. van Dyk, and J. Virto, "Long-distance effects in $B \to K^* \ell\ell$ from analyticity," *Eur. Phys. J. C* **78** no. 6, (2018) 451, arXiv:1707.07305 [hep-ph].

[459] S. Jäger and J. Martin Camalich, "Reassessing the discovery potential of the $B \to K^* \ell^+ \ell^-$ decays in the large-recoil region: SM challenges and BSM opportunities," *Phys. Rev. D* **93** no. 1, (2016) 014028, arXiv:1412.3183 [hep-ph].

[460] M. Ciuchini, M. Fedele, E. Franco, S. Mishima, A. Paul, L. Silvestrini, and M. Valli, "$B \to K^* \ell^+ \ell^-$ decays at large recoil in the Standard Model: a theoretical reappraisal," *JHEP* **06** (2016) 116, arXiv:1512.07157 [hep-ph].

[461] A. Arbey, T. Hurth, F. Mahmoudi, and S. Neshatpour, "Hadronic and New Physics Contributions to $b \to s$ Transitions," *Phys. Rev. D* **98** no. 9, (2018) 095027, arXiv:1806.02791 [hep-ph].

[462] M. Chrzaszcz, A. Mauri, N. Serra, R. Silva Coutinho, and D. van Dyk, "Prospects for disentangling long- and short-distance effects in the decays $B \to K^* \mu^+ \mu^-$," *JHEP* **10** (2019) 236, arXiv:1805.06378 [hep-ph].

[463] M. Ciuchini, A. M. Coutinho, M. Fedele, E. Franco, A. Paul, L. Silvestrini, and M. Valli, "Hadronic uncertainties in semileptonic $B \to K^* \mu^+ \mu^-$ decays," *PoS* **BEAUTY2018** (2018) 044, arXiv:1809.03789 [hep-ph].

[464] T. Hurth, F. Mahmoudi, and S. Neshatpour, "On the new LHCb angular analysis of $B \to K^* \mu^+ \mu^-$: Hadronic effects or New Physics?," arXiv:2006.04213 [hep-ph].

[465] B. Capdevila, S. Descotes-Genon, J. Matias, and J. Virto, "Assessing lepton-flavour non-universality from $B \to K^* \ell\ell$ angular analyses," *JHEP* **10** (2016) 075, arXiv:1605.03156 [hep-ph].

[466] N. Serra, R. Silva Coutinho, and D. van Dyk, "Measuring the breaking of lepton flavor universality in $B \to K^* \ell^+ \ell^-$," *Phys. Rev. D* **95** no. 3, (2017) 035029, arXiv:1610.08761 [hep-ph].

[467] **Belle** Collaboration, S. Wehle *et al.*, "Lepton-Flavor-Dependent Angular Analysis of $B \to K^* \ell^+ \ell^-$," *Phys. Rev. Lett.* **118** no. 11, (2017) 111801, arXiv:1612.05014 [hep-ex].

[468] M. Algueró, B. Capdevila, S. Descotes-Genon, P. Masjuan, and J. Matias, "What R_K and Q_5 can tell us about New Physics in $b \to s\ell\ell$ transitions?," *JHEP* **07** (2019) 096, arXiv:1902.04900 [hep-ph].

[469] **Belle-II** Collaboration, W. Altmannshofer *et al.*, "The Belle II Physics Book," *PTEP* **2019** no. 12, (2019) 123C01, arXiv:1808.10567 [hep-ex]. [Erratum: PTEP 2020, 029201 (2020)].

[470] **LHCb** Collaboration, R. Aaij *et al.*, "Search for the rare decays $B_s^0 \to e^+e^-$ and $B^0 \to e^+e^-$," *Phys. Rev. Lett.* **124** no. 21, (2020) 211802, arXiv:2003.03999 [hep-ex].

[471] **CMS** Collaboration, S. Chatrchyan *et al.*, "Measurement of the $B_s^0 \to \mu^+\mu^-$ Branching Fraction and Search for $B^0 \to \mu^+\mu^-$ with the CMS Experiment," *Phys. Rev. Lett.* **111** (2013) 101804, arXiv:1307.5025 [hep-ex].

[472] **LHCb** Collaboration, R. Aaij *et al.*, "Measurement of the $B_s^0 \to \mu^+\mu^-$ branching fraction and effective lifetime and search for $B^0 \to \mu^+\mu^-$ decays," *Phys. Rev. Lett.* **118** no. 19, (2017) 191801, arXiv:1703.05747 [hep-ex].

[473] **ATLAS** Collaboration, M. Aaboud *et al.*, "Study of the rare decays of B_s^0 and B^0 mesons into muon pairs using data collected during 2015 and 2016 with the ATLAS detector," *JHEP* **04** (2019) 098, arXiv:1812.03017 [hep-ex].

[474] C. Bobeth, M. Gorbahn, T. Hermann, M. Misiak, E. Stamou, and M. Steinhauser, "$B_{s,d} \to l^+l^-$ in the Standard Model with Reduced Theoretical Uncertainty," *Phys. Rev. Lett.* **112** (2014) 101801, arXiv:1311.0903 [hep-ph].

[475] A. Azatov, D. Bardhan, D. Ghosh, F. Sgarlata, and E. Venturini, "Anatomy of $b \to c\tau\nu$ anomalies," *JHEP* **11** (2018) 187, arXiv:1805.03209 [hep-ph].

[476] A. K. Alok, D. Kumar, S. Kumbhakar, and S. Uma Sankar, "Solutions to R_D-R_{D^*} in light of Belle 2019 data," *Nucl. Phys. B* **953** (2020) 114957, arXiv:1903.10486 [hep-ph].

[477] C. Murgui, A. Peñuelas, M. Jung, and A. Pich, "Global fit to $b \to c\tau\nu$ transitions," *JHEP* **09** (2019) 103, arXiv:1904.09311 [hep-ph].

[478] R.-X. Shi, L.-S. Geng, B. Grinstein, S. Jäger, and J. Martin Camalich, "Revisiting the new-physics interpretation of the $b \to c\tau\nu$ data," *JHEP* **12** (2019) 065, arXiv:1905.08498 [hep-ph].

[479] **BaBar** Collaboration, J. Lees *et al.*, "Measurement of an Excess of $\overline{B} \to D^{(*)}\tau^-\overline{\nu}_\tau$ Decays and Implications for Charged Higgs Bosons," *Phys. Rev. D* **88** no. 7, (2013) 072012, arXiv:1303.0571 [hep-ex].

[480] **Belle** Collaboration, M. Huschle *et al.*, "Measurement of the branching ratio of $\overline{B} \to D^{(*)}\tau^-\overline{\nu}_\tau$ relative to $\overline{B} \to D^{(*)}\ell^-\overline{\nu}_\ell$ decays with hadronic tagging at Belle," *Phys. Rev. D* **92** no. 7, (2015) 072014, arXiv:1507.03233 [hep-ex].

[481] **LHCb** Collaboration, R. Aaij *et al.*, "Measurement of the ratio of the $B^0 \to D^{*-}\tau^+\nu_\tau$ and $B^0 \to D^{*-}\mu^+\nu_\mu$ branching fractions using three-prong τ-lepton decays," *Phys. Rev. Lett.* **120** no. 17, (2018) 171802, arXiv:1708.08856 [hep-ex].

[482] L. Di Luzio, A. Greljo, and M. Nardecchia, "Gauge leptoquark as the origin of B-physics anomalies," *Phys. Rev. D* **96** no. 11, (2017) 115011, arXiv:1708.08450 [hep-ph].

[483] L. Calibbi, A. Crivellin, and T. Li, "Model of vector leptoquarks in view of the B-physics anomalies," *Phys. Rev. D* **98** no. 11, (2018) 115002, arXiv:1709.00692 [hep-ph].

[484] M. Bordone, C. Cornella, J. Fuentes-Martin, and G. Isidori, "A three-site gauge model for flavor hierarchies and flavor anomalies," *Phys. Lett. B* **779** (2018) 317–323, arXiv:1712.01368 [hep-ph].

[485] R. Barbieri and A. Tesi, "B-decay anomalies in Pati-Salam SU(4)," *Eur. Phys. J. C* **78** no. 3, (2018) 193, arXiv:1712.06844 [hep-ph].

[486] N. Assad, B. Fornal, and B. Grinstein, "Baryon Number and Lepton Universality Violation in Leptoquark and Diquark Models," *Phys. Lett. B* **777** (2018) 324–331, arXiv:1708.06350 [hep-ph].

[487] J. Heeck and D. Teresi, "Pati-Salam explanations of the B-meson anomalies," *JHEP* **12** (2018) 103, arXiv:1808.07492 [hep-ph].

[488] B. Fornal, S. A. Gadam, and B. Grinstein, "Left-Right SU(4) Vector Leptoquark Model for Flavor Anomalies," *Phys. Rev. D* **99** no. 5, (2019) 055025, arXiv:1812.01603 [hep-ph].

[489] A. Crivellin, C. Greub, D. Müller, and F. Saturnino, "Importance of Loop Effects in Explaining the Accumulated Evidence for New Physics in B Decays with a Vector Leptoquark," *Phys. Rev. Lett.* **122** no. 1, (2019) 011805, arXiv:1807.02068 [hep-ph].

[490] A. Crivellin, D. Müller, and F. Saturnino, "Flavor Phenomenology of the Leptoquark Singlet-Triplet Model," *JHEP* **06** (2020) 020, arXiv:1912.04224 [hep-ph].

[491] M. Bordone, O. Catà, and T. Feldmann, "Effective Theory Approach to New Physics with Flavour: General Framework and a Leptoquark Example," *JHEP* **01** (2020) 067, arXiv:1910.02641 [hep-ph].

[492] **UTfit** Collaboration, M. Bona *et al.*, "Model-independent constraints on $\Delta F = 2$ operators and the scale of new physics," *JHEP* **03** (2008) 049, arXiv:0707.0636 [hep-ph].

[493] A. Greljo and D. Marzocca, "High-p_T dilepton tails and flavor physics," *Eur. Phys. J.* **C77** no. 8, (2017) 548, arXiv:1704.09015 [hep-ph].

[494] M. J. Baker, J. Fuentes-Martín, G. Isidori, and M. König, "High- p_T signatures in vector–leptoquark models," *Eur. Phys. J.* **C79** no. 4, (2019) 334, arXiv:1901.10480 [hep-ph].

[495] L. Calibbi, A. Crivellin, and T. Ota, "Effective Field Theory Approach to $b \to s\ell\ell^{(')}$, $B \to K^{(*)}\nu\overline{\nu}$ and $B \to D^{(*)}\tau\nu$ with Third Generation Couplings," *Phys. Rev. Lett.* **115** (2015) 181801, arXiv:1506.02661 [hep-ph].

[496] I. Doršner, S. Fajfer, A. Greljo, J. Kamenik, and N. Košnik, "Physics of leptoquarks in precision experiments and at particle colliders," *Phys. Rept.* **641** (2016) 1–68, arXiv:1603.04993 [hep-ph].

[497] **Belle** Collaboration, S. Hirose *et al.*, "Measurement of the τ lepton polarization and $R(D^*)$ in the decay $\overline{B} \to D^*\tau^-\overline{\nu}_\tau$," *Phys. Rev. Lett.* **118** no. 21, (2017) 211801, arXiv:1612.00529 [hep-ex].

[498] **Belle** Collaboration, A. Abdesselam *et al.*, "Measurement of $\mathcal{R}(D)$ and $\mathcal{R}(D^*)$ with a semileptonic tagging method," arXiv:1904.08794 [hep-ex].

[499] D. Bigi and P. Gambino, "Revisiting $B \to D\ell\nu$," *Phys. Rev. D* **94** no. 9, (2016) 094008, arXiv:1606.08030 [hep-ph].

[500] F. U. Bernlochner, Z. Ligeti, M. Papucci, and D. J. Robinson, "Combined analysis of semileptonic B decays to D and D^*: $R(D^{(*)})$, $|V_{cb}|$, and new physics," *Phys. Rev. D* **95** no. 11, (2017) 115008, arXiv:1703.05330 [hep-ph]. [Erratum: Phys.Rev.D 97, 059902 (2018)].

[501] D. Bigi, P. Gambino, and S. Schacht, "$R(D^*)$, $|V_{cb}|$, and the Heavy Quark Symmetry relations between form factors," *JHEP* **11** (2017) 061, arXiv:1707.09509 [hep-ph].

[502] S. Jaiswal, S. Nandi, and S. K. Patra, "Extraction of $|V_{cb}|$ from $B \to D^{(*)}\ell\nu_\ell$ and the Standard Model predictions of $R(D^{(*)})$," *JHEP* **12** (2017) 060, arXiv:1707.09977 [hep-ph].

[503] J. F. Kamenik, Y. Soreq, and J. Zupan, "Lepton flavor universality violation without new sources of quark flavor violation," *Phys. Rev.* **D97** no. 3, (2018) 035002, arXiv:1704.06005 [hep-ph].

[504] P. J. Fox, I. Low, and Y. Zhang, "Top-philic Z' forces at the LHC," *JHEP* **03** (2018) 074, arXiv:1801.03505 [hep-ph].

[505] J. E. Camargo-Molina, A. Celis, and D. A. Faroughy, "Anomalies in Bottom from new physics in Top," *Phys. Lett.* **B784** (2018) 284–293, arXiv:1805.04917 [hep-ph].

[506] L. Di Luzio and M. Nardecchia, "What is the scale of new physics behind the B-flavour anomalies?," *Eur. Phys. J. C* **77** no. 8, (2017) 536, arXiv:1706.01868 [hep-ph].

[507] A. Buras, P. Gambino, M. Gorbahn, S. Jager, and L. Silvestrini, "Universal unitarity triangle and physics beyond the standard model," *Phys. Lett. B* **500** (2001) 161–167, arXiv:hep-ph/0007085.

[508] A. L. Kagan, G. Perez, T. Volansky, and J. Zupan, "General Minimal Flavor Violation," *Phys. Rev. D* **80** (2009) 076002, arXiv:0903.1794 [hep-ph].

[509] A. Efrati, A. Falkowski, and Y. Soreq, "Electroweak constraints on flavorful effective theories," *JHEP* **07** (2015) 018, arXiv:1503.07872 [hep-ph].

[510] R. Coy, M. Frigerio, F. Mescia, and O. Sumensari, "New physics in $b \to s\ell\ell$ transitions at one loop," *Eur. Phys. J. C* **80** no. 1, (2020) 52, arXiv:1909.08567 [hep-ph].

[511] M. Ciuchini, M. Fedele, E. Franco, S. Mishima, A. Paul, L. Silvestrini, and M. Valli, "$B \to K^*\ell^+\ell^-$ in the Standard Model: Elaborations and Interpretations," *PoS* **ICHEP2016** (2016) 584, arXiv:1611.04338 [hep-ph].

[512] M. Ciuchini, M. Fedele, E. Franco, S. Mishima, A. Paul, L. Silvestrini, and M. Valli, "Knowns and Unknowns in the Predictions for $B \to K^*\mu^+\mu^-$," *Nucl. Part. Phys. Proc.* **285-286** (2017) 45–49.

[513] M. Ciuchini, A. M. Coutinho, M. Fedele, E. Franco, A. Paul, L. Silvestrini, and M. Valli, "On hadronic uncertainties polluting the New Physics hunt in $b \to s$ transitions," *Nucl. Part. Phys. Proc.* **303-305** (2018) 8–13.

[514] W. Buchmuller and D. Wyler, "Effective Lagrangian Analysis of New Interactions and Flavor Conservation," *Nucl. Phys. B* **268** (1986) 621–653.

[515] W. Altmannshofer, A. J. Buras, D. M. Straub, and M. Wick, "New strategies for New Physics search in $B \to K^*\nu\overline{\nu}$, $B \to K\nu\overline{\nu}$ and $B \to X_s\nu\overline{\nu}$ decays," *JHEP* **04** (2009) 022, arXiv:0902.0160 [hep-ph].

[516] A. J. Buras, J. Girrbach-Noe, C. Niehoff, and D. M. Straub, "$B \to K^{(*)}\nu\overline{\nu}$ decays in the Standard Model and beyond," *JHEP* **02** (2015) 184, arXiv:1409.4557 [hep-ph].

[517] S. Descotes-Genon, S. Fajfer, J. F. Kamenik, and M. Novoa-Brunet, "Implications of $b \to s\mu\mu$ Anomalies for Future Measurements of $B \to K^{(*)}\nu\overline{\nu}$ and $K \to \pi\nu\overline{\nu}$," arXiv:2005.03734 [hep-ph].

[518] J. Aebischer, A. Crivellin, M. Fael, and C. Greub, "Matching of gauge invariant dimension-six operators for $b \to s$ and $b \to c$ transitions," *JHEP* **05** (2016) 037, arXiv:1512.02830 [hep-ph].

[519] C. Bobeth, A. J. Buras, A. Celis, and M. Jung, "Yukawa enhancement of Z-mediated new physics in $\Delta S = 2$ and $\Delta B = 2$ processes," *JHEP* **07** (2017) 124, arXiv:1703.04753 [hep-ph].

[520] G. Buchalla, A. J. Buras, and M. E. Lautenbacher, "Weak decays beyond leading logarithms," *Rev. Mod. Phys.* **68** (1996) 1125–1144, arXiv:hep-ph/9512380.

[521] A. J. Buras, "Weak Hamiltonian, CP violation and rare decays," in *Les Houches Summer School in Theoretical Physics, Session 68: Probing the Standard Model of Particle Interactions*, pp. 281–539. 6, 1998. arXiv:hep-ph/9806471.

[522] L. Silvestrini, "Effective Theories for Quark Flavour Physics," in *Les Houches summer school: EFT in Particle Physics and Cosmology*. 5, 2019. arXiv:1905.00798 [hep-ph].

[523] J. de Blas, G. Durieux, C. Grojean, J. Gu, and A. Paul, "On the future of Higgs, electroweak and diboson measurements at lepton colliders," *JHEP* **12** (2019) 117, arXiv:1907.04311 [hep-ph].

[524] B. Capdevila, A. Crivellin, C. A. Manzari, and M. Montull, "Explaining $b \to s\ell^+\ell^-$ and the Cabbibo Angle Anomaly with a Vector Triplet," arXiv:2005.13542 [hep-ph].

[525] B. Belfatto, R. Beradze, and Z. Berezhiani, "The CKM unitarity problem: A trace of new physics at the TeV scale?," *Eur. Phys. J. C* **80** no. 2, (2020) 149, arXiv:1906.02714 [hep-ph].

[526] Y. Grossman, E. Passemar, and S. Schacht, "On the Statistical Treatment of the Cabibbo Angle Anomaly," arXiv:1911.07821 [hep-ph].

[527] A. Caldwell, D. Kollár, and K. Kröninger, "BAT - The Bayesian analysis toolkit," *Computer Physics Communications* **180** no. 11, (Nov., 2009) 2197–2209, arXiv:0808.2552 [physics.data-an].

[528] **SLD** Collaboration, K. Abe *et al.*, "First direct measurement of the parity violating coupling of the Z0 to the s quark," *Phys. Rev. Lett.* **85** (2000) 5059–5063, arXiv:hep-ex/0006019 [hep-ex].

[529] **ALEPH, DELPHI, L3, OPAL, LEP Electroweak** Collaboration, S. Schael *et al.*, "Electroweak Measurements in Electron-Positron Collisions at W-Boson-Pair Energies at LEP," *Phys. Rept.* **532** (2013) 119–244, arXiv:1302.3415 [hep-ex].

[530] **ATLAS** Collaboration, M. Aaboud *et al.*, "Measurement of the W-boson mass in pp collisions at $\sqrt{s} = 7$ TeV with the ATLAS detector," *Eur. Phys. J. C* **78** no. 2, (2018) 110, arXiv:1701.07240 [hep-ex]. [Erratum: Eur.Phys.J.C 78, 898 (2018)].

[531] **CMS** Collaboration, V. Khachatryan *et al.*, "Measurement of the t-channel single-top-quark production cross section and of the $|V_{tb}|$ CKM matrix element in pp collisions at $\sqrt{s}$= 8 TeV," *JHEP* **06** (2014) 090, arXiv:1403.7366 [hep-ex].

[532] **D0** Collaboration, V. Abazov *et al.*, "Measurement of $\sin^2\theta^{\ell}_{\rm eff}$ and Z-light quark couplings using the forward-backward charge asymmetry in $p\overline{p} \to Z/\gamma^* \to e^+e^-$ events with $\mathcal{L} = 5.0$ fb^{-1} at $\sqrt{s} = 1.96$ TeV," *Phys. Rev. D* **84** (2011) 012007, arXiv:1104.4590 [hep-ex].

[533] **ATLAS** Collaboration, M. Aaboud *et al.*, "Angular analysis of $B^0_d \to K^*\mu^+\mu^-$ decays in pp collisions at $\sqrt{s} = 8$ TeV with the ATLAS detector," *JHEP* **10** (2018) 047, arXiv:1805.04000 [hep-ex].

[534] **CMS** Collaboration, V. Khachatryan *et al.*, "Angular analysis of the decay $B^0 \to K^{*0}\mu^+\mu^-$ from pp collisions at $\sqrt{s} = 8$ TeV," *Phys. Lett.* **B753** (2016) 424–448, arXiv:1507.08126 [hep-ex].

[535] **CMS** Collaboration, A. M. Sirunyan *et al.*, "Measurement of angular parameters from the decay $\mathrm{B}^0 \to \mathrm{K}^{*0}\mu^+\mu^-$ in proton-proton collisions at $\sqrt{s} = 8$ TeV," *Phys. Lett.* **B781** (2018) 517–541, arXiv:1710.02846 [hep-ex].

[536] **LHCb** Collaboration, R. Aaij *et al.*, "Angular analysis of the $B^0 \to K^{*0}e^+e^-$ decay in the low-q^2 region," *JHEP* **04** (2015) 064, arXiv:1501.03038 [hep-ex].

[537] **LHCb** Collaboration, R. Aaij *et al.*, "Measurements of the S-wave fraction in $B^0 \to K^+\pi^-\mu^+\mu^-$ decays and the $B^0 \to K^*(892)^0\mu^+\mu^-$ differential branching fraction," *JHEP* **11** (2016) 047, arXiv:1606.04731 [hep-ex]. [Erratum: JHEP04,142(2017)].

[538] A. Paul and D. M. Straub, "Constraints on new physics from radiative B decays," *JHEP* **04** (2017) 027, arXiv:1608.02556 [hep-ph].

[539] **HFLAV** Collaboration, Y. S. Amhis *et al.*, "Averages of b-hadron, c-hadron, and τ-lepton properties as of 2018," arXiv:1909.12524 [hep-ex].

[540] **LHCb** Collaboration, R. Aaij *et al.*, "Differential branching fractions and isospin asymmetries of $B \to K^{(*)}\mu^+\mu^-$ decays," *JHEP* **06** (2014) 133, arXiv:1403.8044 [hep-ex].

[541] **LHCb** Collaboration, R. Aaij *et al.*, "Angular analysis and differential branching fraction of the decay $B^0_s \to \phi\mu^+\mu^-$," *JHEP* **09** (2015) 179, arXiv:1506.08777 [hep-ex].

[542] **LHCb** Collaboration, R. Aaij *et al.*, "Measurement of the ratio of branching fractions $BR(B_0 \to K^{\star 0}\gamma)/BR(B_{s0} \to \phi\gamma)$ and the direct CP asymmetry in $B_0 \to K^{\star 0}\gamma$," *Nucl. Phys.* **B867** (2013) 1–18, arXiv:1209.0313 [hep-ex].

[543] T. Hurth, F. Mahmoudi, and S. Neshatpour, "Global fits to $b \to s\ell\ell$ data and signs for lepton non-universality," *JHEP* **12** (2014) 053, arXiv:1410.4545 [hep-ph].

[544] **CCFR** Collaboration, S. Mishra *et al.*, "Neutrino tridents and W Z interference," *Phys. Rev. Lett.* **66** (1991) 3117–3120.

[545] **ATLAS** Collaboration, M. Aaboud *et al.*, "Search for new high-mass phenomena in the dilepton final state using 36 fb^{-1} of proton-proton collision data at $\sqrt{s} = 13$ TeV with the ATLAS detector," *JHEP* **10** (2017) 182, arXiv:1707.02424 [hep-ex].

[546] **CMS** Collaboration, A. M. Sirunyan *et al.*, "Search for standard model production of four top quarks with same-sign and multilepton final states in proton–proton collisions at $\sqrt{s} = 13\,\text{TeV}$," *Eur. Phys. J. C* **78** no. 2, (2018) 140, arXiv:1710.10614 [hep-ex].

[547] **ATLAS** Collaboration, M. Aaboud *et al.*, "Search for pair production of heavy vector-like quarks decaying into high-p_T gy bosons and top quarks in the lepton-plus-jets final state in pp collisions at $\sqrt{s} = 13$ TeV with the ATLAS detector," *JHEP* **08** (2018) 048, arXiv:1806.01762 [hep-ex].

[548] **CMS** Collaboration, A. M. Sirunyan *et al.*, "Search for vector-like leptons in multilepton final states in proton-proton collisions at $\sqrt{s} = 13$ TeV," *Phys. Rev. D* **100** no. 5, (2019) 052003, arXiv:1905.10853 [hep-ex].

[549] S. D. Thomas and J. D. Wells, "Phenomenology of Massive Vectorlike Doublet Leptons," *Phys. Rev. Lett.* **81** (1998) 34–37, arXiv:hep-ph/9804359.

[550] F. del Aguila, J. de Blas, and M. Perez-Victoria, "Effects of new leptons in Electroweak Precision Data," *Phys. Rev. D* **78** (2008) 013010, arXiv:0803.4008 [hep-ph].

[551] K. Kannike, M. Raidal, D. M. Straub, and A. Strumia, "Anthropic solution to the magnetic muon anomaly: the charged see-saw," *JHEP* **02** (2012) 106, arXiv:1111.2551 [hep-ph]. [Erratum: JHEP10,136(2012)].

[552] N. Kumar and S. P. Martin, "Vectorlike Leptons at the Large Hadron Collider," *Phys. Rev. D* **92** no. 11, (2015) 115018, arXiv:1510.03456 [hep-ph].

[553] P. N. Bhattiprolu and S. P. Martin, "Prospects for vectorlike leptons at future proton-proton colliders," *Phys. Rev. D* **100** no. 1, (2019) 015033, arXiv:1905.00498 [hep-ph].

[554] J. C. Pati and A. Salam, "Lepton Number as the Fourth Color," *Phys. Rev. D* **10** (1974) 275–289. [Erratum: Phys.Rev.D 11, 703–703 (1975)].

[555] H. Georgi and S. L. Glashow, "Unity of all elementary-particle forces," *Phys. Rev. Lett.* **32** (Feb, 1974) 438–441. https://link.aps.org/doi/10.1103/PhysRevLett.32.438.

[556] D. Bečirević and O. Sumensari, "A leptoquark model to accommodate $R_K^{\rm exp} < R_K^{\rm SM}$ and $R_{K^*}^{\rm exp} < R_{K^*}^{\rm SM}$," *JHEP* **08** (2017) 104, arXiv:1704.05835 [hep-ph].

[557] W. Buchmuller, R. Ruckl, and D. Wyler, "Leptoquarks in Lepton - Quark Collisions," *Phys. Lett. B* **191** (1987) 442–448. [Erratum: Phys.Lett.B 448, 320–320 (1999)].

[558] F. del Aguila, J. de Blas, and M. Perez-Victoria, "Electroweak Limits on General New Vector Bosons," *JHEP* **09** (2010) 033, arXiv:1005.3998 [hep-ph].

[559] R. Alonso, B. Grinstein, and J. Martin Camalich, "Lepton universality violation and lepton flavor conservation in B-meson decays," *JHEP* **10** (2015) 184, arXiv:1505.05164 [hep-ph].

[560] A. Angelescu, D. Beˇ cirević, D. Faroughy, and O. Sumensari, "Closing the window on single leptoquark solutions to the B-physics anomalies," *JHEP* **10** (2018) 183, arXiv:1808.08179 [hep-ph].

[561] **LHCb** Collaboration, R. Aaij *et al.*, "Physics case for an LHCb Upgrade II - Opportunities in flavour physics, and beyond, in the HL-LHC era," arXiv:1808.08865 [hep-ex].

[562] **FCC** Collaboration, A. Abada *et al.*, "FCC Physics Opportunities: Future Circular Collider Conceptual Design Report Volume 1," *Eur. Phys. J. C* **79** no. 6, (2019) 474.

[563] **FCC** Collaboration, A. Abada *et al.*, "FCC-ee: The Lepton Collider: Future Circular Collider Conceptual Design Report Volume 2," *Eur. Phys. J. ST* **228** no. 2, (2019) 261–623.

[564] **CEPC Study Group** Collaboration, M. Dong *et al.*, "CEPC Conceptual Design Report: Volume 2 - Physics & Detector," arXiv:1811.10545 [hep-ex].

[565] P. Bambade *et al.*, "The International Linear Collider: A Global Project," arXiv:1903.01629 [hep-ex].

[566] J. de Blas *et al.*, "The CLIC Potential for New Physics," arXiv:1812.02093 [hep-ph].

[567] **LCC Physics Working Group** Collaboration, K. Fujii *et al.*, "Tests of the Standard Model at the International Linear Collider," arXiv:1908.11299 [hep-ex].

[568] J. De Blas *et al.*, "Higgs Boson Studies at Future Particle Colliders," arXiv:1905.03764 [hep-ph].

[569] Z. Han and W. Skiba, "Effective theory analysis of precision electroweak data," *Phys. Rev. D* **71** (2005) 075009, arXiv:hep-ph/0412166.

[570] F. del Aguila and J. de Blas, "Electroweak constraints on new physics," *Fortsch. Phys.* **59** (2011) 1036–1040, arXiv:1105.6103 [hep-ph].

[571] J. de Blas, "Electroweak limits on physics beyond the Standard Model," *EPJ Web Conf.* **60** (2013) 19008, arXiv:1307.6173 [hep-ph].

[572] L. Berthier and M. Trott, "Towards consistent Electroweak Precision Data constraints in the SMEFT," *JHEP* **05** (2015) 024, arXiv:1502.02570 [hep-ph].

[573] J. de Blas, M. Ciuchini, E. Franco, S. Mishima, M. Pierini, L. Reina, and L. Silvestrini, "Electroweak precision constraints at present and future colliders," *PoS* **ICHEP2016** (2017) 690, arXiv:1611.05354 [hep-ph].

[574] S. Dawson and P. P. Giardino, "Electroweak and QCD corrections to Z and W pole observables in the standard model EFT," *Phys. Rev. D* **101** no. 1, (2020) 013001, arXiv:1909.02000 [hep-ph].